CISM International Centre for Mechanical Sciences 596
Courses and Lectures

Catalin Picu
Jean-François Ganghoffer *Editors*

Mechanics of Fibrous Materials and Applications

Physical and Modeling Aspects

International Centre for Mechanical Sciences

Springer

CISM International Centre for Mechanical Sciences

Courses and Lectures

Volume 596

"For more than 40 years the book series edited by CISM, "International Centre for Mechanical Sciences: Courses and Lectures", has presented groundbreaking developments in mechanics and computational engineering methods. It covers such fields as solid and fluid mechanics, mechanics of materials, micro- and nanomechanics, biomechanics, and mechatronics. The papers are written by international authorities in the field. The books are at graduate level but may include some introductory material."

More information about this series at http://www.springer.com/series/76

Catalin Picu · Jean-François Ganghoffer
Editors

Mechanics of Fibrous Materials and Applications

Physical and Modeling Aspects

Springer

Editors
Catalin Picu
Department of Mechanical, Aerospace and Nuclear Engineering
Rensselaer Polytechnic Institute
Troy, MI, USA

Jean-François Ganghoffer
LEM3 - CNRS, Université de Lorraine
Vandœuvre-lès-Nancy, France

ISSN 0254-1971 ISSN 2309-3706 (electronic)
CISM International Centre for Mechanical Sciences
ISBN 978-3-030-23845-2 ISBN 978-3-030-23846-9 (eBook)
https://doi.org/10.1007/978-3-030-23846-9

This Springer imprint is published by the registered company Springer Nature Switzerland AG
The registered company address is: Gewerbestrasse 11, 6330 Cham, Switzerland

Preface

Materials containing fibers are present in a large variety of applications due to their high mechanical performances at low weight. Reinforcement of continua with fibers has a long history which led to the widely used class of fiber-reinforced composites. Examples include polymers reinforced with fiberglass, high-performance composites made from woven yarns, and 3D woven composites used in cutting-edge areas such as aeronautics.

Different classes of fibrous materials are those containing a crosslinked network of fibers, which may or may not be embedded in a matrix. A prominent example is nonwovens, which are used in many applications such as sound and thermal insulation, clothing, filtration, and geotextiles. Many biological materials have a random complex fibrous structure. Examples include soft connective tissue, such as tendons and ligaments, the arterial walls, and the cellular cytoskeleton. Damage accumulation, fracture, and the related nonlinear behavior under large deformations are important considerations in all these materials.

Due to their discrete architecture, fibrous media have a rather complex mechanical response, especially since multiscale aspects are essential in such structures. Individual fibers or filaments may be assembled in multiscale architectures, from fibers to complex yarns up to woven or braided structures. Their geometrical configuration, which results from the manufacturing method used and the geometry of the fibers, are not easy to capture and characterize. Moreover, they exhibit strong geometrical and material nonlinearities due to the collective motion of the fibers, fiber bundles or yarns, associated nonlinear interactions that include friction and adhesion, and the presence of large local and global deformations with evolving anisotropy and couplings between different deformation modes.

This book brings together lecture notes organized for the CISM course titled *Mechanics of Fibrous Materials and Applications: Physical and Modelling Aspects*, held in Udine from July 9 to July 13, 2018. The course objective was to present the state-of-the-art understanding in this area and to provide an overview of the theoretical, modeling and practical aspects of designing and working with fibrous materials. Six lecturers contributed to the course: Philippe Boisse (INSA Lyon, France), Jean-Francois Ganghoffer (Universite de Lorraine, France), Edoardo

Mazza (ETH Zurich, Switzerland), Mohammad Mofrad (Berkeley University, USA), Catalin Picu (Rensselaer Polytechnic Institute, USA), and Luca Placidi (Universita Uninettuno, Italy). This book summarizes this information through the perspective of four of these six lecturers, and their collaborators.

Chapter 1 by Catalin Picu, titled "Mechanics of Random Fiber Networks: Structure–Properties Relation", discusses aspects of the mechanical behavior of fibrous materials containing a random network of fibers. The focus is on identifying the network parameters that control the mechanics of the structure. Such random networks are encountered in biological tissues, scaffolds for tissue growth, and many engineering materials. The chapter presents a classification of networks based on their architecture, the type of fibers, and the essential interactions that define their overall mechanical behavior. Further, it presents key results for the linear and nonlinear response of networks subjected to tension and compression, including relations between various parameters of the network and the described mechanical behavior. A similar analysis is presented for the strength of networks and its dependence on network parameters. A separate subsection is devoted to crosslinked and non-crosslinked networks in which fibers interact adhesively. In this case, adhesion reorganizes the network and imparts a particular mechanical behavior to the ensemble.

Chapter 2 by Jean-François Ganghoffer, Ibrahim Goda, Khaled ElNady, and Yosra Rahali, titled "Prediction of the Effective Mechanical Properties of Regular and Random Fibrous Materials Based on the Mechanics of Generalized Continua", presents homogenization approaches for fibrous materials, leading to nonlocal continuum formulations. Periodic fibrous preforms and composites are discussed first, for which a dedicated discrete homogenization approach is developed to derive the effective mechanical response of the unit cell, successively in the small and large transformations frameworks. This captures the effect of geometric and mechanical micro-parameters of the fibrous architecture on the overall response of the equivalent continuum. Such computational homogenization methods allow identifying hyperelastic models for fibrous media. Further, this methodology is extended to the more complex random fibrous media. The mechanical response of such random networks is analyzed in both the affine and non-affine deformation regimes, as a function of network density and window size. The homogenization techniques discussed are computationally efficient, are versatile with respect to the topology of the textile, which allows exploring single layer and multilayer 3D textile architectures, and account for intrinsic microstructural effects within the framework of generalized continua.

Chapter 3 by Luca Placidi, Francesco dell'Isola, and Emilio Barchiesi, titled "Heuristic Homogenization of Euler and Pantographic Beams", discusses designs that allow producing at the macro-level a beam which can be both extensible and flexible. Using an asymptotic expansion and rescaling suitably the relevant stiffnesses, it is shown that a pantographic microstructure does induce, at the macro-level, such desired mechanical behavior. Thus, in an analogous fashion to that of variational asymptotic methods, and following a mathematical approach resembling that used by Piola, the asymptotic expansions of kinematic descriptors

are used directly into the postulated energy functional and a heuristic homogenization procedure is presented and applied to the cases of Euler and pantographic beams.

Chapter 4 by Philippe Boisse, titled "Simulation of Continuous Fiber Composite Forming", addresses the issue of forming dry and prepreg continuous fiber composite reinforcements. The manufacture of composite parts often requires the draping of the textile reinforcement on a surface, which involves complex deformations of the prepreg. The prediction and optimization of this process are complicated by the fact that fibers are almost rigid in tension, but slide easily relative to each other. The simulation of the draping process requires specific approaches and constitutive models. The material is modeled macroscopically as a continuum using shell finite elements. The tests necessary to identify the tensile, shear, and bending behavior of the textile material are presented. The influence of different stiffnesses on the modeling of wrinkles is analyzed. The second part of the chapter is devoted to thermoforming, which is a coupled thermo-mechanical problem with temperature-dependent constitutive behavior and heat transfer between material and tool.

We wish to express our gratitude to the lecturers for their efforts and dedication, to the Board of CISM for making this course possible, and to the participants for their interest in this subject and engaging discussions during the course. We also thank Prof. Paolo Serafini, the Executive Editor of the CISM Publications series, and all those involved in the preparation of the present book for publication.

Troy, USA — Catalin Picu
Vandœuvre-lès-Nancy, France — Jean-François Ganghoffer
May 2019

Contents

Chapter 1
Mechanics of Random Fiber Networks: Structure–Properties Relation

Catalin R. Picu

Abstract This chapter presents an overview of the mechanics of random fiber networks with emphasis on the structure–properties relationship. The discussion begins with a classification of the types of fibers, including thermal and athermal fibers, and the types of crosslinks commonly encountered in engineered and biological networks. Further, a classification of networks is presented. The parameters used to describe the network structure are introduced along with geometric relations between quantities such as the density, mean fiber segment length, and crosslink density. The large strains behavior of networks measured in tension and compression, as revealed by models and experiments performed with various types of network materials, is presented. This is characterized by strong non-linearity, large sensitivity of the overall response to network structural parameters, and a large Poisson effect. The strength of networks is discussed in the context of structures with and without pre-existing cracks. It is shown that the strength is independent of the fiber properties and depends on the density and strength of the crosslinks, as well as on the mean fiber segment length. Finally, the structure and mechanical behavior of networks with inter-fiber adhesive interactions are evaluated. These are controlled by the strength of adhesion. In networks with strong adhesion and relatively thin fibers, the fibers self-organize leading to the formation of a cellular network of fiber bundles. Such cellular networks are stable and have a mechanical behavior qualitatively similar to that of crosslinked networks of individual fibers. This discussion demonstrates the broad range of mechanical behaviors that can be obtained with various network structures, hinting to the usefulness of fiber networks in many applications.

C. R. Picu (✉)
Department of Mechanical, Aerospace and Nuclear Engineering, Rensselaer Polytechnic Institute, Troy, NY 12180, USA
e-mail: picuc@rpi.edu

C. Picu and J.-F. Ganghoffer (eds.), *Mechanics of Fibrous Materials and Applications*, CISM International Centre for Mechanical Sciences 596,
https://doi.org/10.1007/978-3-030-23846-9_1

Introduction and Examples of Random Fiber Networks

Materials are, according to the Merriam-Webster Dictionary, "elements, constituents, or substances from which something can be made." In an attempt to make this very general definition more specific, let us imagine a box which we intend to fill with "a material." We could (at least imaginarily) fill this volume with a continuum, i.e., a substance with no subscale structure, which can be infinitely subdivided into smaller, similar, and featureless parts. We could also fill it with discrete entities such as beads or filaments. In this case, the condition is to "properly fill the box," in the sense that a load applied on it would be transmitted across, such that the content of the box has nonzero stiffness. It is clear that the two situations are not identical. In the first case, the box is filled entirely and there is no free volume, while in the second case, there are many empty spaces due to the way the discrete objects are packed. In the continuum case, the box has nonzero stiffness in all loading modes, while in the second, there may exist zero stiffness loading modes, as, for example, when a box filled with beads is stretched equally in all directions.

Although one may be inclined to prefer to work with the continuum, which is what technology has been doing for a long time, one observes that the second type of "material" presents some interesting advantages. First, it is much lighter and potentially cheaper to make since it uses less "building material." In the fiber-based case, percolation can be obtained at much smaller volume fractions than in the granular case. In principle, one needs only three fibers orthogonal to one another and which span the box to gain nonzero stiffness in the three directions of space, and in this case, the volume fraction of "building material" used is vanishingly small. The second observation is that a "material" made from discrete entities exhibits behaviors which are qualitatively different from those observed in the case of a continuum and hence this offers new engineering opportunities.

This comparison of continuum-like, granular, and fibrous materials points to the benefits that materials made from distinct constituents, and in particular, fibrous materials present. They are of much lower density, potentially cheaper since very little solid material is used for their construction, and exhibit an interesting set of thermomechanical properties. Therefore, it is not surprising that materials made from fibers are a common occurrence in our everyday life. The purpose of this chapter is to provide a broad overview of the mechanical behavior of a subset of fibrous materials, which have a random fiber network as their main constituent.

A network differs from a collection of fibers by the simple fact that in a network, the fibers interact and the overall behavior emerges as the net effect of these interactions mediated by the behavior of individual fibers. Furthermore, the network should span the entire problem domain in order to provide nonvanishing stiffness. We define the class of materials in which a network of filaments is the main structural component and plays the main mechanical function as "network materials."

The following brief outline indicates that network materials are ubiquitous in nature.

The cytoskeleton of eukaryotic cells is composed of a set of interpenetrating semiflexible macromolecular networks which provide the structural integrity of the cell, host the cellular organelle, and perform important functions in cellular division, migration, and chemo-mechanical transduction (Boal 2012). The cytoskeleton mechanics is a subject of intense research today driven by the desire to gain control of the biochemical activity of the cell. F-actin forms the main component of this network. It is a dense structure which is assembled from and decomposes into separate actin monomers as dictated by biochemical signals. F-actin filaments branch forming a tree-like structure. The filaments are crosslinked by myosin motors which apply forces causing the overall contraction of the network. Microtubules are polymeric chains of tubulin that are generally oriented from the nucleus to the cell membrane (Boal 2012; Mofrad 2009). These interpenetrate with the F-actin network and play a critical role in transport to and from the nucleus. Both F-actin and microtubules are semiflexible filaments, i.e., they are rather stiff in bending and have large persistence length which, in the case of the microtubules, is larger than the size of the cell. It is generally considered that microtubules are loaded mostly in compression, while the F-actin network, which concentrates and transmits the contractile force of the cell, is mostly loaded in tension (Fletcher and Mullins 2010; Ingber et al. 2014). Understanding the biomechanics of this complex network is of central importance in cellular biology.

Connective tissue restricts the relative motion of bones and other tissues, transmits loads between muscles and bones, and generally performs structural functions in the human and animal bodies. Tendons, cartilage, and ligaments belong to this class. The main component of connective tissue is collagen, which has a hierarchical fibrillar structure, Fig. 1.1a. Tropocollagen, composed of three polypeptide chains coiled around each other, forms the elementary building block of collagen. Tropocollagen organizes into bundles of collagen fibrils, which organize further at larger scales in networks of collagen fibers (Scheibel 2008). The fibers are bundles of fibrils crosslinked internally. The resulting network structure is complex and differs from

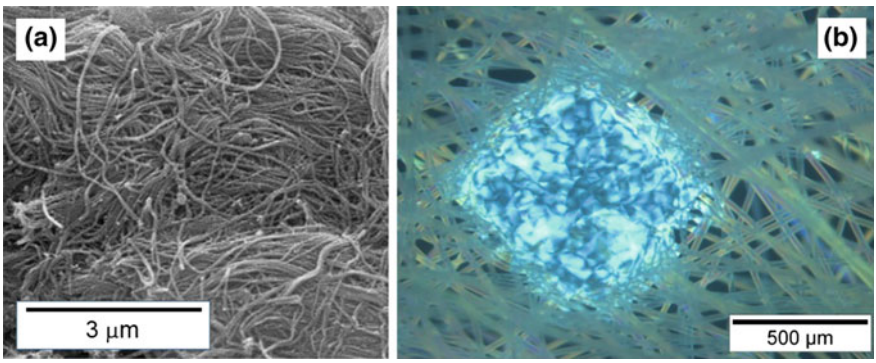

Fig. 1.1 Examples of **a** collagen network and **b** thermally bonded polypropylene nonwoven. **b** A thermal bond surrounded by the nonwoven mat. The image was obtained with cross-polarizers

one connective tissue to another. For example, in the facet capsule ligament of the cervical spine, collagen fibers are organized in sub-domains, each sub-domain having preferential orientation in space (Ban et al. 2017). The orientation in neighboring sub-domains is not correlated, such that the tissue appears as a patchwork of sub-networks. Cartilage is another example of an exquisitely organized collagen structure. Cartilage is a hydrated collagen network which embeds polar molecules called proteoglycans. These comb-like molecules bind water and swell the collagen network. Their swelling function is essential for the proper function of cartilage. It controls the response of the tissue to compressive loads and, importantly, the rate of drainage of free water when the tissue is loaded (Athesian 2009). Collagen is oriented in the direction tangential to the cartilage surface close to the surface, and acquires a more random orientation in the tissue median layers (Federico and Herzog 2008). Collagen orientation close to the bone insertion is also preferential perpendicular to the bone. Collagen networks are omnipresent in the body, beyond the examples discussed here, in skin (dermis), membranes such as the liver capsule and the amnion, trachea, blood vessels, etc.

Other protein-based fibers in the body are fibrin and elastin. Fibrin is a non-globular protein which polymerizes to form a hemostatic network which embeds platelet and assists wound healing (Weisel and Litvinov 2013). Elastin typically forms co-networks with collagen and ensures the elasticity of blood vessels and other tissues. The elastin network component has higher stiffness than the collagen component at small strains, but collagen strain stiffens much more at large strains (Omelyanenko et al. 2017). Therefore, in elastin-rich tissue, the elasticity of the co-network is provided mainly by the elastin, while protection against overloads is provided by the collagen component.

Many artificial materials include fibers and a subset of them can be classified as network materials. Fiber composites include cases in which a matrix is reinforced with short fibers randomly distributed and oriented. High-performance composites contain woven fabric layers stacked together and embedded in a matrix. Such fabrics are woven with fiber bundles, as opposed to individual fibers. The fibers are long, nominally spanning the composite, and are the main load-carrying components of the material. The fabric can be regarded as a periodic network of bundles. The mechanics of woven, whether in the context of textiles or composites, has been studied extensively and is outside the scope of this discussion.

Composites that embed a percolating random network can be classified as network materials. Gels belong to this category. Gels are molecular networks, in which the molecular strands are either physically or chemically crosslinked, and which contain a fluid medium (water). The fluid is usually non-draining, and hence the network is constrained to deform at constant volume, as dictated by the matrix. Since the gel is swollen and the molecular strands are not closely packed, the material exhibits substantial elasticity and can undergo large deformations. On the other hand, a dehydrated gel has lost its hyperelasticity and is brittle. This is due to the fact that the molecular strands interact closely and are much less mobile in this case.

A classic example of network material is rubber. Natural rubber is a network of polyisoprene chains crosslinked with sulfur. Before vulcanization, rubber is a liquid, while after it becomes a thermoset. Vulcanized natural rubber does not contain addi-

tives and is a network material with no matrix or embedded phases. The network is continuous across the volume occupied by the material. However, there is much less free volume in rubber compared with hydrated gels. The molecular strands are densely packed—although, in absence of strain-induced crystallization, they remain random—and volume filling. In ambient conditions, rubber is above the glass transition temperature and hence the chains have sufficient mobility to accommodate relative deformation despite the packed structure of the material on the molecular scale. Therefore, the mechanical behavior of rubber is dictated much less by the weak intermolecular interactions than by the response of the network. If the material is cooled below the glass transition temperature, chain mobility is drastically reduced and the network response, which requires large local deformations, is not reflected in the material behavior; rubber becomes brittle and loses its hyperelasticity under these conditions.

Paper is a man-made material with a 2,000 years history. It is a dense network of cellulose fibers with a large density of crosslinks. The fibers are ribbon-like and hollow (Rigdahl and Hallmark 1986). The nature of the crosslinks is still a matter of debate. These are generally considered to be produced by hydrogen bonds between fiber surfaces brought in close contact. However, fine fibrils have been observed emerging from the contact area when pulling apart two initially bonded fibers (Schmied et al. 2013). This suggests a finer scale structure to the bond, which could be nevertheless mediated by hydrogen bonding on even finer scales. Because of its high density and crosslink density, regular paper does not exhibit hyperelastic behavior and fails at relatively small strains (Alava and Niskanen 2006).

Nonwovens form a large family of materials with applications in textiles, packaging, consumer, and hygiene products, to name a few. These are made from polymeric fibers spun from the melt onto a support surface. The fibers solidify during deposition and form a fiber mat. Standard fiber spinning obtained by forcing the melt through a spinneret produces fibers with diameter on the order of tens of microns, while electrospinning, which accelerates further the spinning filament using an electric field, can produce fibers with diameter smaller than 1 μm (Wendorff et al. 2012). The as-deposited mat is not bonded. Fibers are continuous, of large length, and are curved and randomly oriented in the plane of the mat. If the support on which the mat is deposited moves during deposition, preferential fiber alignment results on the scale of the mat, but a large degree of disorder of the fibrous structure is preserved on local scales. In most commercial products, nonwovens are used after bonding. This is usually performed by passing the mat between calendering rollers with heated punches. The fibers coming in contact with these punches melt and resolidify fast upon exit. A thermal bond results which blends together a large number of fibers (Fig. 1.1b). These bonds are distributed in a periodic pattern over the mat while the remainder of the nonwoven is not modified by the bonding process. Thermal bonds impart substantial strength and toughness to the mat and make possible the use of this cheap material (Fig. 1.1b) in a large range of applications.

Network Types and Classification

The diversity of networks encountered in applications is large and a classification is desirable. Multiple criteria can be used for classification and any network material may belong to multiple categories function of the criterion used. The classification proposed below emphasizes commonalities between various network materials.

(i) Based on fiber arrangement

Fiber networks can be woven or nonwoven/random. Obviously, woven materials are artificial, while all biological networks, and many man-made fibrous materials, have random structure. Wovens have a repeat structure and this implies that deformation is affine on the length scale of periodicity. Nonwovens have no repeat unit and deformation is entirely non-affine, in the sense that the strain measured on the local scale is different from that applied in the far field and varies spatially. This is an important difference which has implications for the overall mechanical behavior of the material. This chapter focuses on the properties of random networks.

(ii) Based on the presence of components other than the network

For the purpose of this discussion, we divide networks into three categories. The first category includes situations in which the network is the only constituent of the respective network material, as, for example, in the case of fiberglass insulation and nonwovens. We call these, simply, "networks." The second category encompasses cases in which the network is embedded in a matrix which, in turn, can be a solid or a fluid. This category includes most biological networks, gels, and some composites. In a two-phase network material, the matrix is space-filling and no pores or additional components are present in the structure. We call these "embedded networks." The third category includes networks with or without matrix which embed inclusions. These can be particles of various shapes, vesicles, or fiber-like inclusions which are not crosslinked to the network, but are trapped in the network structure. Most biological networks embed such entities, specifically, the cytoskeleton embeds various organelle and connective tissue embeds proteoglycans and cells. We call these "networks with inclusions."

These three categories correspond to generic problems of interest in network mechanics. It is of importance to consider generic network structures and establish how their parameters are related to various aspects of the mechanical behavior of the network material. The matrix, whether solid or fluid, makes a significant contribution to the behavior of the network material. Finally, one may consider, with broad generality and applicability, networks embedding various types of inclusions, and inquire how the presence of such inclusions reflects in the behavior of the network material. In the present chapter, we only review results relevant for the first category of generic networks.

(iii) Based on the nature of interfiber interactions

Interactions between fibers are of various types. Excluded volume interactions, which amount to the condition that fibers cannot penetrate or cross each other, are always

present. Such interactions are important in compression, but are largely irrelevant in tension. Excluded volume interactions are expected to be important when the network volume is a large fraction of the volume of the material. In all networks without matrix and in swollen networks, the network occupies a small volume fraction, the free volume is large, and hence excluded volume interactions are of minimal importance.

Fibers can be crosslinked or not. In addition, fibers may interact through surface forces such as adhesion. In absence of surface interactions and crosslinks, fibers interact exclusively through excluded volume interactions and the ensemble is generally stable only in compression.

The mechanics of these three classes of networks—crosslinked networks, networks without crosslinks and with interfiber surface interactions, and networks without crosslinks and without surface interactions but with excluded volume interactions—is very different. In this chapter, we review the mechanical behavior of crosslinked networks and the behavior of crosslinked and un-crosslinked networks with surface interactions.

(iv) Based on the nature of constituent fibers

Given the broad range of network materials, one expects a multitude of "fiber" types. These can be molecules in molecular networks, such as rubber and gels, filaments composed of many molecular strands, as in the case of tropocollagen, filaments of submicron diameter, as in the case of nanofiber mats, and polymeric fibers of diameter larger than 10 μm, as in most nonwovens. Here, we divide this broad spectrum of "fibers" into thermal and athermal. Athermal fibers are large enough such that thermal fluctuations do not influence their mechanical behavior, which is entirely enthalpic. Thermal fibers are flexible molecular strands which are entirely subjected to thermal fluctuations and behave entropically. Semiflexible fibers are defined at the transition between thermal and athermal. These are subjected to thermal fluctuations, but the enthalpic contribution to the free energy is not negligible. They have large persistence length, which represents the length along the fiber over which thermal fluctuations perturb filament orientation. The persistence length is proportional to the fiber bending rigidity, $E_f I_f$, and inversely proportional to the thermal energy, $k_B T$, such that, as the filament bending rigidity increases, the behavior approaches that of athermal fibers.

Yet another way to classify the fibers is based on their mechanical properties. One may envision situations in which a network is made from the same type of fibers, and cases in which fibers of different type are used. In the case of athermal fibers, the important fiber parameters are their bending, $E_f I_f$, and axial, $E_f A_f$, rigidities. If both these parameters are identical for all fibers in the network, the respective case is considered a "homogeneous network." Otherwise, the structure is a "composite network." It is interesting to observe that, based on this definition, all thermal networks are composite. The effective stiffness of a thermal strand depends on the number of repeat units or Kuhn segments in the strand and, since strand lengths in the network are polydisperse, strand stiffnesses are also polydisperse. This detail is generally not considered in the classical model for thermal networks.

Types of Fibers and Interfiber Interactions

This section is divided into three parts that discuss the representation of fibers, of crosslinks, and of interfiber surface interactions. In each case, the focus is on abstracting the actual mechanical behavior such as to be representative, as well as useful, in large-scale network models.

Representation of Fibers

Based on the classification of the previous section, fibers are considered thermal or athermal, function of whether thermal fluctuations play a role in their mechanics or not.

Athermal Fibers

Athermal fibers are treated as beams and the important parameters describing them are the axial, bending, and shear rigidities, $E_f I_f$, $E_f A_f$, and $G_f A_f$, respectively, where E_f and G_f are the Young's and shear moduli of the fiber material. Assuming a linear behavior for the fiber material, the total energy of the system is the sum of the strain energies associated with bending, axial, and shear deformation of each fiber, i.e.,

$$U = \frac{1}{2} \sum_{fibers} \int E_f I_f \left(\frac{d\psi(s)}{ds} \right)^2 + E_f A_f \left(\frac{du(s)}{ds} \right)^2 + \lambda G_f A_f \left(\frac{dv(s)}{ds} - \psi(s) \right)^2 ds \tag{1.1}$$

In this expression, $v(s)$ represents the transverse displacement and $\frac{du(s)}{ds}$ is the axial strain at position s along the fiber. The rotation of the fiber cross section is $\frac{dv(s)}{ds}$, while $\psi(s)$ represents the rotation of a plane which remains perpendicular to the neutral axis of the beam. Hence, $\frac{dv(s)}{ds} - \psi(s)$ quantifies the shear deformation of the beam. λ is a constant which takes the value 0.88 for beams with circular cross section. This equation corresponds to the Timoshenko model of the beam. Note that the Euler–Bernoulli model is more often used for fibers. In this case, the energy of the system is computed with the same expression (Eq. 1.1), without the third term under the integral. The two models give identical predictions for long, slender beams (beam length significantly larger than the cross-sectional dimension), while the Timoshenko model gives more accurate predictions for short beams. A discussion of conditions under which using a Euler–Bernoulli model is appropriate is presented in Shahsavari and Picu (2012).

It is important to observe that the energy associated with the torsion mode of the beams is not included in Eq. (1.1). This is a result of multiple observations

made using models representing various network structures in 3D indicating that, in random networks, the torsion mode does not store significant amounts of strain energy and hence can be neglected. Given the complexity of the network structure, the physical explanation for this result is not apparent. However, representations in which the torsion energy is and is not accounted for provide essentially identical results for realistic selection of parameters.

The advantage of using a beam model for fibers is that of simplicity and reduced computational cost. The disadvantage is associated with the fact that beam representations do not enforce the excluded volume constraints if no additional conditions are imposed. Alternative representations are based on the bead-spring and discrete element models (Rodney et al. 2005; Picu and Subramanian 2011), which are commonly employed as coarse-grained representations of polymeric chains in polymer physics (e.g., Kremer and Grest 1990). The advantage of these models is that the excluded volume constraint is enforced at all times during deformation. However, they are much more computationally expensive than models representing fibers as beams or trusses. In addition, the presence of a large number of degrees of freedom, which are not essential to the mechanics of fibers, increases the dimensionality of the phase space and the degree of degeneracy of the solution. Bead-spring and discrete element representations also introduce artificial fiber surface roughness which produces spurious interlocking at fiber contacts, particularly at segments which are not straight.

When writing Eq. (1.1), fibers are assumed to be akin to macroscopic beams and made from a homogeneous, isotropic, and linear material. By the fact that a single value of $E_f I_f$ is used, it is also implicit that fibers have the same bending rigidity in all directions. Given the broad range of physical filaments that are to be represented by athermal models, it may be considered adequate to relax some of these assumptions. Fibers with noncircular cross section having two principal directions of inertia leading to two principal bending rigidities have been considered (Deogekar and Picu 2017). This is a natural option when investigating paper mechanics since fibers have close to rectangular hollow cross sections. It was observed that, in such situations and in 3D, the torsional mode of fibers becomes important. In presence of a soft and a stiff bending mode, it may be energetically favorable for the fiber to twist and bend in the soft mode, rather than engaging in bending in a stiff mode. This leads to such coupling between bending and torsion.

It should be also observed that the three rigidities in Eq. (1.1) do not have to be related to each other (as is the case when the fiber cross section is circular, for example). Fibers may represent molecular bundles which may exhibit beam-like mechanics, but with effective rigidities which are independent parameters. A separate homogenization is needed to be performed on the scale of individual filaments in such circumstances in order to determine the best effective beam-like representation of the actual mechanics.

The mechanical behavior of the fiber material may not be linear elastic. It can be rendered time dependent (e.g., viscoelastic), nonlinear elastic or elastic–plastic, as needed in specific applications. A vast amount of work has been performed on characterizing the properties of various types of fibers and placing this behavior

in relation to fiber processing conditions (Wendorff et al. 2012; Magnusson et al. 2013; Quigley et al. 2018). The constitutive nonlinearity of fibers can be of strain-stiffening or strain-softening type. In some situations, fibers may exhibit behavior quite different from that of the corresponding bulk material. For example, polystyrene nanofibers become very ductile and neck in tension, despite that large diameter fibers of the same material are quite brittle (Kolluru and Chasiotis 2015). With all these complexities, the main question is to what extent these details reflect in the behavior of the network. While the answer to this question should depend on the property of interest, a consideration that appears to provide some level of simplification and generality is the following. In random networks which are not densely crosslinked and exhibit hyperelastic overall behavior, the nonlinearity is predominantly geometric in nature. Fibers orient in the direction of loading leading to drastic changes in the network structure, strong Poisson effect, and strongly nonlinear stress–strain curves (Picu et al. 2018). In this process, fiber-level strains remain rather small, despite the large strains reached on the scale of the network (Puxkandl et al. 2002). Hence, in such networks, fibers stand a good chance to remain in the elastic regime and therefore their constitutive nonlinearity is not reflected on the scale of the network. The fiber constitutive behavior reflects more closely in the network behavior in dense and/or densely crosslinked networks which are important in some applications (e.g., paper), but less important in most biological and artificial soft materials.

Thermal Fibers

Fibers of small diameter and small persistence length are strongly affected by thermal fluctuations. The entropic spring concept is a popular representation of such situation (Neumann 1977). This model starts from the thermodynamic definition of the force produced by a strand as the derivative of the free energy relative to the imposed perturbation which, in this case, is the variation of the strand length. This implies that the force has energetic and entropic components associated with the variation of the enthalpy and entropy with the variation of the strand length. The entropic spring model postulates that the enthalpic component is much smaller than the entropic one and hence can be neglected. Further, it relies on the estimate of the entropy of a chain of links function of the distance between the two ends of the chain to evaluate the force. Specifically, considering a chain of n links, each of length a, and assuming these are rotating independent of each other, the model leads to a tensile force required to hold the end-to-end distance at a specified value R of magnitude (e.g., Rubinstein and Colby 2003):

$$f = \frac{3k_BT}{na^2}R \tag{1.2}$$

The strand behaves similar to a linear elastic spring of stiffness linear in temperature (the signature of the entropic nature of the model) and inversely proportional to na^2. This quantity is also the square of the mean end-to-end distance of a random

walk of n steps, each of length a. It is important to note that the force is always tensile and vanishes when the two ends are co-located. This would imply that a network of such strands would need to be always stretched to prevent it from collapsing. The balance force which internally equilibrates the network comes, in this model, from the excluded volume of the network. While this argument may be considered valid in the case of rubber, which has a small free volume, it cannot hold for gels and other swollen networks. Nevertheless, the entropic spring concept is the dominant model of stress production in molecular thermal networks.

Equation (1.2) applies for small extensions of the strand and for contour lengths na much larger than the persistence length $l_p = E_f I_f / k_B T$ (a beam of length l_p subjected to bending and storing $k_B T$ strain energy has a deflection on the order of l_p). For large extensions, when the end-to-end vector length, R, becomes comparable to the maximum possible stretch of the chain, $R \sim R_{max} = na$, one obtains (Bustamante et al. 1994; Marko and Siggia 1995)

$$f = \frac{k_B T}{2a}\left(\frac{R_{max}}{R_{max} - R}\right)^2 \tag{1.3}$$

Accounting for both the enthalpic and entropic contributions to the constitutive response of a filament is more involving (Fixman and Kovac 1973; Odijk 1995; Krog and Frey 1996; Morse 1998; Storm et al. 2005; Wilhelm and Frey 1996). Thermal fluctuations producing transverse vibrations of the filament act against the filament bending stiffness. If the energy equipartition condition requiring that the same amount of energy is associated with all vibration modes is imposed, one may compute the amplitudes of all modes and hence estimate the set of shapes the chain may take. This derivation was performed in Hendricks et al. (1995), van Dillen et al. (2008) where the relation between the applied force and the end-to-end vector length is given in the implicit form:

$$R(f) - R(0) = \frac{R_{max}^2}{\pi^2 l_p} \sum_{i=1}^{\infty} \frac{f/f_0}{i^2\left(i^2 + \frac{f}{f_0}\right)}, \tag{1.4}$$

with $f_0 = \pi^2 E_f I_f / R_{max}^2$ and $R(0)$ some conventional reference end-to-end length. This provides a Langevin-like relationship between the applied force, f, and the variation of the strand end-to-end length.

All thermal models are concerned with the axial force required to modify the length of the strand. Filaments are always in tension. If this model is used as constitutive description of fibers in the network, the fibers represent central force interactions which are asymmetric in tension and compression. This imposes severe limitations on the stability of the network, as discussed in section "Stability Considerations" of this chapter.

Representation of Crosslinks

Crosslinks are connectors bonding two fibers at specific sites. They impose kinematic constraints that force the fibers to have the same displacement and/or the same rotation at the respective site.

The nature of the crosslinks depends on the way the network is constructed. In some nonwovens, the fibers are bonded by pressing the mat between heated plates, which allows surface interdiffusion at contacts between polymeric fibers. The cross sections of fibers subjected to this operation merge partially. The crosslink in this case is a "weld" tightly connecting the two participating fibers. An extreme case of fiber interpenetration is shown schematically in Fig. 1.2a.

In most other situations, fibers also precede network formation, but their bonding is insured by separate additives or physical entities. Individual molecules or molecular complexes (as in the case of collagen), or smaller scale fibrils (as in paper and cellulose products) may form the connector. Figure 1.2b shows a situation in which a single fibril or molecule binds the two fibers, while Fig. 1.2c indicates that multiple fibrils may contribute to the formation of a crosslink. In both cases, the two fibers are continuous through the crosslink.

The distinction made between configurations shown in Fig. 1.2b, c suggests that these behave mechanically differently. In case Fig. 1.2b, the crosslink restricts the relative translation of the two fibers at the contact point, but allows relative rotation. The crosslink in Fig. 1.2c, coupled with the excluded volume constraint for the two fibers, restricts both the relative translation and rotation.

Figure 1.3 shows three conceptual mechanical models which capture the broad range of behaviors encountered in diverse applications, while neglecting the details of the load transfer at the scale of the crosslink. The crosslinks are "pin joints," "rotating," or "welded." The pin joint represents a situation in which the crosslink imposes only translational constraints and transmits only forces. A rotating joint transmits forces between fibers, but allows the fibers to be continuous across and hence both forces and moments are transmitted along each individual fiber. This

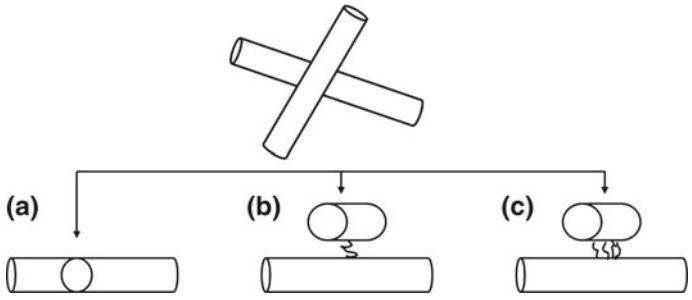

Fig. 1.2 Schematic representation showing three possible types of crosslinks. In **a** the two fibers interpenetrate, while in **b** and **c** they are connected by smaller scale fibrils, molecules, or molecular complexes. A single such fibril forms the crosslink in (**b**), while multiple fibrils are involved in (**c**)

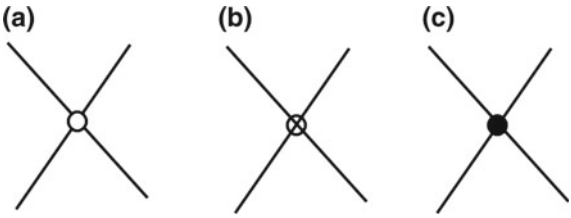

Fig. 1.3 Schematic representation of three types of crosslinks: **a** pin joint, **b** rotating joint, and **c** a welded joint

case corresponds to the situation in Fig. 1.2b. A weld constrains both translations and rotation at the crosslink site and hence both forces and moments are transmitted along and between fibers. This corresponds to the situations in Fig. 1.2a, c.

It should be noted that crosslinks may have their own constitutive behavior. A soft and deformable crosslink does not enforce fully the respective kinematic constraints. Furthermore, given the stochastic process by which random networks are crosslinked in most situations, the properties of crosslinks, their stiffness, and strength may not be identical for all such sites in a specific network. Considering the large variability of possible practical situations, it is important to inquire under what conditions the internal crosslink behavior, beyond the distinction between the three cases shown in Fig. 1.3, reflects in the overall network behavior. This question has been only partly, and indirectly, addressed in the current literature (Kasza et al. 2010).

The situation is more complex in transient networks in which crosslinks can break and reform at other locations (e.g., Astrom et al. 2008). A subset of this class is composed of networks in which fibers are only topologically interlocked and interact frictionally. Entanglements in thermoplastic polymers are of this type and are often represented in conceptual models as transient crosslinks (Vernerey 2018). In the realm of athermal filaments of micrometer diameter, fibers may not be chemically bonded at all, but the network may still exist due to topological and frictional interactions (Benitez and Walther 2017; Negi and Picu 2019b). The models in Fig. 1.3 may represent such cases only in the small deformation limit.

Surface Interactions

Crosslinks are thought to apply moments and/or forces between specific sites along fibers. On the other hand, surface interactions are more uniformly distributed along fibers. These may be of Van der Waals type, and produce adhesion, or may be interactions between sites of specific chemistry which are distributed along filaments. While the nature of interactions and the energetics may be different in these two cases, the mechanics is essentially identical, as the two can be mapped to an effective interaction energy which leads to a work of adhesion.

The difference between crosslinks and surface interactions can be understood by comparing the schematics in Figs. 1.2 and 1.4. In Fig. 1.4a, two fibers are shown forming a bundle over some portion of their length (BC). They are held in the respective

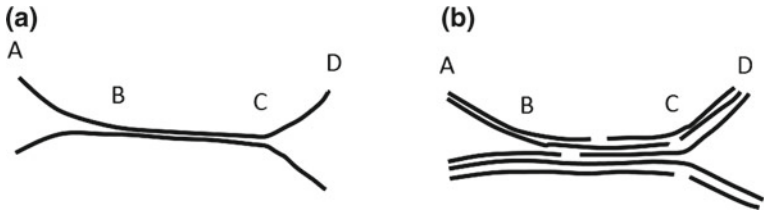

Fig. 1.4 **a** Two fibers interacting via surface forces along segment BC. Both fibers bend to allow the formation of the contact along BC. **b** Adhesion between two fiber bundles. Fibers end and begin at stochastic sites along the bundle. They are held together by interfiber surface forces

configuration by short-range interactions taking place between their surfaces. These interactions favor fiber bonding but, if the two fibers are connected in the network, the formation of the bundle BC requires paying an energetic penalty associated with the bending of segments AB and CD.

The short-range nature of surface interactions limits their ability to organize the network and drive its evolution from the crosslinked state of Fig. 1.3 to the bundled state of Fig. 1.4a. In order to produce configurations similar to that shown in Fig. 1.4a, fibers have to be brought in contact by some other means. These include capillary forces or simple mechanical mixing. Once in contact, surface interactions are engaged and play a significant role in the overall mechanics of the network (Picu and Sengab 2018), as discussed in section "Networks with Adhesive Fiber Interactions—Networks of Bundles" of this chapter.

Figure 1.4b shows a structure similar to that shown in Fig. 1.4a, but involving fiber bundles. Segment BC is the common region of two bundles and the structure is stabilized by surface interactions between fibers in the bundle and between bundles. Fibers may be long compared with the scale of the picture, or may end and start at random sites along the bundle. Bundles can be homogenized and rendered equivalent to "effective fibers." Through such procedure, the structure in Fig. 1.4b is mapped to that shown in Fig. 1.4a.

Characterization of Network Structure

A physical network is defined by the underlying graph, i.e., by the connectivity, and by the positions of the crosslinks. A random network has random connectivity and random nodal positions. Fiber networks are less general than this definition due to the fact that connectivity is limited by the fiber length and shape, while crosslink positions must coincide with fiber locations.

Physical networks have diverse structures, but can be classified in two broad categories: fibrous and cellular networks. Most real networks are of fibrous type. In such structures, the fibers are longer than the distance between two crosslinks, and therefore each fiber has multiple crosslinks with other fibers. Figure 1.5 shows

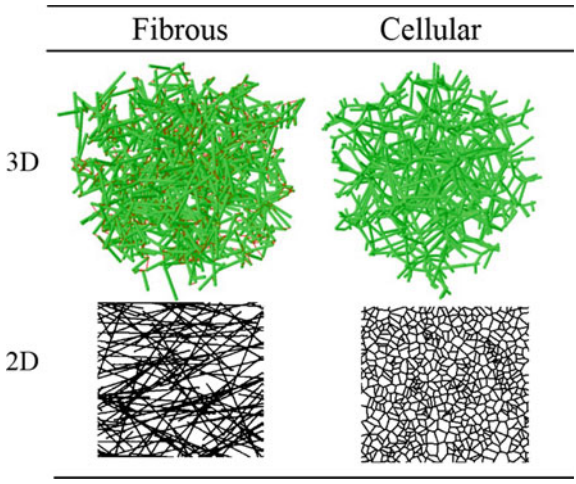

Fig. 1.5 Fibrous and cellular networks. The first line shows three-dimensional realizations, while the second line shows equivalent two-dimensional structures

3D and 2D examples of fibrous networks, with the 2D version being also called Mikado. In 2D, fibers of specified length, L_f, are placed with random orientations and random positions of their centers of mass in a two-dimensional domain, and crosslinks are defined at all fiber crossing points (the "fully crosslinked" case) or at a subset of these. In 3D, fibers are also placed randomly in the problem domain and crosslinks are defined wherever the minimum distance between fibers is smaller than some threshold (e.g., smaller than one fiber diameter). The number of fiber segments merging into a crosslink, or the connectivity number, is $z = 4$ in both 2D and 3D. Note that segments at the end of fibers may be "dangling," i.e., may have only one crosslink to the rest of the network. Therefore, these segments do not store strain energy and do not contribute directly to the network mechanics. They may contribute to the excluded volume, but are expected to influence the network mechanical behavior only in dense networks. If dangling ends are excluded, the connectivity number becomes polydisperse. In such cases, most crosslinks have $z = 4$, but crosslinks with $\bar{z} = 3$ and even with $z = 2$ appear. Therefore, the average connectivity number $\bar{z}$ becomes smaller than 4.

Common office paper has a structure very close to that of a 2D Mikado network, but with large crosslink density and short mean segment lengths between crosslinks (Alava and Niskanen 2006). Nonwoven mats are, in projection on the plane of the mat, also of Mikado type, but their degree of crosslinking is smaller. Collagen structures are also of fibrous type. Collagen is laid down by cells as continuous fibrils that become crosslinked by proteoglycans or surface interactions. Mycelium foams are made from filaments (hyphae) that grow independently in search of nutrition (Glass et al. 2004). Filaments may merge if they meet at some points in space creating a crosslink. Mycelium forms dense fiber networks in the ground and was recently used to bind cellulose particles into a biodegradable material (Islam et al. 2018). Cytoskeleton is a special type of fibrous network. F-actin creates a tree-like, branched

structure as it polymerizes. Crosslinks between such branched "fibers" are introduced by myosin and other actin-binding proteins (Mofrad 2009; Boal 2012).

Cellular networks are similar to Voronoi tessellations of space. They are composed of fibers with only two crosslinks per fiber, located at the two ends. The connectivity number is $z = 3$ in 2D and $z = 4$ in 3D. Dangling segments do not exist or are only exceptionally present. Examples of such networks are the open cell foams, which can be made from various materials, ranging from liquids to metal (Gibson and Ashby 1999).

These structures are characterized by a set of parameters which are either controllable or may be directly measured. The key such parameters are as follows:

- Fiber density, ρ, represents the total length of fiber per unit volume (in 3D) or area (in 2D) of the network. It is directly controllable when a network is produced. It is related to the volume fraction of the network, ϕ, through $\phi = \rho A_f$, with A_f being the cross-sectional area of fibers. The volume fraction represents the volume occupied by the fiber material out of the total volume of the network. The units of ρ are m^{-1} or m^{-2} in 2D and 3D, respectively.
- Bond density, ρ_b, represents the number of crosslinks per unit volume of network. Its units are m^{-2} and m^{-3} in 2D and 3D, respectively.
- The mean connectivity number, $\bar{z}$, represents the average number of fiber segments merging into a crosslink.

An important derived parameter is the mean fiber segment length, l_c, or the distance between two successive crosslinks along given fiber. The segment length is Poisson distributed in most networks, with the probability to find a segment of length l being $p(l) = 1/l_c \exp(-l/l_c)$. The fact that segment lengths are Poisson distributed is inherited from, and is representative for, the random nature of the network structure. The Kallmes–Corte relation for Mikado fibrous networks in 2D indicates that l_c and the network density are related as $\rho l_c = \pi/2$ (Kallmes and Corte 1960). In 3D, the equivalent relation is $\rho l_c^2 = q$, so one can write (Deogekar et al. 2019)

$$\rho l_c^{D-1} = q \tag{1.5}$$

where q is a constant and D is the embedding space dimensionality. Figure 1.6 shows the scaling of ρ with l_c for 3D networks ($D = 3$) of several types. Circles correspond to cases in which fibers are straight.

In most situations, fibers are not straight, rather their contour length is larger than the end-to-end length. Denote by l_c the mean end-to-end segment length, and by l_{cl} the mean contour length of segments. The crimp parameter, c, is defined as $l_c = c l_{cl}$, with $c < 1$. In presence of crimp, the fiber density becomes a function of c, $\rho(c)$. If all fibers have the same crimp, $\rho(c) = \rho(1)/c$, where $\rho(1) \equiv \rho$ in the straight fiber case.

In presence of crimp, Eq. (1.5) becomes

$$\rho(c) l_{cl}^{D-1} = q/c^3 \tag{1.6}$$

which becomes Eq. (1.5) if all fibers are straight and $c = 1$. Figure 1.6 includes data from networks with crimp, with various values of parameter c, and demonstrates the validity of both Eqs. (1.5) and (1.6).

Another geometric relation between network parameters is

$$\rho(c) = \rho_b l_{cl} \bar{z}/2 \tag{1.7}$$

which emerges from the mass balance written at the scale of the average crosslink.

The orientation of fibers and fiber segments is an important parameter controlling the mechanical behavior of the network. Orientation is usually computed based on the end-to-end vector of the respective segment and may be quantified using the second Legendre polynomial $P_2(\theta) = 1/2\left(3cos^2\theta - 1\right)$ (This expression is to be used in 3D. The corresponding expression for 2D is $P_2(\theta) = 2cos^2\theta - 1.$), where θ is the angle between the respective vector and a fixed direction in space (e.g., one of the axes of the coordinate system). Random orientation of vectors leads to the system average value $\overline{P}_2 = 0$, while perfect alignment in the reference direction gives $\bar{P}_2 = 1$. Preferential fiber orientation induces strong mechanical anisotropy.

The structure of networks can be characterized in a number of other ways which are less important for mechanics, but hold relevance for transport across the network. In 2D, fiber crossing defines polygons. Goudsmit (1945) derived several geometric properties of such materials, including the number of polygons formed by given number of lines. Miles (1964) showed that the fraction of polygons that are triangles is 36% and the mean number of sides per polygon is 4. The distribution of pore radii is well approximated by the gamma distribution (Richards 1964; Dodson and Sampson 1996; Eichhom and Sampson 2005). For a detailed discussion of the geometry of polygons in structures formed by randomly depositing lines in 2D, see Stoyan et al. (1987). The effect of accounting for the nonzero fiber diameter is discussed in Eichhorn and Sampson (2005). The broad distribution of pore sizes indicates that such structures are multiscale, with small polygons embedded in larger polygons, which are then embedded in even larger polygons.

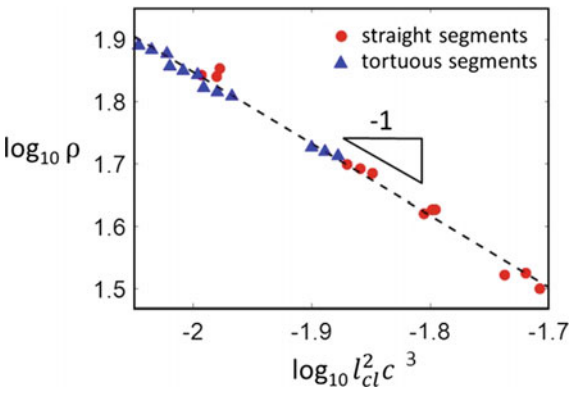

Fig. 1.6 Relation between network density, ρ, and the mean contour length of fiber segments, l_{cl}, and the fiber tortuosity, c. The red circles represent networks with no tortuosity, case in which $l_{cl} \equiv l_c$ and $\alpha = 1$. Adapted from Deogekar et al. (2019)

Small and Large Strain Mechanical Behavior

The literature on the mechanics of fiber networks is rich, with the first studies, mostly related to paper, being reported more than half a century ago (see a review in Rigdahl and Hollmark 1986). During approximately the same period of time, but in a different community, work has been performed on thermal molecular networks such as rubber (Guth and James 1941; Treloar 1975). The objective was to derive constitutive equations describing deformation at the macroscopic scale and to relate this behavior to smaller scale parameters of the network. This is in line with the general trend in Mechanics of Materials over the last part of the twentieth century, when micromechanics (and more recently, multiscale methods) was used to place macroscopic constitutive behavior on a firm ground. Recently, significant attention was devoted to semiflexible random networks, due to their applications in the mechanics of the cell, tissue, and artificial tissue constructs; see reviews of their physical behavior in Picu (2011), Broedersz and MacKintosh (2014).

As with other materials, the mechanical behavior of networks encompasses the study of the constitutive response and that of damage and rupture. The objective is to associate features of the observed behavior with structural parameters of the network, which would render network mechanics controllable. This section refers to the constitutive response of networks, while the discussion of damage and strength is deferred to section "Damage and Rupture in Random Networks."

For simplicity, only isostatic networks with no matrix, no embedded particles or reinforcements, and no prestress are discussed here. This represents the reference case against which more complex cases, including networks with matrix and embedded entities, are compared.

Stability Considerations

The Maxwell criterion (Maxwell 1864) defines the conditions in which a pin-jointed structure of trusses is stable, i.e., has nonzero stiffness. Such structures are called isostatic. A structure composed of N_t trusses, having N_b crosslinks and defined in a space of dimensionality D is stable if $N_t \geq N_b D$. Considering that a truss has a crosslink at each end and each crosslink has, in average, a connectivity number $\bar{z}$, it results that $N_t = N_b \bar{z}/2$. Therefore, the Maxwell criterion requires

$$\bar{z} \geq 2D \tag{1.8}$$

for the structure to be isostatic.

To account for situations in which fibers are added to the structure without constraining additional degrees of freedom, the Maxwell formula may be modified as (Calladine 1978), $N_t - N_b D \geq C - M$, where C is the number of overconstraints and M is the number of mechanisms. For example, for two-dimensional frames, the

formula becomes $N_t - N_b D \geq -3$, where the three mechanisms are two rigid body translations and one in-plane rotation.

Most physical networks being fibrous, their connectivity number is between $\bar{z} = 3$ and 4. Equation (1.8) indicates that in 3D, with $D = 3$, all such structures with pin-jointed crosslinks are sub-isostatic and are mechanisms with zero stiffness in the unloaded state.

Networks can be stabilized in various ways without modifying $\bar{z}$. The simplest route is to consider that athermal fibers are actually beams of finite bending stiffness. The bending rigidity stabilizes the network and structures with $\bar{z}$ much smaller than the Maxwell threshold gain nonzero stiffness.

A related perspective is based on the dichotomy between transport and stiffness percolation. Transport percolation refers to the formation of a continuous path of fibers across the problem domain during the process of network generation. The density of the network at the percolation threshold ρ_{th} in two-dimensional arrangements is related to the dimensions of the fibers, in particular to their length, through $\rho_{th} L_f = 5.71$. Clearly, longer fibers allow percolation to happen at a smaller fiber number density and a smaller ρ. If fibers have nonzero bending stiffness, the transport and stiffness percolation thresholds are identical, ρ_{th}. If fibers have only axial stiffness and the network is a network of trusses, the stiffness percolation threshold is larger than the transport threshold, as required by the Maxwell criterion, Eq. (1.8). The transition is continuous in all cases, with the elastic moduli increasing smoothly from zero. It is generally considered that both Young's and shear moduli become nonzero simultaneously, at the same value of the density. However, this is not of universal validity given the fact that networks may be floppy in one deformation mode and rigid in a different deformation mode.

The presence of residual, self-equilibrated internal stress may alter the mechanical stability of the network (Alexander 1998). Internal stresses restrict the applicability of the Maxwell counting rule (Connelly and Whiteley 1966), and hence may change conclusions regarding the rigidity state of the network. Head (2004) has shown that the presence of an internal stress field in a random spring network changes the nature of the rigidity transition from continuous to first order (elastic moduli take finite values at the onset of rigidity). First-order percolation transitions were observed in Bethe lattices (Moukarzel and Duxbury 1995) and in some networks of infinitely rigid rods (Obukhov 1995) in the absence of residual stresses, but not in other random networks. The observation is important because it applies to systems which are not relaxed to their minimum energy state as are many of the systems encountered in the physical world.

Mechanical Behavior in Tension and Compression

Network materials are usually soft and are subjected to large deformations. The consistent way of representing their material behavior requires using work conjugate

definitions of stress and strain. Several other representations are used in the literature. These are reviewed here, for completeness.

Stress formulations used are the Cauchy, $\boldsymbol{\sigma}$, and first and second Piola–Kirchhoff (PK) stresses, $\mathbf{S}$ and $\boldsymbol{\Pi}$, respectively. These quantities are related as

$$\mathbf{S} = J\boldsymbol{\sigma}\mathbf{F}^{-T} \tag{1.9}$$

and

$$\boldsymbol{\Pi} = J\mathbf{F}^{-1}\boldsymbol{\sigma}\mathbf{F}^{-T}, \tag{1.10}$$

where $\mathbf{F}$ is the deformation gradient and $J = \det \mathbf{F}$ is the Jacobian of the transformation. The first PK stress, $\mathbf{S}$, is work conjugate with $\mathbf{F}$, while the second PK stress, $\boldsymbol{\Pi}$, is work conjugate with the Green strain $\mathbf{E}$, which is related to the deformation gradient as $\mathbf{E} = 1/2\left(\mathbf{F}^{\mathrm{T}}\mathbf{F} - \mathbf{I}\right)$. Under small strains, the three measures of stress become approximately identical and $\mathbf{E}$ becomes equivalent to the small strain tensor, $\boldsymbol{\varepsilon}$.

This implies that it is optimal to express the mechanical behavior as $\boldsymbol{\Pi}(\mathbf{E})$, or as $\mathbf{S}(\mathbf{F})$. In uniaxial deformation (e.g., applied in direction x_1), one may use $\Pi_{11}(\mathrm{E}_{11})$ or $\mathrm{S}_{11}(\lambda)$, where λ is the stretch ratio in the loading direction.

A popular way of representing the response in uniaxial loading is by using the true stress, σ_t, and true strain, ε_t. The true stress is the Cauchy stress, $\sigma_t \equiv \sigma_{11}$ (with loading in direction x_1). It is important to note that $\sigma_t = (1/J)\lambda \mathrm{S}_{11}$. In metals, which deform plastically at constant volume, $J \approx 1$ and hence $\sigma_t \approx \lambda \mathrm{S}_{11}$. However, networks do not deform at constant volume and the simplified formula is not adequate. The true strain is given by $\varepsilon_t = \ln \lambda$. The true stress and true strain are not work conjugates.

Tension

The generic response of a network to uniaxial tension is shown schematically in Fig. 1.7. Displacements are applied on the top and bottom surfaces of the sample, while the lateral faces are kept traction free. In order for the test to be representative of the material behavior, the points where displacements are applied should be kept free in the directions perpendicular to the direction of the load. If the sample is

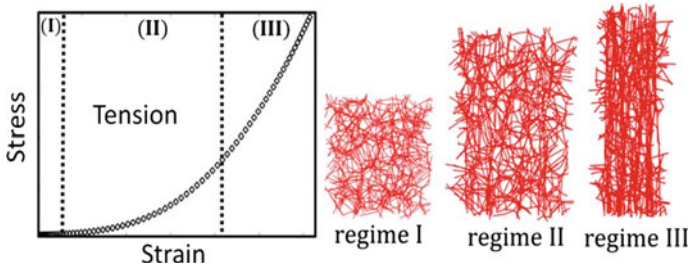

Fig. 1.7 Generic behavior of a network without matrix subjected to uniaxial tension

constrained laterally, it develops an hourglass shape (in tension) and the various sub-volumes experience different stress states and loading path histories.

The tensile stress–strain curve typically exhibits three regimes (Broedersz and Mackintosh 2014):

Regime I: at small strains, the network response is linear elastic, with effective Young's and shear moduli, E_0 and G_0. The stiffness of most matrix-free networks is small and stress in this regime remains rather small.

Regime II: in this regime, the network strain stiffens and the load-carrying capacity increases by orders of magnitude. This is primarily due to the gradual alignment of fibers in the loading direction. Hence, the nonlinearity is, in most cases, of geometric type. The strain in fibers in this regime is rather limited and, unless the mechanical behavior of the fiber material is nonlinear at very small values of the stress, most fibers deform in a linear elastic manner. Exceptions from this behavior are discussed below.

Regime III: once strain-stiffening ends, the response becomes linear again. As fibers become oriented in the loading direction, paths along which the load is preferentially transmitted develop (Zagar et al. 2015). Many fibers do not participate in load transmission in this regime. The structure of the load-bearing sub-network in this regime depends on the structure of the initial network and on the loading path. If the fiber material is nonlinear elastic, this regime would not be linear and would follow the type of nonlinearity (with stiffening or softening) characteristic for the fibers.

The schematics associated with the tensile loading in Fig. 1.7 indicates that lateral contraction is limited in regime I, but is pronounced in regime II. Once the loading paths composed of strongly aligned fibers form, as shown in the rightmost network representation in Fig. 1.7, the incremental contraction is weak again.

Two notable exceptions from the tensile response shown in Fig. 1.7 should be mentioned. Networks with large $\bar{z}$, which are stiff in the initial configuration, typically exhibit an intermediate softening regime between regimes I and II. In such cases, the structure is very stable and fiber orientation in the loading direction cannot happen unless a number of fibers lose stability. Buckling occurring at the end of regime I leads to softening and facilitates the further orientation of fibers, which is characteristic for regime II.

Another exception refers to the opposite situation in which fibers are very soft in bending. In this case, the stiffness in regime I is very small. In many biological tissues, the initial stiffness of samples is so small that stress may be below the resolution limit of the testing system and the material appears to have vanishing stiffness. Defining the origin of the strain axis in such experiments is challenging and regime I may be difficult to observe.

Figure 1.8 shows experimental stress–strain curves of two fibrous biomaterials: the dermis of human skin (Bancelin et al. 2015) and renal tubes (Welling et al. 1995). A behavior similar to that shown schematically in Fig. 1.7 is observed with a poorly developed regime I (likely due to the uncertainty associated with identifying the origin of the stress and strain axes) and a well-developed regime II seen in both cases. This response is common to most biological tissues.

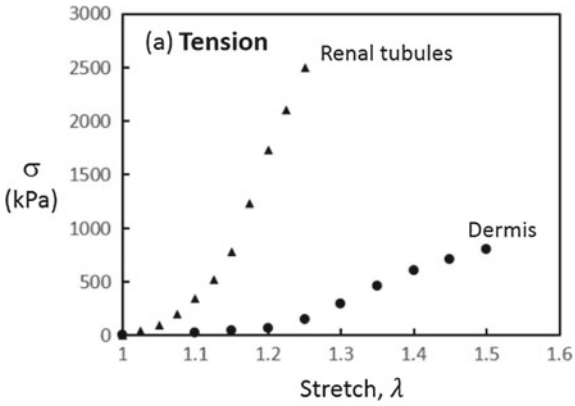

Fig. 1.8 Cauchy stress–stretch curves representing the tensile deformation of renal tubes (data from Welling et al. 1995) and human skin dermis (data from Bancelin et al. 2015)

An alternative representation of these curves results by plotting the tangent stiffness, $E_t = d\sigma/d\lambda$, versus stress, σ. In this format, regimes I and III of the tensile response are horizontal plateaus, while regime II corresponds to a continuously rising branch. Figure 1.9a shows schematically the expected shape of the tensile stress–s-

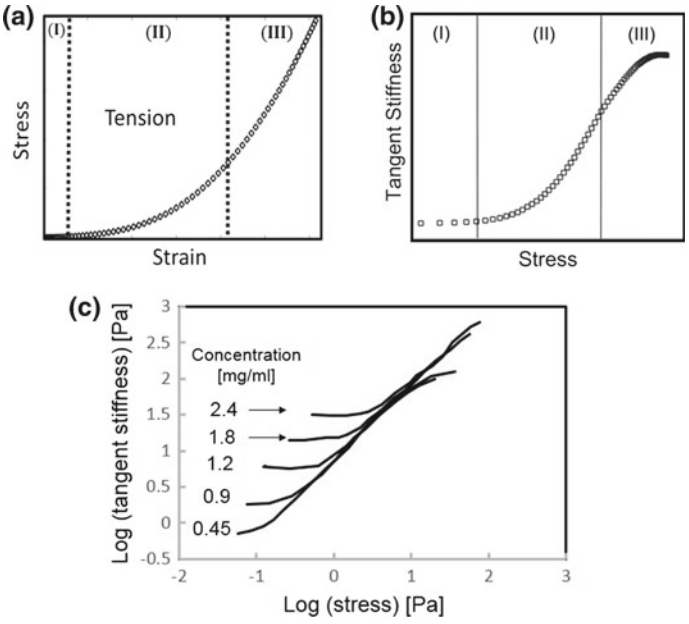

Fig. 1.9 **a** Schematic representation of the tensile stress–strain curve reproduced from Fig. 1.7. **b** Equivalent representation of the curve in (**a**) in terms of the tangent stiffness versus stress. The three regimes are labeled in both (**a**) and (**b**), but are clearly visible in (**b**). **c** Experimental data obtained with reconstructed collagen type I gel subjected to shear at 37 °C. Adapted from Licup et al. (2015)

train curve (similar to Fig. 1.7), while Fig. 1.9b shows the equivalent representation as $\log E_t$ versus $\log \sigma$. The three regimes are clearly visible in Fig. 1.9b. The strong stiffening of the network is also obvious, with the difference between the small strain modulus corresponding to regime I, E_0, and the effective stiffness of regime III being large. Figure 1.9c shows a set of experimental curves obtained with reconstructed collagen type I networks of different concentrations (Licup et al. 2015). E_0 increases with increasing the concentration, i.e., the network density, ρ. However, regime II is largely insensitive to ρ.

The regime II branch in Fig. 1.9c can be approximated by a straight line of slope 1. Hence, $E_t \sim \sigma$, which, in turn, implies that $\sigma \sim \exp(\lambda - 1)$, i.e., the network stiffens exponentially. This type of stiffening is broadly observed in biological fibrous materials (e.g., Mauri et al. 2015; Licup et al. 2015) where it is due to the gradual alignment of fibers in the loading (tensile) direction.

As noted above, densely crosslinked networks, networks with high connectivity number, $\bar{z}$, and/or networks of high density, which are too constrained for significant fiber alignment to be manifest, do not exhibit these three regimes. Their response is limited to regime I. Since their stiffness is large, large stresses are reached. This increases the probability of failure of crosslinks and/or of fibers before the network enters regime II. Failure introduces a softening trend. Softening may be caused by fiber yielding or by a combination of fiber nonlinear deformation and inelastic processes at crosslinks. Figure 1.10 shows an example of this type of behavior obtained with paper of base weight 27 g/m^2 loaded in tension (Borodulina et al. 2012). The initial linear elastic regime is followed by an apparent yield point and subsequent softening. Unloading beyond the yield point leads to a residual strain. Damage accumulates gradually in the nonlinear regime leading to macroscopic localization at peak stress.

If significant damage does not occur in regime I, fibers oriented initially roughly perpendicular to the tensile loading direction undergo a buckling instability. This causes a short softening regime at the end of regime I. Beyond this stage, the material

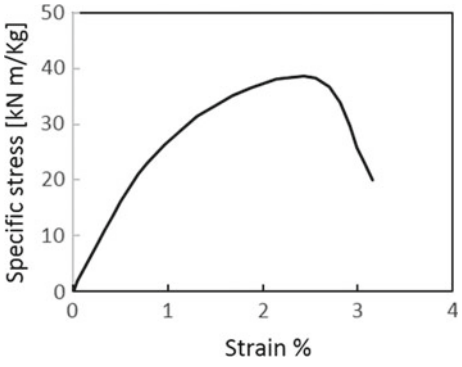

Fig. 1.10 Stress–strain curve for paper of base weight 27 g/m^2. Adapted from Borodulina et al. (2012)

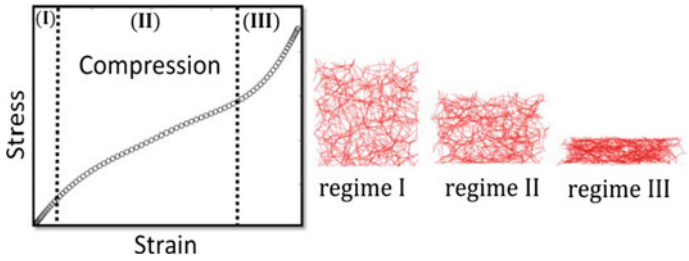

Fig. 1.11 Generic behavior of a network without matrix subjected to uniaxial compression

strain stiffens quickly since the instability removes part of the kinematic constraints and fibers are subsequently free to align in the loading direction.

Compression

The generic response of a network to uniaxial compression is shown schematically in Fig. 1.11.

The compressive stress–strain curve also exhibits three regimes:

Regime I: at small strains, the network response is linear elastic, with effective Young's and shear moduli, E_0 and G_0, typically equal to those measured in tension in regime I.

Regime II: softening is observed in compression after regime I. This behavior is similar to that observed in foams and is associated with strain localization (Gibson and Ashby 1999). Due to the random structure of the network, localization is diffuse and, at least in the initial phases of regime II, no clearly defined strain bands are observed by unaided eye. However, digital image correlation evidences incipient localization bands forming once strain softening is first observed in the stress–strain curve. These bands evolve stochastically and eventually merge forming a compacted region.

Regime III: stiffening is observed in the third regime of the stress–strain curve. This is also similar to the behavior observed in foams. This stiffening regime is due to excluded volume interactions. Specifically, the material becomes sufficiently compacted for the fibers to come in direct, nonbonded contact with each other. Since the number of contacts increases rapidly with compression, the stiffness also increases fast.

The schematic network images in Fig. 1.11 indicate that lateral contraction is limited in compression. This is clearly different from the situation observed in tension (Fig. 1.7).

The regimes discussed above are demonstrated experimentally using a crosslinked glass fiber wool (Mezeix et al. 2009). The microstructure of this material is shown in the inset to Fig. 1.12. It is composed of long glass fibers which are crosslinked by spraying epoxy onto the entangled network. Epoxy beads form at sites where fibers are sufficiently close to each other effectively crosslinking the network. The curve shows clearly the three regimes, in particular regime II and the stiffening regime III shown in Fig. 1.11 are well defined.

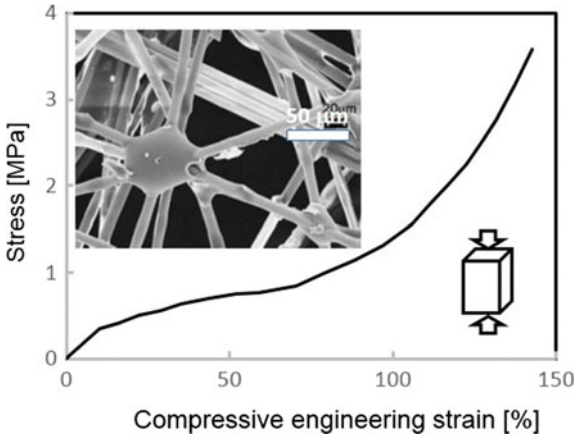

Fig. 1.12 Compression stress–strain curve for a crosslinked glass fiber wool. The fibers are crosslinked with epoxy beads. Adapted from Mezeix et al. (2009). The insets show an image of this fibrous network and the boundary conditions applied during loading

Figure 1.13 demonstrates that the softening transition taking place during compression at the onset of regime II is associated with strain localization. These results are obtained with a mycelium network (Islam et al. 2017). An image of such structure is shown in Fig. 1.13a. The network is obtained by growing mycelium on a nutritive substrate in controlled atmosphere and at controlled temperature. After the network

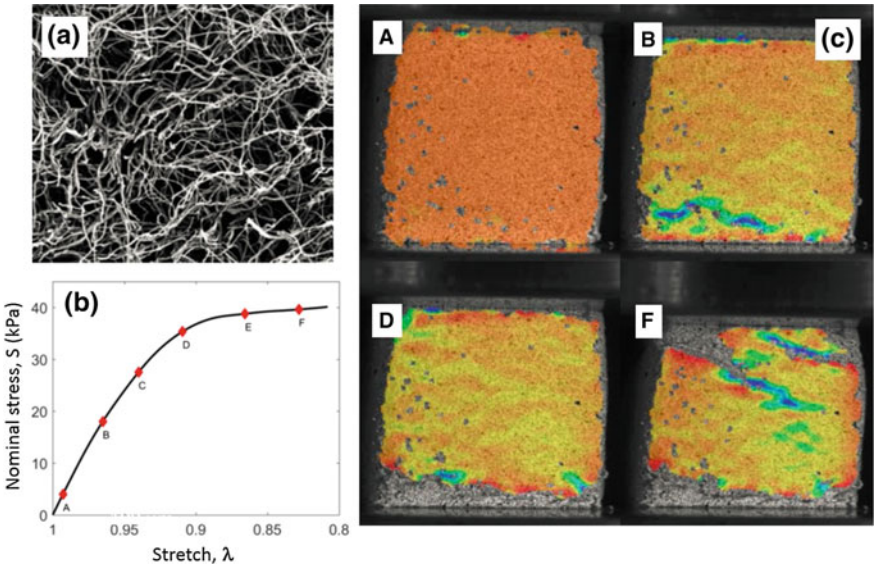

Fig. 1.13 **a** Scanning electron microscopy image of a mycelium network, **b** stress–strain curve of the network in (**a**) subjected to compression, and **c** DIC images of the strain field on the surface of mycelium samples. Snapshots A, B, D, and F correspond to the respective positions indicated by red diamonds in (**b**). Red corresponds to 0 strain and dark blue corresponds to 8% compressive strain, in all images in (**c**). Adapted from Islam et al. (2017)

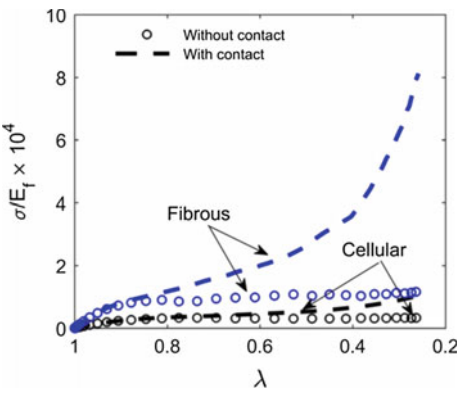

Fig. 1.14 Stress–stretch curves for fibrous and cellular models loaded in compression. The dashed lines correspond to models in which excluded volume interactions are accounted for, while symbols correspond to the same models with the excluded volume interactions turned off

develops to the desired density, the material is thermally treated to remove the biological component and stop the growth. The hyphae are tubules of outer diameter ~1.3 μm and up to centimeters in length. These chitin filaments are entangled and randomly oriented and packed. The hyphae are sparsely crosslinked, but the degree of crosslinking is difficult to estimate. This material was tested in compression and the nominal stress–strain curve is shown in Fig. 1.13b (Islam et al. 2017). Only regime I and the initial part of regime II are shown.

The figure also shows a series of digital image correlation images of the sample surface taken at various stages during deformation. It is seen that localization bands develop at random locations in the sample. As the deformation proceeds, some of these may recede and some others grow. Further compression leads to the densification of the sample corresponding to the regime II part of the stress–strain curve. Due to its very small volume fraction and given the small hyphae diameter, the network has to be compacted significantly in order to reach regime III. Similar behavior has been observed in random foams (Gibson and Ashby 1999). While in periodic foams localization takes the form of a single band which advances across the gage of the sample, in random foams and networks subjected to compression, localization has the diffuse character as shown in Fig. 1.13.

Figure 1.14 demonstrates that the rapid stiffening observed in regime III is due to the excluded volume interaction of fibers. It shows stress–strain curves obtained with models of cellular and fibrous networks of same density. The dashed curves are obtained with models that account for all interfiber interactions, including excluded volume interaction (the conditions that fibers do not cross or overlap). The symbols correspond to curves obtained with the same models after the excluded volume constraint is removed. These curves do not exhibit the stiffening regime III. Furthermore, the strain hardening observed in regime II is much weaker than in the curves obtained with all interactions activated.

Poisson effect

Networks with no embedding matrix exhibit strong Poisson contraction when loaded in uniaxial tension. This is observed in nonwovens and in biological tissue in which

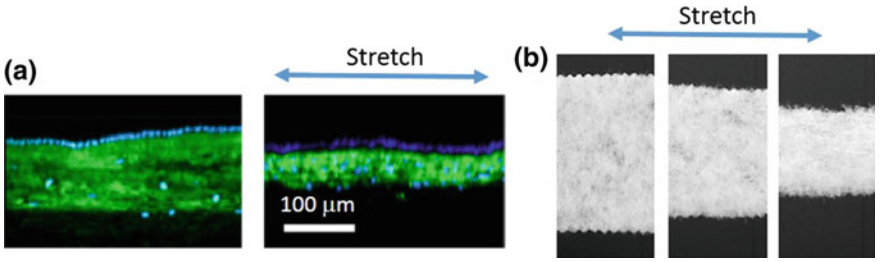

Fig. 1.15 **a** Cross-sectional view of human amnion in the unloaded state (left) and after stretching in the direction shown by 24% (adapted from Mauri et al. 2015). **b** Top view of a nonwoven polymeric felt subjected to uniaxial stretching (adapted from Kabla and Mahadevan 2007). The transverse contraction in both cases is of about 50%

drainage is allowed to happen. Examples are shown in Fig. 1.15. Figure 1.15a shows the cross section of the human amnion in the unloaded state (left image) and after stretching by 24% (Mauri et al. 2015). The thickness of the sample decreases to about half of the original one and the transverse strain is approximately 50%. Figure 1.15b shows a similar result obtained with a polymeric felt (Kabla and Mahadevan 2007). The lateral contraction upon a uniaxial stretch of 40% is close to 50%.

Both examples provided in Fig. 1.15 refer to membranes, with the constituent filaments strongly oriented in the plane of the structure. In both cases, it is observed that the contraction in the in-plane direction is smaller than that in the out-of-plane direction. This indicates that fiber orientation strongly influences the Poisson contraction. Specifically, preferential fiber orientation in the direction of the tensile load leads to a more pronounced Poisson effect.

To quantify the Poisson contraction, we use the incremental Poisson ratio defined by

$$\nu_i = -\frac{d \ln \lambda_2}{d \ln \lambda_1} \tag{1.11}$$

which is computed based on the true strains in the transverse and longitudinal direction. This quantity reduces to the usual definition of the Poisson ratio under small strains. The incremental Poisson ratio is more relevant than the secant version ($\nu_s = -\ln \lambda_2 / \ln \lambda_1$) since it represents the incremental response of the structure relative to the current state.

Figure 1.16 shows the variation of the incremental Poisson ratio for a model network with parameters representing collagen at concentrations relevant for connective tissue, i.e., 1 and 4 mg/ml (Picu et al. 2018). The stress–strain curves for these model networks resemble closely to those measured in several collagen constructs. The Poisson ratio is plotted versus the applied longitudinal stretch ratio, λ_1.

The Poisson ratio is smaller than 0.5 in the initial state and throughout regime I of the deformation. Once the sample enters regime II, the Poisson ratio increases rapidly. The transition between regimes is marked by the vertical arrows in Fig. 1.16. Very

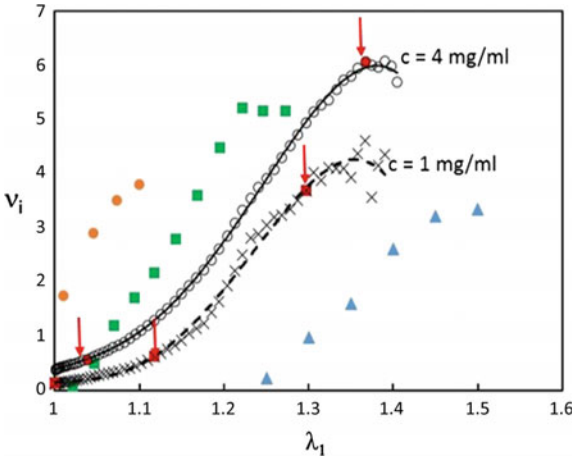

Fig. 1.16 Variation of the incremental Poisson ratio with the stretch ratio for models with c = 1 and 4 mg/ml. The red symbols mark the transition between regimes I, II, and III. The figure includes experimental data for reconstructed collagen gels (orange circles) (Lake and Barocas 2011), human amnion (green squares) (Mauri et al. 2015), and mouse skin (blue triangles) (Bancelin et al. 2015). Reproduced with permission from Picu et al. (2018)

large values of the incremental Poisson ratio are reached. These are much larger than the upper limit of 0.5 allowed by thermodynamics considerations in the continuum theory. The network is not a continuum and hence the respective limit does not apply. Incidentally, it should be noted that even in the continuum case, values of the Poisson ratio larger than 0.5 are thermodynamically acceptable in anisotropic elasticity (Ting and Chen 2005).

The maximum value of the incremental Poisson ratio is reached at the transition from regime II to regime III. Once the fibers are strongly aligned and the stress paths are formed across the sample, the driving force for lateral contraction is reduced. In addition, lateral contraction is limited by the confining effect of fibers which remain oriented in directions other than the loading direction and which are strongly distorted at this stage.

Figure 1.16 includes three sets of experimental data obtained with reconstructed collagen gels (orange circles) (Lake and Barocas 2011), human amnion (green squares) (Mauri et al. 2015), and mouse skin (blue triangles) (Bancelin et al. 2015). The trends observed experimentally, including the rate of increase of ν_i in regime II, are identical to those obtained with the model. The experimental curves are shifted in the horizontal direction due to the uncertainty related to the origin of the strain axis, which is always an issue when working with very soft specimens.

The effect of fiber alignment on the Poisson ratio is shown in Fig. 1.17 (Picu et al. 2018). During uniaxial tension, fibers align and the degree of alignment is measured by the orientation parameter P_2 defined in section "Characterization of Network Structure." Figure 1.17 shows the incremental Poisson ratio versus P_2. The data indicates that the Poisson effect is more pronounced as the network is more

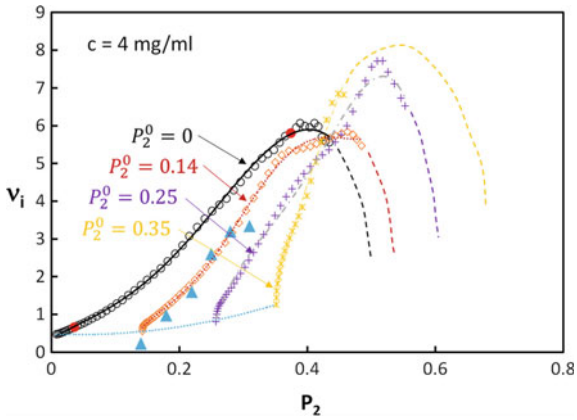

Fig. 1.17 Relationship between the incremental Poisson ratio and the orientation index for models with c = 4 mg/ml and various levels of pre-alignment in the initial, unloaded configuration (P_2^0). The dotted blue line shows the variation of the small strain Poisson ratio with the degree of pre-alignment. The blue triangles represent the measured in-plane incremental Poisson ratio for a pre-aligned sample of mouse skin (Bancelin et al. 2015). Reproduced with permission from Picu et al. (2018)

aligned. This agrees with the observation made above, in connection with Fig. 1.15, that the Poisson contraction of a fibrous membrane in the out-of-plane direction is more pronounced than that in-plane.

Figure 1.17 includes several curves obtained with networks of the same density, but with preferentially oriented fibers in the initial, unloaded configuration (the degree of initial orientation is defined by P_2^0). The blue dotted line shows the variation of the small strain Poisson ratio with the degree of initial orientation. It is seen that the ratio increases slightly with P_2^0, but the effect is not significant. However, the rate of increase of ν_i with increasing P_2 is much more pronounced in the aligned samples than in samples with random initial fiber orientation. The figure includes data for the mouse skin dermis from Bancelin et al. (2015). The experimental data aligns with the model prediction.

Networks without embedding matrix exhibit strong asymmetry in tension and compression with respect to the Poisson effect. In compression, the Poisson effect is weak and samples preserve their lateral dimensions during loading.

Hysteresis

The discussion above refers to the loading part of the stress–strain curve. In principle, in absence of damage (which may occur in the form of crosslink and/or fiber rupture) and with linear elastic fibers, the network behavior is hyperelastic and unloading retraces the loading curve. In reality, additional interfiber interactions occur in most fibrous materials, which introduces dissipation and leads to hysteretic stress–strain curves.

Interactions leading to dissipation include friction between filaments at contacts other than the crosslinks, and the interaction of fibers with an embedding fluidic

matrix. The first occurs, for example, in dense nonwovens, while the second may take place in tissue such as cartilage and ligaments. With nanofilaments, friction is primarily viscous, with the friction force per unit area of contact being a constant (Bowden and Tabor 2001). Adhesion may help preserve fibers in contact. Interaction with an embedding fluidic medium amounts to the flow of fluid within the fibrous body leading to viscous drag and dissipation. Such internal flow may take place under non-draining conditions due to the heterogeneous nature of the structure and the associated non-affine deformation. This phenomenon is known in cartilage which is considered to be a three-phase material, i.e., a collagen fiber network, a soft solid phase formed by proteoglycans, and a fluid. It leads to time-dependent mechanical behavior of cartilage, which is key in the biomechanics of the joint. If the fiber material is elastic–plastic or viscoelastic, dissipation occurs in the fibers as well.

Figure 1.18 shows an example of hysteretic behavior for a mycelium network of the type shown in Fig. 1.13a (Islam et al. 2017). The network is subjected to uniaxial compression in this case. However, similar response is expected under shear. Dissipation occurs in this case due to interfiber friction. The material is dry and there is no embedding matrix. Dissipation is weaker in tension since, due to the open structure of the network, interfiber contacts are sparse at low and moderate strains.

Figure 1.18a shows the response under cyclic loading of 2% strain amplitude. The loading branches are different from cycle to cycle, indicating that the material settles under loading. The unloading branches overlap. A residual strain is measured in each cycle relative to the initial configuration. The cyclic response settles to a stable hysteresis loop after two or three cycles.

Figure 1.18b shows the equivalent behavior under larger strain amplitudes. The maximum strain imposed is sufficiently large to cause strain localization which, in turn, causes softening of the loading branch of the stress–strain curve; see also Fig. 1.13. The cyclic curve settles after few cycles to a stable hysteresis loop, similar to the response observed under small strain amplitude, but the dissipation is much more pronounced.

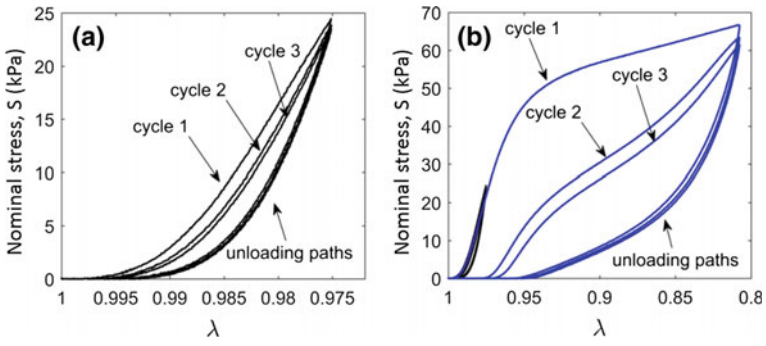

Fig. 1.18 Compressive response of mycelium subjected to cyclic loading under constant strain amplitude. The curve in (**a**) is reproduced in (**b**) for comparison. Adapted from Islam et al. (2017)

It is also of interest that this network exhibits the Mullins effect, as commonly observed in filled rubbers (Mullins 1969). The Mullins effect refers to the reloading branch of the stress–strain curve under cyclic deformation with increasing amplitude from cycle to cycle. The loading branch follows the unloading branch of the previous cycle (say, the curve labeled "cycle 3") up to the maximum strain of the previous cycle. Beyond this strain, the reloading curve follows that which would have been obtained with a sample loaded monotonically. This similarity with the phenomenology observed in rubber is surprising at the first glance due to the very different nature of the two types of networks. The mycelium network discussed here is composed of athermal filaments and has large free volume, with no embedding matrix. Rubber is a molecular, thermal network with essentially no free volume. In rubbers, the Mullins effect is associated with damage produced during loading. Damage is produced in the first cycle, while cycling at constant strain amplitude does not produce additional damage. Damage continues to accumulate when the strain amplitude increases. As in the case of rubber, the origin of the Mullins effect in athermal networks with large free volume is not precisely understood.

Biaxial loading

Biological fibrous membranes and nonwoven mats are generally loaded biaxially. It is therefore of interest to discuss the response of networks to multiaxial loading.

Due to their large Poisson effect observed in uniaxial tension, it is expected that the stress required to deform a fibrous structure in regime II and beyond under multiaxial conditions is larger than that required for uniaxial deformation. Under small strains, the effective Poisson ratio is smaller than 0.5 and the equibiaxial modulus is $E_0/(1-\nu_0)$, where E_0 and ν_0 are the regime I (small strains) Young's modulus and Poisson ratio. ν_0 is equal to the instantaneous value at small strains. Therefore, the effective small strain modulus measured in equibiaxial tension is expected to be larger than E_0.

In regime II of the uniaxial deformation, the Poisson effect is important, with $\nu_i > 1$ (Fig. 1.16), and the difference between equibiaxial and uniaxial tension curves should be significant. In this regime, the structure becomes strongly anisotropic (transversely isotropic under uniaxial and equibiaxial loading) and the simple linear elastic relation between the effective moduli in the two loading modes does not hold.

Figure 1.19 shows the uniaxial and equibiaxial tension stress–strain curves for a Voronoi network of parameters and density relevant for collagen structures (at collagen concentration of 4 mg/ml) (Picu et al. 2018). The nominal stress–stretch curves are shown in Fig. 1.19a, while the corresponding tangent stiffness–stress curves are shown in Fig. 1.19b. The curves in Fig. 1.19b indicate the two regimes of deformation which are equally well defined under uniaxial and biaxial loading. Similar results are obtained experimentally with nonwovens (Ridruejo et al. 2012).

The stress required to deform the sample biaxially is always larger than that measured in uniaxial deformation. The small strain biaxial modulus (see regime I in Fig. 1.19b) is larger than E_0, as discussed above. Interestingly, the slope of the tangent stiffness versus stress curve in regime II is 1 in both uniaxial and biaxial loading modes. This indicates that the stress is an exponential function of stretch in both cases.

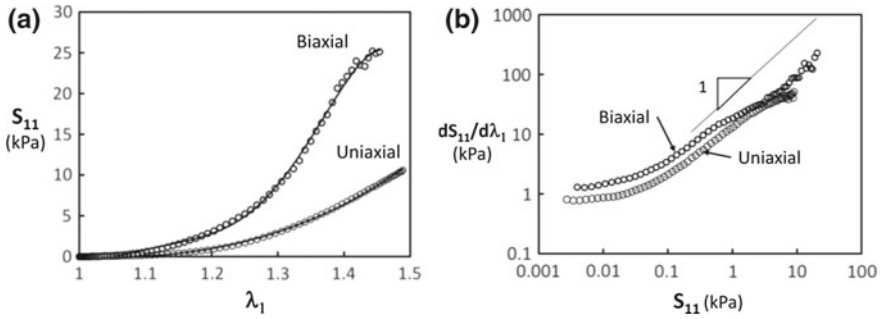

Fig. 1.19 **a** Nominal stress–stretch curves for the uniaxial and equibiaxial deformation of a Voronoi network with characteristics similar to a collagen structure of concentration 4 mg/ml. The tangent stiffness versus stress curve is shown in (**b**) to emphasize regimes I and II of the deformation. Reproduced with permission from Picu et al. (2018)

As the ratio of the tensile stress applied in the two in-plane directions of loading becomes smaller than 1, the biaxial curve shifts to smaller stresses. The uniaxial and equibiaxial curves in Fig. 1.19a are the extremes of all possible biaxial cases.

Affine versus non-affine deformation

Affine deformation refers to a situation in which the fiber-level deformation gradient is identical to the far field, imposed deformation gradient. Each sub-domain of the network, down to individual fibers, follows the kinematics imposed on the network at the macroscale. This type of deformation is not encountered in practice as networks generally deform non-affinely. In fact, all heterogeneous continua deform non-affinely and random fiber networks are, by definition, highly heterogeneous.

The non-affinity can be evaluated using various measures (Picu 2011) and is quite large in most networks without matrix of practical interest. In presence of a solid matrix, the degree of non-affinity is lower.

Given that the affine deformation is an approximation of the real behavior, one may wonder why it is of any importance. The reason is rooted in the simplicity of this model. Since the kinematics is fully defined and the constitutive response of each fiber is known, the stress can be computed analytically. Therefore, the affine model provides the upper bound for the constitutive behavior of real networks. Given its importance in network studies, we outline here the main features of the model.

Given a deformation gradient $\mathbf{F}$ applied macroscopically, a generic fiber of the network of end-to-end vector $\mathbf{R}_0$ deforms into a configuration defined by $\mathbf{R} = \mathbf{F}\mathbf{R}_0$. If the fiber is initially straight, it remains straight during deformation. Therefore, bending is not engaged and only the axial deformation mode is activated. The model implies that fibers, even if of beam type, deform as trusses. This is the major limitation of the affine model: fiber kinematics being restricted to the axial mode, lower energy states that require bending deformation of filaments cannot be represented by the model. Therefore, the effective stiffness predicted by the affine model is always larger than that measured in cases in which multiple deformation modes are possible.

Under the affine assumption, the force that develops in each fiber, i, is given by $\mathbf{F}_i = k_i(\|\mathbf{R}_i\| - \|\mathbf{R}_{0i}\|)$, where the effective axial stiffness is $k_i = E_f A_f / \|\mathbf{R}_{0i}\|$. The stress can be calculated using the virial formula:

$$\boldsymbol{\sigma} = \frac{1}{2V} \sum_i \mathbf{F}_i \otimes \mathbf{R}_i = \frac{1}{2} \rho E_f A_f \left\langle \frac{\|\mathbf{R}_i\|}{\|\mathbf{R}_{0i}\|} - 1 \right\rangle \langle \mathbf{r}_i \otimes \mathbf{r}_i \rangle \tag{1.12}$$

where V is the volume of the network and the summation is performed over all fibers. $\mathbf{r}_i$ represents the versor of $\mathbf{R}_i$. The system average of the dyadic $\mathbf{r}_i \otimes \mathbf{r}_i$ includes information about the orientation of fibers and hence accounts for anisotropy. The ratio $\|\mathbf{R}_i\|/\|\mathbf{R}_{0i}\|$ is the stretch ratio of fiber i and $\langle \|\mathbf{R}_i\|/\|\mathbf{R}_{0i}\| - 1 \rangle$ is the system average axial engineering strain of fibers.

Equation (1.12) indicates that, within the affine approximation, the stress is proportional to the network density, ρ, and to the fiber axial rigidity, $E_f A_f$. The fact that the only relevant fiber property is $E_f A_f$ is a consequence of the kinematic restriction imposed on fiber deformation. Therefore, the stiffness of the network follows $E_0^{affine} \sim \rho E_f A_f$.

Parameters characterizing the mechanical behavior and their dependence on network structure

In this section, we are concerned with the relationship between network microstructure and its mechanical behavior. The response to uniaxial loading is considered representative for the mechanical behavior. This relation is of importance for the overall understanding of network mechanics as well as for network design.

Networks usually perform their function in regimes I and II of the stress–strain curve, Fig. 1.7. Regime I is characterized by the small strain modulus, E_0, and the Poisson ratio, ν_0. Regime II is characterized by the functional form of strain hardening, or the slope of the regime II branch of the curve in Fig. 1.9b (see also Fig. 1.19b).

As discussed in section "Characterization of Network Structure," characterizing the network structure is a complex task. Here we refer to athermal networks with average connectivity $\bar{z}$ close to 4, which are representative for essentially all nonmolecular networks, including networks of semiflexible filaments with persistence length much larger than the mean network segment length, $l_p \gg l_c$. The key parameters of the network are (i) the density, ρ, or the mean segment length, l_c; these two parameters are related through Eq. (1.6), (ii) the crimp, c, (iii) fiber properties, and (iv) fiber preferential orientation, P_2.

To reduce the complexity, we consider the fiber material to be linear elastic. Hence, the fiber behavior is characterized by the axial and bending rigidities, i.e., $E_f A_f$ and $E_f I_f$. The bond density is related to ρ, $\bar{z}$, and c through Eq. (1.7). As discussed in section "Athermal Fibers," fibers do not store significant strain energy in the shear and torsion modes; therefore, the rigidities of these two deformation modes are not included in the list of fiber properties. It should be also noted that $E_f A_f$ and $E_f I_f$ may differ from fiber to fiber; such composite networks are not considered in the present discussion, but relevant data can be found in Ban et al. (2016b).

Also, fibers may not be cylindrical. If so, the cross section has two independent moments of inertia and two parameters, $E_f I_f^{min}$ and $E_f I_f^{max}$, should be considered. This, again, adds to the complexity and we leave this discussion out. Relevant data on the effect of noncircular cross sections of filaments can be found in Deogekar and Picu (2017). Furthermore, we consider structures with random fiber orientation in the initial configuration, $P_2 = 0$. The behavior of networks with preferential fiber alignment in the undeformed state is anisotropic, but qualitatively similar to that discussed here.

The dependence of the network stiffness, E_0, on network parameters was studied by several groups (Head et al. 2003; Heussinger et al. 2007; Shahsavari and Picu 2013a, b). The results are summarized in the plot of Fig. 1.20 for networks without crimp, c = 1. The plot is obtained by evaluating the stiffness of many networks with various sets of parameters. The data is then cast in terms of three nondimensional parameters: E_0/E_0^{affine}, L_0/l_c, and l_b/L_0. Note that L_0/l_c represents the number of crosslinks per fiber. The length-like parameter l_b is known as the "bending length" and is given by $l_b = \sqrt{E_f I_f / E_f A_f}$. For fibers with circular cross section, $l_b = d/4$, where d is the fiber diameter. Therefore, in this case l_b/L_0 represents the aspect ratio of the fiber.

To shed light on the origin of these nondimensional parameters, in the absence of density fluctuations on scales much larger than l_c (flocculation), these structures have three characteristic lengths: d, l_c, and L_0. With one of these taken as unit of length, the two ratios L_0/l_c and l_b/L_0 result as the only independent parameter of the geometry. In networks of "infinite" fibers, such as electrospun networks of polymeric fibers, L_0 is not defined. Its role is taken by the fiber persistence length, l_p.

It is observed that with the proper selection of the exponents of the two nondimensional groups on the horizontal axis, the data points collapse on a master curve.

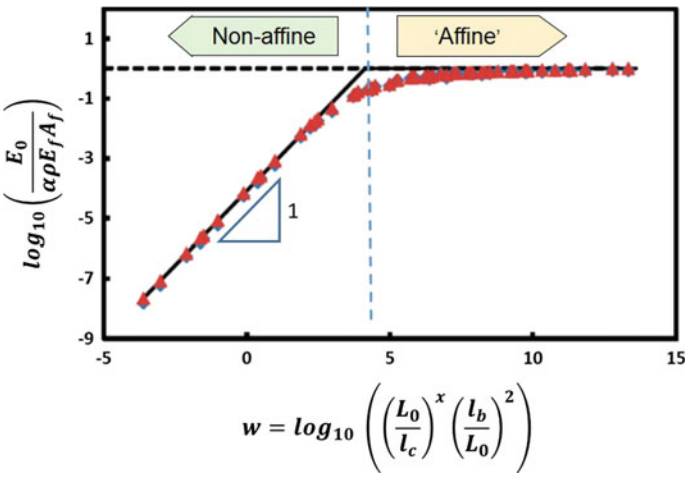

Fig. 1.20 Dependence of the small strain modulus, E_0, on structural parameters of the network

The curve has two regimes. At large values of w, $E_0 = E_0^{affine}$. In this regime, either or both L_0/l_c and l_b/L_0 are large. This happens in networks of high density (small l_c) and of fibers of large enough diameter such as to render the bending deformation mode prohibitively expensive. If the bending mode is inhibited, fibers deform in the axial mode and the network kinematics becomes approximately affine. We note that the deformation is never perfectly affine on the individual fiber scale, but the overall behavior is well approximated by the affine model. As noted above, in this regime $E_0 \sim \rho E_f A_f$.

The behavior is quite different at small values of w. This regime is reached at small ρ (large l_c) and/or when the fiber diameter decreases sufficiently to enable the bending deformation mode. Consequently, it is observed that $E_0 \sim E_f A_f l_b^2 = E_f I_f$, i.e., the network stiffness is proportional to the bending rigidity of fibers, while being independent of their axial rigidity. Network deformation is bending dominated in this regime. Therefore, it appears as if the two deformation modes are connected in series and the softer mode controls the overall behavior. This is quite surprising, given the complex geometry and kinematics of the network.

Interestingly, the bulk modulus in the small strain regime, K_0, has the same behavior at all w values and scales as $K_0 \sim \rho E_f A_f$. The bulk modulus is probed by applying hydrostatic loading to the sample. Under these conditions, the deformation of the network is close to affine and this leads to the observed linear scaling of K_0 with the density and its proportionality to the axial rigidity of fibers.

Network models can be used to compute the partition of energy between the various fiber deformation modes. Figure 1.21 shows such an example. The total strain energy is divided into three components associated with bending, axial, and shear deformation of fibers. The partition is evaluated across the range of variation of parameter w (Fig. 1.20).

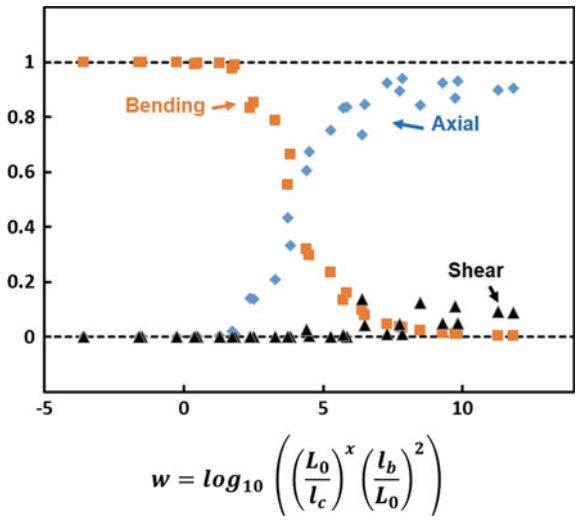

Fig. 1.21 Partition of strain energy in bending, axial, and shear modes function of the structural parameter w defined in Fig. 1.20

The energy is primarily stored in the bending mode for non-affinely deforming networks with small w values, while it is primarily stored in the axial mode when the network deforms affinely, at large w. A small fraction of the energy is stored in the shear mode at very large w. Note that extending the plot into the large w range by decreasing l_c should be done carefully, such as to ensure that fiber segments retain an aspect ratio that allows representing them as beams.

The master plot in Fig. 1.20 indicates that, at small w, in the non-affine regime, $E_0 \sim \rho l_c^{-x}$. Combining Eqs. (1.5) and (1.7), it results that $l_c \sim (\bar{z}\rho_b)^{-1/D}$. Therefore, one can write $E_0 \sim \rho\rho_b^{x/D}$. Specifically, one may keep the density of the network constant and reduce the number of crosslinks per fiber, hence increasing l_c. Then, the density and crosslink density become independent parameters. This expression indicates that the stiffness is more sensitive to ρ_b than to ρ. This issue is discussed, in the context of 2D Mikado networks, in Shahsavari and Picu (2013a).

The exponent x of the nondimensional group L_0/l_c in w requires discussion. This exponent controls the sensitivity of the small strain stiffness to the density of the network and the density of crosslinks. Numerical models determined that x depends on the dimensionality of the embedding space, D. Also, x is different in cellular and fibrous networks, being therefore sensitive to aspects of the architecture which are not quantified by the parameter set used here. Specifically, in 2D Mikado networks, $x = 7$ for all crosslink densities, whether the network is crosslinked at all fiber crossing points, or sparsely (Shahsavari and Picu 2013a). Fibrous 3D networks have $x = 2$ (Broedersz et al. 2012; Islam and Picu 2018; Vader et al. 2009), while cellular 3D network have $x = 1$ (Gibson and Ashby 1999; Islam and Picu 2018). Since in cellular networks fibers have exactly two crosslinks per fiber, one may write directly $E_0 \sim \rho^2$. This relation was also established for 3D open cell foams and can be obtained analytically from a simple periodic model of the cellular structure (Gibson and Ashby 1999).

The transition from a soft regime, with E_0 much smaller than the affine prediction, to a regime in which the affine model holds is supported by the data in Fig. 1.22. This is a collection of experimental results obtained with paper samples of various

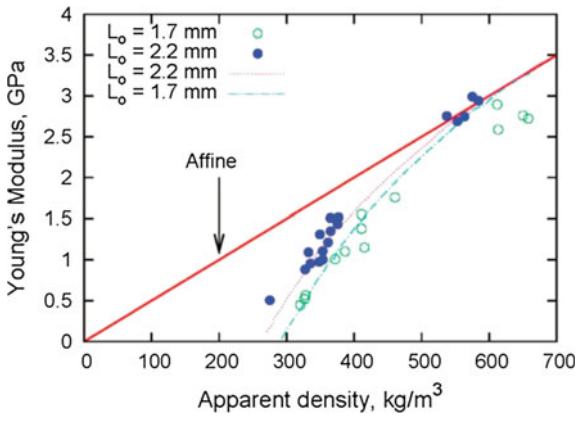

Fig. 1.22 Variation of Young's modulus of paper with the density along with the affine model prediction. Adapted from Rigdahl and Hollmark (1986)

densities and two fiber lengths. The affine prediction is included in the figure for reference. In agreement with the results in Fig. 1.20, the effective network stiffness matches the affine prediction at large fiber densities, but falls below it as the density decreases.

In many networks, fibers are not straight. The degree of crimp in the initial, undeformed configuration is one of the essential parameters describing the network structure. It is of interest to inquire how crimp reflects in the stress–strain response of the material. This issue has been studied by many groups (Huisman et al. 2007; Wen et al. 2012; Raina and Linder 2014; Ban et al. 2016a).

Crimp leads to two important modifications of the stress–strain curve: (i) it reduces E_0 and (ii) postpones the transition from regime I to regime II to larger strains. The nonlinear behavior in regime II is not modified by the presence of crimp. Figure 1.23 demonstrates these effects based on data obtained with a cellular network model (Ban et al. 2016a). The tangent stiffness is plotted versus stress, both axes being normalized by the small strain stiffness of the network with no crimp ($c = 1$). It results that E_0 decreases continuously with increasing the degree of crimp (decreasing c), while the strain stiffening in regime II remains exponential (slope of 1 in Fig. 1.23) for all cases with $c < 1$, and identical to that of the equivalent network without crimp.

Finally, the dependence of the regime II strain hardening on network parameters should be discussed. Strain hardening is typically either of exponential type or of power type. Most works in tissue mechanics report exponential stiffening. In nonwovens, often the stiffening regime is overshadowed by a softening trend associated with the failure of bonds or fibers, and a general conclusion cannot be reached. Models representing various types of networks report generally exponential stiffening (Broedersz and MacKintosh 2011; Picu et al. 2018), but exceptions have been also reported (Zagar et al. 2015; van Dillen et al. 2008). An association of exponential stiffening with cellular networks and of power law stiffening with fibrous networks has been reported in Islam and Picu (2018). The type of behavior shown in Fig. 1.9c and Fig. 1.23 is quite common: varying a parameter of the network (e.g., the network density in Fig. 1.9c and the crimp in Fig. 1.23) leads to the variation of E_0, but the tangent stiffness–stress curves merge in regime II. It is concluded that the nature

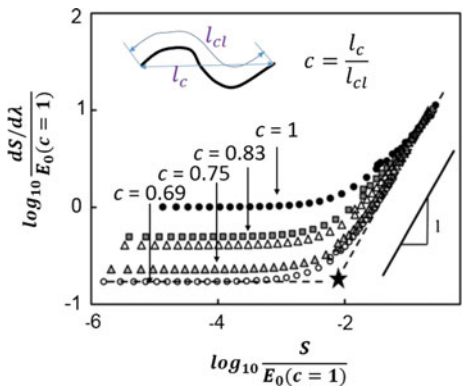

Fig. 1.23 Tangent stiffness versus stress for networks with increasing degree of crimp. The inset shows the definition of the crimp parameter, c. Both axes are normalized with the small strain modulus of the network without crimp, $E_0(c = 1)$. Adapted from Ban et al. (2016a)

of stiffening depends on network architecture (cellular versus fibrous), but, within given network type, it is independent of network parameters. This can be rationalized considering that stiffening is due to the continuous alignment of fibers in the direction of the macroscopic tensile load. The rate at which fibers become aligned depends on their kinematic constraints which, in turn, depend on network architecture.

Thermal networks

Molecular networks, such as gels and rubber, are thermal. Gels are swollen molecular networks in which the network material occupies a small fraction of the total gel volume—a situation similar to that of the non-embedded athermal networks discussed above. Rubber is a non-swollen network above its glass transition temperature (in ambient conditions). The network segments are subjected to thermal fluctuations and are free to sample their configuration phase space.

It is currently believed that the nature of stress in these networks is entropic, while the energetic component can be neglected. Therefore, network segments behave like entropic springs in tension. These can be either linear (Eq. 1.2) or nonlinear Langevin springs (Treloar 1975). The strands do not store energy in the bending, shear, or torsional modes. Therefore, thermal networks can be represented schematically as central force networks with a specific type of constitutive behavior for the strands.

Central force networks in 3D, with connectivity below $\bar{z} = 6$, are sub-isostatic. They acquire stiffness upon stretching and the strain required to reach stability increases with increasing the distance from the isostatic point, $6 - \bar{z}$ (Sharma et al. 2016).

Treloar (1954) and Treloar and Riding (1979) developed a network theory in which chains have full spatial distribution of end-to-end vector orientations and the global stress is obtained by averaging over this distribution. Chain deformation is considered affine, i.e., each end-to-end vector stretches and rotates as dictated by the far field. A simple formula is derived for Young and shear moduli of such networks:

$$E_0 \sim G_0 = Nk_BT. \tag{1.13}$$

Equation (1.13) indicates that the stiffness is proportional to the density of strands, which is a consequence of the affine assumption. It is also proportional to k_BT (increases with increasing temperature), which is a consequence of the entropic nature of stress production.

The affine assumption is a major approximation in these theories. In reality, network nodes are free to fluctuate and move non-affinely in order to reduce the overall free energy. The effect of fluctuations was incorporated in Eq. (1.13) leading to a smaller estimate for the shear modulus:

$$E_0 \sim G_0 = Nk_BT\frac{\bar{z}-2}{\bar{z}}. \tag{1.14}$$

The modulus depends on the coordination number. As $\bar{z}$ increases, the non-affine prediction (Eq. 1.14) converges to the affine result, Eq. (1.13). For $\bar{z} = 4$, the ratio of the non-affine to the affine moduli is only ½, which is small compared to the corre-

sponding value inferred from Fig. 1.20. This large difference is due to the presence of free volume in the networks considered in Fig. 1.20. A review of developments starting from the affine network model is presented in Boyce and Arruda (2000).

It should be observed that the condition of isochoric deformation reduces significantly the degree of non-affinity of the deformation, especially in regime II. Even an athermal network with no embedding matrix and with large free volume would deform almost affinely if subjected to constant volume deformation in the far field. Therefore, isochoricity in the thermal as well as athermal cases renders the affine model approximately applicable.

Damage and Rupture in Random Networks

The discussion of network rupture is divided here in (a) the analysis of the failure of the material with no initial flaws and (b) that of the growth of pre-existing cracks.

Networks with No Pre-existing Flaws

The rupture of networks presents complexities caused by the following specificities:

- Networks have discrete structure. The local mechanics is different from that of a continuum and hence the problem of nucleation of "flaws" is also quite different.
- Networks have stochastic structure. They present fluctuations of fiber and crosslink densities on multiple scales, from l_c to the scale of the network. In this regard, they are similar to composites with stochastic microstructure, whose failure is notoriously difficult to interpret.
- Rupture requires the failure of fibers and/or the failure of crosslinks. Experiments are needed in each application to determine the primary failure mode.

The evolution of rupture can be qualitatively evaluated by direct inspection of the stress–strain curves. These have different appearance in different types of networks. Two examples are provided in Fig. 1.24.

Figure 1.24a shows several stress–stretch curves obtained with a reconstructed collagen network (Ovaska et al. 2017). The collagen is harvested from the sea cucumbers—a marine organism. Several features can be observed. The most obvious is the large variability from sample to sample. This is characteristic for materials with stochastic structure, but is particularly pronounced in network materials. The variability is generally associated with damage accumulation and is most pronounced in the post-critical behavior. The peak of the stress–strain curve defining the material strength is also affected by strong variability.

The material behavior before the peak stress in Fig. 1.24a is typical for network materials and is similar to that presented in Fig. 1.7. The stress–strain curve exhibits all three regimes, including a well-defined strain-hardening regime II, and failure

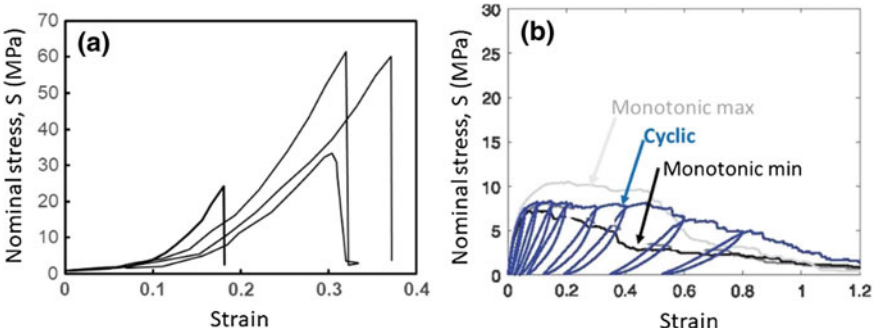

Fig. 1.24 Stress–strain curve of networks that exhibits failure. **a** Reconstructed collagen extracted from sea cucumber; adapted from Ovaska et al. (2017), and **b** geotextile of polypropylene fibers of ~50 μm diameter; adapted from Chen et al. (2016a)

takes place at high stresses, in regime III. Failure is brittle and no sign of damage accumulation exists (the tangent modulus in regime III does not decrease before failure). This type of behavior is also observed in brittle gels.

The behavior shown in Fig. 1.24b (Chen et al. 2016a) is quite different and is characteristic for a broad range of network materials, including paper, nonwovens, and some biological tissue. The response exhibits sample-to-sample variability in this case too; however, the variability is associated with damage accumulation. The figure shows the limit (maximum and minimum) curves obtained with the respective lot of nonwoven samples, and a specific curve for which cyclic loading has been performed. The curves are identical over their initial part, which indicates that the effective, homogenized behavior in absence of damage is not affected by variability. The peak stress and the post-critical branch of the curve exhibit pronounced variability. The material does not exhibit the three regimes outlined in Fig. 1.7 since damage accumulation begins at small stresses. It leads to a gradual reduction of the tangent stiffness before the peak and to gradual softening in the post-critical regime.

The cyclic curve provides useful information. Unloading and reloading cycles are performed at various strains and hysteresis is observed in all cycles. In these materials, hysteresis is associated primarily with interfiber friction. The slope of the reloading branch decreases gradually as the total stretch increases, which is a result of damage accumulation in the sample.

The parameter of interest in all these cases is the value of the peak stress, or the strength of the network. The toughness, represented here by the total area under the stress–strain curve, is also of interest in some applications. However, predicting toughness is particularly difficult given that the material reorganizes during loading, which leads to load redistribution. In addition, material strength and toughness are expected to be significantly load path dependent. We focus the discussion here on the relation between network strength and structure.

To demonstrate the general trends expected when adjusting network parameters, consider the results shown in Fig. 1.25 (Deogekar and Picu 2018). Cellular networks in which crosslinks are allowed to fail at specified effective force, and with a broad

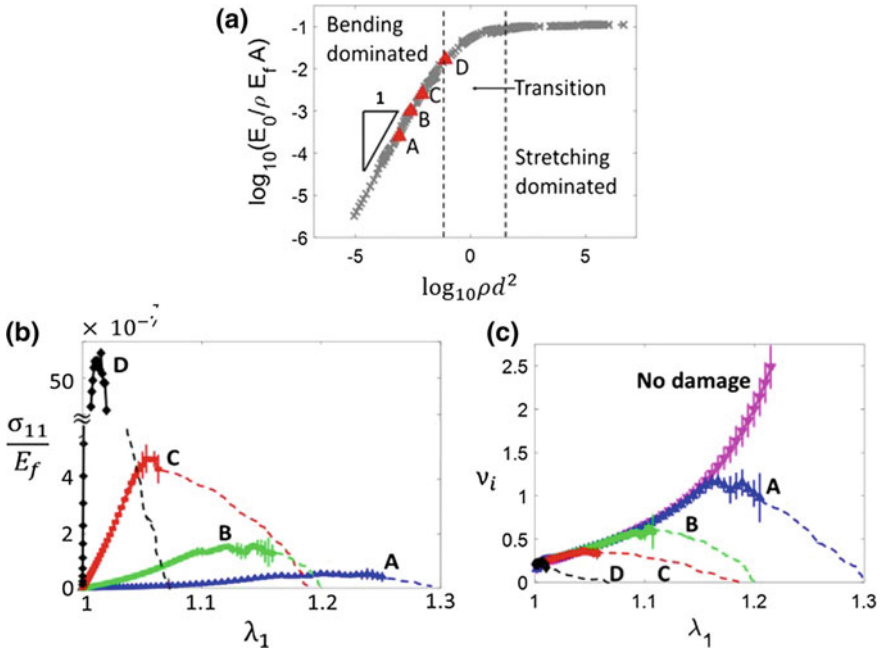

Fig. 1.25 The stress–stretch curves of four networks selected from the non-affine region of the master curve in (**a**) and labeled A, B, C, and D are shown in (**b**). **c** Shows the variation of the incremental Poisson ratio for these networks during deformation. The curve corresponding to network A in which crosslink rupture is prevented is shown in (**c**). Reproduced with permission from Deogekar and Picu (2018)

range of parameters, are constructed. These are classified in terms of a master plot similar to that of Fig. 1.20, which provides the variation of the effective small strain modulus with a nondimensional group of network parameters, ρd^2. For cellular networks, this group is equivalent to parameter w in Fig. 1.20. Four networks from the non-affine range of the master plot are selected (labeled A, B, C, and D in Fig. 1.25a). Their stress–stretch curves are shown in Fig. 1.25b. These networks fail in regime I and II of the deformation. As ρd^2 decreases, both the modulus, E_0, and the strength, σ_c, decrease, while the stretch corresponding to the peak stress increases. The more non-affine the deformation is, the more stretchy, but weaker, the network becomes.

It is observed that a relatively small (order of 5%) number of crosslinks break before the peak stress is reached (Chen et al. 2016b; Deogekar and Picu 2018). The stress–stretch curve departs from that of the equivalent network in which rupture is prevented only close to peak stress. Beyond peak stress, the network softens continuously to full rupture.

Figure 1.25c shows the variation of the incremental Poisson ratio (Eq. 1.11) during deformation for the networks whose stress–stretch curves are shown in Fig. 1.25b (Deogekar and Picu 2018). The Poisson ratio follows the curve corresponding to the

case in which damage is prevented (labeled "no damage") up to the peak stress. A maximum is observed in the incremental Poisson ratio at peak stress. As the network softens, the incremental Poisson ratio decreases. The intense bond failure after peak stress leads to a reduction of the rate of fiber alignment. It also allows the network to rebound laterally under the action of the fibers which run predominantly transverse to the main tensile loading direction. These transverse fibers are highly bent in order to accommodate the formation of load-bearing paths oriented in the loading direction. Bond failure allows their partial relaxation which causes a reduction of the rate of Poisson contraction with increasing stretch.

A detailed analysis of the effect of various network parameters on strength, σ_c, is desirable. Experimental studies of various fibrous materials such as nonwovens (Chocron et al. 2008; Jearanaisilawong 2004), paper (Clark 1985; Forsstrom et al. 2005; Marais et al. 2014; Torgnysdotter and Wågberg 2003), and biological tissues (Akins et al. 2011) highlight various aspects of the structure–strength correlation. Key parameters affecting the overall strength of fiber networks are the network anisotropy (due to preferential fiber alignment) (Farukh et al. 2014; Koh et al. 2013), network density (Heyden and Gustafsson 1998), and the properties of the crosslinks (Berhan and Sastry 2003; Heyden and Gustafsson 1998; Magnusson 2016).

Numerical studies of cellulose networks (Heyden and Gustafsson 1998) and experiments on nonwovens (Chen et al. 2016a) indicate that strength scales linearly with the density. The dependence of material strength on the number of crosslinks and crosslink properties is discussed extensively in the literature on paper mechanics. An increase of the number of interfiber contacts per fiber, due to an increase of fiber flexibility (Clark 1985; Forsstrom et al. 2005) or due to treatment by polyamines (Marais et al. 2014), leads to increased network strength. A similar relation between tensile strength and the number of interfiber crosslinks was also observed in experimental studies on biological tissues (Akins et al. 2011), although a quantitative relation was not established. The strength of crosslinks, which in turn depends on the area of the contact (Malakhovsky and Michels 2007), the strength of molecular adhesion (Marais et al. 2014), and the crosslink failure mode (Magnusson 2016) have a direct relationship with the network strength.

Effect of bond strength

The relationship between network and crosslink strength was studied numerically in Borodulina et al. (2016), Deogekar and Picu (2018). The bonds are of type (c) in Fig. 1.2 and may fail due to mode I (opening) or mode II (shear) loading. Torsion of the crosslink due to the relative rotation of the two fibers about the axis normal to the plane of the contact is not considered to be essential in this mechanics. Rolling of one fiber relative to the other leads to failure in mode I. The crosslink is considered to fail when the effective force transmitted exceeds a critical force, f_c, which is considered a material parameter. The effective force transmitted by the crosslink is

$$F_{eq} = \sqrt{F_{b1}^2 + F_{b2}^2 + \left\langle F_{b3} - \frac{6}{D_b}\sqrt{M_{b1}^2 + M_{b2}^2}\right\rangle^2} \tag{1.15}$$

where F_{b1}, F_{b2}, and F_{b3} are the forces loading the bond in the direction of the three coordinate axes tied to the contact surface (axes x_{b1} and x_{b2} define the contact plane and x_{b3} is perpendicular to the contact), and M_{b1} and M_{b2} are the moments transmitted acting along local axes x_{b1} and x_{b2}. D_b represents the characteristic size of the bond ($D_b < d$) and $< >$ indicates Macaulay bracket, which vanishes if the quantity in the bracket is negative and is equal to the respective quantity when it is positive.

Figure 1.26 shows the variation of the network strength with f_c as obtained from models of cellular networks. The data corresponds to a broad range of non-affinely deforming networks, with parameter $log_{10}\rho d^2$ of the horizontal axis of the master curve in Fig. 1.25a ranging from -3.3 to 0.9. Parameter f_c can be used to control the regime of the network deformation in which the peak stress is reached. Small values of f_c lead to the peak stress occurring in regime I or early regime II of network deformation (e.g., a situation such as that shown in Fig. 1.24b), while large values of f_c shift the peak stress to regime III (see Fig. 1.24a). It is observed that for this broad range of parameters,

$$\sigma_c \sim f_c. \tag{1.16}$$

Similar scaling is observed in the small strain simulations reported in Heyden (2000) and is supported by the experimental results in Forsstrom et al. (2005). In Forsstrom et al. (2005), various types of cellulose networks were tested and the crosslink strengths were measured in separate experiments. A linear relationship between the mean values of the network and crosslink strengths is reported for all pulp types used.

A note should be made regarding the effect of crosslink strength variability. Clearly, in physical networks not all crosslinks have the same strength. It becomes then important to inquire whether increasing the variance of the bond strength distri-

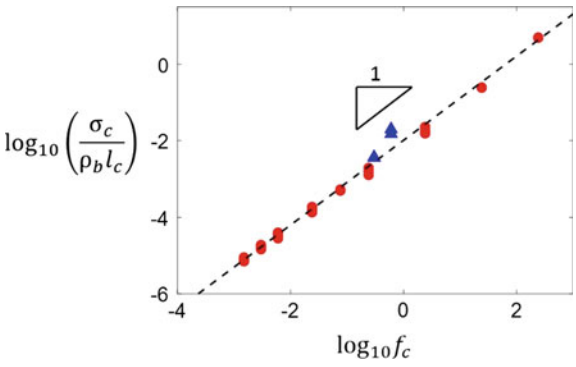

Fig. 1.26 Variation of network strength with the strength of the crosslinks obtained with 3D models of cellular networks. Red circles correspond to peak stress occurring in regime II, while blue triangles indicate that the peak stress occurs in regime III. In the blue triangle case, the network is aligned in the loading direction at the onset of bond failure. In all cases, bond deformation is less than a tenth of the fiber diameter, d

bution, while keeping the mean of the distribution constant, has any effect on σ_c. This issue was discussed in Borodulina et al. (2016) and Deogekar and Picu (2018) with different conclusions. In Borodulina et al. (2016), it is concluded that variability has a weak effect on σ_c; however, the mean crosslink strength was not kept constant while varying the variance of the respective distribution. In Deogekar and Picu (2018), it is observed that σ_c decreases monotonically with increasing the coefficient of variation of f_c, while keeping the mean f_c constant.

Effect of the density and crosslink density

Experimental indications exist that σ_c is proportional to the network density, ρ. However, in most situations, the network density, ρ, and the bond number density, ρ_b, are proportional. The relative contribution of these two parameters to defining the network strength was analyzed in Deogekar et al. (2019) by independently varying ρ_b at constant ρ. Figure 1.27 shows such results for fibrous and cellular networks, with the network strength plotted against each of these two parameters. In Fig. 1.27b, the strength of fibrous networks scales linearly with ρ because for these networks ρ is proportional to ρ_b. However, in cellular networks in which ρ and ρ_b are independent, the strength takes multiple values at prescribed ρ. It results that

$$\sigma_c \sim \rho_b, \tag{1.17}$$

The lack of scaling with ρ can be understood considering a network containing fibers with a large number of dangling ends. The network density is computed based on the total length of fiber per unit volume and includes the dangling ends. However, these are not loaded and hence have no effect on strength as long as excluded volume interactions are not critical (which is the case in uniaxial and multiaxial tension).

General strength–structure relation

A rather general study of the relation between network structure and strength is presented in Deogekar et al. (2019). This study starts from the observations summarized in Eqs. (1.16) and (1.17) and takes a step further by considering the effect of

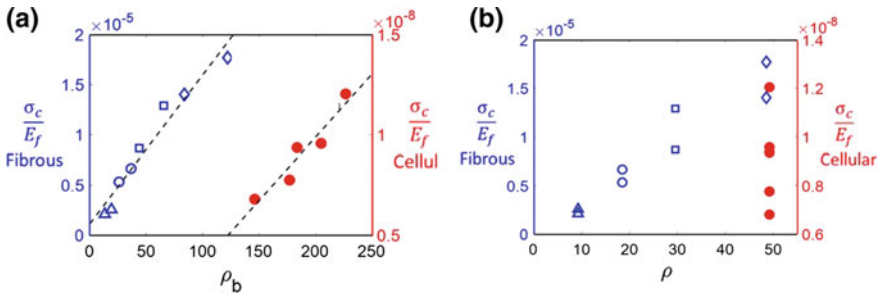

Fig. 1.27 Variation of network strength, σ_c, with **a** the bond number density, ρ_b, and **b** the network density, ρ, for fibrous (open symbols) and cellular (filled circles) networks. For the fibrous networks, symbols of same type indicate networks of same density, ρ. For the cellular networks, the network density is kept constant for all cases shown here (Deogekar et al. 2019)

the fiber bending and axial stiffness and that of fiber tortuosity on network strength. These parameters were varied in a broad range covering a variety of applications. The results are presented in Fig. 1.28 which shows data collapse indicating that

(i) Relations (1.16) and (1.17) apply,
(ii) Network strength is independent of fiber properties (e.g., axial and bending rigidities), and
(iii) Network strength does not depend on fiber tortuosity, c.

The data indicates that, with broad generality,

$$\sigma_c \sim f_c \rho_b l_c. \tag{1.18}$$

With Eqs. (1.6) and (1.7), Eq. (1.18) can be rearranged as

$$\sigma_c \sim \frac{f_c}{l_c^2} \tag{1.19}$$

which emphasizes a physical interpretation of strength: the network responds as if the load is carried by a set of crosslinks arranged in an array of average inter-crosslink distance l_c. The peak stress is reached when these crosslinks are loaded with a force at the critical value of f_c. The constant of proportionality in Eq. (1.19) is identical in fibrous and cellular networks considered in Deogekar et al. (2019), but, in general, may depend on network structure.

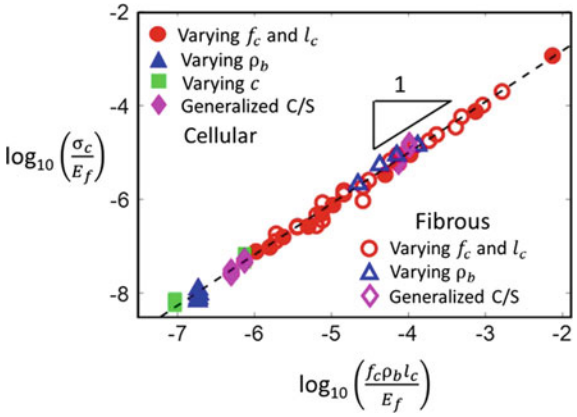

Fig. 1.28 Variation of network strength, σ_c, with the nondimensional group $\rho_b f_c l_c / E_f$ for cellular and fibrous networks with a broad range of network parameters. Generalized C/S stands for the generalized cross-section model of fibers in which the fiber bending and axial rigidities are varied independently and in a broad range of values. Filled symbols represent cellular networks, while open symbols represent fibrous networks (Deogekar et al. 2019)

Growth of Cracks in Fibrous Materials

The fracture mechanics perspective on material strength is based on the concept that cracks pre-exist. Then, predicting strength is equivalent to predicting crack growth. Given the stochastic structure of networks, it is difficult to define pre-existing "cracks" of length comparable with l_c, while cracks much larger than this characteristic length scale of the microstructure rarely exist. The problem of network rupture has to include the nucleation of damage and its evolution up to a state at which macroscopic localization can happen. This point of view is taken in section "Networks with No Pre-existing Flaws."

Nevertheless, some useful results were obtained from studies of networks in which cuts were introduced to mimic macroscopic cracks (Koh et al. 2013; Ridruejo et al. 2015; Chen et al. 2016b). The central result of these studies is the fact that networks are notch insensitive. Figure 1.29 shows results obtained with a series of nonwoven mats of the shape indicated in the inset (Ridruejo et al. 2015). The samples are similar to the common double-notched specimens used in fracture mechanics and are characterized by the width, W, and the ligament size, B. Samples with a range of value for W and B were tested by applying tension perpendicular to the plane of the cracks and ligament. The material is a polypropylene nonwoven with "infinite" fibers. The fibers are bonded at contact points by applying pressure perpendicular to the mat plane, while increasing the temperature. The stress–strain curves resulting from such tests are similar to those shown in Fig. 1.24b.

The data in Fig. 1.29 shows that the nominal strength of notched samples is actually larger than that of unnotched equivalents, and the difference increases as the

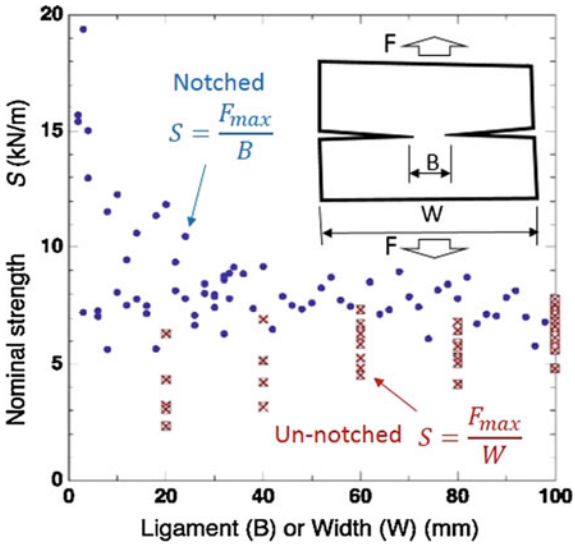

Fig. 1.29 Nominal strength of notched samples. The nominal strength is evaluated as indicated in the figure. Data from samples with and without notches is included. Adapted from Ridruejo et al. (2015)

respective characteristic length (either the sample width in the unnotched case or the ligament size in the notched case) decreases.

The crosslinks fail first in the ligament region. This provides fibers with sufficient kinematic freedom to orient in the loading direction. The structure of the network in the ligament becomes therefore different from that elsewhere and the sample breaks only when the aligned fibers in the ligament break. This situation is not encountered in the unnotched sample which accumulates damage gradually during loading (section "Networks with No Pre-existing Flaws"). Similar toughening introduced by notches was also observed in collagen membranes (Oyen et al. 2004).

Similar situations are expected in the vicinity of other stress concentration sites, such as reentrant corners, macroscopic holes, and blunt notches. Fibers align in the direction of the maximum tensile principal stress, which toughens the material locally and prevents further evolution of damage in the respective region. Notch insensitivity is a very useful property of nonwoven mats and biological tissue.

Networks with Adhesive Fiber Interactions—Networks of Bundles

The role of surface interactions in organizing the network structure is outlined in section "Surface Interactions." Adhesion is a special type of surface interaction. It has short range and can be rather strong and effective in holding filaments together in bundles. These bundles can organize on larger scales to form networks of bundles. While such networks are broadly encountered, as, for example, in buckypaper, nanofilament assemblies and collagen networks, and their structure and mechanics are poorly understood. This section is based on recent articles (Picu and Sengab 2018; Sengab and Picu 2018; Negi and Picu 2019a) which address the problem of adhesion-driven networks self-organization in both crosslinked (Negi and Picu 2019a) and non-crosslinked networks (Picu and Sengab 2018; Sengab and Picu 2018). It was observed that in the case without crosslinks, adhesive interactions lead to the formation of a network structure in which the role of fibers is played by fiber bundles and the crosslinks are specific triangular constructs of fiber bundles which stabilize the network of bundles. The structure resulting upon network self-organization depends on a nondimensional parameter which represents the interplay between adhesive and bending energies. A crosslinked network of fibers which is isostatic, shrinks under the action of adhesive forces. The degree of shrinkage depends on the strength of adhesion. If the network is sub-isostatic, the shrinkage is particularly pronounced. The mechanical behavior of such networks is controlled in part by the adhesive interactions and, in part, by the underlying crosslinked network structure.

Some Basic Considerations Regarding Adhesion of Filaments

To understand the effect of adhesion in this context, it is useful to consider first simple structures constructed from several fibers.

Example 1 Consider fibers of identical diameter, d, identical length, L, and made from the same linear elastic material characterized by Young's modulus, E_f. Adhesion is defined by parameter γ which represents the energy gain per unit length of contact when two surfaces are brought together. Note that γ has units of N and is related to the specific work of adhesion, γ_0, and to the elasticity of the two contacting fibers. The Johnson–Kendall–Roberts (JKR) theory (Johnson et al. 1971) predicts $\gamma \sim \gamma_0^{4/3} E_f^{1/3}$, such that a softer fiber material implies a stronger adhesive effect for given γ_0.

Consider further the initial configuration shown in Fig. 1.30 and its corresponding final state after the fibers are allowed to stick. The crosslink at B is a pin joint which allows free rotation, and the motion of ends A and C is constrained in the horizontal direction. After adhering, fibers form a common segment of length s. The length of this segment can be evaluated analytically and is given by

$$\frac{s}{L} = \cos\frac{\alpha}{2} - \left(9\frac{E_f I_f}{\gamma L^2} sin^2\frac{\alpha}{2}\right)^{1/4}. \tag{1.20}$$

The solution depends on a single nondimensional material parameter:

$$\Psi = \frac{\gamma L^2}{E_f I_f} \tag{1.21}$$

which represents the interplay of adhesion and bending resistance. This parameter can be rearranged as $\Psi = (L/L_{EC})^2$, where the characteristic length $L_{EC} = \sqrt{E_f I_f/\gamma}$ has been defined in the literature as the elastocapillarity length (Roman and Bico 2010). With this, Ψ can be interpreted as expressing a comparison between a characteristic geometric length scale of the problem and the material parameter L_{EC}.

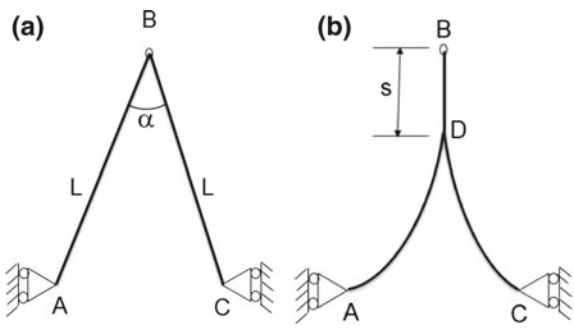

Fig. 1.30 Evolution of two pin-jointed fibers under the action of adhesion. **a** and **b** Show the initial and final states

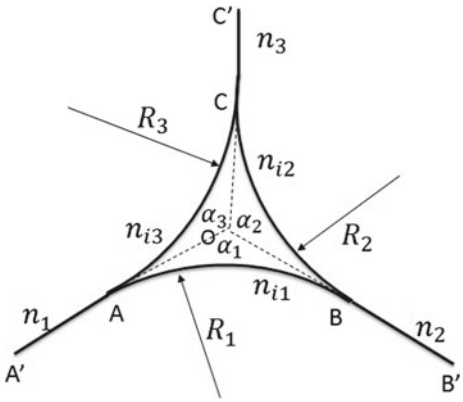

Fig. 1.31 Parameters defining a triangle of fiber bundles. Reproduced with permission from Picu and Sengab (2018)

It is important to observe that s/L decreases rapidly as the fiber diameter increases at constant γ since $I_f \sim d^4$. Hence, for given γ_0, fibers of nanoscale diameter are more susceptible to adhesion than fibers of larger diameter.

The total energy, computed as the difference between the bending and adhesion energies, decreases continuously from 0 in the state in Fig. 1.30a to a minimum in the state of Fig. 1.30b. Hence, no activation is needed to initiate the bundling process.

Example 2 Consider now the triangular structure of fiber bundles shown in Fig. 1.31. This structure emerges upon the relaxation of a non-crosslinked network of fibers with interfiber adhesion (Picu and Sengab 2018). All nodes of the resulting network of bundles are of this type. Here we show that the structure is self-equilibrated and define some of its geometric characteristics.

Each branch of this structure is a bundle of parallel fibers which are much longer than any dimension in Fig. 1.31. The number of fibers in each bundle segment is defined by n. External bundles AA′, BB′, and CC′ are of size n_1, n_2, and n_3 and form angles α_1, α_2, and α_3. The sub-bundles connecting nodes A, B, and C are of size n_{i1}, n_{i2}, and n_{i3} and the obvious conservation conditions $n_1 = n_{i1} + n_{i3}$, $n_2 = n_{i1} + n_{i2}$, and $n_3 = n_{i2} + n_{i3}$ hold.

Bundles AB, BC, and AC forming the triangle are loaded in pure bending and hence are arcs of circle of radii R_1, R_2, and R_3. Since these circles must be tangent to each other at A, B, and C, segments OA, OB, and OC are also of equal length, l_{tr}. If the incoming bundles AA′, BB′, and CC′ are straight, i.e., the entire bending energy is concentrated in the triangle, the bending moments loading the three edges of the triangle are equal, M_{tr}.

The equilibrium configuration of the structure results by minimizing the total energy, for given bundle sizes and set of angles, relative to the size of the triangle, l_{tr}. The bending moment results are as given below:

$$M_{tr} = \sqrt{\frac{2\gamma E_f I_f}{\pi}} B \tag{1.22}$$

where B depends only on the bundle sizes and angles α_i:

$$B = \sum_{k=1,3} n_{ik} n_c(n_k) \tan \frac{\pi - \alpha_k}{2} - n_{ik} n_c(n_{ik})(\pi - \alpha_k) \tag{1.23}$$

Structure of Networks with Interfiber Adhesion and No Crosslinks

Assemblies of non-crosslinked athermal fibers that interact adhesively are considered here. This problem has been studied in the context of carbon nanotube (CNT) structures and buckypaper in Li and Kroger (2012), Volkov and Zighilei (2010). CNTs have very strong adhesion and, when in sufficient proximity, self-assemble into bundles (Volkov and Zighilei 2010). Once deposited, further adhesion-driven self-organization of the mat is possible provided the level of friction with the background is not too high. The resulting structure is a network of CNT bundles. The present section discusses the geometric features of such network.

The concept of self-organization of a fibrous structure under the action of surface interactions is shown in Fig. 1.32. Consider a network of fibers deposited on a substrate and forming a quasi-2D mat. The structure is three dimensional, but fibers are laying on top of each other and are preferentially oriented in the plane of the mat. It is not particularly important if the fibers are straight or crimped in the initial state. If friction is low (as is the case with CNTs), and if some activation is provided, either by mechanical means or by capillarity, the fibers begin to assemble under the action of adhesion. The cellular structure shown in the right panel of Fig. 1.32 is a network of fiber bundles. The crosslinks of this network are triangles of bundles such as that shown in Fig. 1.31. These triangles play the central role in the stabilization of the network of bundles.

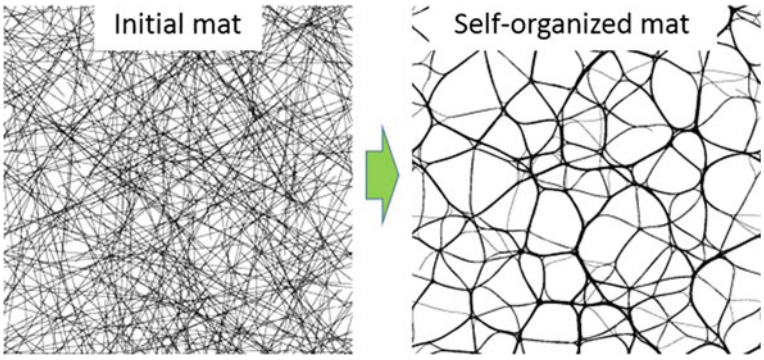

Fig. 1.32 Self-organization of a mat of fibers interacting adhesively

It is of interest to inquire how the parameters of the system influence the structure of the network of bundles in Fig. 1.32. The system parameters are the fiber length, L_f, the initial network density, defined as the total length of fiber per unit (projected) area of the mat, ρ, fiber properties, such as $E_f A_f$ and $E_f I_f$, and the strength of adhesion represented by parameter γ. A dimensional analysis (Sengab and Picu 2018) indicates that there are only two important nondimensional groups in this problem: ρL_f and $\Psi = \gamma L_f^2 / E_f I_f$.

Such networks can take one of three possible states. These are represented in the phase diagram of Fig. 1.33 drawn in the space of the two system parameters, ρL_f and $\Psi = \gamma L_f^2 / E_f I_f$.

The figure indicates that for small ρL_f, $\rho L_f < 5.71$, the initial set of fibers do not form a network. Such initial structures are too sparse to percolate (the limit value of 5.71 represents the transport percolation threshold of 2D noninteracting structures of fibers) and hence the problem addressed here is not defined. For larger ρL_f, as-deposited fiber networks may evolve under the action of surface forces and three possible final states exist, function of the nondimensional parameter Ψ. The boundary AB in Fig. 1.33 defines the percolation limit.

Small values of Ψ correspond to weak adhesion. Specifically, small Ψ results either when γ is small or when fibers are stiff in bending, i.e., $E_f I_f$ is large. Under such conditions, the structure does not evolve and remains locked in the initial state. For large values of Ψ, the structure of fibers evolves. The boundary between the domains of locked and evolving structures (AC in Fig. 1.33) is described by the equation $\Psi \sim (\rho L_f)^2$, which is derived in Picu and Sengab (2018). This boundary also depends on interfiber friction Sengab and Picu (2018). With nanofibers, friction is usually not Coulombic (friction force proportional to the normal force on the contact), rather, a situation in which the resistant force is constant or scales weakly with the relative velocity of the two surfaces (viscous) is more probable. If friction

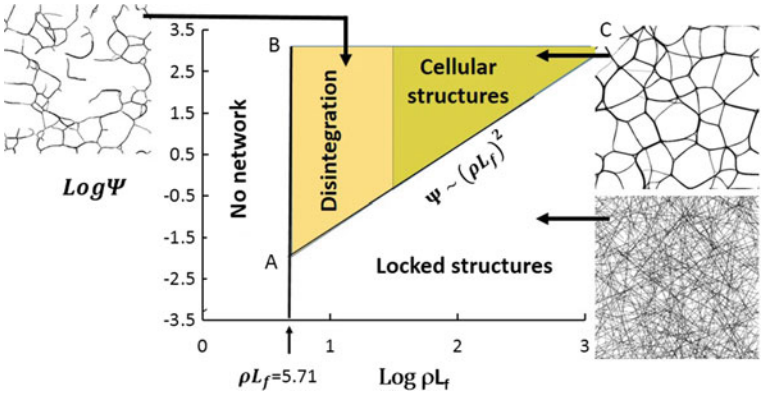

Fig. 1.33 Phase diagram in the field of nondimensional network parameters ρL_f and Ψ indicating the stable states of the system of non-crosslinked, adhesively interacting fibers. Adapted from Picu and Sengab (2018)

takes place at contacts between fibers, boundary AC moves up, increasing the range of locked structures. We conclude that, in order for the structure to evolve, the strength of adhesion should be sufficiently large, fibers should be thin and flexible, with low $E_f I_f$, the density should be low, such that the length of fiber segments between two contacts along given fiber, l_c, is large enough to allow fibers to bend, and friction should be relatively weak. These conditions are expected to be fulfilled in the case of nanofilaments, such as CNTs, collagen, and fibrin.

Evolving structures may fully disintegrate or may form stable cellular structures similar to that shown in Fig. 1.33. To understand the cause of network disintegration, consider two aligned fibers, each of length L_f. In order to minimize the potential energy, these will align along their entire length forming a bundle of length L_f. In complex networks of filaments, this lowest energy state cannot be reached due to topological reasons. However, the network may separate in a multitude of isolated bundles. This is shown in the left upper panel of Fig. 1.33. This phenomenon is expected to occur at low ρL_f.

When ρL_f is sufficiently large, the topology of the evolving network of bundles prevents disintegration. This argument is discussed in detail in Picu and Sengab (2018). Under such conditions, cellular structures such as that shown in the right upper panel of Fig. 1.33 form and become stable.

Cellular networks of bundles are stabilized by the triangular features of Fig. 1.31. These store strain energy and are self-equilibrated. The entire structure stores adhesion energy. Bundle segments between triangles (i.e., the cell walls) tend to be straight and hence do not store strain energy. These structures are stable as long as the cell size remains small relative to L_f, such that, during evolution, the structure does not cross the vertical boundary between cellular and disintegrating domains in Fig. 1.33.

Structure of Networks with Interfiber Adhesion and Crosslinks

In the presence of crosslinks, fibers are not entirely free to rearrange under the action of surface forces. Therefore, the degree of structural reorganization of the network is expected to be much smaller than in the case of non-crosslinked networks (section "Structure of Networks with Interfiber Adhesion and No Crosslinks"). This issue was studied in Negi and Picu (2019a) using a novel finite-element-based technology applied to 2D models of fiber networks.

It is of interest to discuss separately networks which are isostatic and sub-isostatic in the absence of surface interactions. It is observed that in both cases, adhesive interactions lead to a reduction of the network volume (or area, in 2D). In the isostatic case, this contraction is opposed by the intrinsic elasticity of the network. In the sub-isostatic case, the contraction is much more pronounced since the structure acquires stiffness only after some degree of deformation.

Figure 1.34 shows the variation of the network area associated with the action of adhesive interactions. Figure 1.34a refers to an isostatic network, while Fig. 1.34b refers to a sub-isostatic network. The vertical axis shows the engineering volumetric

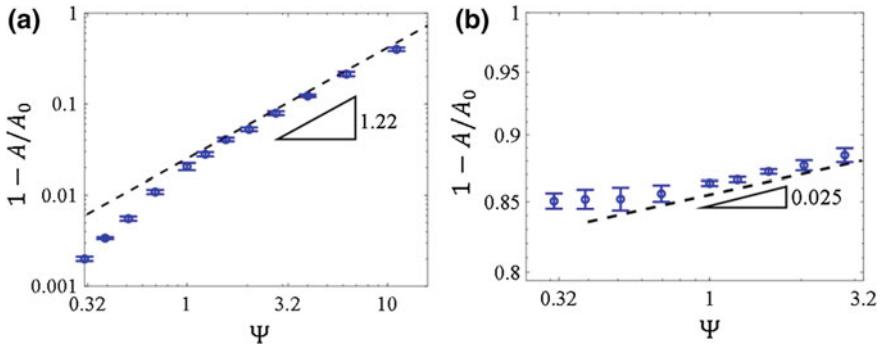

Fig. 1.34 Variation of the reduction of area function of Ψ for **a** an isostatic network and **b** a sub-isostatic network. Reproduced with permission from Negi and Picu (2019a)

strain. It is observed that as the strength of adhesion, Ψ, increases, the network shrinks. This trend is well defined in the isostatic case, but is weak in the sub-isostatic case. Sub-isostatic networks are much floppier and can shrink by more than 80% even with weak adhesion. In these cases, further increasing the strength of adhesion does not lead to a substantial increase in shrinkage.

Tensile Behavior of Networks with Interfiber Adhesion and Crosslinks

Networks with adhesive interactions and crosslinks exhibit a specific behavior under external loading. Consider a structure which is collapsed under the action of adhesive forces, as described in section "Structure of Networks with Interfiber Adhesion and Crosslinks." The degree of bundling in such states is much less extensive than that observed with non-crosslinked networks simply because the kinematic constraints imposed by the crosslinks prevent the formation of large bundles. Nevertheless, even bundling of pairs of fibers emerging from a common crosslink leads to stress–strain curves quite different from those typically observed in absence of adhesion. This problem was studied in Negi and Picu (2019a) and a brief account of the main results is presented here.

Figure 1.35a shows a set of stress–strain curves for networks with increasing Ψ. The representation of these curves as tangent stiffness versus stress is shown in Fig. 1.35b. The central observations are (i) the small strain modulus decreases significantly as the strength of adhesion increases. The network becomes very soft and the strain range of the linear regime I increases considerably. While regime I barely extends to 1% strain in the reference case without adhesion, it extends to almost 20% strain when $\Psi = 11.11$, the largest value considered in the respective study. (ii) At larger strains, the network with adhesion strain stiffens (regime II) just like the reference network without surface interactions ($\Psi = 0$).

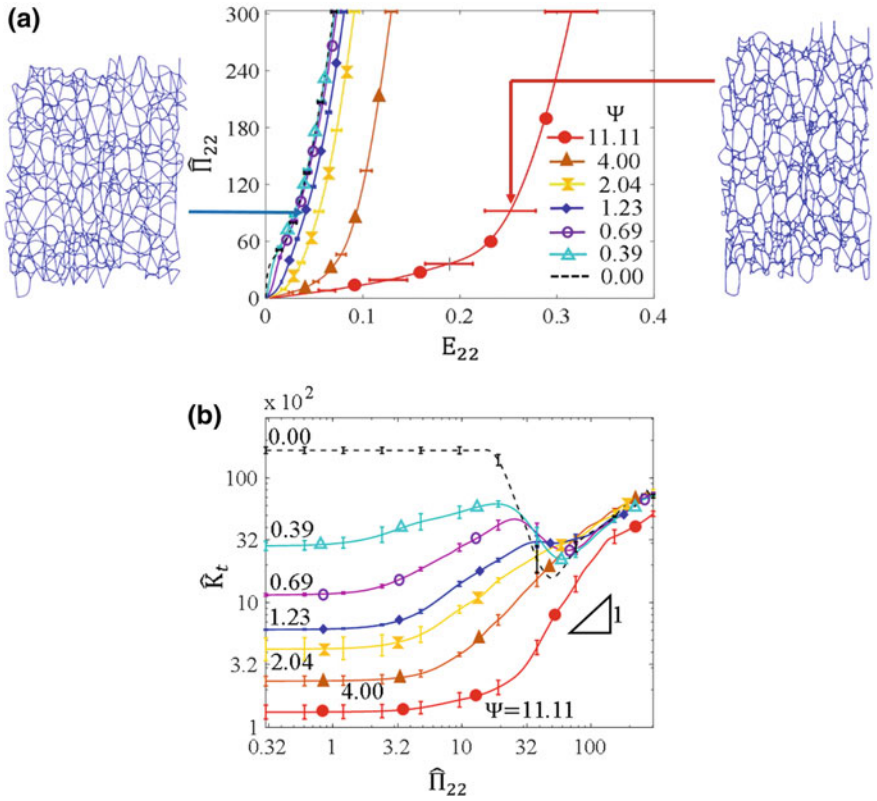

Fig. 1.35 **a** Normalized second Piola–Kirchhoff stress versus Green–Lagrange strain for Delaunay networks with various Ψ subjected to uniaxial tension. The side panels represent deformed configurations with $\Psi = 1.23$ at 5% strain and with $\Psi = 11.11$ at 25% strain. The data in (**a**) is replotted in (**b**) as normalized tangent stiffness, $\widehat{K}_t$, versus stress. Reproduced with permission from Negi and Picu (2019a)

The behavior is controlled by adhesion at small strains, and by the underlying crosslinked network at large strains. The observation that adhesion drastically transforms the network behavior in the small strain regime is of importance in applications. It implies that the softness of some "soft materials" is not that much related to the network structure, as it is with the effect of interfiber surface interactions of adhesive type. It is of great interest that adhesion transforms a network which at $\Psi = 0$ has a strongly nonlinear response into a much softer material with linear constitutive behavior up to large strains.

Sub-isostatic networks with adhesion also exhibit interesting behavior. Figure 1.36 shows stress–strain curves for Voronoi networks with various values of Ψ. In the $\Psi = 0$ state, these networks have zero stiffness at small strains. Figure 1.36a shows that, in presence of adhesion, the small strain stiffness is finite and increases with increasing Ψ. At small strains, this structure unbundles as it deforms. The stress–strain curve

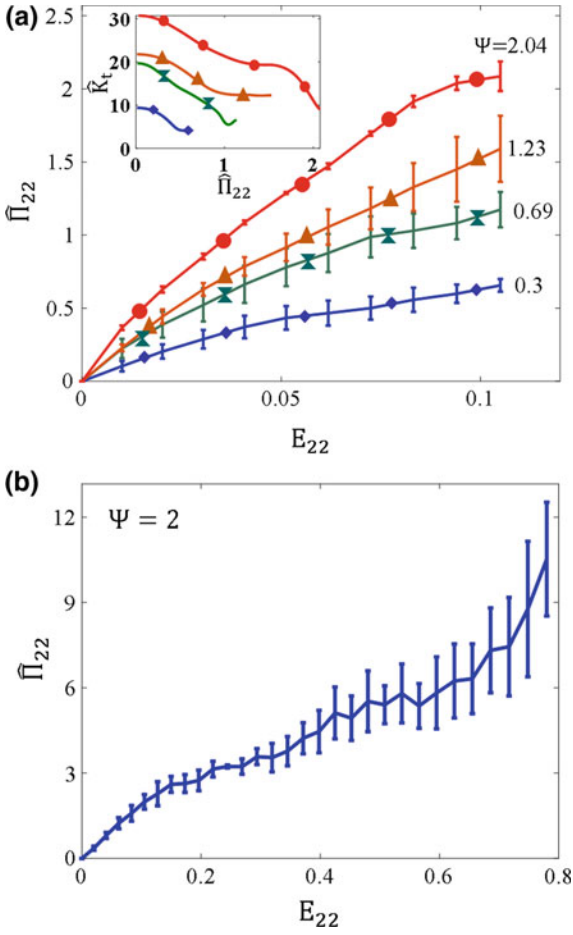

Fig. 1.36 **a** Second Piola–Kirchhoff stress versus Green–Lagrange strain for Voronoi networks with various Ψ subjected to uniaxial tension. **b** Extension of the curve in (**a**) corresponding to $\Psi = 2$ to large strains. Reproduced with permission from Negi and Picu (2019a)

softens as unbundling progresses. Stress–strain curve with softening is not observed in networks without interfiber surface interactions and in absence of failure.

The response becomes controlled by the crosslinked structure of the network at larger strains. This can be seen in Fig. 1.36b where one of the curves in Fig. 1.36a is extended to large strains (Negi and Picu 2019a). Strain stiffening is observed in this regime. Hence, once again, adhesion introduces a bimodal response, controlled by adhesion at small strains and more akin to that of the reference network without adhesion at large strains.

Concluding Remarks and Outlook

Network materials are ubiquitous in our daily lives. In biological materials, in bio-engineering constructs and other artificial engineering materials, random networks perform structural functions ensuring the integrity of the respective materials under loads. Most network materials have random microstructures and this motivates the focus of this chapter on networks with stochastic architecture. A separate branch of activity is devoted to periodic or quasiperiodic structures made from filaments. A common example is that of woven composites in which fiber bundles are weaved into an approximately periodic structure. Intense activity is devoted at present to the class of so-called metamaterials, which are periodic structures made from trusses or beams designed such to exhibit specific behaviors at the macroscopic scale. The viewpoint taken in this sub-field is that, in principle, any type of mechanical response can be obtained with the proper design of the network architecture. Periodicity is desirable in order to keep the phase space of possible designs limited. Once a repeat unit is defined, a material can be constructed (e.g., by additive manufacturing) which reproduces at the macroscale the behavior of the unit cell or a collective, emerging behavior of a group of repeat units. Although related, this area or research is sufficiently different from the topics discussed here to prevent its inclusion in this review.

The discussion in this section is limited to networks without an embedding matrix. Many biological fibrous materials have a fluid or viscoelastic solid matrix. The interaction of the network with the matrix is complex and the quantitative understanding available at this time in this area is sparse. This limitation notwithstanding, there are situations in which the material response is controlled by the network and the matrix has secondary role. The results discussed here apply in such situations.

It is also of interest to further investigate the behavior of networks with interfiber surface interactions. The results discussed in this chapter indicate that interesting effects result from the competition of these interactions with the behavior of the underlying network and such synergies may be exploited to great advantage in specific applications. This is likely occurring in many biological applications in which fibers are composed of smaller scale filaments organized in bundles. Networks of bundles have complex microstructures, which are quite different from those of cellular and fibrous networks discussed here. Examples of this type are discussed in the last part of the present chapter.

Significant progress has been made in this field over the last two decades. It is envisioned that the near future will see the development of new fibrous materials that make use of the principles discussed here. These also provide an avenue to deepen our understanding of the role of mechanics in biomaterials and biology.

References

Akins, M. L., Luby-Phelps, K., Bank, R. A., & Mahendroo, M. (2011). Cervical softening during pregnancy: Regulated changes in collagen cross-linking and composition of matricellular proteins in the mouse1. *Biology of Reproduction, 84,* 1053–1062.

Alava, M., & Niskanen, K. (2006). The physics of paper. *Reports on Progress in Physics, 69,* 669–723.

Alexander, S. (1998). *Physics Reports, 296,* 65.

Astrom, J. A., Kumar, P. B. S., Vattulainen, I., & Karttunen, M. (2008). Strain hardening, avalanches, and strain softening in dense cross-linked actin networks. *Physical Review E, 77,* 051913.

Athesian, G. A. (2009). The role of interstitial fluid pressurization in articular cartilage lubrication. *Journal of Biomechanics, 42,* 1163–1176.

Ban, E., Barocas, V., Shephard, M. S., & Picu, R. C. (2016a). Effect of fiber crimp on the elasticity of random fiber networks with and without embedding matrices. *Journal of Applied Mechanics, 83,* 041008.

Ban, E., Picu, R. C., Barocas, V., & Shephard, M. S. (2016b). Softening in random networks of non-identical beams. *Journal of the Mechanics and Physics of Solids, 87,* 38–50.

Ban, E., Zhang, S., Zarei, V., Barocas, V. H., Winkelstein, B. A., & Picu, R. C. (2017). Collagen organization in facet capsular ligaments varies with spinal region and with ligament deformation. *Journal of Biomechanical Engineering, 139,* 071009.

Bancelin, S., Lynch, B., Bonod-Bidaud, C., Ducourthial, G., Psilodimitrakopoulos, S., Dokladal, P., et al. (2015). Ex-vivo multiscale quantitation of skin biomechanics in wild-type and genetically-modified mice using multiphoton microscopy. *Scientific Reports, 5,* 17635.

Benitez, A. J., & Walther, A. (2017). Cellulose nanofibril nanopaper and bioinspired nanocomposites: A review to understand the mechanical properties space. *Journal of Materials Chemistry A, 5,* 16003–16024.

Berhan, L., & Sastry, A. M. (2003). On modeling bonds in fused, porous networks: 3D simulations of fibrous-particulate joints. *Journal of Composite Materials, 37,* 715–740.

Boal, D. (2012). *Mechanics of the cell*. Cambridge University Press.

Borodulina, S., Kulachenko, A., Galland, S., & Nygards, M. (2012). The stress-strain curve of paper revisited. *Nordic Pulp & Paper Research Journal, 27,* 318.

Borodulina, S., Motamedian, H. R., & Kulachenko, A. (2016). Effect of fiber and bond strength variations on the tensile stiffness and strength of fiber networks. *International Journal of Solids and Structures, 154,* 19–32.

Bowden, F. P., & Tabor, D. (2001). *The friction and lubrication of solids*. Oxford: Oxford University Press.

Boyce, M. C., & Arruda, E. M. (2000). Constitutive models of rubber elasticity: A review. *Rubber Chemistry and Technology, 73,* 504–523.

Broedersz, C. P., & MacKintosh, F. C. (2011). Molecular motors stiffen non-affine semiflexible polymer networks. *Soft Matter, 7,* 3186–3191.

Broedersz, C. P., & Mackintosh, F. C. (2014). Modeling semiflexible polymer networks. *Reviews of Modern Physics, 86,* 995–1036.

Broedersz, C. P., Sheinman, M., & MacKintosh, F. C. (2012). Filament-length-controlled elasticity in 3D fiber networks. *Physical Review Letters, 108,* 078102.

Bustamante, C., Marko, J. F., Siggia, E. D., & Smith, S. (1994). Entropic elasticity of lambda-phage DNA. *Science, 265,* 1599–1600.

Calladine, C. R. (1978). Buckminster Fuller's "Tensegrity" structures and Clerk Maxwell's rules for the construction of stiff frames. *International Journal of Solids and Structures, 14,* 161–172.

Chen, N., Koker, M. K. A., Uzun, S., & Silberstein, M. N. (2016a). In-situ X-ray study of the deformation mechanisms of non-woven polypropylene. *International Journal of Solids and Structures, 97–98,* 200–208.

Chen, Y., Ridruejo, A., González, C., Llorca, J., & Siegmund, T. (2016b). Notch effect in failure of fiberglass non-woven materials. *International Journal of Solids and Structures, 96,* 254–264.

Chocron, S., Pintor, A., Gálvez, F., Roselló, C., Cendón, D., & Sánchez-Gálvez, V. (2008). Lightweight polyethylene non-woven felts for ballistic impact applications: Material characterization. *Composites Part B: Engineering, 39,* 1240–1246.

Clark, J. D. A. (1985). Wet fibre compactibility. In *Pulp technology and treatment for paper* (p. 560). San Francisco: Miller Freeman Inc.

Connelly, R., & Whiteley, W. (1966). Second order rigidity and pre-stress stability for tensegrity frameworks. *SIAM Journal on Discrete Mathematics, 9,* 453–491.

Deogekar, S., Islam, M. R., & Picu, R. C. (2019). Parameters controlling the strength of stochastic fibrous materials. *International Journal of Solids and Structures* (in press).

Deogekar, S., & Picu, R. C. (2017). Structure-properties relation for random networks of fibers with non-circular cross-section. *Physical Review E, 95,* 033001.

Deogekar, S., & Picu, R. C. (2018). On the strength of random fiber networks. *Journal of the Mechanics and Physics of Solids, 116,* 1–16.

Dodson, C. T. J., & Sampson, W. W. (1996). The effect of *paper* formation and grammage on its pore size distribution. *Journal of Pulp and Paper Science, 22,* J165–J169.

Eichhorn, S. J., & Sampson, W. W. (2005). Statistical geometry of pores and statistics of porous nanofibrous assemblies. *Journal of the Royal Society, Interface, 2,* 309–318.

Farukh, F., Demirci, E., Sabuncuoglu, B., Acar, M., Pourdeyhimi, B., & Silberschmidt, V. V. (2014). Numerical analysis of progressive damage in nonwoven fibrous networks under tension. *International Journal of Solids and Structures, 51,* 1670–1685.

Federico, S., & Herzog, W. (2008). On the anisotropy and inhomogeneity of permeability in articular cartilage. *Biomechanics and Modeling in Mechanobiology, 7,* 367–378.

Fixman, M., & Kovac, J. (1973). Polymer conformational statistics. III. Modified Gaussian models of stiff chains. *Journal of Chemical Physics, 58,* 1564.

Fletcher, D. A., & Mullins, R. D. (2010). Cell mechanics and the cytoskeleton. *Nature, 463,* 485–492.

Forsstrom, J., Andreasson, B., & Wagberg, L. (2005). Influence of fiber/fiber joint strength and fibre flexibility on the strength of papers from unbleached kraft fibres. *Nordic Pulp & Paper Research Journal, 20,* 186–191.

Gibson, L. J., & Ashby, M. F. (1999). *Cellular materials*. Cambridge University Press.

Glass, N. L., Rasmussen, C., Roca, M. G., & Read, N. D. (2004). Hyphal homing, fusion and mycelial interconnectedness. *Trends in Microbiology, 12,* 135–141.

Goudsmit, S. (1945). Random distribution of lines on a plane. *Reviews of Modern Physics, 17,* 321–327.

Guth, E., & James, H. M. (1941). Elastic and thermoelastic properties of rubber like materials. *Industrial and Engineering Chemistry, 33,* 624–662.

Head, D. A. (2004). First-order rigidity transition and multiple stability regimes for random networks with internal stresses. *Journal of Physics A: Mathematical and Theoretical, 37,* 10771.

Head, D. A., Levine, A. J., & MacKintosh, F. C. (2003). Distinct regimes of elastic response and deformation modes of cross-linked cytoskeletal and semiflexible polymer networks. *Physical Review E, 68,* 61907.

Hendricks, J., Kawakatsu, T., Kawasaki, K., & Zimmermann, W. (1995). Confined semiflexible polymer chains. *Physical Review E, 51,* 2658–2661.

Heussinger, C., Schaefer, B., & Frey, E. (2007). Nonaffine rubber elasticity for stiff polymer networks. *Physical Review E, 76,* 1–12.

Heyden, S. (2000). *Network modelling for the evaluation of mechanical properties of cellulose fibre fluff*. Ph.D. thesis, Lund University, Sweden.

Heyden, S., & Gustafsson, P. J. (1998). Simulation of fracture in a cellulose fibre network. *Journal of Pulp and Paper Science, 25,* 160–165.

Huisman, E., van Dillen, T., Onck, P., & van der Giessen, E. (2007). Three-dimensional cross-linked F-actin networks: Relation between network architecture and mechanical behavior. *Physical Review Letters, 99,* 208103–208106.

Ingber, D. E., Wang, N., & Stamenovic, D. (2014). Tensegity, biophysics and the mechanics of living systems. *Reports on Progress in Physics, 77*(4), 046603.

Islam, M. R., & Picu, R. C. (2018). Effect of network architecture on the mechanical behavior of random fiber networks. *Journal of Applied Mechanics, 85,* 081011.

Islam, M. R., Tudryn, G., Bucinell, R., Schadler, L. S., & Picu, R. C. (2017). Morphology and mechanics of fungal mycelium. *Scientific Reports, 7,* 13070.

Islam, M. R., Tudryn, G., Bucinell, R., Schadler, L. S., & Picu, R. C. (2018). Mechanical behavior of mycelium-based particulate composites. *Journal of Materials Science, 53,* 16371–16382.

Jearanaisilawong, P. (2004). *Investigation of deformation and failure mechanisms in woven and nonwoven fabrics under quasi-static loading conditions*. Ph.D. thesis, Massachusetts Institute of Technology.

Johnson, K. L., Kendall, K., & Roberts, A. D. (1971). Energy and the contact of elastic solids. *Proceedings of the Royal Society, A324,* 301–313.

Kabla, A., & Mahadevan, L. (2007). Nonlinear mechanics of soft fibrous networks. *Journal of the Royal Society, Interface, 4,* 99–106.

Kallmes, O. J., & Corte, H. (1960). The structure of paper—The statistical geometry of an ideal two dimensional fiber network. *Tappi Journal, 43,* 737–752.

Kasza, K. E., Broedersz, C. P., Koenderink, G. H., Lin, Y. C., Messner, W., Millman, E. A., et al. (2010). Actin filament length tunes elasticity of flexibly cross-linked actin networks. *Biophysical Journal, 99,* 1091–1100.

Koh, C. T., Strange, D. G. T., Tonsomboon, T., & Oyen, M. L. (2013). Failure mechanisms in fibrous scaffolds. *Acta Biomaterialia, 9,* 7326–7334.

Kolluru, P. V., & Chasiotis, I. (2015). Interplay of molecular and specimen length scales in the large deformation mechanical behavior of polystyrene nanofibers. *Polymer, 56,* 507–515.

Kremer, K., & Grest, G. S. (1990). Dynamics of entangled linear polymeric melts: A molecular dynamics simulation. *Journal of Chemical Physics, 92,* 5057.

Kroy, K., & Frey, E. (1996). Force-extension relation and plateau modulus for wormlike chains. *Physical Review Letters, 77,* 306–310.

Lake, S. P., & Barocas, V. H. (2011). Mechanical and structural contribution of non-fibrillar matrix in uniaxial tension: A collagen-agarose co-gel model. *Annals of Biomedical Engineering, 39,* 1891–1903.

Li, Y., & Kroger, M. (2012). A theoretical evaluation of the effects of carbon nanotube entanglement and bundling on the structural and mechanical properties of buckypaper. *Carbon, 50,* 1793–1806.

Licup, A. J., Münster, S., Sharma, A., Sheinman, M., Jawerth, L. M., Fabry, B., et al. (2015). Stress controls the mechanics of collagen networks. *Proceedings of the National Academy of Sciences, 112,* 9573–9578.

Magnusson, M. S. (2016). Investigation of interfibre joint failure and how to tailor their properties for paper strength. *Nordic Pulp & Paper Research Journal, 31,* 109–122.

Magnusson, M. S., Zhang, X., & Östlund, S. (2013). Experimental evaluation of the interfibre joint strength of papermaking fibres in terms of manufacturing parameters and in two different loading directions. *Experimental Mechanics, 53,* 1621–1634.

Malakhovsky, I., & Michels, M. A. J. (2007). Effect of disorder strength on the fracture pattern in heterogeneous networks. *Physical Review B, 76,* 1–13.

Marais, A., Magnusson, M. S., Joffre, T., Wernersson, E. L. G., & Wågberg, L. (2014). New insights into the mechanisms behind the strengthening of lignocellulosic fibrous networks with polyamines. *Cellulose, 21,* 3941–3950.

Marko, J. F., & Siggia, E. D. (1995). Stretching DNA. *Macromolecules, 28,* 8759–8770.

Mauri, A., Ehret, A. E., Perrini, M., Maake, C., Ochsenbein-Kolble, N., Ehrbar, M., et al. (2015). Deformation mechanism of human amnion: Quantitative studies based on second harmonic generation microscopy. *Journal of Biomechanics, 48,* 1606–1613.

Maxwell, J. C. (1864). *Philosophical Magazine, 27,* 27.

Mezeix, L., Bouvet, C., Huez, J., & Poquillon, D. (2009). Mechanical behavior of entangled fibers and entangled cross-linked fibers during compression. *Journal of Materials Science, 44,* 3652–3661.

Miles, R. E. (1964). Random polygons determined by random lines on a plane. *Proceedings of the National Academy of Sciences of the United States of America, 52,* 901–907.
Mofrad, M. R. K. (2009). Rheology of the cytoskeleton. *Annual Review of Fluid Mechanics, 41,* 433–453.
Morse, D. (1998). Viscoelasticity of tightly entangled solutions of semiflexible polymers. *Physical Review E, 58,* 1237R.
Moukarzel, C., & Duxbury, P. M. (1995). Stressed backbone and elasticity of random central force systems. *Physical Review Letters, 75,* 4055–4059.
Mullins, L. (1969). Softening of rubber by deformation. *Rubber Chemistry and Technology, 42,* 339–362.
Negi, V., & Picu, R. C. (2019a). Mechanical behavior of cross-linked random fiber networks with inter-fiber adhesion. *Journal of the Mechanics and Physics of Solids, 122,* 418–434.
Negi, V., & Picu, R. C. (2019b). Mechanical behavior of random fibrous mats with friction and adhesion. *Soft Matter* (submitted).
Neumann, R. M. (1977). The entropy of a single Gaussian macromolecule in a noninteracting solvent. *Journal of Chemical Physics, 66,* 870–871.
Obukhov, S. P. (1995). First order rigidity transitions in random rod networks. *Physical Review Letters, 74,* 4472–4476.
Odijk, T. (1995). Stiff chains and filaments under tension. *Macromolecules, 28,* 7016–7018.
Omelyanenko, N. P., Slutsky, L. I., & Mironov, S. P. (2017). *Connective tissue: Histophysiology, biochemistry and molecular biology*. CRC Press.
Ovaska, M., Bertalan, Z., Miksic, A., Sugni, M., di Benedetto, C., Ferrario, C., et al. (2017). Deformation and fracture of echinoderm collagen networks. *Journal of the Mechanical Behavior of Biomedical Materials, 65,* 42–52.
Oyen, M. L., Cook, R. F., & Calvin, S. E. (2004). Mechanical failure of human fetal membrane tissues. *Journal of Materials Science, 15,* 651–658.
Picu, R. C. (2011). Mechanics of random fiber networks—A review. *Soft Matter, 7,* 6768–6785.
Picu, R. C., Deogekar, S., & Islam, M. R. (2018). Poisson contraction and fiber kinematics in tissue: Insight from collagen network simulations. *Journal of Biomechanical Engineering, 140,* 021002.
Picu, R. C., & Sengab, A. (2018). Structural evolution and stability of non-cross-linked fiber networks with inter-fiber adhesion. *Soft Matter, 14,* 2254.
Picu, R. C., & Subramanian, G. (2011). Correlated heterogeneous deformation of entangled fiber networks. *Physical Review E, 83,* 052160.
Puxkandl, R., Zizakt, I., Paris, O., Keckes, J., Tesch, W., Bernstorff, S., et al. (2002). Viscoelastic properties of collagen: Synchrotron radiation investigations and structural model. *Philosophical Transactions of the Royal Society of London, 357,* 191–197.
Quigley, A. S., Bancelin, S., Deska-Gauthier, D., Legare, F., Veres, S. P., & Kreplak, L. (2018). Combining tensile testing and structural analysis at the single collagen fibril level. *Scientific Data, 5,* 180229.
Raina, A., & Linder, C. (2014). A homogenization approach for nonwoven materials based on fiber undulations and reorientation. *Journal of the Mechanics and Physics of Solids, 65,* 12–34.
Richards, P. I. (1964). Averages of polygons formed by random lines. *Proceedings of the National Academy of Sciences of the United States of America, 52,* 1160–1164.
Ridruejo, A., González, C., & Llorca, J. (2012). Failure locus of polypropylene nonwoven fabrics under in-plane biaxial deformation. *Comptes Rendus Mecanique, 340*(4–5), 307–319.
Ridruejo, A., Jubera, R., González, C., & Llorca, J. (2015). Inverse notch sensitivity: Cracks can make nonwoven fabrics stronger. *Journal of the Mechanics and Physics of Solids, 77,* 61–69.
Rigdahl, M., & Hollmark, H. (1986). Network mechanics. In J. A. Bristow & P. Koleth (Eds.), *Paper structure and properties* (pp. 241–266, Ch. 12, p. 241). New York: Marcel Dekker.
Rodney, D., Fivel, M., & Dendievel, R. (2005). Discrete modeling of the mechanics of entangled materials. *Physical Review Letters, 95,* 108004.
Roman, B., & Bico, J. (2010). Elasto-capilarity: Deforming an elastic structure with a droplet. *Journal of Physics, 22,* 493101.

Rubinstein, M., & Colby, R. H. (2003). *Polymer physics*. Oxford: Oxford University Press.
Scheibel, T. (2008). *Fibrous proteins*. CRC Press.
Schmied, F. J., Teichert, C., Kappel, L., Hirn, U., Bauer, W., & Schennach, R. (2013). What holds paper together: Nanometre scale exploration of bonding between paper fibres. *Scientific Reports, 3,* 1–6.
Sengab, A., & Picu, R. C. (2018). Filamentary structures self-organized due to adhesion. *Physical Review E, 97,* 032506.
Shahsavari, A., & Picu, R. C. (2012). Model selection for athermal cross-linked fiber networks. *Physical Review E, 86,* 011923.
Shahsavari, A., & Picu, R. C. (2013a). Elasticity of sparsely cross-linked random fiber networks. *Philosophical Magazine Letters, 93,* 356–361.
Shahsavari, A., & Picu, R. C. (2013b). Size effect on mechanical behavior of random fiber networks. *International Journal of Solids and Structures, 50,* 3332–3338.
Sharma, A., Licup, A. J., Rens, R., Vahabi, M., Jansen, A., Koenderink, G. H., et al. (2016). Strain-driven criticality underlies nonlinear mechanics of fibrous networks. *Physical Review E, 94,* 042407.
Storm, C., Pastore, J. J., MacKintosh, F. C., Lubensky, T. C., & Janmey, P. A. (2005). Non-linear elasticity in biological gels. *Nature, 435,* 191–194.
Stoyan, D., Kendall, W. S., & Mecke, J. (1987). *Stochastic geometry and its applications. Probability and mathematical statistics*. : Wiley.
Ting, T. C. T., & Chen, T. (2005). Poisson ratio for anisotropic elastic materials can have no bounds. *Quarterly Journal of Mechanics and Applied Mathematics, 58,* 73–82.
Torgnysdotter, A., & Wågberg, L. (2003). Study of the joint strength between regenerated cellulose fibres and its influence on the sheet strength. *Nordic Pulp & Paper Research Journal, 18,* 455–459.
Treloar, L. R. G. (1954). The photoelastic properties of short chain molecular networks. *Transactions of the Faraday Society, 50,* 881–896.
Treloar, L. R. G. (1975). *Physics of rubber elasticity*. Oxford: Oxford University Press.
Treloar, L. R. G., & Riding, G. (1979). A non-Gaussian theory of rubber in biaxial strain: Mechanical properties. *Proceedings of the Royal Society of London, A369,* 261–280.
Vader, D., Kabla, A., Weitz, D., & Mahadevan, L. (2009). Strain-induced alignment in collagen gels. *PLoS ONE, 4,* 5902.
van Dillen, T., Onck, P. R., & van der Giessen, E. (2008). Models for stiffening in cross-linked biopolymer networks: A comparative study. *Journal of the Mechanics and Physics of Solids, 56,* 2240–2264.
Vernerey, F. J. (2018). Transient response of non-linear polymer networks: A kinetic theory. *Journal of the Mechanics and Physics of Solids, 115,* 230–247.
Volkov, A. N., & Zhigilei, L. V. (2010). Structural stability of carbon nanotube films: The role of bending buckling. *ACS Nano, 4,* 6187–6195.
Weisel, J. W., & Litvinov, R. I. (2013). Mechanisms of fibrin polymerization and clinical implications. *Blood, 121,* 1712–1719.
Welling, L. W., Zupka, M. T., & Welling, D. J. (1995). Mechanical properties of basement membrane. *Physiology, 10,* 30–35.
Wen, Q., Basu, A., Janmey, P., & Yodh, A. (2012). Non-affine deformations in polymer hydrogels. *Soft Matter, 8,* 8039–8049.
Wendorff, J. H., Agarwal, S., & Greiner, A. (2012). *Electrospinning: Materials, processing and applications*. Weinheim: Wiley.
Wilhelm, J., & Frey, E. (1996). Radial distribution function of semiflexible polymers. *Physical Review Letters, 77,* 2581–2585.
Zagar, G., Onck, P., & van der Giessen, E. (2015). Two fundamental mechanisms govern the stiffening of crosslinked networks. *Biophysical Journal, 108,* 1470–1479.

Chapter 2
Prediction of the Effective Mechanical Properties of Regular and Random Fibrous Materials Based on the Mechanics of Generalized Continua

Jean-François Ganghoffer, Ibrahim Goda, Khaled ElNady and Yosra Rahali

Abstract The micromechanics of regular fibrous materials is first investigated to evaluate the large strains effective elastic response of repetitive fibrous microstructures at the level of a repetitive unit cell. This is representative for instance of 3D interlocks subjected to complex macroscopic loadings leading to internal stresses; unit cell based analyses are convenient to derive an effective constitutive law at the intermediate scale which can be used to perform macroscopic scale computations at a reasonable computational cost. A dedicated discrete homogenization approach has been developed to derive the effective mechanical response of the unit cell successively in a small and large transformations framework. The proposed micromechanical approach is particularly appealing, due to the difficulty to measure the effective properties for textiles considering their discreteness. The computed full set of effective ansotropic properties of fibrous media structures in the small strains regime reflect the influence of the geometrical and mechanical micro-parameters of the fibrous architecture on the overall response of the chosen equivalent continuum. Internal scale and microstructural effects are captured by a micropolar effective continuum model, capturing the pronounced rotations of fibers responsible for the large shape capacity of fibrous materials. The setting up of such computational homogenization methods allows to identify hyperelastic models for fibrous media. The same methodology for the identification of the overall properties has been extended to the more complex random fibrous media. The deformation of random fibrous networks is extremely non-affine (the motion of the fibers do in general not follow the imposed strain over the boundary of the WOA), especially for such structures that

J.-F. Ganghoffer (✉) · K. ElNady
LEM3 - CNRS, Université de Lorraine, 2, avenue de la Forêt de Haye, 54500 Vandœuvre-lès-Nancy, France
e-mail: jean-francois.Ganghoffer@univ-lorraine.fr

I. Goda
LPMT, Université de Haute-Alsace, Mulhouse, France

Y. Rahali
IPEIB, Université de Carthage, BP 64, 7021 Zarzouna, Bizerte, Tunisia

C. Picu and J.-F. Ganghoffer (eds.), *Mechanics of Fibrous Materials and Applications*, CISM International Centre for Mechanical Sciences 596,
https://doi.org/10.1007/978-3-030-23846-9_2

store energy predominantly in the bending deformation mode of fibers. The degree of non-affinity increases rapidly with decreasing bending stiffness of the filaments, the importance of which being quantified by the internal bending length, the ratio of the fiber bending modulus to its axial stiffness. We especially analyze the mechanical response of such RFN in both affine and non affine deformation regimes, depending on the network density and window size. The ability of such generalized continua to reach a response that become independent of the size of the window of analysis is one objective of the performed analyses.

Introduction

The micromechanics of fibrous materials is investigated to evaluate the large strains effective elastic response of repetitive fibrous microstructures at the level of a repetitive unit cell. A systematic methodology is established, allowing the prediction of the full set of effective properties of these structures in the small strains regime, reflecting the influence of the geometrical and mechanical micro-parameters of the fibrous architecture on the overall response of the chosen equivalent continuum. Internal scale effects of the initially discrete structure are captured by a micropolar effective continuum model.

The outline of this contribution is as follows: section "Effective Mechanical Properties of Periodic Fibrous Materials in the Small Strains Regime" is devoted to the modeling of periodic fibrous materials as effective micropolar continua, whereby the effective classical and micropolar properties are evaluated in the small strains range. The extension to the computation of the effective large strains response is done in section "Large Configuration Changes of Lattices Based on Discrete Homogenization Method", with applications to textiles monolayers and 3D interlock done in section "Computed Response of Monolayers and 3D Interlocks". In section "Identification of Hyperelastic Models for Textile Monolayers", virtual simulations based on the developed discrete homogenization technique are used for the calibration of a strain energy density of a hyperelastic model for textiles. The construction of generalized continuum models for random fibrous media is performed in section "Generalized Continuum Models of Random Fibrous Networks", focusing on couple stress models. We conclude by a summary of the work and perspectives of developments in section "Summary and Future Work".

A few words regarding notations are in order. Vectors and higher order tensors are denoted with boldface symbols. The summation convention on repeated indices is presently adopted, otherwise explicitly stated. The second-order identity tensor is denoted as $\mathbf{I}$.

Effective Mechanical Properties of Periodic Fibrous Materials in the Small Strains Regime

The discrete homogenization technique can be described as a mathematical approach used to derive the equivalent continuous medium behavior of periodic discrete media. It is inspired from the homogenization of periodic media developed, since more than 30 years by Sanchez-Palencia (1980) and more recently applied by Warren and Byskov (2002), Mourad et al. (2003). This technique has been also combined with the energy method by Sab and Pradel (2009) and applied to discrete homogenization. The importance of the discrete homogenization technique is that it delivers the full compliance (or rigidity) matrix, reflecting the sometimes complex anisotropy of the so-built equivalent continuum; it is worth noting that the material symmetry group of the discrete media is encompassed in the material symmetry group of the homogenized medium (Trovalusci and Masiani 1999). Such complex constitutive laws may then nurture macroscopic simulations (Feyel and Chaboche 2000).

In the present approach, we rely on the so-called discrete homogenization method (DH in shortcut) suitable for lattice materials comprising a periodic array of beams; instead of making full structural computations over the entire lattice—which would be computationally too expensive—we derive a nonlinear constitutive model at the mesoscopic scale based on a continuum description, avoiding the explicit description of the individual struts of the initial lattice (ElNady et al. 2016).

Initially, the DH approach is exposed in the linear small strains regime in order to compute the initial effective moduli of the effective substitution continuum. Then, it is extended to the nonlinear regime in order to account for the variation of the lattice geometry under a kinematic loading prescribed over an identified representative unit cell (RUC in short). The nonlinear response of the lattice is homogenized at the level of RUC, thereby providing the stress–strain relation, based on an incremental scheme accounting in essence for geometrical nonlinearities.

As a first step, the nonlinear computations include the calculation of the elastic properties in the small strains regime, followed by a succession of updating steps at the microstructure level of the unit cell geometry. This entails an update of the homogenized mechanical variables (strain and stress) at the mesoscopic level of the effective continuum.

Small Strains Homogenization: Determination of the Initial Elastic Response

We consider a repetitive beam like network material in which a unit cell can be identified. A small parameter can be defined as the ratio of unit cell size to a macroscopic characteristic length of the entire network.

The asymptotic expansion of the nodal displacement $\mathbf{u}^{\varepsilon}$ is written up to the second order as

$$\mathbf{u}^{\varepsilon}(\beta^{\varepsilon}) = \mathbf{u}_0(\beta^{\varepsilon}) + \varepsilon\,\mathbf{u}_1(\beta^{\varepsilon}) + \varepsilon^2\mathbf{u}_2(\beta^{\varepsilon}) \tag{2.1}$$

where ε is the ratio of unit cell size to a characteristic size of the entire structure.

The displacement difference $\Delta\mathbf{U}^{\mathrm{b}\varepsilon}$ between the extremity and origin node of each beam is expressed by a Taylor series development, according to

$$\begin{aligned}
&\Delta\mathbf{U}^{\mathrm{b}\varepsilon} = \mathbf{u}^{\varepsilon}(E(b)) - \mathbf{u}^{\varepsilon}(O(b)) \\
&= \varepsilon \underbrace{\left(\mathbf{u}_1^{E_{R(b)}}(\beta^{\varepsilon}) - \mathbf{u}_1^{O_{R(b)}}(\beta^{\varepsilon}) + \frac{\partial \mathbf{u}_0(\beta^{\varepsilon})}{\partial\beta^i}\delta^{ib}\right)}_{\Delta\mathrm{U}_1^{\mathrm{b}}} + \varepsilon^2 \underbrace{\left(\mathbf{u}_2^{E_{R(b)}}(\beta^{\varepsilon}) - \mathbf{u}_2^{O_{R(b)}}(\beta^{\varepsilon})\right)}_{\Delta\mathrm{U}_2^{\mathrm{b}}} \\
&= \qquad \varepsilon\,\Delta\mathbf{U}_1^{\mathrm{b}} \qquad\qquad + \qquad \varepsilon^2\,\Delta\mathbf{U}_2^{\mathrm{b}}
\end{aligned} \tag{2.2}$$

with δ^{ib} the shift factor (equal to ± 1) for nodes belonging to a neighboring cell, and nil for nodes located inside the considered cell.

The asymptotic expansion of nodal microrotation $\boldsymbol{\varphi}^{n\varepsilon}$ is limited to the first order in ε. It is defined successively at the origin and extremity of each beam as

$$\boldsymbol{\varphi}^{O(b)\varepsilon} = \boldsymbol{\varphi}_0^{O_{R(b)}} + \varepsilon\boldsymbol{\varphi}_1^{O_{R(b)}};\ \boldsymbol{\varphi}^{E(b)\varepsilon} = \boldsymbol{\varphi}_0^{E_{R(b)}} + \varepsilon\left(\frac{\partial\boldsymbol{\varphi}_0}{\partial\beta^i}\delta^{ib} + \boldsymbol{\varphi}_1^{E_{R(b)}}\right) \tag{2.3}$$

wherein we have parameterized any point within the surface element representative of the lattice by curvilinear coordinates β^i (viewed as continuous lines within the body). This allows treating lattice structures with curved material lines following the fibers in their reference state.

In the framework of 3D Timoshenko beams, the normal and transverse forces as well as the moments exerted on the beam extremities are obtained after lengthy calculations and expressed as follows:

$$F_x^{\varepsilon b} = \frac{E_s^b A^{\varepsilon b}}{l^{\varepsilon b}}\left(\mathbf{e}_x \cdot \left(\varepsilon\,\Delta\mathbf{U}_1^{\mathrm{b}} + \varepsilon^2\,\Delta\mathbf{U}_2^{\mathrm{b}}\right)\right) \tag{2.4}$$

$$F_y^{\varepsilon b} = \frac{12E_s^b I_z^{\varepsilon b}}{\left(l^{\varepsilon b}\right)^3\left(1+\Phi_y^{\varepsilon}\right)}\left(\begin{array}{l}\mathbf{e}_y \cdot \left(\varepsilon\,\Delta\mathbf{U}_1^{\mathrm{b}} + \varepsilon^2\,\Delta\mathbf{U}_2^{\mathrm{b}}\right) - \\ \frac{l^{\varepsilon b}}{2}\left(\mathbf{e}_z \cdot \left(\boldsymbol{\varphi}_0^{O_{R(b)}} + \boldsymbol{\varphi}_0^{E_{R(b)}} + \varepsilon\left(\boldsymbol{\varphi}_1^{O_{R(b)}} + \boldsymbol{\varphi}_1^{E_{R(b)}} + \frac{\partial\boldsymbol{\varphi}_0}{\partial\beta^i}\delta^{ib}\right)\right)\right)\end{array}\right) \tag{2.5}$$

$$F_z^{\varepsilon b} = \frac{12E_s^b I_y^{\varepsilon b}}{\left(l^{\varepsilon b}\right)^3\left(1+\Phi_z^{\varepsilon}\right)}\left(\begin{array}{l}\mathbf{e}_z \cdot \left(\varepsilon\,\Delta\mathbf{U}_1^{\mathrm{b}} + \varepsilon^2\,\Delta\mathbf{U}_2^{\mathrm{b}}\right) + \\ \frac{l^{\varepsilon b}}{2}\left(\mathbf{e}_y \cdot \left(\boldsymbol{\varphi}_0^{O_{R(b)}} + \boldsymbol{\varphi}_0^{E_{R(b)}} + \varepsilon\left(\boldsymbol{\varphi}_1^{O_{R(b)}} + \boldsymbol{\varphi}_1^{E_{R(b)}} + \frac{\partial\boldsymbol{\varphi}_0}{\partial\beta^i}\delta^{ib}\right)\right)\right)\end{array}\right) \tag{2.6}$$

$$\begin{aligned}
M_x^{O(b)\varepsilon} &= \frac{G_s^b J^{\varepsilon b}}{l^{\varepsilon b}}\varepsilon\left(\mathbf{e}_x \cdot \left(\boldsymbol{\varphi}_1^{O_{R(b)}} - \left(\frac{\partial\boldsymbol{\varphi}_0}{\partial\beta^i}\delta^{ib} + \boldsymbol{\varphi}_1^{E_{R(b)}}\right)\right)\right) \\
M_x^{E(b)\varepsilon} &= \frac{G_s^b J^{\varepsilon b}}{l^{\varepsilon b}}\varepsilon\left(\mathbf{e}_x \cdot \left(\boldsymbol{\varphi}_1^{E_{R(b)}} - \boldsymbol{\varphi}_1^{O_{R(b)}} + \frac{\partial\boldsymbol{\varphi}_0}{\partial\beta^i}\delta^{ib}\right)\right)
\end{aligned} \tag{2.7}$$

$$
\begin{aligned}
M_y^{O(b)\varepsilon} &= \frac{6E_s^b I_y^{\varepsilon b}}{\left(l^{\varepsilon b}\right)^2(1+\Phi_z^\varepsilon)}\left(\mathbf{e}_z\cdot\left(\varepsilon\,\Delta\mathbf{U}_1^{\mathrm{b}}+\varepsilon^2\,\Delta\mathbf{U}_2^{\mathrm{b}}\right)\right)\\
&\quad+\frac{E_s^b I_y^{\varepsilon b}}{l^{\varepsilon b}(1+\Phi_z^\varepsilon)}\left(\mathbf{e}_y\cdot\left(4\boldsymbol{\varphi}_0^{O_{R(b)}}+2\boldsymbol{\varphi}_0^{E_{R(b)}}+\varepsilon\left(4\boldsymbol{\varphi}_1^{O_{R(b)}}+2\boldsymbol{\varphi}_1^{E_{R(b)}}+2\frac{\partial\boldsymbol{\varphi}_0}{\partial\beta^i}\delta^{ib}\right)\right)\right)\\
M_y^{E(b)\varepsilon} &= \frac{6E_s^b I_y^{\varepsilon b}}{\left(l^{\varepsilon b}\right)^2}\left(\mathbf{e}_z\cdot\left(\varepsilon\,\Delta\mathbf{U}_1^{\mathrm{b}}+\varepsilon^2\,\Delta\mathbf{U}_2^{\mathrm{b}}\right)\right)\\
&\quad+\frac{E_s^b I_y^{\varepsilon b}}{l^{\varepsilon b}}\left(\mathbf{e}_y\cdot\left(2\boldsymbol{\varphi}_0^{O_{R(b)}}+4\boldsymbol{\varphi}_0^{E_{R(b)}}+\varepsilon\left(2\boldsymbol{\varphi}_1^{O_{R(b)}}+4\boldsymbol{\varphi}_1^{E_{R(b)}}+4\frac{\partial\boldsymbol{\varphi}_0}{\partial\beta^i}\delta^{ib}\right)\right)\right) \qquad (2.8)\\
M_z^{O(b)\varepsilon} &= \frac{6E_s^b I_z^{\varepsilon b}}{\left(l^{\varepsilon b}\right)^2(1+\Phi_y^\varepsilon)}\left(-\mathbf{e}_y\cdot\left(\varepsilon\,\Delta\mathbf{U}_1^{\mathrm{b}}+\varepsilon^2\,\Delta\mathbf{U}_2^{\mathrm{b}}\right)\right)\\
&\quad+\frac{E_s^b I_z^{\varepsilon b}}{l^{\varepsilon b}(1+\Phi_y^\varepsilon)}\left(\mathbf{e}_z\cdot\left(4\boldsymbol{\varphi}_0^{O_{R(b)}}+2\boldsymbol{\varphi}_0^{E_{R(b)}}+\varepsilon\left(4\boldsymbol{\varphi}_1^{O_{R(b)}}+2\boldsymbol{\varphi}_1^{E_{R(b)}}+2\frac{\partial\boldsymbol{\varphi}_0}{\partial\beta^i}\delta^{ib}\right)\right)\right)\\
M_z^{E(b)\varepsilon} &= \frac{6E_s^b I_z^{\varepsilon b}}{\left(l^{\varepsilon b}\right)^2(1+\Phi_y^\varepsilon)}\left(-\mathbf{e}_y\cdot\left(\varepsilon\,\Delta\mathbf{U}_1^{\mathrm{b}}+\varepsilon^2\,\Delta\mathbf{U}_2^{\mathrm{b}}\right)\right)\\
&\quad+\frac{E_s^b I_z^{\varepsilon b}}{l^{\varepsilon b}(1+\Phi_y^\varepsilon)}\left(\mathbf{e}_z\cdot\left(2\boldsymbol{\varphi}_0^{O_{R(b)}}+4\boldsymbol{\varphi}_0^{E_{R(b)}}+\varepsilon\left(2\boldsymbol{\varphi}_1^{O_{R(b)}}+4\boldsymbol{\varphi}_1^{E_{R(b)}}+4\frac{\partial\boldsymbol{\varphi}_0}{\partial\beta^i}\delta^{ib}\right)\right)\right) \qquad (2.9)
\end{aligned}
$$

wherein E_s^b and G_s^b are the tensile and shear modulus of bulk material, and with $\Phi_y^\varepsilon=\frac{12E_s^bI_z^{\varepsilon b}}{G_s^bA^{\varepsilon b}k_s\left(L^{\varepsilon b}\right)^2}$, $\Phi_z^\varepsilon=\frac{12E_s^bI_y^{\varepsilon b}}{G_s^bA^{\varepsilon b}k_s\left(L^{\varepsilon b}\right)^2}$, k_s successively the shear correction factors and the shear coefficient. In the forthcoming development, a circular section of the beams is considered; hence, the following geometrical parameters are computed: the cross-sectional area $A^{\varepsilon b}=\pi(\varepsilon r)^2$, the quadratic moment of the beam $I_y^{\varepsilon b}=I_z^{\varepsilon b}=\pi\frac{(\varepsilon r)^4}{4}$, and the torsional constant $J^{\varepsilon b}=\pi\frac{(\varepsilon r)^4}{2}$.

The asymptotic development of the virtual velocity and rotation rate are next expressed. For any virtual velocity field $\mathbf{v}^\varepsilon(\beta)$, a Taylor series expansion truncated at first order leads to

$$
\mathbf{v}^\varepsilon(\mathrm{O(b)})-\mathbf{v}^\varepsilon(\mathrm{E(b)})\approx\varepsilon\frac{\partial\mathbf{v}(\beta^\varepsilon)}{\partial\beta^{\mathrm{i}}}\delta^{\mathrm{ib}} \qquad (2.10)
$$

The rotation rate field is similarly expanded taking into account the central node of the beam, so that a change of curvature of any beam can be captured:

$$
\mathbf{w}^{\mathrm{O(b)}\varepsilon}(\beta)=\mathbf{w}(\beta);\quad \mathbf{w}^{\mathrm{E(b)}\varepsilon}\left(\beta+\varepsilon\delta^{\mathrm{i}}\right)=\mathbf{w}(\beta)+\varepsilon\frac{\partial\mathbf{w}(\beta)}{\partial\beta^{\mathrm{i}}}\delta^{\mathrm{i}} \qquad (2.11)
$$

Note that the present beam model and subsequent derivations of the effective mechanical response are not specific to textile materials but can be applied to any lattice materials showing interactions between tension, bending, and torsion.

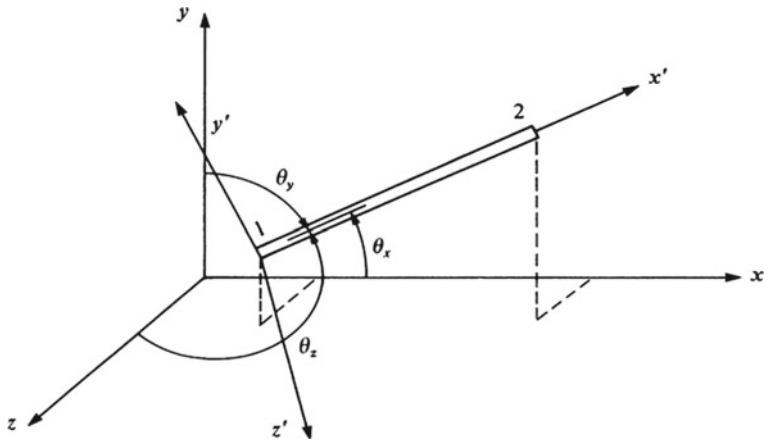

Fig. 2.1 Direction cosines associated with the x-axis (Goda et al. 2013b)

We introduce the unit vectors $\mathbf{e}_x = \left[\, Cxx' \;\; Cyx' \;\; Czx' \,\right]^T$, $\mathbf{e}_y = \left[\, Cxy' \;\; Cyy' \;\; Czy' \,\right]^T$, and $\mathbf{e}_z = \left[\, Cxz' \;\; Cyz' \;\; Czz' \,\right]^T$, in which $Cxx' = \cos\ \theta_x$, $Cyx' = \cos\ \theta_y$, and $Czx' = \cos\ \theta_z$ are the direction cosines of x', describing the transformation between the local and global coordinate systems in 3D (Fig. 2.1). Similarly, the components of $\mathbf{e}_y$ and $\mathbf{e}_z$ are the direction cosines of y' and z', respectively.

The equilibrium of forces in the absence of external forces for the whole lattice is written in virtual power form and after asymptotic development as follows:

$$\sum_{\upsilon^i \in \mathbb{Z}^2} \sum_{\mathrm{b} \in \mathbf{B}_\mathrm{R}} \mathbf{F}^{\varepsilon \mathrm{b}} \cdot \left(\mathbf{v}^{\varepsilon}(\mathrm{O(b)}) - \mathbf{v}^{\varepsilon}(\mathrm{E(b)}) \right) = 0 \tag{2.12}$$

where $\mathbf{v}(\cdot)$ is the virtual velocity field vanishing on the unit cell edges. The vector of effort $\mathbf{F}^{\varepsilon \mathrm{b}}$ splits into a normal and transverse forces as

$$\mathbf{F}^{\varepsilon \mathrm{b}} = \mathrm{F}_\mathrm{x}^{\varepsilon \mathrm{b}} \mathbf{e}_\mathrm{x} + \mathrm{F}_\mathrm{y}^{\varepsilon \mathrm{b}} \mathbf{e}_\mathrm{y} + \mathrm{F}_\mathrm{z}^{\varepsilon \mathrm{b}} \mathbf{e}_\mathrm{z} \tag{2.13}$$

We denote by $\mathbf{B}_R$, the set of beams within the reference unit cell.

We then write the discrete equilibrium of moments. It can be expressed in two different ways: first one considers the equilibrium of moments for the unit cell nodes. This is actually essential to solve for the kinematic unknowns; it is written in asymptotic form as

$$\sum_{\upsilon^i \in \mathbb{Z}^3} \sum_{b \in \mathbf{B}_R} \left(\mathbf{M}^{O(b)\varepsilon} \cdot \mathbf{w}^{\varepsilon}(O(b)) + \mathbf{M}^{E(b)\varepsilon} \cdot \mathbf{w}^{\varepsilon}(E(b)) \right) = 0 \tag{2.14}$$

Another writing involving the local equilibrium of each individual beam is considered for the purpose of homogenization. The equilibrium is written at the center of each beam in asymptotic form as

$$\sum_{\upsilon^i \in \mathbb{Z}^3} \sum_{b \in \mathbf{B}_R} \left(\mathbf{M}^{O(b)\varepsilon} \cdot \mathbf{w}^{\varepsilon}(O(b)) + \mathbf{M}^{E(b)\varepsilon} \cdot \mathbf{w}^{\varepsilon}(E(b)) + \varepsilon l^b \left(\mathbf{e}_x \wedge \mathbf{F}^{\varepsilon b} \right) \cdot \mathbf{w}^{\varepsilon}(C(b)) \right) = 0 \tag{2.15}$$

with $\mathbf{w}(\cdot)$ the rotation rate field. More details related to the homogenization in the micropolar framework can be found in Goda et al. (2014). The homogenization of the equilibrium of forces leads to the following continuous self-equilibrium equation in virtual power form

$$\int_{\Omega} \mathbf{S}^i \cdot \frac{\partial \mathrm{v}(\beta)}{\partial \beta^{\mathrm{i}}} d\beta = 0 \tag{2.16}$$

with the stress vector $\mathbf{S}^i$ therein decomposing into first- and second-order contributions, viz., $\mathbf{S}^i = \mathbf{S}_1^i + \varepsilon \mathbf{S}_2^i$, with

$$\mathbf{S}_1^i = \sum_{b \in \mathbf{B}_R} \left(\begin{array}{r} \frac{\pi E_s^b (r^b)^2}{l^b} (\mathbf{e}_x \cdot \Delta \mathbf{U}_1^{\mathrm{b}}) \mathbf{e}_x + \left(\frac{3\pi E_s^b (r^b)^4}{(l^b)^3} \left(\mathbf{e}_y \cdot \Delta \mathbf{U}_1^{\mathrm{b}} - \frac{l^b}{2} \left(\mathbf{e}_z \cdot \left(\boldsymbol{\varphi}_0^{O_{R(b)}} + \boldsymbol{\varphi}_0^{E_{R(b)}} \right) \right) \right) \right) \mathbf{e}_y \\ + \left(\frac{3\pi E_s^b (r^b)^4}{(l^b)^3} \left(\mathbf{e}_z \cdot \Delta \mathbf{U}_1^{\mathrm{b}} + \frac{l^b}{2} \left(\mathbf{e}_y \cdot \left(\boldsymbol{\varphi}_0^{O_{R(b)}} + \boldsymbol{\varphi}_0^{E_{R(b)}} \right) \right) \right) \right) \mathbf{e}_z \end{array} \right) \delta^{ib}$$

$$\mathbf{S}_2^i = \sum_{b \in \mathbf{B}_R} \left(\begin{array}{r} \frac{\pi E_s^b (r^b)^2}{l^b} (\mathbf{e}_x \cdot \Delta \mathbf{U}_2^{\mathrm{b}}) \mathbf{e}_x + \left(\frac{3\pi E_s^b (r^b)^4}{(L^b)^3} \left(\mathbf{e}_y \cdot \Delta \mathbf{U}_2^{\mathrm{b}} - \frac{l^b}{2} \left(\mathbf{e}_z \left(\boldsymbol{\varphi}_1^{O_{R(b)}} + \boldsymbol{\varphi}_1^{E_{R(b)}} + \frac{\partial \boldsymbol{\varphi}_0}{\partial \beta^i} \delta^{ib} \right) \right) \right) \right) \mathbf{e}_y \\ + \left(\frac{3\pi E_s^b (r^b)^4}{(l^b)^3} \left(\mathbf{e}_z \cdot \Delta \mathbf{U}_2^{\mathrm{b}} + \frac{l^b}{2} \left(\mathbf{e}_y \cdot \left(\boldsymbol{\varphi}_1^{O_{R(b)}} + \boldsymbol{\varphi}_1^{E_{R(b)}} + \frac{\partial \boldsymbol{\varphi}_0}{\partial \beta^i} \delta^{ib} \right) \right) \right) \right) \mathbf{e}_z \end{array} \right) \delta^{ib}$$

Likewise to the development of the force equilibrium, the equilibrium of moment (2.14) is homogenized by inserting the asymptotic expansion, expression (2.11) of the virtual rotation rate. Passing to the limit $\varepsilon \to 0$ in the discrete sum, this in turn leads to the following continuous self-equilibrium in virtual power:

$$\int_{\Omega} \boldsymbol{\mu}^i \cdot \frac{\partial \mathbf{w}(\beta)}{\partial \beta^{\mathrm{i}}} d\beta = 0 \tag{2.17}$$

with the couple stress vector $\boldsymbol{\mu}^i$ that incorporate moments, also identified on two orders, viz., $\boldsymbol{\mu}^i = \varepsilon \boldsymbol{\mu}_1^i + \varepsilon^2 \boldsymbol{\mu}_2^i$, with

$$\begin{aligned} \boldsymbol{\mu}_1^{\mathrm{i}} &= \sum_{\mathrm{b} \in \mathbf{B}_{\mathrm{R}}} \left(\frac{1}{2} \left(\mathrm{M}_{1\mathrm{y}}^{\mathrm{E(b)}} - \mathrm{M}_{1\mathrm{y}}^{\mathrm{O(b)}} \right) \mathbf{e}_{\mathrm{y}} + \frac{1}{2} \left(\mathrm{M}_{1\mathrm{z}}^{\mathrm{E(b)}} - \mathrm{M}_{1\mathrm{z}}^{\mathrm{O(b)}} \right) \mathbf{e}_{\mathrm{z}} \right) \delta^{\mathrm{ib}}, \\ \boldsymbol{\mu}_2^{\mathrm{i}} &= \sum_{\mathrm{b} \in \mathbf{B}_{\mathrm{R}}} \left(\mathrm{M}_{2\mathrm{x}}^{\mathrm{E(b)}} \mathbf{e}_{\mathrm{x}} + \frac{1}{2} \left(\mathrm{M}_{2\mathrm{y}}^{\mathrm{E(b)}} - \mathrm{M}_{2\mathrm{y}}^{\mathrm{O(b)}} \right) \mathbf{e}_{\mathrm{y}} + \frac{1}{2} \left(\mathrm{M}_{2\mathrm{z}}^{\mathrm{E(b)}} - \mathrm{M}_{2\mathrm{z}}^{\mathrm{O(b)}} \right) \mathbf{e}_{\mathrm{z}} \right) \delta^{\mathrm{ib}} \end{aligned} \tag{2.18}$$

The general form of the continuum constitutive law can presently be identified from the expressions of the homogenized stress and couple stress tensors together with the expressions of the stress and couple stress vectors $\mathbf{S}^{\mathrm{i}}$ and $\boldsymbol{\mu}^{\mathrm{i}}$:

$$\boldsymbol{\sigma} = \frac{1}{g}\mathbf{S}^{\mathrm{i}} \otimes \frac{\partial \mathbf{R}}{\partial \beta^{\mathrm{i}}} = \frac{1}{g}\left(\mathbf{S}_1^{\mathrm{i}} + \varepsilon \mathbf{S}_2^{\mathrm{i}}\right) \otimes \frac{\partial \mathbf{R}}{\partial \beta^{\mathrm{i}}} = \underbrace{\frac{1}{g}\mathbf{S}_1^{\mathrm{i}} \otimes \frac{\partial \mathbf{R}}{\partial \beta^{\mathrm{i}}}}_{[\mathbf{K}^s]\{\boldsymbol{\varepsilon}\}} + \underbrace{\frac{1}{g}\varepsilon \mathbf{S}_2^{\mathrm{i}} \otimes \frac{\partial \mathbf{R}}{\partial \beta^{\mathrm{i}}}}_{[\mathbf{B}]\{\boldsymbol{\chi}\}}$$

$$\mathbf{m} = \frac{1}{g}\boldsymbol{\mu}^{\mathrm{i}} \otimes \frac{\partial \mathbf{R}}{\partial \beta^{\mathrm{i}}} = \frac{1}{g}\left(\varepsilon \boldsymbol{\mu}_1^{\mathrm{i}} + \varepsilon^2 \boldsymbol{\mu}_2^{\mathrm{i}}\right) \otimes \frac{\partial \mathbf{R}}{\partial \beta^{\mathrm{i}}} = \underbrace{\frac{1}{g}\varepsilon \boldsymbol{\mu}_1^{\mathrm{i}} \otimes \frac{\partial \mathbf{R}}{\partial \beta^{\mathrm{i}}}}_{[\mathbf{B}]\{\boldsymbol{\varepsilon}\}} + \underbrace{\frac{1}{g}\varepsilon^2 \boldsymbol{\mu}_2^{\mathrm{i}} \otimes \frac{\partial \mathbf{R}}{\partial \lambda^{\mathrm{i}}}}_{[\mathbf{K}^{\mu}]\{\boldsymbol{\chi}\}} \tag{2.19}$$

where $\boldsymbol{g}$ is the Jacobian of the transformation from Cartesian to curvilinear coordinates and $\mathbf{R}$ is the position vector of any material point within the lattice.

Because all periodical uniform structures are endowed with a central symmetry, the stiffness coefficients are invariant under a coordinate inversion. This in turn entails that the pseudo-tensor $\mathbf{B}_{ijkl}$ vanishes in (2.19). The previous constitutive equations then imply that both vectors $\boldsymbol{\mu}_1^{\mathrm{i}}$ and $\mathbf{S}_2^{i}$ in (2.19) vanish; this leads to an important simplification of the stress and couple stress vectors in (2.19), successively

$$\begin{aligned} \mathbf{S}^{i} = \mathbf{S}_1^{i} &= \sum_{b \in \mathbf{B}_R} \left(F_{x1}^{b}\mathbf{e}_x + F_{y1}^{b}\mathbf{e}_y + F_{z1}^{b}\mathbf{e}_z\right)\delta^{ib} \\ \boldsymbol{\mu}^{\mathrm{i}} = \boldsymbol{\mu}_2^{\mathrm{i}} &= \sum_{b \in \mathbf{B}_R} \left(M_{2x}^{E(b)}\mathbf{e}_x + \tfrac{1}{2}\left(M_{2y}^{E(b)} - M_{2y}^{O(b)}\right)\mathbf{e}_y + \tfrac{1}{2}\left(M_{2z}^{E(b)} - M_{2z}^{O(b)}\right)\mathbf{e}_z\right)\delta^{ib} \end{aligned} \tag{2.20}$$

with F_{x1}^{b}, F_{y1}^{b}, F_{z1}^{b}, M_{2x}^{n}, M_{2y}^{n}, and M_{2z}^{n}, respectively, the first-order longitudinal and transverse forces and the second-order moment about x′, y′, and z′. These expressions still in fact involve the unknown displacements $\mathbf{u}_1^{n}$, $\mathbf{u}_2^{n}$ and rotations $\boldsymbol{\varphi}_0^{n}$, $\boldsymbol{\varphi}_1^{n}$, which are determined for all nodes by solving the equilibrium Eqs. (2.12) and (2.14).

The algorithm for the computation of the effective moduli in the framework of micropolar theory is explained as follows:

1. Definition of the position vector $\mathbf{R}$ such that $\boldsymbol{x} = \mathbf{R}(\lambda^1, \lambda^2, \lambda^3)$.
2. Transformation of the displacement gradients and rotation gradients from Cartesian to curvilinear coordinates (Dos Reis and Ganghoffer 2012).
$$\left(\frac{\partial \mathrm{U}}{\partial \lambda_i}\right)_{(\mathrm{Y}_1,\mathrm{Y}_2,\mathrm{Y}_3)} \mapsto \left(\frac{\partial \mathrm{U}}{\partial \lambda_i}\right)_{(\mathrm{e}_x,\mathrm{e}_y,\mathrm{e}_z)} \left(\frac{\partial \phi}{\partial \lambda_i}\right)_{(\mathrm{Y}_1,\mathrm{Y}_2,\mathrm{Y}_3)} \mapsto \left(\frac{\partial \phi}{\partial \lambda_i}\right)_{(\mathrm{e}_x,\mathrm{e}_y,\mathrm{e}_z)}$$
3. For each beam **b** within the unit cell, we define
   (a) The origin node $O = O_R(b)$ and the extremity node $E = E_R(b)$ of a beam.
   (b) The tensile rigidity $K_l^b = \frac{E_s^b A^{\varepsilon b}}{l^{\varepsilon b}}$, flexural rigidity $K_f^b = \frac{12E_s^b I^{\varepsilon b}}{\left(l^{\varepsilon b}\right)^3}$, and torsional rigidity $K_r^b = \frac{G_s^b J^{\varepsilon b}}{l^{\varepsilon b}}$ with E_s^b, G_s^b the tensile and shear moduli of the beam material, $A^{\varepsilon b}$, $L^{\varepsilon b}$ the beam section and beam length, respectively, $I^{\varepsilon b}$ the quadratic moment and $J^{\varepsilon b}$ the torsional rigidity.
   (c) The first-order displacement difference between the beam extremity nodes $\Delta \mathrm{U}_1^b = \mathrm{u}_1^{E_b} - \mathrm{u}_1^{O_b} + \frac{\partial \mathrm{U}}{\partial \lambda_i}\delta^{ib}$, with $\delta^i \in \{-1, 0, 1\}$ the shift factor. The Taylor

series expansion of the relative displacement between the beam extremity nodes is written

$$\begin{aligned}\Delta \mathrm{U}^{\mathrm{b}\varepsilon} &= \mathrm{u}^{\varepsilon}(E(b)) - \mathrm{u}^{\varepsilon}(O(b)) \\ &= \underbrace{\varepsilon\left(\mathrm{u}_1^{E_{(b)}}(\lambda^{\varepsilon}) - \mathrm{u}_1^{O_{(b)}}(\lambda^{\varepsilon}) + \frac{\partial \mathrm{U}(\lambda^{\varepsilon})}{\partial \lambda_i}\delta^{ib}\right)}_{\Delta \mathrm{U}_1^{\mathrm{b}}} + \varepsilon^2 \underbrace{\left(\mathrm{u}_2^{E_{(b)}}(\lambda^{\varepsilon}) - \mathrm{u}_2^{O_{(b)}}(\lambda^{\varepsilon})\right)}_{\Delta \mathrm{U}_2^{\mathrm{b}}}\end{aligned}$$

The asymptotic expansion of the microrotation $\phi^{\varepsilon n} = (\varphi_x, \varphi_y, \varphi_z)$ written at the extremity nodes of any beam written as

$$\phi^{O(b)\varepsilon} = \phi_0^{O_{(b)}} + \varepsilon\phi_1^{O_{(b)}}; \phi^{E\varepsilon} = \phi_0^{E_{(b)}} + \varepsilon\left(\frac{\partial \phi_0}{\partial \lambda_i}\delta^{ib} + \phi_1^{E_{(b)}}\right)$$

Material points within the microstructure have been parameterized by curvilinear coordinates λ_{i}; they can represent, for instance, parameterization along the fibers or yarns within regular fibrous microstructures.

(d) Expressions of the efforts and moments at the beam extremities in the context of (3D) Timoshenko beam model (Goda et al. 2013a).

4. Computation of the unknown kinematic variables (displacements and rotations u_1^n, ϕ_0^n) by solving the so-called unit cell localization problem from the equilibrium of forces and moments:

$$\sum_{v^i \in \mathbb{Z}^3} \sum_{b \in \mathrm{B}_R} F^{\varepsilon b} \cdot (\mathrm{v}^{\varepsilon}(O(b)) - \mathrm{v}^{\varepsilon}(E(b))) = 0$$
$$\sum_{v^i \in \mathbb{Z}^3} \sum_{b \in \mathrm{B}_R} \left(\mathrm{M}^{O(b)\varepsilon} \cdot \mathrm{w}^{\varepsilon}(O(b)) + \mathrm{M}^{E(b)\varepsilon}\mathrm{w}^{\varepsilon}(E(b))\right) = 0$$

v^{ε} and w^{ε} are, respectively, the virtual velocity and rotation.

5. Identification of the microrotation over the unit cell, variable $\phi = \left(\phi_x, \phi_y, \phi_z\right)$.
6. Repeat items 3 and 4 for the second-order displacements and rotations u_2^n, ϕ_1^n, such that

$$\begin{aligned}\Delta \mathrm{U}_2^b &= \mathrm{u}_2^E - \mathrm{u}_2^O \\ F_{x2}^b &= \frac{E_s^b A^b}{L_b}\left(e_x \cdot \left(\Delta \mathrm{U}_2^{\mathrm{b}}\right)\right) \\ F_{y2}^b &= \frac{12E_s^b I_z^b}{L_b^3(1+\Phi_y)}\left(e_y \cdot \left(\Delta \mathrm{U}_2^{\mathrm{b}}\right) - \frac{L_b}{2}\left(e_z \cdot \left(\phi_1^O + \phi_1^E + \frac{\partial \phi_0}{\partial \lambda_i}\delta^{ib}\right)\right)\right) \\ F_{z2}^b &= \frac{12E_s^b I_y^b}{L_b^3(1+\Phi_z)}\left(e_z \cdot \left(\Delta \mathrm{U}_2^{\mathrm{b}}\right) + \frac{L_b}{2}\left(e_y \cdot \left(\phi_1^O + \phi_1^E + \frac{\partial \phi_0}{\partial \lambda_i}\delta^{ib}\right)\right)\right) \\ M_{2x}^O &= \frac{G_s^b J^b}{L_b}\left(e_x \cdot \left(\phi_1^O - \left(\frac{\partial \phi_0}{\partial \lambda_i}\delta^{ib} + \phi_1^E\right)\right)\right), M_{2x}^E = \frac{G_s^b J^b}{L_b}\left(e_x \cdot \left(\phi_1^E - \phi_1^O + \frac{\partial \phi_0}{\partial \lambda_i}\delta^{ib}\right)\right)\end{aligned}$$

$$M_{2y}^{O}=\frac{E_s^b I_y^b}{L_b^2(1+\Phi_z)}\left(\left(6\,e_z\cdot\left(\Delta \mathrm{U}_2^{\mathrm{b}}\right)\right)+L_b\left(e_y\cdot\left((4+\Phi_z)\phi_1^O+(2-\Phi_z)\phi_1^E+(2-\Phi_z)\frac{\partial\phi_0}{\partial\lambda_i}\delta^{ib}\right)\right)\right)$$

$$M_{2y}^{E}=\frac{E_s^b I_y^b}{L_b^2(1+\Phi_z)}\left(\left(6\,e_z\cdot\left(\Delta \mathrm{U}_2^{\mathrm{b}}\right)\right)+L_b\left(e_y\cdot\left((2-\Phi_z)\phi_1^O+(4+\Phi_z)\phi_1^E+(4+\Phi_z)\frac{\partial\phi_0}{\partial\lambda_i}\delta^{ib}\right)\right)\right)$$

$$M_{2z}^{O}=\frac{E_s^b I_z^b}{L_b^2(1+\Phi_y)}\left(\left(-6\,e_y\cdot\left(\Delta \mathrm{U}_2^{\mathrm{b}}\right)\right)+L_b\left(e_z\cdot\left((4+\Phi_y)\phi_1^O+(2-\Phi_y)\phi_1^E+(2-\Phi_y)\frac{\partial\phi_0}{\partial\lambda_i}\delta^{ib}\right)\right)\right)$$

$$M_{2z}^{E}=\frac{E_s^b I_z^b}{L_b^2(1+\Phi_y)}\left(\left(-6\,e_y\cdot\left(\Delta \mathrm{U}_2^{\mathrm{b}}\right)\right)+L_b\left(e_z\cdot\left((2-\Phi_y)\phi_1^O+(4+\Phi_y)\phi_1^E+(4+\Phi_y)\frac{\partial\phi_0}{\partial\lambda_i}\delta^{ib}\right)\right)\right)$$

7. Building of the stress vector S^{i} and couple stress vector μ^{i}.
8. Building of the Cauchy stress $[\sigma]=\frac{1}{g}\mathrm{S}^{\mathrm{i}}\otimes\frac{\partial \mathrm{R}}{\partial\lambda^{\mathrm{i}}}=\underbrace{\frac{1}{g}\mathrm{S}_1^{\mathrm{i}}\otimes\frac{\partial \mathrm{R}}{\partial\lambda^{\mathrm{i}}}}_{[K^s]\{\epsilon\}}+\underbrace{\frac{1}{g}\varepsilon\mathrm{S}_2^{\mathrm{i}}\otimes\frac{\partial \mathrm{R}}{\partial\lambda^{\mathrm{i}}}}_{[B]\{\chi\}}$ and couple stress tensor $[\mathrm{m}]=\frac{1}{g}\mu^{\mathrm{i}}\otimes\frac{\partial \mathrm{R}}{\partial\lambda^{\mathrm{i}}}=\underbrace{\frac{1}{g}\varepsilon\mu_1^{\mathrm{i}}\otimes\frac{\partial \mathrm{R}}{\partial\lambda^{\mathrm{i}}}}_{[B]\{\epsilon\}}+\underbrace{\frac{1}{g}\varepsilon^2\mu_2^{\mathrm{i}}\otimes\frac{\partial \mathrm{R}}{\partial\lambda^{\mathrm{i}}}}_{[K^\mu]\{\chi\}}$, with g the determinant of the Jacobian matrix of the transformation of Cartesian to curvilinear coordinates, **R** the position vector of a material point within the microstructure, $\{\epsilon\}$ the strain tensor and $\{\chi\}$ the microcurvature tensor.
9. Building of the homogenized rigidity matrices $\left[K^S\right]$, $[B]$.
10. Extraction and identification of the effective mechanical properties in engineering format from the compliance matrix $[S]=\left[K^S\right]^{-1}$:

- Homogenized tensile moduli: $E_x^*=[1/S_{11}]$, $E_y^*=[1/S_{22}]$, $E_z^*=[1/S_{33}]$.
- Homogenized shear moduli G_{xy}^*, G_{yz}^*, G_{xz}^*, with $G^*=\mu^*+\kappa/2$, and μ^*, κ therein the effective micropolar moduli.
- Poisson's coefficients: $\nu_{xy}^*=-S_{21}E_x^*$, $\nu_{yx}^*=-S_{12}E_y^*$, $\nu_{zx}^*=-S_{13}E_z^*$.
- Define the characteristic lengths in flexion and torsion as the ratio of the second-order moduli to first-gradient moduli, viz.,

$$l_{b_{xy}}=\sqrt{K_{xz}^{\mu}/2\left(K_{xy}^s+K_{yx}^s\right)},\ l_{t_{yx}}=\sqrt{\left(K_{yz}^{\mu}+K_{zy}^{\mu}\right)/\left(K_{yx}^s+K_{xy}^s\right)}$$

$$l_{b_{yx}}=\sqrt{K_{yz}^{\mu}/2\left(K_{yx}^s+K_{xy}^s\right)};\ l_{t_{xy}}=\sqrt{\left(K_{xz}^{\mu}+K_{zx}^{\mu}\right)/\left(K_{xy}^s+K_{yx}^s\right)} \tag{2.21}$$

Couple Stress Models of Textile Preforms

Homogeneous anisotropic couple stress models as substitutes for 3D heterogeneous woven reinforcements are developed by both discrete homogenization and finite element methods in the sequel. The architecture of the woven preforms is obtained from an idealized geometry and a model of the yarns organization within a representative unit cell (RUC in short). In order to predict the effective elastic constants based on the discrete homogenization method; the RUC is represented as a set of structural

beam-like elements that describe the representative volume element, with periodicity boundary conditions. The effective properties of the RUC are also obtained from its finite element response under prescribed boundary conditions. Specific boundary conditions, including both traction and displacement boundary conditions, are applied to the boundaries of the RUC. The classical Cauchy and nonclassical mechanical moduli are deduced on the basis of the extended Hill–Mandel principle of energy equivalence, stating that the average microscopic strain energy over the RUC is given by the corresponding strain energy of the postulated effective generalized continuum (here the couple stress medium). The characteristic bending lengths will be identified from the resulting homogenized moduli. The proposed approach is quite general and applicable to any textile preforms and composite materials.

The Orthogonal 3D Interlock

It consists of a network of yarns oriented in three orthogonal directions, two of which are oriented in the warp and weft directions, which can either be mutually interlaced or stacked at 0°/90°, and a network of yarns to strengthen the preform in the thickness, building the binder yarns. Figure 2.2 shows an example of such a 3D reinforcement deserving the name interlock. A homogenized micropolar model is next constructed as a substitution medium, in which the discrete rotations at the nodes (the yarns crossing points) become after homogenization a microrotation field which completes the kinematic description of the identified couple stress continuous medium (homogenized). The mechanical and geometrical parameters of the warp, weft, and binding yarns are given in Table 2.1. The mechanical properties of the yarns are taken from Younes and Zaki (2011). It is essential to be noted that the same mechanical properties are used for all the 3D preforms studied. The indices f, p, b, and c refer, respectively, to the weft, warp, binder yarns, and contact beams (beams connecting the warp/weft son and binder/weft yarns at the cross points). Beams of elliptical cross section are chosen, which determines the quadratic moments $I_y = \frac{\pi\, a\, b^3}{4}$, $I_z = \frac{\pi\, b\, a^3}{4}$, the torsional rigidity $J = \frac{\pi a^3 b^3}{a^2+b^2}$, and the Timoshenko shear coefficient is calculated as

$$k_s = \frac{6\,a^2\left(3\,a^2+b^2\right)(1+\nu)^2}{20\,a^4+8\,a^2b^2+\nu\left(37\,a^4+10\,a^2\,b^2+b^4\right)+\nu^2\left(17\,a^4+2\,a^2b^2-3b^4\right)}$$

wherein a, b are, respectively, the big and small radii of the elliptic section of the yarn, and ν is the Poisson's ratio.

The spacing between the warp and weft yarns is equal to Lf2 and Lp1, respectively. The geometrical model of the elementary cell of the orthogonal interlock reinforcement is shown schematically in Fig. 2.3. The different yarns and their intercrossing are represented by a network of beams connected at nodes and the interaction between yarns is modeled by contact beams whose radius is equal to the average of the radii of the two beams in contact (Goda et al. 2013a).

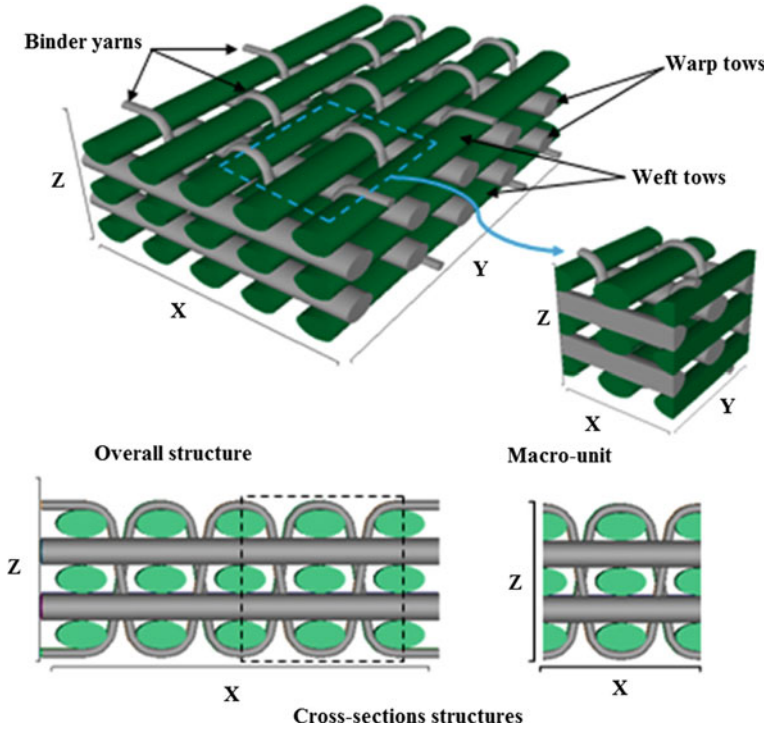

Fig. 2.2 Schematic representation of the 3D orthogonal interlock (Rahali et al. 2016)

Table 2.1 Mechanical and geometrical properties of the yarns

Fiber	Density (g/cm^3)	Young modulus (GPa)	Poisson's ratio	Shear modulus (GPa)
T300	1.76	230	0.34	85.82
		Width (mm)	Thickness (mm)	Beam lengths (mm)
Weft yarn		0.27	0.15	$L_{f1} = 0.473$ $L_{f2} = 0.2365$
Warp yarn		0.25	0.15	$L_{p1} = 0.429$ $L_{p2} = L_{p1}/2$
Binding yarns		0.08	0.05	$L_{b1} = 0.096$ $L_{b2} = 0.101$ $L_{b3} = 0.609$
Radii of the contact beams [41]		$r_{c_1} = \frac{\text{radius}_{\text{weft}} + \text{radius}_{\text{warp}}}{2}$ $r_{c_2} = \frac{\text{rayon}_{\text{weft}} + \text{radius}_{\text{binder}}}{2}$		$L_{c1} = 0.15$ $L_{c2} = 0.1$

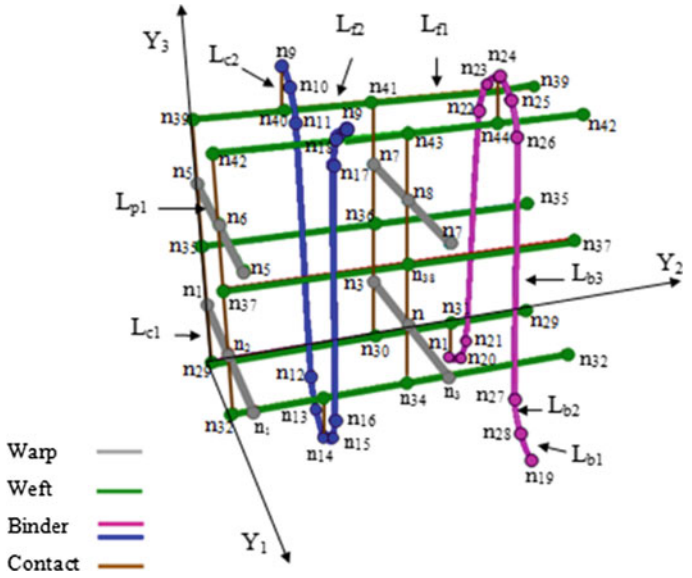

Fig. 2.3 Geometrical model of the RUC of the 3D orthogonal interlock (Rahali et al. 2016)

The periodicity vectors $\mathbf{Y}_1 = \begin{pmatrix} 1 & 0 & 0 \end{pmatrix}$, $\mathbf{Y}_2 = \begin{pmatrix} 0 & 1 & 0 \end{pmatrix}$, $\mathbf{Y}_3 = \begin{pmatrix} 0 & 0 & 1 \end{pmatrix}$ pictured in Fig. 2.3 define the translation vectors which generate the complete structure; their lengths are $L_1 = 2L_{p1}$, $L_2 = 2L_{f1}$, $L_3 = 1$.

3D Layer-to-Layer Orthogonal Interlock

Figure 2.4 shows a schematic representation of a 3D orthogonal layer-to-layer interlock preform created with the TexGen software by choosing the same number of weft and warp layers and the same geometric parameters of the yarns as previously, in order to compare it with the 3D orthogonal reinforcement. The difference between the two reinforcements is the arrangement of the binding threads. As mentioned before, the geometrical parameters of the different yarns are the same as for 3D orthogonal preform, as exposed in Table 2.1; only the lengths of the beams of the binding threads differ, denoted L_b, namely, $L_{b1} = 0.041$, $L_{b2} = 0.072$, and $L_{b3} = 0.251$.

The geometric model of the RUC of the layer-to-layer interlock reinforcement is shown schematically in Fig. 2.5, with the periodicity vectors given by $Y_1 = (1, 0, 0)$, $Y_2 = (0, 1, 0)$, and $Y_3 = (0, 0, 1)$; they are the translation vectors that generate the complete structure; their lengths are, respectively, equal to $L_1 = 2L_{p1}$, $L_2 = 2L_{f1}$, and $L_3 = 1$.

3D Through-the-Thickness Angle Interlock

The preform of the 3D through-the-thickness angle interlock is weaved with three types of yarns (in warp and weft directions, and with a third yarn crossing the sample thickness around the weft layers) as indicated in Fig. 2.6. The beam lengths of the binder yarns are chosen as $L_{b1} = 0.08$, $L_{b2} = 0.16$, and $L_{b3} = 1.1$. The spacing between warp and binder yarns and weft yarns is equal to L_{f2} and L_{p2}, respectively. The geometrical model of the RUC is shown in Fig. 2.7, such that the periodicity vector lengths are $L_1 = 5L_{p1}$, $L_2 = 5L_{f1}$, and $L_3 = 1$.

2.5D Layer-to-Layer and Layer–Layer Angle Interlock Preforms

The 2.5D angle interlock includes a wide set of possible arrangements of the yarns within the RUC; we shall here focus on types of waves in this family, namely, the 2.5D layer-to-layer angle interlock and the 2.5D layer–layer angle interlock, with geometrical parameters given in Table 2.2.

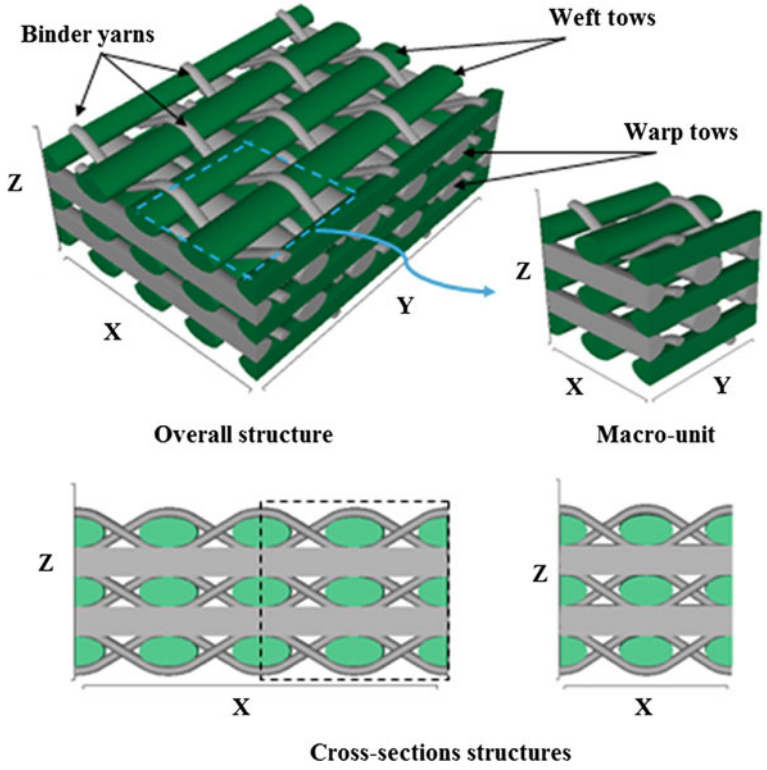

Fig. 2.4 Schematic representation of the 3D layer-to-layer orthogonal interlock (Rahali et al. 2016)

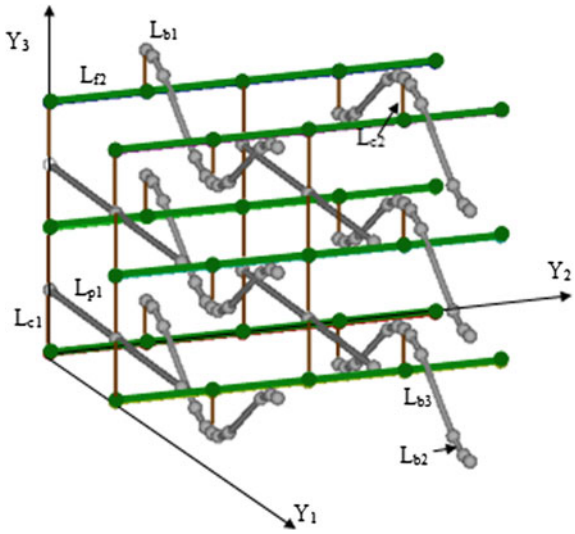

Fig. 2.5 Geometrical model of the RUC of the 3D layer-to-layer orthogonal interlock (Rahali et al. 2016)

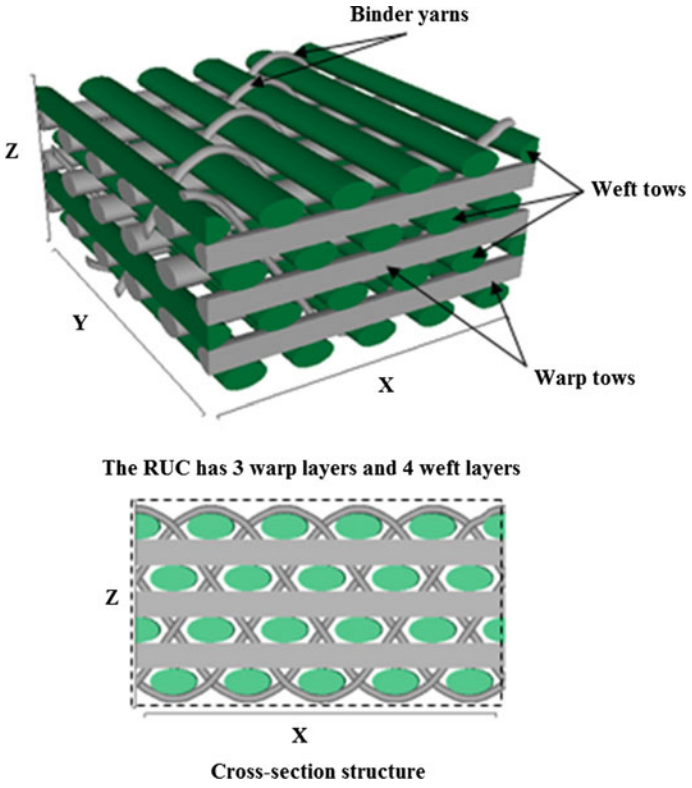

Fig. 2.6 Preform of the 3D through-the-thickness angle interlock (Rahali et al. 2016)

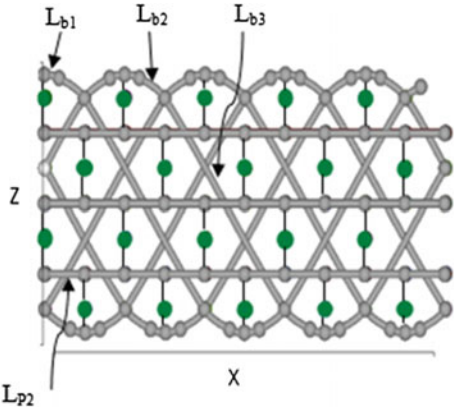

Fig. 2.7 Geometrical model of the RUC of the through-the-thickness angle interlock (Rahali et al. 2016)

Parameters C_L and C_T therein are, respectively, the distances between the two adjacent weft and warp in the same layer.

The set of warp crimps through the successive layers of the weft and different arrangements of the yarns can be envisaged. The specific architecture of the 2.5D layer-to-layer angle interlock preform considered in this work is shown in Fig. 2.8. The geometrical model of this RUC reinforcement is also given in Fig. 2.9.

The architecture and geometrical model of the RUC of the considered 2.5D layer–layer angle interlock preform are, respectively, illustrated in Figs. 2.10 and 2.11.

Effective Properties of the Micropolar Constitutive Law for Textile Preforms

We next expose the micropolar constitutive law adopted for the effective medium of these textile preforms, which will be identified. For a centrosymmetric anisotropic medium, the linear elastic constitutive law is expressed as (Rahali et al. 2016)

$$\begin{aligned} \sigma_{ij} &= K^{s}_{ijkl}\,\epsilon_{kl} \\ m_{ij} &= K^{\mu}_{ijkl}\,\chi_{kl} \end{aligned} \tag{2.22}$$

Table 2.2 Geometrical parameters of the 2.5 angle interlock woven fabrics

	Width (mm)	Thickness (mm)	Distance between yarns (mm)
Warp	0.25	0.15	$C_T = 0.5$
Weft	0.25	0.15	$C_L = 1$

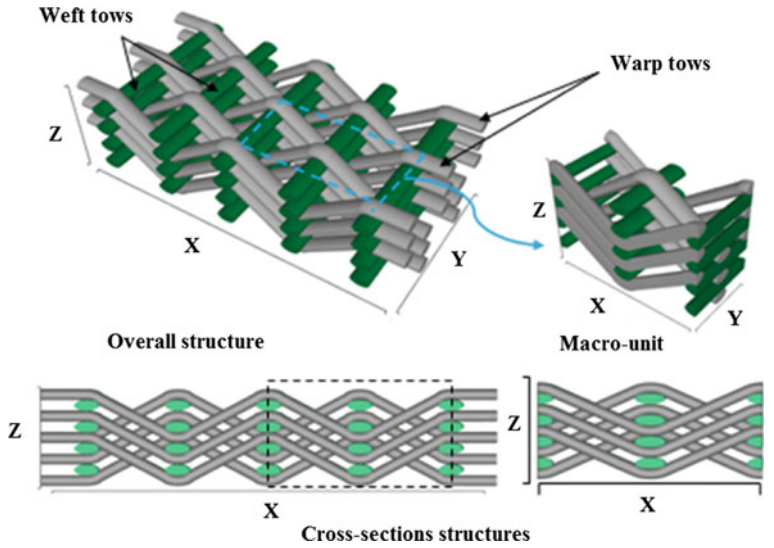

Fig. 2.8 Representation of the architecture of the layer-to-layer 2.5D angle interlock (Rahali et al. 2016)

Fig. 2.9 Geometrical model of the RUC of the layer-to-layer 2.5D angle interlock (Rahali et al. 2016)

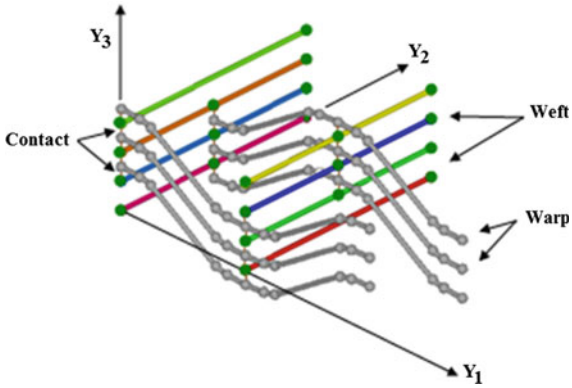

with K^s_{ijkl}, K^μ_{ijkl} therein, the Cauchy and micropolar fourth-order rigidity tensors: tensor K^s_{ijkl} relates the Cauchy stress σ_{ij} to the linearized strain tensor ϵ_{kl}, while K^μ_{ijkl} relates the couple stress tensor m_{ij} to the microcurvature tensor χ_{kl}. In explicit form, Eqs. (2.22) can be written as

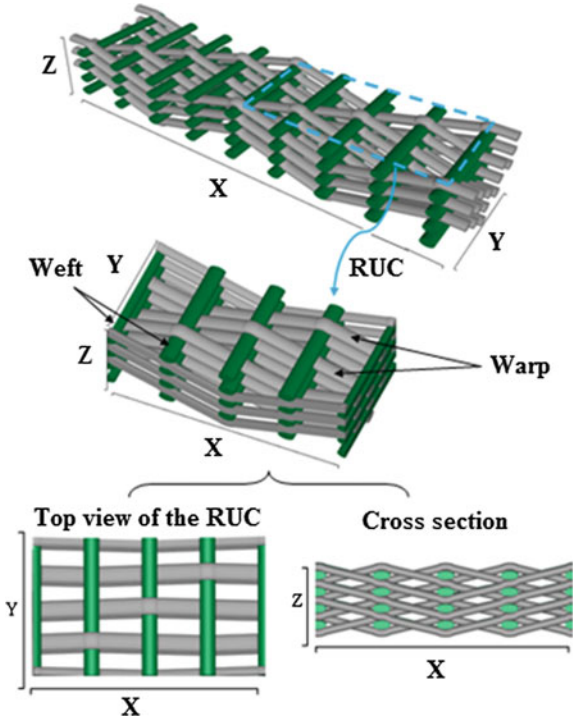

Fig. 2.10 Representation of the architecture of the RUC of the 2.5D layer–layer interlock (Rahali et al. 2016)

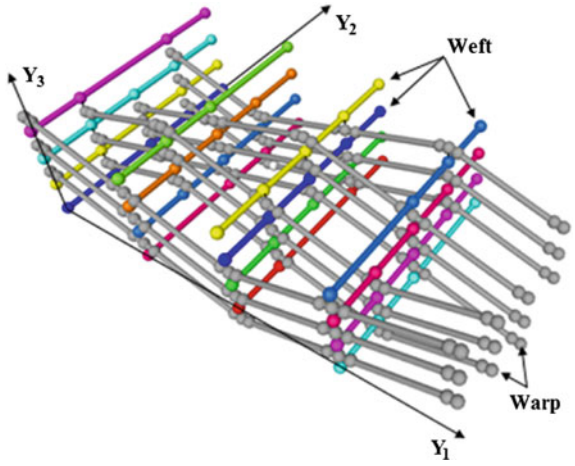

Fig. 2.11 Geometrical model of the RUC of the 2.5D layer–layer interlock (Rahali et al. 2016)

$$\begin{bmatrix} \sigma_{xx} \\ \sigma_{yy} \\ \sigma_{zz} \\ \sigma_{xy} \\ \sigma_{yx} \\ \sigma_{yz} \\ \sigma_{zy} \\ \sigma_{zx} \\ \sigma_{xz} \end{bmatrix} = \begin{bmatrix} K^s_{xx} & & & \cdots & & & \\ & K^s_{yy} & & & & & \\ & & K^s_{zz} & & & & \\ & & & K^s_{xy} & & & \\ \vdots & & & & K^s_{yx} & & \vdots \\ & & & & & K^s_{yz} & \\ & & & & & & K^s_{zy} \\ & & & & & K^s_{zx} & \\ & & & \cdots & & & K^s_{xz} \end{bmatrix} \begin{bmatrix} \epsilon_{xx} \\ \epsilon_{yy} \\ \epsilon_{zz} \\ \epsilon_{xy} \\ \epsilon_{yx} \\ \epsilon_{yz} \\ \epsilon_{zy} \\ \epsilon_{zx} \\ \epsilon_{xz} \end{bmatrix} \tag{2.23}$$

$$\begin{bmatrix} m_{xx} \\ m_{yy} \\ m_{zz} \\ m_{xy} \\ m_{yx} \\ m_{yz} \\ m_{zy} \\ m_{zx} \\ m_{xz} \end{bmatrix} = \begin{bmatrix} K^\mu_{xx} & & & \cdots & & & \\ & K^\mu_{yy} & & & & & \\ & & K^\mu_{zz} & & & & \\ & & & K^\mu_{xy} & & & \\ \vdots & & & & K^\mu_{yx} & & \vdots \\ & & & & & K^\mu_{yz} & \\ & & & & & & K^\mu_{zy} \\ & & & & & K^\mu_{zx} & \\ & & & \cdots & & & K^\mu_{xz} \end{bmatrix} \begin{bmatrix} \chi_{xx} \\ \chi_{yy} \\ \chi_{zz} \\ \chi_{xy} \\ \chi_{yx} \\ \chi_{yz} \\ \chi_{zy} \\ \chi_{zx} \\ \chi_{xz} \end{bmatrix} \tag{2.24}$$

with the strain and stress tensors conveniently written in vector format:

$$\underline{\epsilon} = \left[\frac{\partial u_x}{\partial x} \; \frac{\partial u_y}{\partial y} \; \frac{\partial u_z}{\partial z} \; \frac{\partial u_y}{\partial x} - \phi_z \; \frac{\partial u_x}{\partial y} + \phi_z \; \frac{\partial u_z}{\partial y} - \phi_x \; \frac{\partial u_y}{\partial z} + \phi_x \; \frac{\partial u_x}{\partial z} - \phi_y \; \frac{\partial u_z}{\partial x} + \phi_y \right]^{\mathrm{T}}$$

$$\underline{\chi} = \left[\frac{\partial \phi_x}{\partial x} \; \frac{\partial \phi_y}{\partial y} \; \frac{\partial \phi_z}{\partial z} \; \frac{\partial \phi_y}{\partial x} \; \frac{\partial \phi_x}{\partial y} \; \frac{\partial \phi_z}{\partial y} \; \frac{\partial \phi_y}{\partial z} \; \frac{\partial \phi_x}{\partial z} \; \frac{\partial \phi_z}{\partial x} \right]^{\mathrm{T}}$$

The components m_{xx}, m_{yy}, m_{zz} are the torsional couple stresses, and the components m_{xy}, m_{yz}, m_{xz} are the flexural couple stresses. The computed classical and couple stress effective moduli together with the associated characteristic lengths are evaluated in Table 2.3 for the studied preforms denoted with the abbreviations OR, AI, TTT, LL, and LTL, which stand successively for the orthogonal, angle interlock, through-the-thickness, layer–layer, and layer-to-layer. The Poisson's ratio is found close to zero, which means that the preforms do nearly not change their lateral dimensions due to the dense packing of yarns.

One can notice that for the same geometric and mechanical parameters, the effective properties calculated for both the 3D orthogonal and 3D layer-to-layer orthogonal preforms are almost similar. This result tends to show that the effective properties are little affected by the combinations of arrangement of the yarns in the 3D orthogonal preforms. Compared to the first two reinforcements, the 3D interlock angle "through-the-thickness" has much higher moduli (since it contains more layers), which allows it to have a better resistance to delamination.

Table 2.3 Effective mechanical properties of the set of 2.5D and 3D preforms

	3D OR	3D LTL OR	3D TTT AI	2.5D LL AI	2.5D LTL AI
$\mathbf{K}^s_{xx}$ (MPa)	34583.41	32475.47	49542.81	20660.11	11038.1
$\mathbf{K}^s_{yy}$ (MPa)	60907.34	57280.49	77057.84	26149.73	20565.52
$\mathbf{K}^s_{zz}$ (MPa)	5565.63	6412.45	8872.95	299	8032.22
$\boldsymbol{G}^*_{xy} = \mathbf{K}^s_{xy}$ (MPa)	538.26	460.56	3055.07	1368.175	790.5
$\boldsymbol{G}^*_{yz} = \mathbf{K}^s_{yz}$ (MPa)	1280	1080.64	3904.3	1037.69	805
$\boldsymbol{G}^*_{xz} = \mathbf{K}^s_{xz}$ (MPa)	1241	890.3	3546.83	3304.38	2756.044
$\mathbf{K}^\mu_{xz}$ (N)	133.81	136.22	962	253.94	303.18
$\mathbf{K}^\mu_{yz}$ (N)	214.38	236.7	813.44	1853.3	1696.86
$l_{b\,\mathrm{xy}}$ (mm)	0.249	0.271	0.258	0.251	0.265
$l_{b\,\mathrm{yx}}$ (mm)	0.239	0.314	0.248	0.272	0.472
$l_{\mathrm{t\,xy}}$ (mm)	0.352	0.384	0.364	0.304	0.333
$l_{\mathrm{t\,yx}}$ (mm)	0.339	0.444	0.35	0.385	0.668
H (mm)	0.85	0.85	1.15	1.35	1.35
L_1 (mm)	0.858	0.858	2.145	4	2
L_2 (mm)	0.946	0.946	2.365	2	1

The characteristic lengths in bending and torsion of the 3D orthogonal and the 3D layer-to-layer orthogonal are smaller by a factor of 3 and 2, respectively, in the x-y and y-x directions with respect to the periodicity lengths L_1 and L_2. In order to further assess the importance of micropolar effects, we compare in the case of plane stress the simplified equation of a micropolar beam incorporating an interlock angle microstructure (3D or 2.5D) in pure bending. This amounts considering a one-dimensional beam with many elementary cells repeated periodically along the longitudinal direction, and a single unit cell in the thickness direction.

The equilibrium equation of a micropolar beam subjected to a uniform bending moment is written in both x-z and y-z planes:

$$\underbrace{\left(E^*_x I_z + K^\mu_{xz} H\right)}_{\kappa^\mu_{xz}} \frac{\partial \phi_z}{\partial x} = -M\,, \quad \underbrace{\left(E^*_y I_z + K^\mu_{yz} H\right)}_{\kappa^\mu_{yz}} \frac{\partial \phi_z}{\partial y} = -M \tag{2.25}$$

with E^*_x, E^*_y therein are the homogenized moduli of a macroscopic beam with a fibrous microstructure, M is the moment of flexion, $I_z = \frac{H^3}{12}$ is the quadratic moment of the beam along z, and K^μ_{xz}, K^μ_{yz} are the micropolar moduli. Parameter H is the height of the unit cell; this means that the size effect of the RUC is analyzed via parameter H. When the micropolar effect is not accounted for, the beam bending response is analyzed based on the classical flexural rigidities κ^c_{xz} and κ^c_{yz} such that the homogenized beam bending obeys the equations:

Table 2.4 Classical and micropolar effective bending rigidities for the macrobeam under pure flexion

	3D orthogonal	3D TTT angle interlock	2.5D LL angle interlock	2.5D LTL angle interlock
k^{μ}_{xz} (Nmm)	1883.61	7385.33	4578.78	2672.44
k^{c}_{xz} (Nmm)	1769.87	6279.03	4235.96	2263.15
$\%gr_{xz}$	6.42	17.61	8.09	18.08
k^{μ}_{yz} (Nmm)	3299.28	10701.73	7863.46	6507.33
k^{c}_{yz} (Nmm)	3117.06	9766.27	5361.51	4216.57
$\%gr_{yz}$	5.84	9.57	46.66	54.32
H (mm)	0.85	1.15	1.35	1.35

$$\underbrace{\left(E_x^* I_z\right)}_{\kappa^C_{xz}} \frac{\partial \phi_z}{\partial x} = -M\,, \quad \underbrace{\left(E_y^* I_z\right)}_{\kappa^C_{yz}} \frac{\partial \phi_z}{\partial y} = -M \tag{2.26}$$

The values computed for the classical and micropolar flexural rigidities are given in Table 2.4.

The gain in flexural rigidity accounting for the micropolar effect is defined as the scalar $\%gr = \frac{\kappa^{\mu} - \kappa^{c}}{\kappa^{c}} \times 100$. It is noticed that the flexural gain is significant in comparison with a conventional beam (without a micropolar effect), since it varies between 6 and 18% for the x-z plane, and between 5 and 54% for the y-z plane. It can also be seen that the gain in flexural rigidity is greater in the layer-to-layer 2.5D interlock angle preform than for the other preforms: this result is in agreement with the characteristic lengths calculated for the different interlocks in Table 2.3.

Comparison of the Homogenized Moduli with the FE Computations

In this section, a 3D FE model of 3D orthogonal interlock preform and the 2.5D layer-to-layer angle interlock is developed at the unit cell level to evaluate the accuracy of the predicted effective properties from the discrete homogenization method previously discussed. One here aims to estimate the mechanical properties of the RUC of a woven-reinforced composite with a minimum modeling and computational effort. To this end, the geometrical modeling of the RUC is done with the open-source code TexGen, while the simulation aspects are performed using ABAQUS. The geometric models of the elementary cells made in TexGen are exported in an ABAQUS file, whether in "ABAQUS Dry Fiber file" to predict the effective properties of a dry reinforcement or in "ABAQUS Voxel file" to predict the effective properties of the composite (when the resin is also considered). In this method, the elementary cell

is divided into a regular grid (voxel) of hexahedral elements whose number in each direction is set by the user, see Fig. 2.12. The advantage of this method is its rapidity in comparison to traditional FE models that require much more time. The type of element chosen for meshing woven structures is C3D8, since it proves to be the most relevant element for these analyses (Dixit et al. 2013). The previous Tables 2.1 and 2.2 provide a complete and detailed description of the mechanical and geometrical parameters needed to build the FE models. Based on these parameters, the geometry of the RUC is constructed. This procedure involves modeling the unit cell instead of modeling the entire structure of the weave.

For anisotropic materials, the micropolar constitutive equations for centrosymmetric microstructures are written in decoupled form as follows: the Cauchy stress is related to the elastic strain (equal to the total strain) with the elastic rigidity matrix $[K^s]$ as

$$\{\sigma\} = \left[K^s\right]\{\epsilon\} \tag{2.27}$$

Similarly, the couple stress is related to the microcurvature through the couple stress rigidity matrix $[K^\mu]$ as follows:

$$\{m\} = \left[K^\mu\right]\{\chi\} \tag{2.28}$$

The set of effective moduli is next evaluated in a sequential manner based on the Hill–Mandel energy equivalence principle: a set of kinematic boundary conditions is applied over the RUC boundary, each displacement field allowing the identification of one modulus. Thereby, the average microscopic strain energy U_{cell} evaluated numerically by FE simulations is equated to the energy of the equivalent micropolar continuum (Goda and Ganghoffer 2015), so that it holds the identity

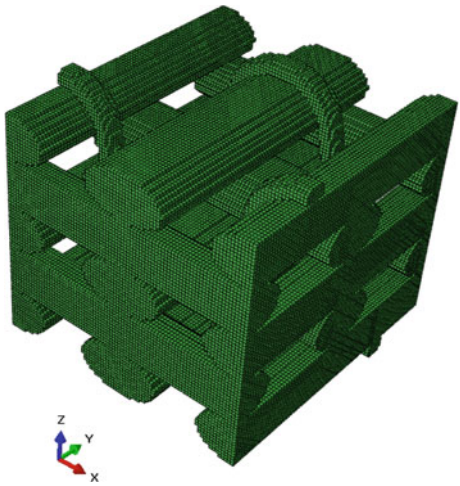

Fig. 2.12 RUC for the 3D orthogonal interlock with 80 voxels per direction (Rahali et al. 2016)

$$U_{cell} = U_{couple\,stress} = \frac{V}{2}\left[\epsilon_{ij} K^{s}_{ijkl} \epsilon_{kl} + \chi_{ij} K^{\mu}_{ijkl} \chi_{kl}\right] \tag{2.29}$$

with $V = |\Omega|$ the volume of the RUC. In the couple stress theory, the microrotation ϕ_i is identical to the macrorotation accounted for by the antisymmetric part of the displacement gradient, so that it holds

$$\phi_x = \frac{1}{2}\left(\frac{\partial u_z}{\partial y} - \frac{\partial u_y}{\partial z}\right);\ \phi_y = \frac{1}{2}\left(\frac{\partial u_x}{\partial z} - \frac{\partial u_z}{\partial x}\right);\ \phi_z = \frac{1}{2}\left(\frac{\partial u_y}{\partial x} - \frac{\partial u_x}{\partial y}\right) \tag{2.30}$$

and

$$\begin{aligned}
&\frac{\partial \phi_x}{\partial x} = \frac{1}{2}\left(\frac{\partial^2 u_z}{\partial x \partial y} - \frac{\partial^2 u_y}{\partial z \partial x}\right);\ \frac{\partial \phi_y}{\partial y} = \frac{1}{2}\left(\frac{\partial^2 u_x}{\partial y \partial z} - \frac{\partial^2 u_z}{\partial x \partial y}\right);\ \frac{\partial \phi_z}{\partial z} = \frac{1}{2}\left(\frac{\partial^2 u_y}{\partial x \partial z} - \frac{\partial^2 u_x}{\partial y \partial z}\right);\\
&\frac{\partial \phi_y}{\partial x} = \frac{1}{2}\left(\frac{\partial^2 u_x}{\partial z \partial x} - \frac{\partial^2 u_z}{\partial x^2}\right);\ \frac{\partial \phi_z}{\partial y} = \frac{1}{2}\left(\frac{\partial^2 u_y}{\partial x \partial y} - \frac{\partial^2 u_x}{\partial y^2}\right);\ \frac{\partial \phi_z}{\partial x} = \frac{1}{2}\left(\frac{\partial^2 u_y}{\partial x^2} - \frac{\partial^2 u_x}{\partial x \partial y}\right)
\end{aligned} \tag{2.31}$$

Adopting displacement boundary conditions (uniform strain for the identification of the or uniform curvature), the components of the rigidity tensors $[K^s]$, and $[K^\mu]$ of the elementary unit cell can be evaluated. The motivation for applying such boundary conditions lies in the fact that periodicity boundary conditions cannot be used for the evaluation of the second gradient effective rigidity tensor $[K^\mu]$, since they lead to a deformation field which is not periodical (Goda and Ganghoffer 2015; Goda et al. 2016). Eight elementary virtual tests are performed for the sequential evaluation of the entire set of effective moduli, including six virtual tests to evaluate the tensile and shear effective moduli in $[K^s]$ and two virtual tests to compute the flexural rigidities K^{μ}_{xz} and K^{μ}_{yz} in the effective couple stress rigidity tensor $[K^\mu]$. Only one test for each of the two types of moduli is exposed in this chapter.

In order to evaluate K^{s}_{xy} (shear mode), one applies a uniform strain component $\epsilon_{xy} = 1$ on the boundary of the unit cell, by imposing the following linear displacement:

$$\begin{aligned}
u_x(x) &= y/2 \text{ edge with normal } \mathbf{n}_y\\
u_y(x) &= x/2 \text{ edge with normal } \mathbf{n}_x\\
u_z(x) &= 0 \quad \text{edge with normal } \mathbf{n}_z
\end{aligned} \tag{2.32}$$

This displacement field entails the shear modulus $K^{s}_{xy} = \frac{2U^{\text{cell}}}{V}$.

In order to determine the curvature component K^{μ}_{yz}, a uniform unit curvature $\chi_{yz} = 1$ is applied to the unit cell boundary by imposing the following quadratic displacement field:

$$\begin{aligned}
u_x(x) &= -y^2/2 \text{ edge with normal } \mathbf{n}_x\\
u_y(x) &= xy \quad\ \ \text{edge with normal } \mathbf{n}_y\\
u_z(x) &= 0 \quad\ \ \text{edge with normal } \mathbf{n}_z
\end{aligned} \tag{2.33}$$

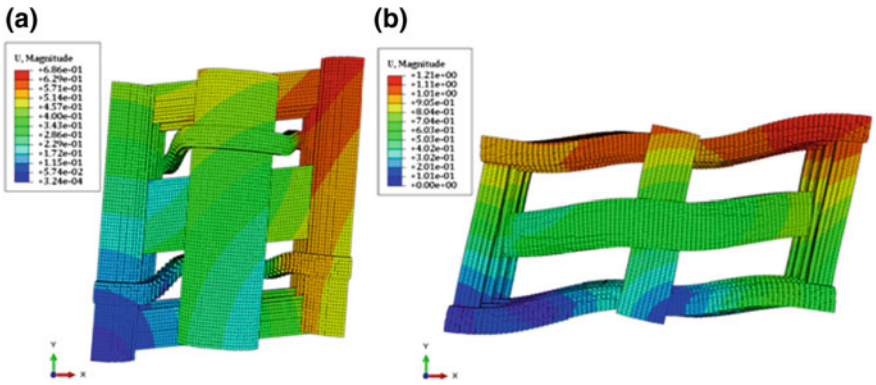

Fig. 2.13 Displacement distributions on the RUC of **a** 3D orthogonal interlock and **b** 2.5D layer-to-layer angle interlock submitted to in-plane shear ($\epsilon_{xy} = 1$) (Rahali et al. 2016)

Table 2.5 Effective elastic moduli for the 3D orthogonal and 2.5 D layer-to-layer interlock based on FE simulations and the discrete homogenization method

	Discrete homogenization		FE simulations (voxel 80)		Relative variation (%)	
	3D OR	2.5D LTL AI	3D OR	2.5D LTL AI	3D OR	2.5D LTL AI
$\mathbf{K}^{S}_{xx}$ (MPa)	34583.41	11038.1	34231.61	11620.43	1.01	5.01
$\mathbf{K}^{S}_{yy}$ (MPa)	60907.34	20565.52	61254.25	21610.03	0.56	4.83
$\mathbf{K}^{S}_{zz}$ (MPa)	5565.63	8032.22	5705.34	8227.45	2.44	2.37
$\boldsymbol{G_{xy}}$ (MPa)	538.26	790.5	505.8	846	6.03	6.56
$\boldsymbol{G_{yz}}$ (MPa)	1280	805	1408.77	676.83	9.14	15.92
$\boldsymbol{G_{xz}}$ (MPa)	1241	2756.044	1449.44	2711.78	14.37	1.6
$\mathbf{K}^{\mu}_{xz}$ (N)	133.81	303.18	132.61	276.45	0.89	8.81
$\mathbf{K}^{\mu}_{yz}$ (N)	214.38	1726.86	185.2	2280.57	13.61	24.27

This displacement field entails the flexural rigidity $K^{\mu}_{yz} = \frac{2U^{\text{cell}}}{V} - K^{s}_{yy}x^2$.

When the coordinates of the origin are placed in the center of the elementary cell (center of gravity), the additional geometric contribution in the previous expression vanishes. The deformation modes for these two virtual tests, within the elementary cells of the 3D orthogonal interlock and the 2.5D layer-to-layer angle interlock preforms, are illustrated in Figs. 2.13 and 2.14.

The effective moduli in traction, simple shear, and flexion computed, thanks to discrete homogenization, and by FE simulations are summarized in Table 2.5 for the set of tested textile preforms.

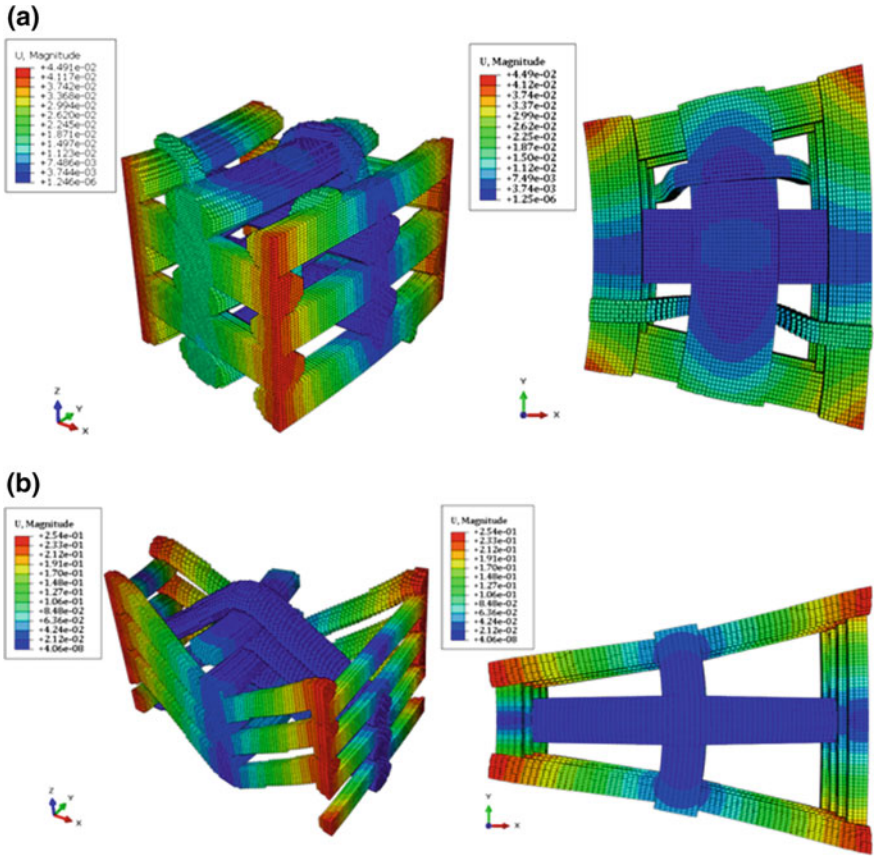

Fig. 2.14 Displacement distribution on the RUC of **a** 3D orthogonal interlock and **b** 2.5D layer-to-layer angle interlock submitted to a uniform curvature $\chi_{yz} = 1$ (Rahali et al. 2016)

A good agreement is obtained between the homogenized moduli and their numerical FE counterpart, with 14.37% maximum difference for the 3D orthogonal fabric for the shear modulus in x-z plane and 24.27% for the 2.5D layer-to-layer interlock for the flexion modulus. The percentage of difference for the other moduli varies between 0.56 and 13.61% for the 3D orthogonal interlock, and between 1.6 and 15.92% for the 2.5D layer-to-layer angle interlock. These differences can be attributed to several factors that will be next analyzed.

In the discrete homogenization scheme, the geometric representation of the elementary cells of the preforms has some limitations, which are underlined in the following. Whether in TexGen or in finite element simulations, the curvilinear trajectories of the strands in the 3D geometric models have been described by Bezier curves, while in the discrete homogenization, the trajectories of the beams are modeled by straight lines with sharp angles at crossing points; this implies that the line

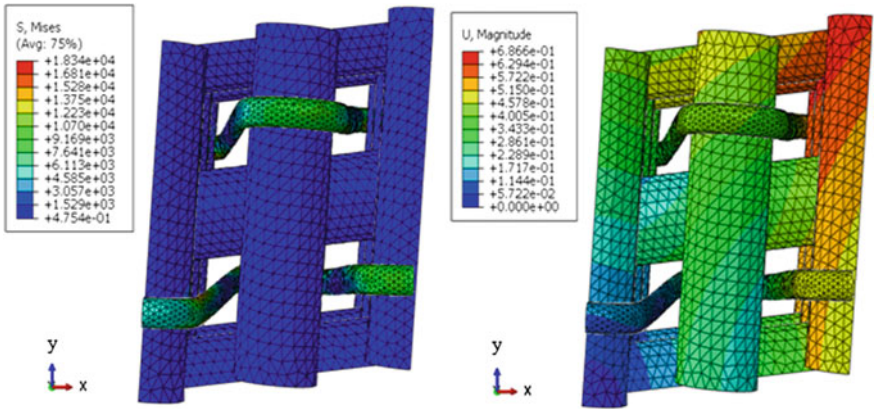

Fig. 2.15 Distributions of von Mises stress and of the displacement within the unit cell for the 3D orthogonal interlock under in-plane shear (in x-y plane) (Chaouachi et al. 2014)

will not follow the trajectory precisely and that the weaving of the yarns will be slightly different from the finite element model, which will in turn have an impact on the macroscopic behaviors.

Incorporation of a Hertz Contact Model Between Yarns

Another limitation of the homogenized models is the use of a sticky, nonslip contact, so if we do a shear test in the xy plane by a finite element simulation in ABAQUS on one of the considered preforms (for example the 3D orthogonal interlock, Fig. 2.15), by allowing sliding between yarns, a very small value is obtained for the shear modulus (of the order of 3 MPa), in comparison with that calculated by the discrete homogenization. In order to take into account the possible displacements between the yarns, a contact with friction is introduced with a master/slave approach. The tangential behavior at the contact surfaces is defined using the penalty method with a coefficient of friction chosen here equal to 0.05.

The interactions between the various yarns (weft, warp, and binders) within the reinforcements are modeled by contact beams whose radius is equal to the average of the radii of the two beams into contact: this hypothesis also increases the percentage of error since the extent of the contact area is not precisely calculated. A more accurate method is to find a general formulation for the contact reactions at each yarn intersection in the multilayer fabrics, based on the theory of unilateral Hertz contact, in order to more accurately account for the extent of the contact surface. This point will be analyzed in the sequel for the plain weave. We conduct a comparative analysis by varying the point contact area to an extended (elliptical) contact based on Hertz contact theory, as detailed in Chaouachi et al. (2014). The wording "point"

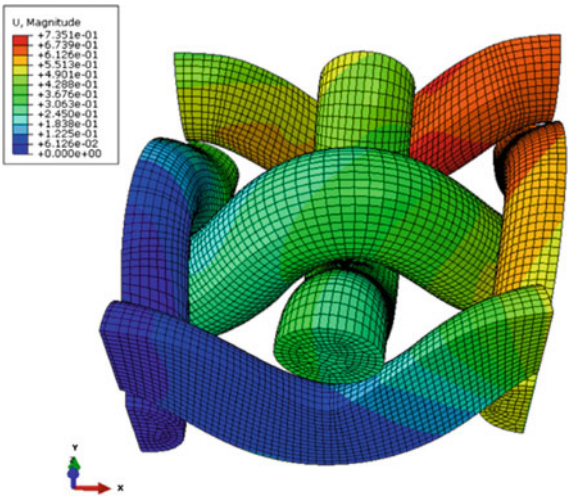

Fig. 2.16 Distribution of the displacement within the plain weave elementary cell under uniaxial tension along x (Chaouachi et al. 2014)

refers to the use of contact beam elements with a circular cross section. This approach allows estimating the effect of the contact on the moduli of plain weave (represent in Fig. 2.16) and to compare them with those computed by finite elements. We further assume that the contact between yarns is perfect and does not induce relative slip. In the sequel, we rely on the following expressions of the small and large radii of the contact ellipse (Chaouachi et al. 2014)

$$a = m_1 \sqrt[3]{\frac{3\pi N(k_1 + k_2)}{2(C_1 + C_1' + C_2 + C_2')}}, \quad b = \frac{m_2}{m_1} a \tag{2.34}$$

in order to estimate the contact area more accurately than based on the contact radius given by $r^b_{\text{contact}} = \frac{r^b_{weft} + r^b_{warp}}{2}$ (Goda et al. 2013a).

In Eq. (2.34), m_1, m_2 are two coefficients expressed in Aublin et al. (1998) in terms of a fictive angle φ depending on the curvatures (C_1, C_1', C_2, C_2') and on the angle θ between the planes of principal curvatures, viz.,

$$\varphi = \arccos\left(\frac{\sqrt{(C_1 - C_1')^2 + (C_2 - C_2')^2 + 2(C_1 - C_1')(C_2 - C_2')\cos(2\theta)}}{C_1 + C_1' + C_2 + C_2'}\right) \tag{2.35}$$

In expression (2.34), N denotes the normal resultant on the contact zone, noted N_1 in the initial state (in the absence of external load) (Chaouachi et al. 2014). The relation between the applied normal effort and the yarn crimp is written for plain weave as

Table 2.6 Effective moduli obtained in situations of punctual contact or extended contact between yarns, based on discrete homogenization or FE simulations

Mechanical properties	Discrete homogenization		FE predictions
	Punctual contact	Elliptic contact area	
$K^S_{xx} = K^S_{yy}$ (MPa)	82.5	92.4	96
K^S_{xy} (MPa)	26.3	31.6	28
$E_x* = E_y*$ (MPa)	74.2	81.57	86.7
$\nu_{xy} = \nu_{yx}$	0.318	0.32	0.292

$$N_1 = \frac{\pi^4}{2} \frac{B_{ch} N_{tr}^3}{L_{ch}^3} w_{so-ch}^{j,k} \tag{2.36}$$

The effective moduli of plain weave for the situations of a punctual and extended contact area are given for plain weave in Table 2.6. Note that the proposed methodology for the modeling of an extended contact area between yarns within preforms is general, although its numerical implementation is more involved for complex fibrous microstructures.

The evolution of the contact surface between the two sets of yarns seems to have a significant effect on the actual elastic constants, which become closer to the values found by FE simulations, with a maximum percentage of difference that does not exceed 11%, compared to those found with the hypothesis of a point contact that shows an error of 20%. The contact surface for multilayer textiles is more difficult to model and requires an independent and specific study for each type of preform.

A micromechanical model based on the discrete homogenization method has been developed to calculate the effective mechanical properties of 3D textile preforms. The yarns are described as corrugated beams with tensile and bending stiffnesses. The method is able to calculate very efficiently (with a low computational cost) the entire set of homogenized anisotropic mechanical properties, including flexural and torsional moduli, taking into account the effects of internal scales. In comparison with the FE computations of these moduli requiring the application of many loads in a sequential manner on the selected RVE, the entire set of classical and nonclassical moduli is here obtained in a single step, since the periodicity is embedded into the DH method. In addition, the description of the yarns within the preform by beam elements is an effective way to model the complex organization of the yarns within these 3D preforms. The proposed approach is particularly interesting, considering the difficulty of measuring the out-of-plane effective properties of complex interlocking weaves. The nonclassical moduli have a significant impact on the bending response of 3D textiles, as shown by calculations of the bending behavior of the macroscopic beam, so they need to be accounted for directly at the constitutive level. A good agreement is obtained between the moduli obtained by homogenization and those calculated by FE. Apart from a few limitations, all the obtained results underline the relevance of the proposed model, in particular, we have shown from initial simulations performed on monolayer textiles that the incorporation of the true area of contact

between yarns improves the predictions of the DH model. The implementation of unilateral contact conditions based on the Hertz model in the case of nonslip of the yarns in combination with the proposed homogenization technique is a promising development prospect.

Since the fibers and yarns are prone to large rotations within the preform, large deformation aspects need to be accounted for, especially geometrical nonlinearity; this is the object of the next section.

Large Configuration Changes of Lattices Based on Discrete Homogenization Method

To account for the large changes of configuration of the networks, we next expose the extension of the previous discrete homogenization method to the nonlinear regime. This should result in an algorithm for the computation of the large strains response of the underlined networks. Here, the analysis is performed on the RUC chosen as the lattice unit cell, based on recent results (Vigliotti et al. 2014). This demonstrates that the size of RUC has no effect on the predicted effective homogenized response in the nonlinear regime, as long as no bifurcations happen.

Microscopic Incremental Problem over the RUC

We next extend the linear framework developed in section "Effective Mechanical Properties of Periodic Fibrous Materials in the Small Strains Regime" and consider the impact of a variation of the RUC geometry on the effective structure behavior. Thus, we write down the nonlinear equilibrium problem associated to the large perturbations of the lattice network. The geometrical nonlinearity is induced due to the beam directors and beam lengths changing with the loading applied over the RUC.

As a starting point, the principle of virtual displacements in continuum mechanics is expressed in incremental form as

$$\delta W_{ext} - \delta W_{int} = 0 \Rightarrow \delta V = \int_D \boldsymbol{\sigma} \cdot \delta \mathbf{E}_G dV = \mathbf{F}_e \cdot \delta \mathbf{u} \tag{2.37}$$

with W_{ext}, W_{int}, V, $\mathbf{E}_G$, $\mathbf{F}_e$ therein the virtual variation of the external and internal works, the total potential energy, the Green-Lagrange strain and the external applied force, respectively.

We next write the problem of nonlinear equilibrium linked to the large perturbations of the lattice. The nonlinearity is as a result of the large displacements and microrotations, which in turn are responsible for the large changes of beam directors orientation and beam lengths. Relying on this, we set up a kinematically driven

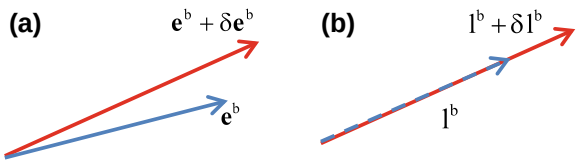

Fig. 2.17 Variation of the beam orientation (**a**) and length (**b**) (ElNady et al. 2016)

scheme which will be based on the incremental writing of the equilibrium equations of forces and moments, sequentially the two following equations:

$$
\begin{aligned}
&\forall \mathbf{v} \in R^3,\\
&\sum_{b\in \mathbf{B}_R} \left(\delta F_x^{\varepsilon b(k)} \mathbf{e}_x^{b(k)} + F_x^{\varepsilon b(k)} \delta \mathbf{e}_x^{b(k)}\right)\cdot \Delta \mathbf{v} + \sum_{b\in \mathbf{B}_R} \left(F_x^{\varepsilon b(k)} \mathbf{e}_x^{b(k)}\right)\cdot \Delta \mathbf{v}\\
&\quad + \sum_{b\in \mathbf{B}_R} \left(\delta F_y^{\varepsilon b(k)} \mathbf{e}_y^{b(k)} + F_y^{\varepsilon b(k)} \delta \mathbf{e}_y^{b(k)}\right)\cdot \Delta \mathbf{v} + \sum_{b\in \mathbf{B}_R} \left(F_y^{\varepsilon b(k)} \mathbf{e}_y^{b(k)}\right)\cdot \Delta \mathbf{v}\\
&\quad + \sum_{b\in \mathbf{B}_R} \left(\delta F_z^{\varepsilon b(k)} \mathbf{e}_z^{b(k)} + F_z^{\varepsilon b(k)} \delta \mathbf{e}_z^{b(k)}\right)\cdot \Delta \mathbf{v} + \sum_{b\in \mathbf{B}_R} \left(F_z^{\varepsilon b(k)} \mathbf{e}_z^{b(k)}\right)\cdot \Delta \mathbf{v} = 0\\
&\forall \mathbf{w} \in R^3,\ \sum_{b\in \mathbf{B}_R} \begin{pmatrix} \delta\left(M_x^{\varepsilon E(b)(k)} \mathbf{e}_x^{b(k)} + M_y^{\varepsilon E(b)(k)} \mathbf{e}_y^{b(k)} + M_z^{\varepsilon E(b)(k)} \mathbf{e}_z^{b(k)}\right)\cdot \mathbf{w}^{E(b)} + \\ \delta\left(M_x^{\varepsilon O(b)(k)} \mathbf{e}_x^{b(k)} + M_y^{\varepsilon O(b)(k)} \mathbf{e}_y^{b(k)} + M_z^{\varepsilon O(b)(k)} \mathbf{e}_z^{b(k)}\right)\cdot \mathbf{w}^{O(b)} \end{pmatrix}\\
&\quad + \sum_{b\in \mathbf{B}_R} \delta\left(\varepsilon L^b \left(\mathbf{e}_x \wedge \mathbf{F}^{\varepsilon b}\right)\right)\cdot \mathbf{w}^{C(b)} + \sum_{b\in \mathbf{B}_R} \left(M^{\varepsilon E(b)(k)}\cdot \mathbf{w}^{E(b)} + M^{\varepsilon O(b)(k)}\cdot \mathbf{w}^{O(b)}\right)\\
&\quad + \sum_{b\in \mathbf{B}_R} \left(\varepsilon l^b \left(\mathbf{e}_x \wedge \mathbf{F}^{\varepsilon b}\right)\cdot \mathbf{w}^{C(b)}\right) = 0
\end{aligned}
\tag{2.38}
$$

where $\Delta\mathbf{v} = \mathbf{v}(E_R(b)) - \mathbf{v}(O_R(b))$ is the relative virtual velocity of the two extremity nodes of any beam, and $\mathbf{w}$ is the virtual rotational velocity. Introducing the beam vector $\mathbf{B}^b = l^b \mathbf{e}_x^b$ (Fig. 2.17) with l^b the beam length and unit beam director, respectively, the quantities $l^b = \left\|\mathbf{B}^b\right\|$ and $\mathbf{e}_x^b = \frac{\mathbf{B}^b}{l^b}$.

For any beam in the lattice $b \in B_R$, the beam vector is evaluated from the imposed transformation gradient $\mathbf{G}^j$ and the relative position vector between the two extremity nodes, quantity $\mathbf{R}^{E_R(b)} - \mathbf{R}^{O_R(b)}$ as

$$
\mathbf{B}^b := \mathbf{R}^{E_R(b)} - \mathbf{R}^{O_R(b)} + \mathbf{G}^j \delta^{jb} \tag{2.39}
$$

In a similar manner, the relative microrotation $\boldsymbol{\varphi}^b$ is defined and expressed against the imposed microcurvature $\mathbf{M}$ as

$$
\boldsymbol{\varphi}^b := \boldsymbol{\varphi}^{E_{R(b)}} - \boldsymbol{\varphi}^{O_{R(b)}} = \left(\boldsymbol{\varphi}_1^{E_{R(b)}} - \boldsymbol{\varphi}_1^{O_{R(b)}} + \mathbf{M}^j \delta^{ib}\right) \tag{2.40}
$$

The following symbolizations are introduced: $\mathbf{G}^j = \frac{\partial \mathbf{R}}{\partial \beta^j}$, $\mathbf{M}^j = \frac{\partial \boldsymbol{\varphi}^0}{\partial \beta^j}$ are, respectively, the imposed mesoscopic transformation gradient and microcurvature mapping over the unit cell, and $\mathbf{R}^{\mathrm{E_R(b)}} - \mathbf{R}^{\mathrm{O_R(b)}}$ and $\boldsymbol{\varphi}_1^{\mathrm{E_R(b)}} - \boldsymbol{\varphi}_1^{\mathrm{O_R(b)}}$ are the unknowns kinematic relative positions and rotations; they are computed incrementally, as will be described afterward.

Insertion of the subsequent expressions of the increments of forces and moments into the incremental equilibrium (2.38) entails identification and extraction of the total tangent stiffness matrix $\mathbf{K}_\mathrm{T}$, which in turn is divided to the stress stiffness $\mathbf{K}_\mathrm{T}^\mathrm{S}$ and the micropolar stiffness $\mathbf{K}_\mathrm{T}^\mathrm{m}$. It is noticed that the stress stiffness leads to identify three type of stiffness matrices $\mathbf{K}_{\mathrm{So}}$, $\mathbf{K}_\mathrm{u}$, $\mathbf{K}_\sigma$, respectively, the linear stiffness matrix, the initial displacement stiffness matrix, and initial stress stiffness matrix; it is obtained as follows:

$$\mathbf{K}_\mathrm{T}^\mathrm{S} = \sum_{\mathrm{b}\in\mathbf{B}_\mathrm{R}} \left(\mathbf{K}_{\mathrm{So}}^\mathrm{b} + \mathbf{K}_\mathrm{u}^\mathrm{b} + \mathbf{K}_\sigma^\mathrm{b}\right) \tag{2.41}$$

For the micropolar nonlinear response, the tangent stiffness matrix is written as

$$\mathbf{K}_\mathrm{T}^\mathrm{m} = \sum_{\mathrm{b}\in\mathbf{B}_\mathrm{R}} \left(\mathbf{K}_{\mathrm{mo}}^\mathrm{b} + \mathbf{K}_\mathrm{m}^\mathrm{b}\right) \tag{2.42}$$

where $\mathbf{K}_{\mathrm{mo}}^\mathrm{b}$ is the initial micropolar stiffness matrix and $\mathbf{K}_\mathrm{m}^\mathrm{b}$ is the tangent micropolar stiffness matrix, which are next expressed.

We shall consider lattices which are much softer in bending in comparison to tension, so that we shall presently address geometrical nonlinearities, which are traduced by changes of beam orientation and length, pictured in Fig. 2.17.

These variations are obtained after straightforward calculations as follows:

$$\begin{aligned}
&\delta\mathbf{e}_\mathrm{x}^\mathrm{b} = \mathbf{C}\cdot\mathbf{P}\cdot\delta\mathbf{B}^\mathrm{b}/\mathrm{l}^\mathrm{b},\\
&\delta\mathbf{e}_\mathrm{y}^\mathrm{b} = \boldsymbol{\Omega}_\mathrm{z}\cdot\delta\mathbf{e}_\mathrm{x}^\mathrm{b},\ \delta\mathbf{e}_\mathrm{z}^\mathrm{b} = \boldsymbol{\Omega}_\mathrm{y}\cdot\delta\mathbf{e}_\mathrm{x}^\mathrm{b},\\
&\delta\mathrm{l}^\mathrm{b} = \mathbf{B}\cdot[\mathbf{I}+\mathbf{C}\cdot\mathbf{P}]\cdot\delta\mathbf{B}^\mathrm{b}/\mathrm{l}^\mathrm{b}
\end{aligned} \tag{2.43}$$

In (2.43), the projection operators $\mathbf{P}$ and $\mathbf{C}$ are expressed as

$$\mathbf{P} := \left(\mathbf{I} - \mathbf{e}_\mathrm{x}^\mathrm{b}\otimes\mathbf{e}_\mathrm{x}^\mathrm{b}\right),\ \mathbf{C} := \left(\mathbf{I} - \frac{1}{2}\mathbf{e}_\mathrm{x}^\mathrm{b}\otimes\mathbf{e}_\mathrm{x}^\mathrm{b}\right) \tag{2.44}$$

We also introduced the two orthogonal transformations:

$$\boldsymbol{\Omega}_\mathrm{z}\left(\mathbf{e}_\mathrm{x}^\mathrm{b}, \mathbf{e}_\mathrm{y}^\mathrm{b}, \mathrm{z}\right) = \begin{bmatrix} \cos\left(\frac{\pi}{2}\right) & -\sin\left(\frac{\pi}{2}\right) & 0 \\ \sin\left(\frac{\pi}{2}\right) & \cos\left(\frac{\pi}{2}\right) & 0 \\ 0 & 0 & 1 \end{bmatrix},\ \boldsymbol{\Omega}_\mathrm{y}\left(\mathbf{e}_\mathrm{x}^\mathrm{b}, \mathbf{e}_\mathrm{z}^\mathrm{b}, \mathrm{y}\right) = \begin{bmatrix} \cos\left(\frac{\pi}{2}\right) & 0 & \sin\left(\frac{\pi}{2}\right) \\ 0 & 1 & 0 \\ -\sin\left(\frac{\pi}{2}\right) & 0 & \cos\left(\frac{\pi}{2}\right) \end{bmatrix} \tag{2.45}$$

In the large strains regime, the beam length is changing, so we have to expand it versus the asymptotic expansion parameter ε like for all other static and kinematic variables:

$$l^b = l_0^b + \varepsilon\, l_1^b + \varepsilon^2 l_2^b + \cdots + \varepsilon^p l_p^b \tag{2.46}$$

The induced perturbations of the efforts and moments are then obtained as

$$\begin{aligned}
\delta F_x^{b(k)} \mathbf{e}_x^b &= \frac{1}{l^b}\frac{dF_x^{b(k)}}{dl^b}(\mathbf{B}^b \otimes \mathbf{B}^b[\mathbf{I}+\mathbf{C}\cdot\mathbf{P}])\cdot\delta\mathbf{B}^b \\
\delta F_y^{b(k)} \mathbf{e}_y^b &= \frac{1}{l^b}\frac{dF_y^{b(k)}}{dl^b}\left(\mathbf{e}_y^b \otimes \mathbf{B}^b[\mathbf{I}+\mathbf{C}\cdot\mathbf{P}]\right)\cdot\delta\mathbf{B}^b + \left(\frac{-6E_s^b I_z}{(l^b)^2}\right)\left[\left(\mathbf{e}_y^b\otimes\mathbf{e}_z^b\right)\cdot\delta\boldsymbol{\varphi}^{O(b)} + \left(\mathbf{e}_y^b\otimes\mathbf{e}_z^b\right)\cdot\delta\boldsymbol{\varphi}^{E(b)}\right] \\
\delta F_z^{b(k)} \mathbf{e}_z^b &= \frac{1}{l^b}\frac{dF_z^{b(k)}}{dl^b}(\mathbf{e}_z^b \otimes \mathbf{B}^b[\mathbf{I}+\mathbf{C}\cdot\mathbf{P}])\cdot\delta\mathbf{B}^b + \left(\frac{6E_s^b I_y}{(l^b)^2}\right)\left[\left(\mathbf{e}_z^b\otimes\mathbf{e}_y^b\right)\cdot\delta\boldsymbol{\varphi}^{O(b)} + \left(\mathbf{e}_z^b\otimes\mathbf{e}_y^b\right)\cdot\delta\boldsymbol{\varphi}^{E(b)}\right] \\
\delta M_x^O \mathbf{e}_x^b &= \left(\frac{G_s^b J^b}{l^b}\right)\left[\left(\mathbf{e}_x^b\otimes\mathbf{e}_x^b\right)\cdot\delta\boldsymbol{\varphi}^{O(b)} - \left(\mathbf{e}_x^b\otimes\mathbf{e}_x^b\right)\cdot\delta\boldsymbol{\varphi}^{E(b)}\right] \\
\delta M_x^E \mathbf{e}_x^b &= \left(\frac{G_s^b J^b}{l^b}\right)\left[\left(\mathbf{e}_x^b\otimes\mathbf{e}_x^b\right)\cdot\delta\boldsymbol{\varphi}^{E(b)} - \left(\mathbf{e}_x^b\otimes\mathbf{e}_x^b\right)\cdot\delta\boldsymbol{\varphi}^{O(b)}\right] \\
\delta M_y^O \mathbf{e}_y^b &= \frac{dM_y^O}{dl^b}(\mathbf{B}^b \otimes \mathbf{B}^b[\mathbf{I}+\mathbf{C}\cdot\mathbf{P}])\cdot\boldsymbol{\Omega}_z\cdot\delta\mathbf{B}^b + \left(\frac{E_s^b I_y^b}{l^b}\right)\left[4\left(\mathbf{e}_y^b\otimes\mathbf{e}_y^b\right)\cdot\delta\boldsymbol{\varphi}^{O(b)} - 2\left(\mathbf{e}_y^b\otimes\mathbf{e}_y^b\right)\cdot\delta\boldsymbol{\varphi}^{E(b)}\right] \\
\delta M_y^E \mathbf{e}_y^b &= \frac{dM_y^E}{dl^b}(\mathbf{B}^b \otimes \mathbf{B}^b[\mathbf{I}+\mathbf{C}\cdot\mathbf{P}])\cdot\boldsymbol{\Omega}_z\cdot\delta\mathbf{B}^b + \left(\frac{E_s^b I_y^b}{l^b}\right)\left[2\left(\mathbf{e}_y^b\otimes\mathbf{e}_y^b\right)\cdot\delta\boldsymbol{\varphi}^{E(b)} - 4\left(\mathbf{e}_y^b\otimes\mathbf{e}_y^b\right)\cdot\delta\boldsymbol{\varphi}^{O(b)}\right] \\
\delta M_z^O \mathbf{e}_z^b &= \frac{dM_z^O}{dl^b}(\mathbf{B}^b \otimes \mathbf{B}^b[\mathbf{I}+\mathbf{C}\cdot\mathbf{P}])\cdot\boldsymbol{\Omega}_y\cdot\delta\mathbf{B}^b + \left(\frac{E_s^b I_z^b}{l^b}\right)\left[4(\mathbf{e}_z^b\otimes\mathbf{e}_z^b)\cdot\delta\boldsymbol{\varphi}^{O(b)} - 2(\mathbf{e}_z^b\otimes\mathbf{e}_z^b)\cdot\delta\boldsymbol{\varphi}^{E(b)}\right] \\
\delta M_z^E \mathbf{e}_z^b &= \frac{dM_z^E}{dl^b}(\mathbf{B}^b \otimes \mathbf{B}^b[\mathbf{I}+\mathbf{C}\cdot\mathbf{P}])\cdot\boldsymbol{\Omega}_y\cdot\delta\mathbf{B}^b + \left(\frac{E_s^b I_z^b}{l^b}\right)\left[2(\mathbf{e}_z^b\otimes\mathbf{e}_z^b)\cdot\delta\boldsymbol{\varphi}^{E(b)} - 4(\mathbf{e}_z^b\otimes\mathbf{e}_z^b)\cdot\delta\boldsymbol{\varphi}^{O(b)}\right]
\end{aligned} \tag{2.47}$$

The total tangent stiffness matrix $\mathbf{K}_T^S = \sum_{b\in\mathbf{B}_R}\left(\mathbf{K}_{So}^b + \mathbf{K}_u^b + \mathbf{K}_\sigma^b\right)$, with $\mathbf{K}_{So}, \mathbf{K}_u, \mathbf{K}_\sigma$ therein, respectively, the linear stiffness, the initial displacement stiffness, and initial stress stiffness are expressed in closed form in the sequel. The linear stiffness receives the expression:

$$\mathbf{K}_{So}^b = \frac{E_S^b A^b}{l^b}\left(\mathbf{e}_x^b\otimes\mathbf{e}_x^b\right) + \left(\frac{12E_S^b I_y^b}{\left(l^b\right)^3}\right)\left(\mathbf{e}_y^b\otimes\mathbf{e}_y^b\right) + \left(\frac{12E_S^b I_z^b}{\left(l^b\right)^3}\right)\left(\mathbf{e}_z^b\otimes\mathbf{e}_z^b\right) \tag{2.48}$$

The initial displacement stiffness matrix is expressed as

$$\begin{aligned}
\mathbf{K}_u^b = \frac{E_S^b A^b}{L}\Bigg[&\left(\frac{1}{l^b}\right)\left(\mathbf{e}_x^b\otimes\left(\mathbf{B}^b-\mathbf{B}_o^b\right)\right)\cdot(\mathbf{C}\cdot\mathbf{P}) - \frac{(\mathbf{B}^b-\mathbf{B}_o^b)\cdot\mathbf{e}_x^b}{\left(l^b\right)^2}\left(\left(\mathbf{e}_x^b\otimes\mathbf{B}^b\right)\cdot[\mathbf{I}+\mathbf{C}\cdot\mathbf{P}]\right)\Bigg] \\
&+\left(\frac{12E_S^b I_y^b}{\left(l^b\right)^3}\right)\left[\left(\begin{array}{l}\left(\frac{1}{l^b}\right)\left(\mathbf{e}_y^b\otimes\left(\mathbf{B}^b-\mathbf{B}_o^b\right)\right)\cdot(\boldsymbol{\Omega}_z\cdot\mathbf{C}\cdot\mathbf{P}) - \\ \frac{(\mathbf{B}-\mathbf{B}_o^b)\cdot\mathbf{e}_y^b}{\left(l^b\right)^2}\left(\left(\mathbf{e}_y^b\otimes\mathbf{B}^b\right)\cdot[\mathbf{I}+\mathbf{C}\cdot\mathbf{P}]\right)\end{array}\right)\right]
\end{aligned}$$

$$+\left(\frac{12E_S^bI_z^b}{\left(l^b\right)^3}\right)\left[\left(\begin{array}{l}\left(\frac{1}{l^b}\right)\left(\mathbf{e}_z^b\otimes\left(\mathbf{B}^b-\mathbf{B}_o^b\right)\right)\cdot\left(\boldsymbol{\Omega}_y\cdot\mathbf{C}\cdot\mathbf{P}\right)-\\ \frac{\left(\mathbf{B}-\mathbf{B}_o^b\right)\cdot\mathbf{e}_z^b}{\left(l^b\right)^2}\left(\left(\mathbf{e}_z^b\otimes\mathbf{B}^b\right)\cdot[\mathbf{I}+\mathbf{C}\cdot\mathbf{P}]\right)\end{array}\right)\right] \tag{2.49}$$

The initial stress stiffness matrix is expressed as

$$\begin{aligned}\mathbf{K}_\sigma^b=&\left[\left(\frac{F_x^b}{l^b}\right)\mathbf{C}\cdot\mathbf{P}\right]+\left[\left(\frac{2F_y^b}{\left(l^b\right)^2}\right)\left(\left(\mathbf{e}_y^b\otimes\mathbf{B}^b\right)\cdot[\mathbf{I}+\mathbf{C}\cdot\mathbf{P}]\right)\right]\\&+\left[\left(\frac{2F_z^b}{\left(l^b\right)^2}\right)\left(\left(\mathbf{e}_z^b\otimes\mathbf{B}^b\right)\cdot[\mathbf{I}+\mathbf{C}\cdot\mathbf{P}]\right)\right]\\&+\left[\left(\frac{F_y^b}{l^b}\right)\left(\boldsymbol{\Omega}_z\cdot\mathbf{C}\cdot\mathbf{P}\right)\right]+\left[\left(\frac{F_z^b}{l^b}\right)\left(\boldsymbol{\Omega}_y\cdot\mathbf{C}\cdot\mathbf{P}\right)\right]\end{aligned} \tag{2.50}$$

Likewise, the tangent stiffness matrix for the micropolar nonlinear response is expressed as

$$\mathbf{K}_T^m=\sum_{b\in\mathbf{B}_R}\left(\mathbf{K}_{mo}^b+\mathbf{K}_m^b\right) \tag{2.51}$$

with the tangent coupled stress stiffness matrix therein given by

$$\begin{aligned}\mathbf{K}_{mo}^b=&\left(\frac{-6E_s^bI_y^b}{\left(l^b\right)^2}\right)\left(\mathbf{e}_y^b\otimes\mathbf{e}_z^b\right)+\left(\frac{-6E_s^bI_z^b}{\left(l^b\right)^2}\right)\left(\mathbf{e}_z^b\otimes\mathbf{e}_y^b\right)\\&+\left(\frac{E_s^bJ^b}{l^b}\right)\left(\mathbf{e}_x^b\otimes\mathbf{e}_x^b\right)+\left(\frac{E_s^bI_y^b}{l^b}\right)\left(\mathbf{e}_y^b\otimes\mathbf{e}_y^b\right)+\left(\frac{E_s^bI_z^b}{l^b}\right)\left(\mathbf{e}_z^b\otimes\mathbf{e}_z^b\right)\\\mathbf{K}_m^b=&\left[\left(\frac{M_x^{E(b)}}{l^b}\right)\mathbf{C}\cdot\mathbf{P}+\left(\frac{M_x^{O(b)}}{l^b}\right)\mathbf{C}\cdot\mathbf{P}\right]\\&+\left[\left(\frac{M_y^{E(b)}}{l^b}\right)\boldsymbol{\Omega}_z\cdot\mathbf{C}\cdot\mathbf{P}+\left(\frac{M_y^{O(b)}}{l^b}\right)\boldsymbol{\Omega}_z\cdot\mathbf{C}\cdot\mathbf{P}\right]\\&+\left[\left(\frac{M_z^{E(b)}}{l^b}\right)\boldsymbol{\Omega}_y\cdot\mathbf{C}\cdot\mathbf{P}+\left(\frac{M_z^{O(b)}}{l^b}\right)\boldsymbol{\Omega}_y\cdot\mathbf{C}\cdot\mathbf{P}\right]\end{aligned} \tag{2.52}$$

The left-hand side of Eqs. (2.39) and (2.40) contains both the imposed mesoscopic transformation gradient $\mathbf{G}^j=\frac{\partial\mathbf{R}^o}{\partial\beta^j}$ and the microcurvature $\mathbf{M}^j=\frac{\partial\boldsymbol{\varphi}^0}{\partial\beta^j}$ over the elementary unit cell, and the unknown differences of the kinematic quantities $\mathbf{R}^{E_R(b)}-\mathbf{R}^{O_R(b)}$ and $\boldsymbol{\varphi}^{E_R(b)}-\boldsymbol{\varphi}^{O_R(b)}$. We get the solution for these differences by solving iteratively the previous incremental scheme based on the method of modified Newton–Raphson.

The incremental scheme provides an update for the kinematic variables $\mathbf{B}^{b(k+1)}$, $\boldsymbol{\varphi}^{b(k+1)}$ at any iteration $(k+1)$, from their values at previous iteration k

within the reference unit cell. For a given imposed mesoscopic transformation gradient and microcurvature, respectively, the variables $\mathbf{G}^{\mathrm{j}}$, $\mathbf{M}^{\mathrm{j}}$, the update of the position, and microrotation vectors are written as follows:

$$\begin{aligned}
&\mathbf{B}^{\mathrm{b(k+1)}} = \mathbf{B}^{\mathrm{b(k)}} + \delta\mathbf{B}^{\mathrm{b(k)}},\\
&\text{with}\quad \mathbf{B}^{\mathrm{b(k)}} = \mathbf{R}^{\mathrm{E_R(b)(k)}} - \mathbf{R}^{\mathrm{O_R(b)(k)}} + \mathbf{G}^{\mathrm{j}}\delta^{\mathrm{jb}}\\
&\boldsymbol{\varphi}^{\mathrm{b(k+1)}} = \boldsymbol{\varphi}^{\mathrm{b(k)}} + \delta\boldsymbol{\varphi}^{\mathrm{b(k)}} \Rightarrow \boldsymbol{\varphi}^{\mathrm{b(k)}} = \boldsymbol{\varphi}^{\mathrm{E_R(b)(k)}} - \boldsymbol{\varphi}^{\mathrm{O_R(b)(k)}} + \mathbf{M}^{\mathrm{j}}\delta^{\mathrm{jb}}
\end{aligned} \tag{2.53}$$

For a given β^{ε} and for each $\frac{\partial \mathbf{R}}{\partial \beta^j}\delta^{jb}$, $\frac{\partial \boldsymbol{\varphi}}{\partial \beta^j}\delta^{jb}$, $j = 1, 2, 3$, we can determine the quantities $\mathbf{B}^b$, $\mathbf{e}_x^b$, $\mathbf{e}_y^b$, $\mathbf{e}_z^b$, F_x^b, F_y^b, F_z^b, M_x^b, M_y^b, M_z^b, for any $b \in \mathbf{B}_R$, allowing to calculate the stress and the couple stress vectors $\mathbf{S}^i$ and $\boldsymbol{\mu}^i$, respectively.

The mesoscopic incremental equations are next written at the continuum level of the lattice RUC.

Mesoscopic Equations over the Reference Unit Cell

Similar to the small displacements theory described in the previous subsection, the discrete equilibrium takes after homogenization a form similar to its continuum counterpart, viz.,

$$\sum_{v^{\mathrm{i}}\in Z^{\varepsilon}}\sum_{\mathrm{b}\in\mathbf{B}_{\mathrm{R}}} \mathbf{F}^{\mathrm{b}}\cdot\mathbf{v}^{\varepsilon} + \sum_{v^{\mathrm{i}}\in Z^{\varepsilon}}\sum_{\mathrm{b}\in\mathbf{B}_{\mathrm{R}}} \mathbf{M}^{\mathrm{b}}\cdot\mathbf{W}^{\varepsilon} = 0 \Rightarrow \int_{\Omega} \delta\mathbf{S}^{\mathrm{i(k)}}\cdot\frac{\partial \mathbf{v}}{\partial\beta^i}\mathrm{d}\beta + \int_{\Omega}\delta\boldsymbol{\mu}^{\mathrm{i(k)}}\cdot\frac{\partial\mathbf{w}}{\partial\beta^i}\mathrm{d}\beta = 0 \tag{2.54}$$

where $\delta\mathbf{S}^{\mathrm{i(k)}}$ and $\delta\mathbf{m}^{\mathrm{i(k)}}$ are, respectively, the incremental stress and couple stress vectors. The integral formulation in (2.54) constitutes the incremental variational form of the self-equilibrium posed over the Lagrangian domain Ω occupied by the reference unit cell.

We next aim to write the incremental constitutive law at the mesoscopic level. First, we recall a few needed symbols from nonlinear continuum mechanics. A generic particle occupies a reference position $\mathbf{X}$. When the body deforms due to prescribed tractions or displacements, the spatial position of the particle originally occupying the spatial position $\mathbf{X}$ is given by $\mathbf{x} = \mathrm{f}(\mathbf{X})$, with the function f supposed to be a smooth one-to-one point mapping. The displacement $\mathbf{u}(\mathbf{X})$ of the particle is defined by $\mathbf{u}(\mathbf{X}) = \mathrm{f}(\mathbf{X}) - \mathbf{X}$, and the deformation gradient elaborated as $\mathbf{F}(\mathbf{X}) = \nabla\mathrm{f}(\mathbf{X})$.

We shall perform kinematic-controlled loadings over the lattice unit cell; we impose at each increment the discretized version of $\mathbf{F}$, or the microcurvature, which is specific to each type of loading. We subsequently investigate the response of lattices under uniaxial tension, equibiaxial tension, simple shear, and bending. The kinematic load parameter is started at zero and incremented, and the equilibrium solution is computed at each increment; we shall in the sequel denote $\mathbf{n}$ the step number.

In the view of setting up the incremental scheme for the resolution of the non-linear mesoscopic BVP (boundary value problem), we shall in the sequel write the discretized version of the elastic constitutive equation between the incremental stress $\Delta\mathbf{S}_{\mathrm{n}}^{(\mathrm{k})}$ and the incremental strain $\Delta\mathbf{E}_{\mathrm{Gn}}^{(\mathrm{k})}$, and between the incremental couple stress $\Delta\mathbf{M}_{\mathrm{n}}^{(\mathrm{k})}$ and incremental curvature tensor $\Delta\boldsymbol{\Gamma}_{\mathrm{n}}^{(\mathrm{k})}$. These two increments are in fact imposed over the RUC as follows:

$$\Delta\mathbf{S}_{\mathrm{n}}^{(\mathrm{k})} = \mathrm{K}_{\mathrm{T,\,n}}^{\mathrm{S}} : \Delta\mathbf{E}_{\mathrm{Gn}}^{(\mathrm{k})},\ \Delta\mathbf{M}_{\mathrm{n}}^{(\mathrm{k})} = \mathrm{K}_{\mathrm{T,n}}^{\mathrm{m}} : \Delta\boldsymbol{\Gamma}_{\mathrm{n}}^{(\mathrm{k})} \tag{2.55}$$

The Green-Lagrange strain $\mathbf{E}_G$ in (2.55) is defined as $\mathbf{E}_G = \frac{1}{2}\left(\mathbf{F}^{\mathbf{T}} \cdot \mathbf{F} - \mathrm{I}\right)$. The natural Lagrangian wryness $\boldsymbol{\Gamma}$ is next expressed as versus the selected definition of the finite rotation vector written as $\boldsymbol{\varphi} = \varphi_i \mathbf{e}_i$, among other possible choices (Pietraszkiewicz and Eremeyev 2009). The natural Lagrangian wryness measure $\boldsymbol{\Gamma}$ written in the following second-order tensor:

$$\boldsymbol{\Gamma} = \mathrm{Grad}\boldsymbol{\varphi}\left[\frac{\sin(\|\boldsymbol{\varphi}\|)}{\|\boldsymbol{\varphi}\|}\mathbf{I} - \frac{1-\cos(\|\boldsymbol{\varphi}\|)}{\|\boldsymbol{\varphi}\|^2}\boldsymbol{\varphi}\times\mathbf{I} + \frac{\|\boldsymbol{\varphi}\| - \sin(\|\boldsymbol{\varphi}\|)}{\|\boldsymbol{\varphi}\|^3}\boldsymbol{\varphi}\otimes\boldsymbol{\varphi}\right] \tag{2.56}$$

The second-order identity tensor is denoted $\mathbf{I}$. One can rewrite this rotation by three successive rotations $\phi_x,\ \phi_y, \phi_z$ about the axes $x,\ y,\ z$.

For a given elementary loading characterized by a continuously varying scalar loading parameter λ_{n}, the incremental Lagrangian strain $\Delta\mathbf{E}_{\mathrm{Gn}}$ is related to the increment of the loading parameter λ_{n} and the increment $\Delta\mathbf{F}_{\mathrm{n}}$ as given in Holzapfel et al. (2000):

$$\Delta\mathbf{E}_{\mathrm{Gn}}(\lambda_{\mathrm{n}}, \Delta\lambda_{\mathrm{n}}) = \mathrm{sym}(\mathbf{F}_{\mathrm{n}}(\lambda_{\mathrm{n}}) \cdot \mathrm{grad}\Delta\mathbf{u}_{\mathrm{n}}) \equiv \mathrm{sym}(\mathbf{F}_{\mathrm{n}}(\lambda_{\mathrm{n}}) \cdot \Delta\mathbf{F}_{\mathrm{n}}(\Delta\lambda_{\mathrm{n}})) \tag{2.57}$$

together with the relation

$$\mathbf{F}_{\mathrm{n}}(\lambda_{\mathrm{n}}) = \mathrm{I} + \mathrm{grad}\mathbf{u}_{\mathrm{n}} \rightarrow \Delta\mathbf{F}_{\mathrm{n}}(\Delta\lambda_{\mathrm{n}}) = \Delta\mathrm{grad}\mathbf{u}_{\mathrm{n}} \equiv \mathrm{grad}\Delta\mathbf{u}_{\mathrm{n}} \tag{2.58}$$

The algorithmic tangent stiffness matrix $\mathbf{K}_{\mathrm{T,n}}^{\mathrm{S}}$ therein results from the assembly of the microscopic tangent stiffness matrices; it is obtained at each increment as given in relations (2.48) and (2.51). We recall that the stress increment $\Delta\mathbf{S}_{\mathrm{n}}^{(\mathrm{k})}$ is expressed versus the strain increment $\Delta\mathbf{E}_{\mathrm{Gn}}$ according to Eq. (2.55).

We next obtain the updated Cauchy stress tensor by a push forward of the incremental Lagrangian stress $\Delta\mathbf{S}_{\mathrm{n}}^{(\mathrm{k})}$ from configuration Ω_{n} to $\Omega_{\mathrm{n+1}}$, as

$$\boldsymbol{\sigma}_{\mathrm{n+1}}^{(\mathrm{k})} = \underbrace{\left(\mathrm{J}_{\mathrm{n}}^{-1}\mathbf{F}_{\mathrm{n}} \cdot \mathbf{S}_{\mathrm{n}}^{(\mathrm{k})} \cdot \mathbf{F}_{\mathrm{n}}^{\mathrm{T}}\right)}_{\boldsymbol{\sigma}_{\mathrm{n}}^{(\mathrm{k})}} + \underbrace{\left(\mathrm{J}_{\mathrm{n}}^{-1}\mathbf{F}_{\mathrm{n}} \cdot \left(\Delta\mathbf{S}_{\mathrm{n}}^{(\mathrm{k})}\right) \cdot \mathbf{F}_{\mathrm{n}}^{\mathrm{T}}\right)}_{\Delta\boldsymbol{\sigma}_{\mathrm{n}}^{(\mathrm{k})}} \tag{2.59}$$

with $\mathrm{J} := \det(\mathbf{F})$ the Jacobian, defined as the determinant of the deformation gradient tensor, k stands for iteration index which is inside the increment loop. The Cauchy stress at increment $\mathrm{n}+1$ is therefore given from its counterpart at previous increment

n, based on the initial stress $\mathbf{S}_n^{(k)}$ (the first contribution on the RHS of (2.59)) and the incremental stress $\Delta\boldsymbol{\sigma}_n^{(k)}$ (the second term on the RHS).

To obtain an update for the incremental couple stress tensor, we have to exploit a similar relation beforehand derived for the Cauchy stress

$$\mathbf{m}_{n+1}^{(k)} = \underbrace{\left(\bar{\mathbf{R}}_n \cdot \mathbf{M}_n^{(k)} \cdot \mathbf{F}_n^{T}\right)}_{\mathbf{m}_n^{(k)}} + \underbrace{\left(\bar{\mathbf{R}}_n \cdot \left(\Delta\mathbf{M}_n^{(k)}\right) \cdot \mathbf{F}_n^{T}\right)}_{\Delta\mathbf{m}_n^{(k)}} \tag{2.60}$$

with $\bar{\mathbf{R}}_n$ therein the micropolar rotation tensor. It is defined as $\bar{\mathbf{R}}_n = \exp(\mathrm{spn}(\boldsymbol{\varphi}))$ and expressed in closed form using the Euler–Rodrigues formula.

Within a specified type of loading (either imposed transformation gradient or microcurvature over the unit cell), one has to determine the adequate macroscopic displacement boundary conditions that have to be imposed over the RUC; this is next done for uniaxial tension, simple shear, equibiaxial tension, and bending considered as elementary loadings.

Additionally, in the linear situation, the internal bending lengths of the micropolar effective nonlinear continuum are evaluated from both the effective classical and micropolar tangent stiffness matrices. Then, these internal lengths are computed at each increment of the (incremental) scheme; an example shall be given later on in this work. The DH in large strains can be summarized in the algorithmic format as follows. The homogenized constitutive law is first evaluated in the linear framework. Then, we set up a kinematic driven algorithm by which, for each load increment, the incremental stress and couple stress tensors are computed versus the imposed mesoscopic loading (transformation gradient and microcurvature). The evolution of the kinematic and static quantities follows the update of the unit cell geometry.

In order to solve for the nodal displacements and microrotations unknowns of each beam within the repetitive unit cell, a dedicated code is constructed from the proposed algorithm. This code uses an input file the initial reference unit cell geometry and mechanical properties and delivers as an output the effective classical and micropolar moduli and stress–strain response for a given deformation path. The response is evaluated more specifically for each of the aforementioned elementary loadings. The algorithm is exposed as follows:

For each load increment $\Delta\mathbf{E}_{Gn}^{(k)}$, $\Delta\boldsymbol{\Gamma}_n^{(k)}$:
For each iteration k inside the increment loop:

1. Compute the effective mechanical properties in the linear regime based on the linear DH framework, Eq. (2.19).
2. Define the incrementally imposed strain and microcurvature applied over the RUC.
3. Compute the incremental second Piola-Kirchhoff stress tensor and couple stress tensor, Eq. (2.55).

4. Check convergence at iteration k; if it is attained, go to next step.
5. Compute the incremental deformation gradient, Eq. (2.58), and its Jacobian.
6. Update Cauchy stress and couple stress at increment (n + 1), by a push forward of their Lagrangian counterpart from Ω_n to Ω_{n+1}, Eqs. (2.59) and (2.60):
7. Update the network configuration from Ω_n to Ω_{n+1}.

In the next sections, different examples are exposed to illustrate the proposed computational method. We will compute the nonlinear mechanical response for dry woven textiles including 2D and 3D geometries.

Computed Response of Monolayers and 3D Interlocks

In the present section, we compute the nonlinear response of dry textile preforms which exhibit strong geometrical nonlinearities. In fact, several modeling approaches have been used to analyze the mechanical behavior of fabrics, which can be divided into analytical and numerical models. Many analytical models at the mesostructure level have been developed for the study of the behavior of dry woven fabrics (Goda et al. 2013a) and references therein. The literature survey done in ElNady et al. (2016) displays that FE analyses and analytical methods are powerful tools for studying the mechanical properties of woven fabrics. However, the complexity of the microstructure is proportional to the number of parameters controlling the mechanical properties. Therefore, in order to simplify the analysis, various assumptions should be proposed.

Nonlinear Response of Monolayer Fabrics

In order to be specific, plain weave and twill monolayer fabrics patterns are considered as representative examples of 2D preforms (Fig. 2.18). In this work, we construct and model the RUC of the monolayer fabric as a network of beams connected by nodes at cross points of the interwoven yarns within the fabric. These beams have extensional and flexural rigidities to represent yarn stretching and flexion. The interactions between yarns at the crossover points are captured by beam segments connecting the nodes. The proposed methodology is used for the analysis of monolayer fabrics subjected to large applied strains. The responses of stress–strain are assessed after applying boundary condition to the RUC, considering the following three elementary loading cases: uniaxial tension, biaxial tension, and simple shear.

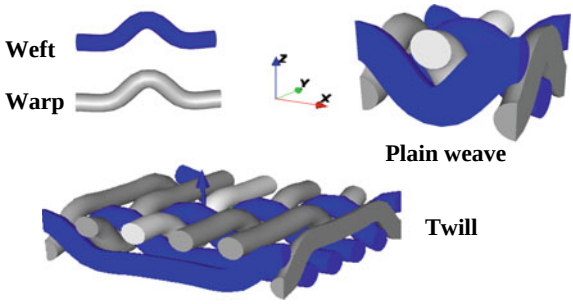

Fig. 2.18 Representative unit cells of plain weave and twill woven fabric (ElNady et al. 2016)

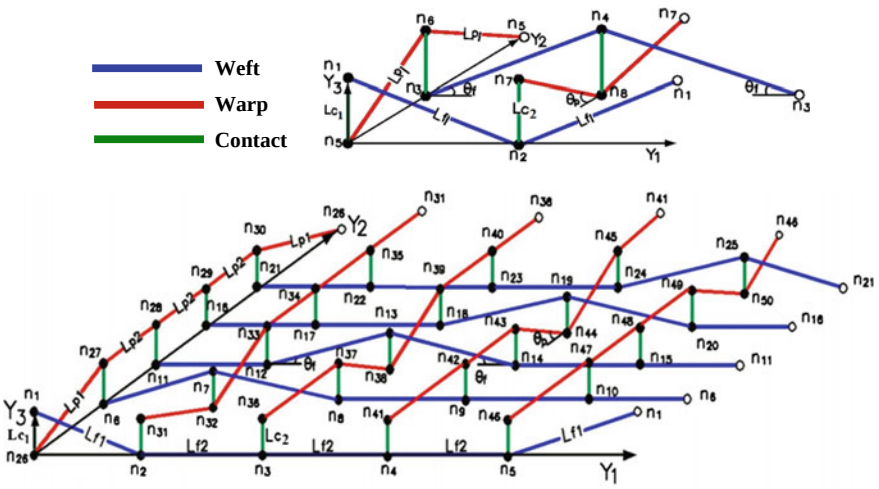

Fig. 2.19 Geometric representation of the unit cell of plain weave (top) and twill (bottom) (ElNady et al. 2016)

Most woven fabrics models are based on the definition of the geometry of the unit cell and include the main architectural parameters to evaluate the effective mechanical properties. The elementary cell is chosen as the smallest unit of fabric that, when tiled, will produce the full-scale fabric. The initial geometric model of the elementary cell is generated using the free- and open-source software TexGen. After that, the geometric files are exported to ABAQUS software where the FE analysis is subsequently done.

For the selected applications of (a) plain weave and (b) twill, the geometrical parameters for the unit cell pattern and the associated periodicity vectors are displayed in Fig. 2.19. The geometrical and mechanical parameters of these two fabrics are given, respectively, in Tables 2.7 and 2.8.

The elastic properties of the yarns of plain weave and twill unit cells are the same. The tensile, flexural, and torsion rigidities of the connected beams are exposed in Table 2.9.

Table 2.7 Geometrical parameters of plain weave and twill fabrics

Weave	Set of input geometric data required for modeling			
Plain				
Weft	$L_{f1} = 0.618$ mm	–	$\theta_f = 40°$	$d_f = 0.27$ mm
Warp	$L_{p1} = 0.56$ mm	–	$\theta_p = 40°$	$d_p = 0.25$ mm
Twill				
Weft	$L_{f1} = 0.618$ mm	$L_{f2} = 0.487$ mm	$\theta_f = 40°$	$d_f = 0.27$ mm
Warp	$L_{p1} = 0.56$ mm	$L_{p2} = 0.41$ mm	$\theta_p = 40°$	$d_p = 0.25$ mm

Table 2.8 Mechanical properties of weft and warp yarns

Set of input material data			
Weft	$E_{sf} = 1889$ MPa	$G_{sf} = 756$ MPa	$\nu_f = 0.25$
Warp	$E_{sp} = 13853$ Mpa	$G_{sp} = 5541$ Mpa	$\nu_p = 0.25$

Table 2.9 Tensile, bending, and torsional rigidities of weft, warp, and contact beams

Beam rigidity	Beams at		
	Weft	Warp	Contact
Tensile	$k_{lf_{1,2}} = \frac{E_{sf}A_f}{L_{f_{1,2}}}$	$k_{lp_{1,2}} = \frac{E_{sp}A_p}{L_{p_{1,2}}}$	$k_{lc_{1,2}} = \frac{E_{sc}A_c}{L_{c_{1,2}}}$.
Flexural	$k_{tf1} = \frac{12E_{sf}I_f}{(L_{f1})^3}$	$k_{tp1} = \frac{12E_{sp}I_p}{(L_{p1})^3}$	$k_{tc_{1,2}} = \frac{12E_{sc}I_c}{\left(L_{c_{1,2}}\right)^3}$
Torsional	$k_{rf1} = \frac{G_{sf}J_f}{L_{f1}}$	$k_{rp1} = \frac{G_{sp}J_p}{L_{p1}}$	$k_{rc_{1,2}} = \frac{G_{sc}J_c}{L_{c_{1,2}}}$

Moreover, for the contact beam, the geometric and material parameters are as follows: $L_{c_{1,2}} = Lf_1 Sin\theta_f, Lp_1 Sin\theta_p$, $r_c = \frac{r_f + r_p}{2}$, $G_{sc} = \frac{G_{sf}+G_{pf}}{2}$, and $E_{sc} = \frac{E_{sf}+E_{pf}}{2}$, where $L_{c1,2}$, r_c, G_{sc}, and E_{sc}, respectively, stand for the lengths, radius, shear, and Young's modulus of beams connecting the warp and weft yarns at their crossing points.

Small strains DH schemes were developed in Goda et al. (2014) to compute the effective mechanical properties of textiles monolayers, with the stiffness matrix components expressed in terms of the material and microstructural geometric parameters. The DH approach as detailed in section "Large Configuration Changes of Lattices Based on Discrete Homogenization Method" has been implemented for the two types of woven fabric. Analyses of periodic reinforcements modeled as RUC are implemented within a dedicated code considering the impact of a variation of the structure geometry simultaneously in a nested manner. We next perform a comparison between the mechanical response of plain weave and twill fabrics under three different types of loading (uniaxial tension, biaxial tension, and simple shear).

Uniaxial tensile test: We illustrate in Fig. 2.20 a comparison between the Cauchy stress response versus stretch under a uniaxial tensile loading test, for both plain weave and twill fabrics. The initial effective tensile rigidities in the weft direction

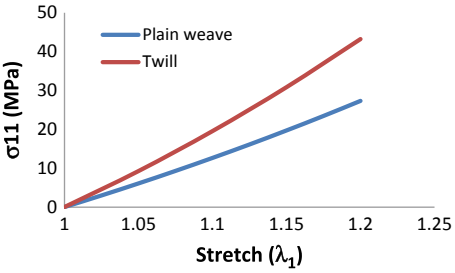

Fig. 2.20 Evolutions of Cauchy stress against stretch for plain weave and twill fabric (ElNady et al. 2016)

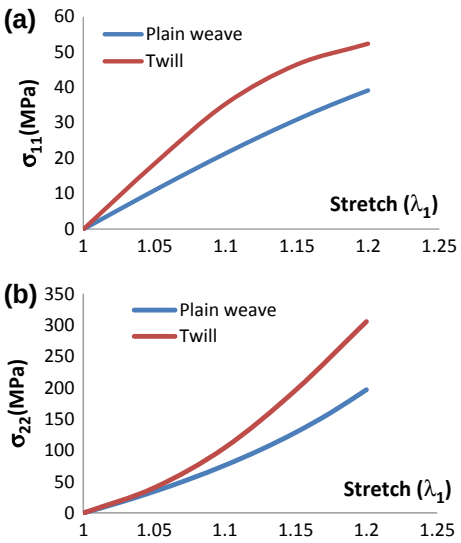

Fig. 2.21 Comparison between Cauchy stress evolutions versus stretch for plain weave and twill in **a** x-direction and **b** y-direction versus strain with a biaxial strain ratio equal to two (ElNady et al. 2016)

are, respectively, 113.5 MPa and 170.4 MPa for plain weave and twill. The most stiff response obtained for twill can be explained by the fact that yarns within the representative unit cell are more aligned in the direction of traction; we anticipate this tendency to be valid for any loading.

Biaxial tensile test: We perform the biaxial tension simulation by applying a strain in the longitudinal direction of warp and weft yarns. The biaxial strain ratio shall be defined as $\varepsilon_2/\varepsilon_1$, with ε_1 the primary textile strain corresponding to weft direction, and ε_2 the secondary strain in warp direction. The comparison of the biaxial response for plain weave and twill configuration is shown in Fig. 2.21. Twill pattern shows as for uniaxial tension a stiffer response.

Simple shear test: For both fabric types, the shear response shows nearly the same trend up to a shear strain of 0.15, with a small difference occurring for large strains, as shown in Fig. 2.22. This can be explained by the fact that the initial yarn crimp does not play an important role in simple shear; this is contrary to uniaxial loading conditions.

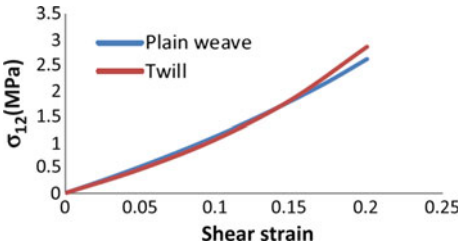

Fig. 2.22 Large shear response for plain weave and twill (ElNady et al. 2016)

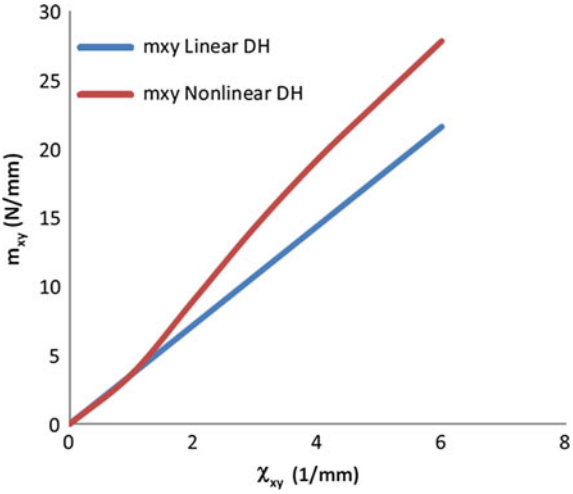

Fig. 2.23 Nonlinear and linear responses of the couple stress versus microcurvature for twill fabric (ElNady et al. 2016)

Bending test: In this test, bending is applied to the twill fabric by imposing an increasing microcurvature over the representative unit cell; the incremental bending response is then computed based on the incremental scheme exposed in section "Large Configuration Changes of Lattices Based on Discrete Homogenization Method". Note that although we perform a pure bending test, we need to solve both the equilibrium equations of forces and moments (see Fig. 2.23). Since we shall focus on bending applied along one coordinate axis, a straightforward computation shows that the natural Lagrangian wryness expressed in (2.56) simplifies to $\mathbf{\Gamma}_n(\beta_n) = \mathrm{Grad}(\boldsymbol{\varphi}_n)$. As an illustration, we compute the out-of-plane bending response of twill performed over its representative unit cell. The small bending stiffness which is needed to initiate the nonlinear bending computations is related to the linearized curvature ($\chi_{xy} = \partial\varphi_y/\partial x$) by

$$m_{xy} = K^m_{T,xy}\,\chi_{xy} \tag{2.61}$$

We then evaluate the internal bending length for twill pattern from the computed effective rigidities by the expression built from the ratio of the tangent bending modulus to the summation of the corresponding tangent shear moduli as follows:

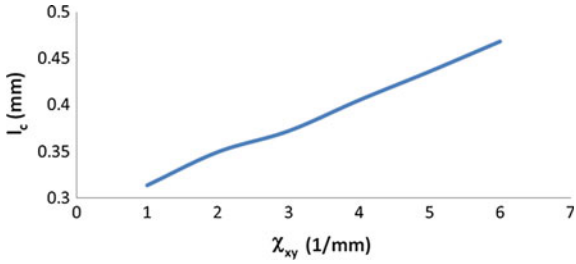

Fig. 2.24 Characteristic length of twill versus curvature (ElNady et al. 2016)

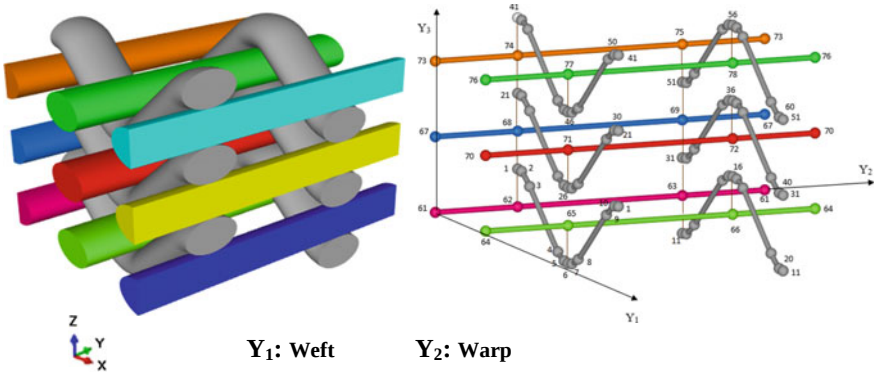

Fig. 2.25 Schematic representations of 2.5D layer-to-layer angle interlock: RUC (left) and geometrical model of an elementary cell (right) (ElNady et al. 2016)

$$l_c = \sqrt{\left(K^m_{T,xy}/2\left(K^S_{T,xz} + K^S_{T,yz}\right)\right)} \tag{2.62}$$

Figure 2.24 shows a linear increase of the characteristic length versus the applied curvature. The components of the tangent stiffness therein evolve versus the imposed curvature based on the effective constitutive law under bending, relation (2.61).

The next section is devoted to the computation of the large strains response of 2.5D layer-to-layer angle interlock preform.

Large Strain Response of 2.5D Layer-to-Layer Interlock

The homogenization method is quite general to be applicable for any networks having a periodical architecture. In view of this generalization, a 3D textile multilayer is analyzed. We consider as specific structures textile multilayer fabrics patterns, viz., 2.5D layer-to-layer angle interlock. In the same way, an RUC of the 3D fabric is constructed and modeled as a network of beams connected by nodes at cross points of the interwoven yarns within the fabric (Fig. 2.25).

Table 2.10 2.5D layer-to-layer interlock yarn geometrical parameters

	Width (mm)	Thickness (mm)
Weft	0.25	0.15
Warp	0.25	0.15

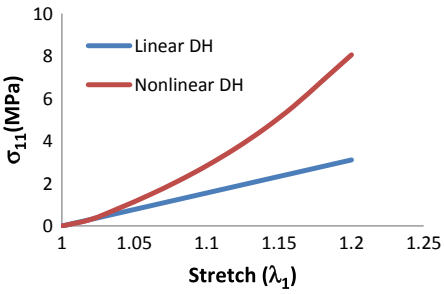

Fig. 2.26 Evolution of Cauchy stress versus stretch for 2.5D layer-to-layer interlock (ElNady et al. 2016)

The material data for the plain weave and twill, which are used to define the material parameter for the 2.5D interlock RUC, are provided in Tables 2.8 and 2.9. The entire geometry of the unit cell is constructed based on the geometrical parameters as summarized in Table 2.10.

The proposed DH method is used to analyze the deformation of the 2.5D layer-to-layer interlock which will be subjected to uniaxial and equibiaxial loading tests. Similarly, we plot the Cauchy stress component versus the corresponding stretch (see Fig. 2.26). Results of uniaxial tension in warp direction depict an essential difference between the linear and the geometrical nonlinear analysis.

The response of 2.5D layer-to-layer interlock fabric under equibiaxial tension is displayed in Fig. 2.27, in terms of the evolution of Cauchy stress components along x and y.

The noticeable nonlinearity of the response along x reveals the change of crimp of the yarn which tends to align in this direction as the stretch level is increased (for both uniaxial and biaxial tensions). On the opposite, since the transverse yarn is initially straight, it does not produce geometrical nonlinearities, as one can deduce from the rather linear response observed in Fig. 2.27b. Such behavior obviously demonstrates geometrical nonlinearities present in these fabric structures.

Comparison of the Responses from DH with FE Simulations

We here make evident the practicality of the unit cell approach in FE analyses to calculate the uniaxial, biaxial, and shear mechanical responses accounting for large configuration changes. A comparison to FE results in targets to evaluate the effectiveness and exactness of the DH approach. The FE method consists in determining

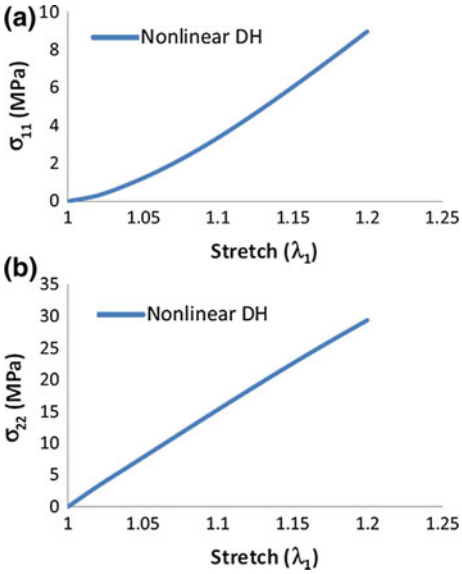

Fig. 2.27 Cauchy stress of **a** x-direction and **b** y-direction versus stretch for 2.5D layer-to-layer interlock (ElNady et al. 2016)

the overall effective nonlinear mechanical response over an RUC of the considered fabric structure, relying on an FE discretization of the unit cell geometry.

The homogenized nonlinear responses previously obtained for the considered fabric structures plain weave, twill, and 2.5D layer-to-layer interlock are validated by comparing the evolution of stresses with those obtained, thanks to FE computations implemented over the corresponding RUC.

FE Validation of the Nonlinear Responses of Plain Weave and Twill Fabrics

In the present section, 3D FE models of woven fabrics at mesostructure are developed to evaluate the accuracy of the homogenized mechanical properties predicted from DH. The FE model is capable of simulating elementary cells under simultaneous axial loadings along both yarn directions. The previous results for the stress–strain response obtained with the DH technique are now compared with numerical results obtained from the FE method (ABAQUS), under the specified types of loadings (we restrict the validation of the computed response to uniaxial and biaxial tests), with appropriate boundary conditions. The warp and weft yarns are meshed with the eight-node solid linear hexahedral element (ABAQUS element-type C3D8). We use a total of 14,804 elements to model the balanced plain weave fabric. To account for the possible relative displacements between the yarns, a contact with friction is considered with a master/slave approach. Contact is considered to be an intrinsic character of woven fabrics which cannot be neglected during the meso-level analysis. Contact conditions are prescribed between the possible interlacing surfaces of the

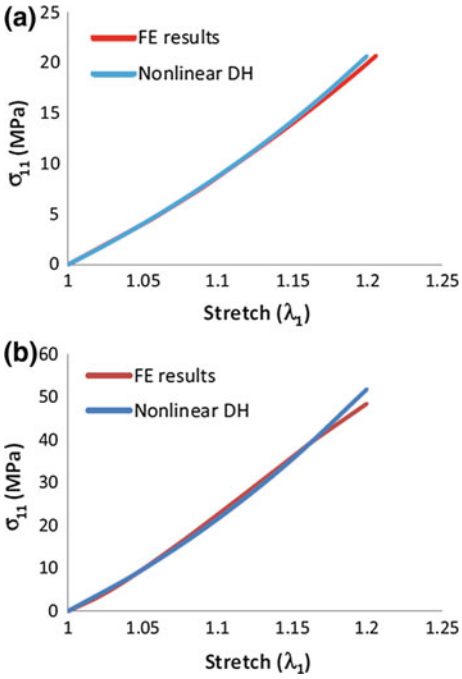

Fig. 2.28 Comparison of the uniaxial tensile response for **a** balanced plain weave **b** twill between the DH method and FE simulations (ElNady et al. 2016)

yarns under loading and are the same for all loading cases. The tangential behavior at the contact surfaces in the frame of Coulomb friction model is defined using the penalty method with a friction coefficient selected as 0.05.

The uniaxial response for the balanced plain weave is depicted in Fig. 2.28a. A good agreement is obtained using both methods (DH and FE simulations), with a maximum discrepancy close to 1.41% in the uniaxial test for the considered unit cell of plain weave (Fig. 2.28a), and close to 6% at 20% for twill submitted to uniaxial strain (Fig. 2.28b).

The distribution of displacement over the RUC for both plain weave and twill patterns are displayed in Fig. 2.29.

Validation of the Homogenized Nonlinear Response of 3D Textile Structures

The stress–strain responses obtained with the DH method are validated with FE computations implemented under the specified types of loadings (uniaxial and equibiaxial) applied on the RUC of 2.5D layer-to-layer interlock (Fig. 2.30).

The displacement distributions over the RUC of the 2.5D layer-to-layer interlock under both uniaxial and biaxial testing conditions are given in Fig. 2.31.

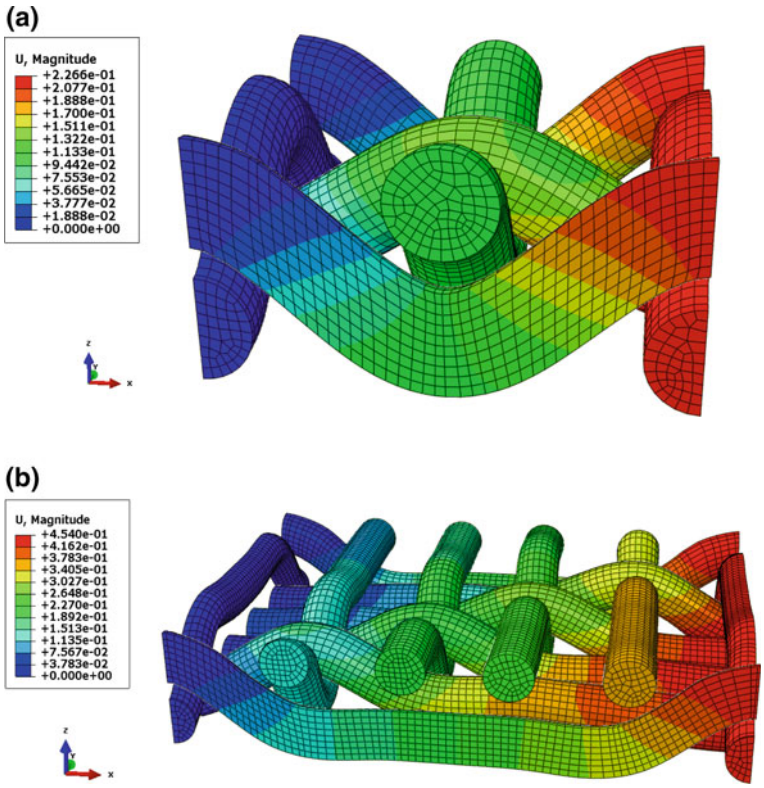

Fig. 2.29 Displacement distributions over **a** balanced plain weave **b** twill subjected to a uniaxial test in x-direction (ElNady et al. 2016)

The difference of about 15% at 20% strain is observed between the response computed by DH and FE simulations. This is possibly due to the choice of the contact beam rigidities. Accordingly, we next perform a sensitivity analysis to asses the influence of the contact beam rigidities including tensile, flexural, and torsional rigidities on the overall behavior of the 2.5D layer-to-layer angle interlock. The range of variation of the contact beam rigidity is selected to be 0.1–10 times the longitudinal beam rigidity. The evolutions of the x component of the Cauchy stress versus stretch obtained with the DH technique are compared with FE results, under an equibiaxial loading, for five values of the flexural rigidity of the contact beams.

The computations demonstrate that the tensile and torsion rigidities of the contact beams have relatively small influence on the nonlinear response. On the contrary, a variation of the flexural rigidity shows a noteworthy effect, with the percentage of different variations between DH and FE results from 13.31 to 2.89% for the Cauchy stress in x-direction and from 14 to 9.52% for the stress in y-direction, as illustrated in Fig. 2.32.

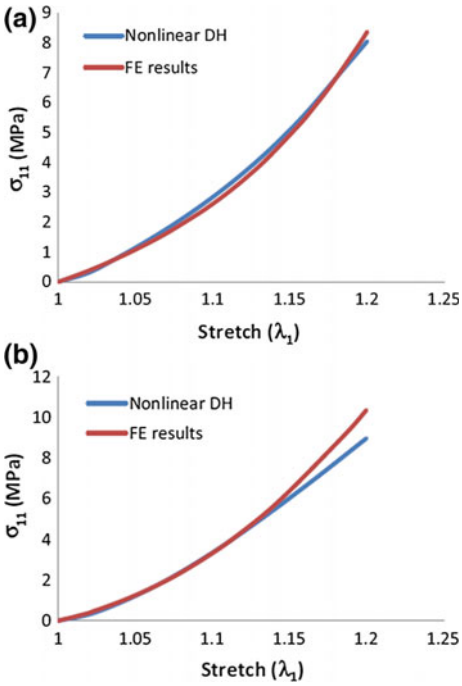

Fig. 2.30 Comparison of **a** the uniaxial tensile response and **b** the equibiaxial tensile response for the 2.5D layer-to-layer interlock between the DH method and FE simulations (ElNady et al. 2016)

Regarding the computation cost of the employed DH method compared to FE computations, considering to be specific the 2.5D layer-to-layer interlock is explained as follows: the computational time is much reduced with the DH method (about 10 min) compared to FE computations (1 h on the same machine). This reduction of the computation cost is essentially due to the strong reduction of the number of degrees of freedom, within the RUC for the DH method, in comparison with the FE computations.

Identification of Hyperelastic Models for Textile Monolayers

Since the DH method is predictive, it can be conceived as a virtual testing method to provide a database of responses in different loading conditions (uniaxial, equibiaxial, shear) to identify a strain energy density for an assumed hyperelastic effective homogeneous material. The nonlinear response of such networks can be captured by either hypoelastic or hyperelastic models; the former, however, may suffer from a well-known fictitious hysteresis (Holzapfel et al. 2000, 2002); thus, one shall presently instead adopt a hyperelastic modeling framework.

The selected strain energy density is expressed versus the two relative stretches in the global coordinate system λ_1, λ_2 and the shear angle ϑ according to

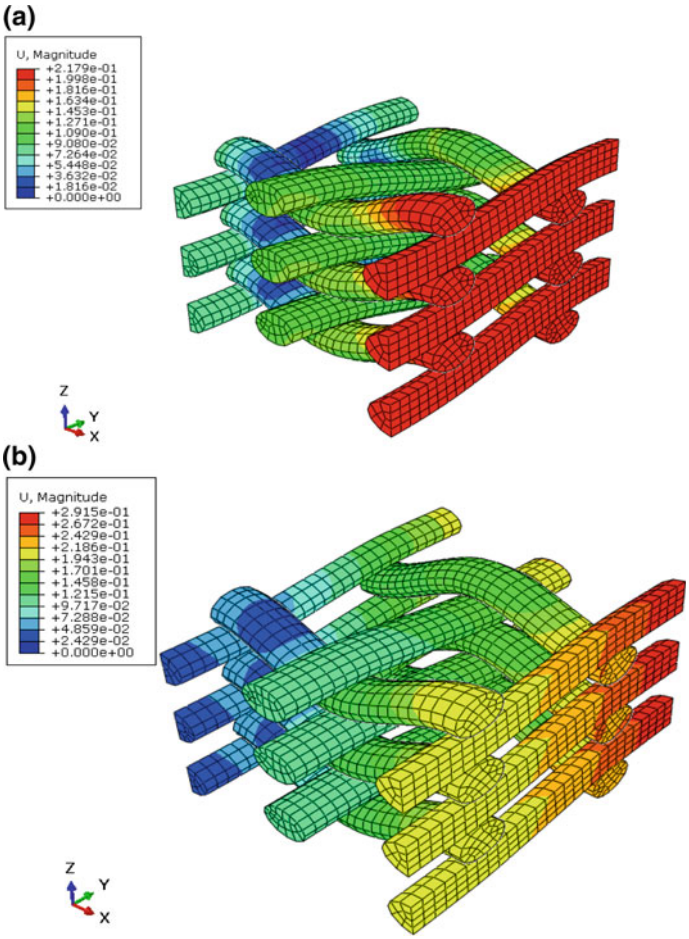

Fig. 2.31 Displacement field within the 2.5D layer-to-layer interlock due to **a** uniaxial extension in x-direction **b** equibiaxial extension in xy-direction (ElNady et al. 2016)

$$\tilde{W} = \sum_{\alpha=0}^{m} \frac{1}{\alpha+2} a_\alpha \left(\lambda_1^{\alpha+2} - 1\right) + \sum_{\beta=0}^{n} \frac{1}{\beta+2} b_\beta \left(\lambda_2^{\beta+2} - 1\right) + \\ + \sum_{\gamma=1}^{p} \frac{1}{\gamma+1} c_\gamma \cos^{\gamma+1} \vartheta + k_{r1} \lambda_1 \lambda_2 + k_{r2} (\lambda_1 \lambda_2)^2 \tag{2.63}$$

where a_α, b_β, c_γ, k_{r1}, k_{r2} are the set of material parameters to be identified. It shall be noticed that the two coefficients k_{r1}, k_{r2} therein are required to introduce a dependency of the two stress components S_{11}, S_{22} versus both stretches. The second Piola-Kirchhoff stress is then formally obtained from the previous density as

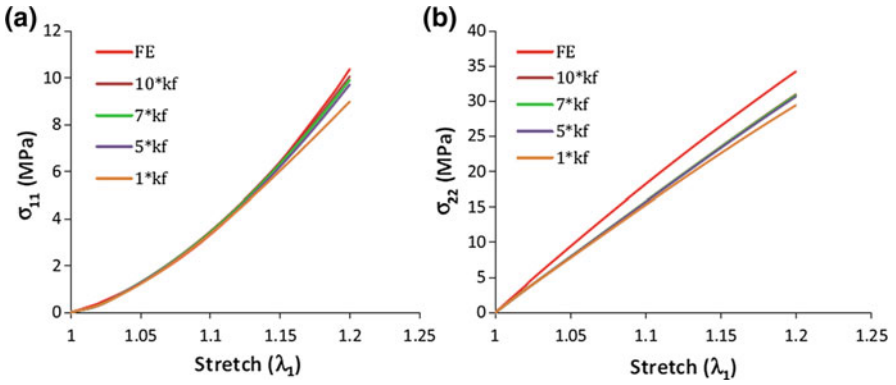

Fig. 2.32 Effect of the flexural rigidity of the contact beam on the tensile stress–strain response from nonlinear discrete homogenization in comparison with FE simulations (ElNady et al. 2016)

$$\mathbf{S} = 2\frac{\partial \widetilde{\mathrm{W}}}{\partial \mathbf{C}} = 2\left[\frac{\partial \widetilde{\mathrm{W}}}{\partial \lambda_1}\frac{\partial \lambda_1}{\partial \mathbf{C}} + \frac{\partial \widetilde{\mathrm{W}}}{\partial \lambda_2}\frac{\partial \lambda_2}{\partial \mathbf{C}} + \frac{\partial \widetilde{\mathrm{W}}}{\partial \cos\vartheta}\frac{\partial \cos\vartheta}{\partial \mathbf{C}}\right] \tag{2.64}$$

Previous expression leads to the three independent stress components

$$\begin{aligned}
S_{11} &= \left(\frac{1}{\lambda_1}\left[\sum_{\alpha=0}^{m} a_\alpha\left(\lambda_1^{\alpha+1}\right) + k_{r1}(\lambda_2) + 2k_{r2}\left(\lambda_1\lambda_2^2\right)\right] - \frac{\cos\theta}{\lambda_1^2}\left[\sum_{\gamma=0}^{p} c_\gamma\ \cos^\gamma\theta\right]\right)\\
S_{22} &= \left(\frac{1}{\lambda_2}\left[\sum_{\beta=0}^{n} b_\beta\left(\lambda_2^{\beta+1}\right) + k_{r1}(\lambda_1) + 2k_{r2}\left(\lambda_2\lambda_1^2\right)\right] - \frac{\cos\theta}{\lambda_2^2}\left[\sum_{\gamma=0}^{p} c_\gamma\ \cos^\gamma\theta\right]\right)\\
S_{12} &= \frac{1}{\lambda_1\lambda_2}\left[\sum_{\gamma=0}^{p} c_\gamma\ \cos^\gamma\theta\right]
\end{aligned} \tag{2.65}$$

The material parameters are identified based on a combination of virtual tensile, equibiaxial, and simple shear tests performed over the unit cell of the considered unit cell of twill (so that a sufficiently rich database of responses is produced); their identification proceeds from the minimization of the following functional with respect to the set of parameters a_α, b_β, c_γ, k_{r1}, k_{r2}:

$$\begin{aligned}
&\underset{a_\alpha, b_\beta, c_\gamma, k_{r1}, k_{r2}}{\mathrm{Min}}\ \mathrm{S}^{\mathrm{e}}\left(a_\alpha, b_\beta, c_\gamma, k_{r1}, k_{r2}\right) :=\\
&\left\{\left\|\mathbf{S}_{11}^{\mathrm{DH}} - \mathbf{S}_{11}\right\|^2 + \left\|\mathbf{S}_{22}^{\mathrm{DH}} - \mathbf{S}_{22}\right\|^2 + \left\|\mathbf{S}_{12}^{\mathrm{DH}} - \mathbf{S}_{12}\right\|^2\right\}^{1/2}
\end{aligned} \tag{2.66}$$

The function $\mathrm{S}^{\mathrm{e}}\left(a_\alpha, b_\beta, c_\gamma, k_{r1}, k_{r2}\right)$ is built as the quadratic measure of the error between the DH stress components and their analytical counterpart, obtained from

Table 2.11 Optimal material parameters of the potential function for multiple deformation modes. Units in MPa

a_1	a_2	a_3	b_1	b_2	b_3	k_{r1}	k_{r2}	c_1	c_2	c_3
−340.2	−101.2	197.8	674.6	−999.1	−271.9	360.4	−58.49	8.81	7.7	99.1

the hyperelastic potential. Note that it is necessary to incorporate therein the stresses obtained from the three considered deformation modes simultaneously, so that the identified strain energy density has the capability to properly describe the response of the networks under different loadings not based on these used for the identification of the strain energy density in (2.66). The stress responses are adjusted with a third-order polynomial, using the least square procedure in the Matlab toolbox.

In order to exemplify the methodology, the strain energy density is identified for the 2D structures textile monolayer fabrics patterns, namely, twill. The response of this structure is computed under uniaxial tension (applied in weft and warp directions), biaxial tension, and simple shear load tests. The stress–strain responses obtained from the nonlinear DH technique for those loadings are illustrated in Fig. 2.33 together with their third-order polynomial adjustments. The material constants of the model are identified from a least square method (nine sampling points are used), using uniaxial tension, biaxial tension (with strain ratio k = 2), and simple shear as loading tests, as shown below. A function *Lsqcurvefit* in the Optimization Toolbox of MATLAB has been used. The identified optimal parameters of the strain energy function are recorded in Table 2.11.

Based on the identified hyperelastic strain energy density for the twill tows, we predict the response of the twill structure under an equibiaxial test; an excellent agreement is obtained between the stress–strain results determined from discrete homogenization and those computed based on the strain energy function (Fig. 2.34).

Generalized Continuum Models of Random Fibrous Networks

Nature exhibits a large diversity of materials presenting a stochastic fibrous microstructure, building highly complex, and multifunctional parts. Protein, for instance, is frequently found in nature in a fibrous form; the most abundant fibrous protein in mammals is collagen, which constitutes the major part of tendons and ligaments, and most of the organic matrix in bone and dentin. It confers mechanical stability, strength, and toughness of these tissues (Fratzl 2008). The structural characteristics of random fibrous networks depend upon the properties of the fibers, and thus their modeling is necessary in order to understand the mechanism of deformation and failure on system subscale, due to the difficulty of measuring the in situ deformation mechanisms of the fibrous microstructure. The tradeoff between local axial stretching and bending deformations of the fibers has an important impact on

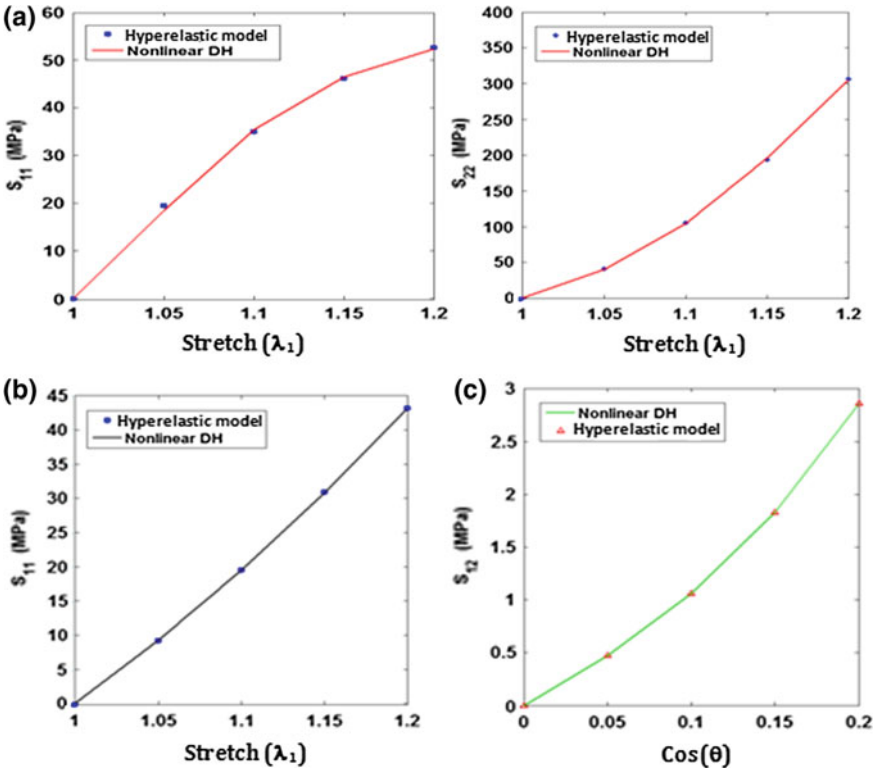

Fig. 2.33 Second Piola-Kirchhoff stress components for **a** biaxial tension (k = 2) **b** uniaxial tension in weft direction **c** simple shear responses evaluated from nonlinear discrete homogenization and from the hyperelastic model (ElNady et al. 2016)

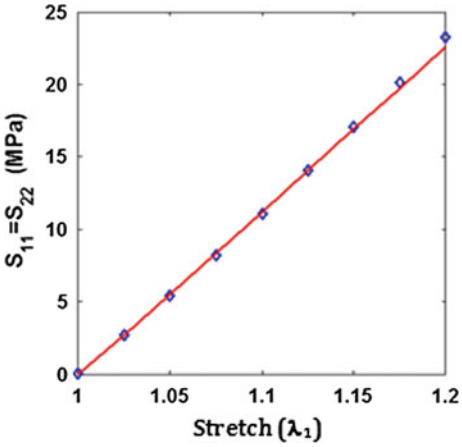

Fig. 2.34 Second Piola-Kirchhoff stress components from nonlinear discrete homogenization (solid line) and equivalent response computed from the hyperelastic model (dots) (ElNady et al. 2016)

the overall mechanical response; especially, the response of the network to imposed deformations is likely to be non-affine, the degree of non-affinity being controlled by the fiber bending length, a scalar quantity which quantifies the relative importance of the bending to the stretching stiffness, as pointed out in Hatami-Marbini and Picu (2008, 2009), who evidenced that the network shifts from the non-affinely deforming structure to an affinely deforming one by increasing the fiber bending length. In Shahsavari and Picu (2013) and Lee and Jasiuk (1995), the authors further concluded that the degree of heterogeneity decreases by increasing the network density; one of the most important results as to scale effects is that the heterogeneity leads to a strong dependency of the apparent moduli on the size of the probed network domain; this has been modeled in Hatami-Marbini and Picu (2008) by evaluating the correlation functions of the tensile modulus versus window size. As described in Lee and Jasiuk (1995), models in the literature developed to simulate the mechanical behavior of fibrous networks fall into two main categories, namely, phenomenological models and micromechanical models. Micromechanical models overcome the shortcomings of the phenomenological models, which very often are not able to capture the relation of the fiber properties to the model parameters. The primary focus of micromechanically based constitutive models of nonwoven fibrous networks is the elastic behavior. Cox (1952) was one of the first authors to propose a model for the elastic modulus of paper based on the mechanics of the fiber network, with all fibers extending from one end of the mat to the other, and assuming stretching of the fibers as the dominant deformation mechanism. However, since fibers have a relatively low stiffness and are randomly oriented, bending is an important feature, particularly in the absence of a supporting medium (Petterson 1959; Wu and Dzenis 2005).

Generation of Random Fibrous Networks RVEs

According to the criteria identified in Kallmes and Corte (1960), we consider random structures to be a special class of stochastic fibrous networks and classify a random process as one where the events are independent of each other and equally likely.

The generated random network consists of finite fibers distributed with a random orientation, each passing through a point distributed according to a Poisson point process in a plane. Many fibrous networks are very close to being two-dimensional because the dimensions perpendicular to their plane are very small relative to the in-plane dimensions. Here, we consider systems of 2D networks in which the fibers are of uniform length L_0 and are deposited on squared regions of dimensions L. A typical fibrous network generated under the abovementioned conditions is displayed in Fig. 2.35.

The mutual interactions of fibers be responsible for the network connectivity; its nonuniformity can be captured by the fiber number density N which is defined as the number of fiber centers per unit area or rather the density of network, scalar quantity $D = NL_0$, within different windows of linear size L occupying a much bigger network. The window size is taken large enough in all simulations to avoid any scale

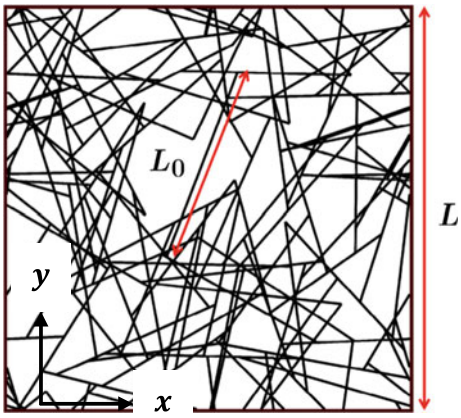

Fig. 2.35 Typical window of analysis (WOA) for a random fibrous network (Berkache et al. 2018)

effect. In fact, we checked numerically that the homogenized moduli are stable when we increase the window size. In practice, window sizes such that the ratio $L/L_0 > 10$ are selected. The cross-links are introduced at all points where fibers intersect, at which the coordination number is $z = 4$; they are here modeled as welded, so that the fibers are loaded both axially and in bending. The angle between intersecting fibers is preserved and leads to a transfer of the bending moments between fibers. Numerical computations with welded joints type are more stable than those with pin joints type, as discussed in Shahsavari and Picu (2013). Nevertheless, computations point out that there is no influence on the type of interactions (welded or free) on the homogenized classical and nonclassical moduli.

Computation of the Homogenized Properties Based on Couple Stress Continua

The deformation of random fibrous networks is extremely non-affine (the motion of the fibers do not follow the imposed strain over the boundary of the WOA), especially for such structures that store energy predominantly in the bending deformation mode of fibers (Hatami-Marbini and Picu 2008). The degree of non-affinity increases rapidly with decreasing bending stiffness of the filaments, the importance of which being quantified by the internal bending length $l_b = \sqrt{E_f I / E_f A}$, a parameter elaborated from the ratio of the fiber bending modulus to its axial stiffness, where E_f is the fiber tensile modulus, I is the quadratic moment of inertia, and A is the fiber section area. Increasing the level of heterogeneity leads to more pronounced size effects, which have deserved previous works (Hatami-Marbini and Picu 2008). Size effects can be computed by generalized continuum theories, as it has been demonstrated for a wide class of materials in the literature, including biomaterials (Goda et al. 2013b, 2014; ElNady et al. 2016).

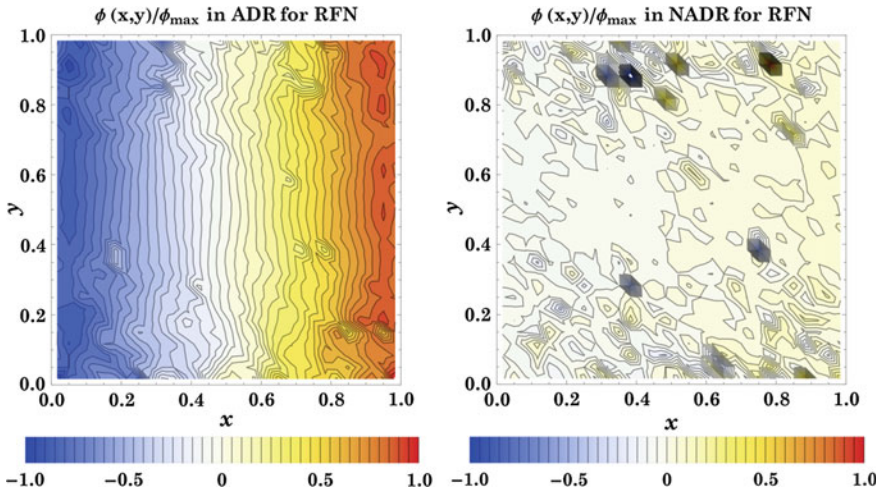

Fig. 2.36 Distribution of the rotation field in the affine and non-affine deformation regime inside the WOA of a random fibrous network subjected to bending (Berkache et al. 2018)

The rotation field inside the WOA of a random network submitted to pure bending in FE simulations (in the small strains regime) is reconstructed from the discrete fiber rotations, as depicted in Fig. 2.36, in both affine and non-affine regimes. The abbreviations ADR and NADR are used here to represent the affine deformation regime and non-affine deformation regime, respectively. The rotation field is normalized by maximum value $\phi_{\max}$ in each regime of deformation. The fiber rotation shows a nearly uniform gradient in the affine deformation regime (left view in Fig. 2.36), since it is controlled by the flexion applied to the boundary of the WOA, whereas the rotation field clearly does not follow the kinematics of the boundary for the non-affine situation (right view in Fig. 2.36). The presence of pronounced microrotations and their gradients therefore motivates the identification of a couple stress substitution medium for the initial discrete random fibrous network.

In the theory of micropolar, the deformation is defined by the displacement vector **u** and an independent rotation vector ϕ, whereas in the couple stress theory, the rotation vector ϕ is not independent from the displacement vector, since it is identified as the antisymmetric part of the displacement gradient. This leads in the present 2D context to the expression of the microrotation around the z-axis as

$$\phi = \frac{1}{2}\left(\frac{\partial v}{\partial x} - \frac{\partial u}{\partial y}\right) \tag{2.67}$$

Based on couple stress theory in a 2D plane stress condition, the stress tensor has four independent components $\sigma_{xx}, \sigma_{yy}, \sigma_{xy}, \sigma_{yx}$ and the couple stress tensor has two components m_{xz}, m_{yz}. The four independent deformation components and the two

independent microcurvature components κ_{xz}, κ_{yz} are expressed versus the displacement gradients and the microrotation as follows:

$$\varepsilon_{xx} = \frac{\partial u}{\partial x},\ \varepsilon_{yy} = \frac{\partial v}{\partial y},\ \varepsilon_{xy} = \frac{\partial v}{\partial x} - \phi,\ \varepsilon_{yx} = \frac{\partial u}{\partial y} + \phi; \kappa_{xz} = \frac{\partial \phi}{\partial x}, \kappa_{yz} = \frac{\partial \phi}{\partial y} \quad (2.68)$$

Due to of the kinematic coupling (2.67) in the couple stress theory, the strain tensor ε_{ij} is symmetrical with components defined as

$$\varepsilon_{xy} = \varepsilon_{yx} = \frac{1}{2}\left(\frac{\partial v}{\partial x} + \frac{\partial u}{\partial y}\right) \quad (2.69)$$

The dynamical equilibrium in translation and rotation after ignoring body forces and body moments is written as

$$\frac{\partial \sigma_{xx}}{\partial x} + \frac{\partial \sigma_{xy}}{\partial y} = 0,\ \frac{\partial \sigma_{yx}}{\partial x} + \frac{\partial \sigma_{yy}}{\partial y} = 0,\ \frac{\partial m_{xz}}{\partial x} + \frac{\partial m_{yz}}{\partial y} + \sigma_{xy} - \sigma_{yx} = 0 \quad (2.70)$$

The balance equation of internal bending momentum (2.70) implies the equality of both shear stress components $\sigma_{xy} = \sigma_{yx}$. Therefore, the constitutive equation for a centrally symmetric unit cell structure can be expressed in the following uncoupled form:

$$\begin{Bmatrix} \sigma_{xx} \\ \sigma_{yy} \\ \sigma_{xy} \\ m_{xz} \\ m_{yz} \end{Bmatrix} = \begin{pmatrix} A_{11} & A_{12} & 0 & 0 & 0 \\ A_{12} & A_{22} & 0 & 0 & 0 \\ 0 & 0 & A_{33} & 0 & 0 \\ 0 & 0 & 0 & D_{11} & 0 \\ 0 & 0 & 0 & 0 & D_{22} \end{pmatrix} \begin{Bmatrix} \varepsilon_{xx} \\ \varepsilon_{yy} \\ \varepsilon_{xy} \\ \kappa_{xz} \\ \kappa_{yz} \end{Bmatrix} \quad (2.71)$$

in which the coefficients A_{ij} are the classical moduli, and coefficients D_{ij} are the micropolar moduli that relate the two independent non-nil couple stress components to the corresponding curvatures. The effective Young's moduli can be expressed versus coefficients A_{ij} as

$$E_x = A_{11} - \frac{A_{12}^2}{A_{22}},\ E_y = A_{22} - \frac{A_{12}^2}{A_{11}} \quad (2.72)$$

Moreover, the effective Poisson ratios are computed as

$$\nu_{xy} = \frac{A_{12}}{A_{22}} \text{ and } \nu_{yx} = \frac{A_{12}}{A_{11}} \quad (2.73)$$

The main objective of this section is then to determine the effective constitutive constants of the couple stress continuum from the response of random fibrous networks within the WOA of different sizes. We design different boundary condi-

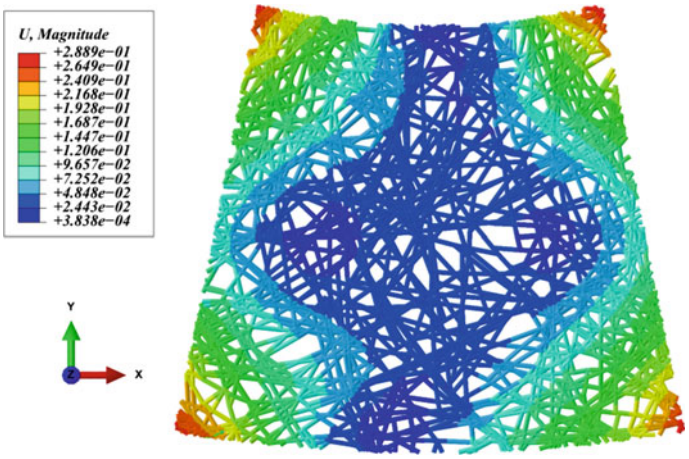

Fig. 2.37 Displacement distributions corresponding to boundary conditions applied to determine the effective constitutive coefficient D_{11} (Berkache et al. 2018)

tions for the identification of the independent components of the constitutive elastic constants over a domain Ω with boundary $\partial\Omega$. An example of the deformed shape of the WOA subjected to in-plane bending for the identification of a couple stress coefficient is shown in Fig. 2.37 based on the following boundary conditions $u = -xy,\ v = x^2/2,\ \text{on}\ \partial\Omega$. For each test, we force the WOA to bear a set of specific deformation, as described in Berkache et al. (2018), and compute numerically the total elastic strain energy U_{WOA} stored in the WOA under the corresponding boundary conditions.

To identify the effective elastic constants, we follow the same procedures as used in Goda et al. but here restricted to a 2D situation. In this approach, the total strain energy stored in the WOA is equated to the energy of an equivalent homogeneous couple stress continuum as follows:

$$U_{WOA} = U_{couple-stress} = \frac{V}{2}\left[\varepsilon_{ij}A_{ijkl}\varepsilon_{kl} + \kappa_{ij}D_{ijkl}\kappa_{kl}\right] \tag{2.74}$$

where V is the volume of the WOA. The strain energy stored in the effective homogeneous couple stress continuum can be obtained by the prescribed strain/stress fields. The fiber bending length is defined as the ratio between the axial stiffness to the bending stiffness, parameter $l_b = \sqrt{E_f I/E_f A}$. In Figs. 2.38 and 2.39, we plot in logarithmic scales the evolution of the Cauchy and couple stress moduli versus the fiber bending length l_b, for a constant network density. Low values of l_b enhance local rotations of the fibers, which do not follow the imposed deformation over the boundary of the window of analysis, and thus the network responds essentially in a non-affine manner; opposite to this, high values of l_b lead to a rather affine response, while intermediate l_b values correspond to the transition regime. The variation of

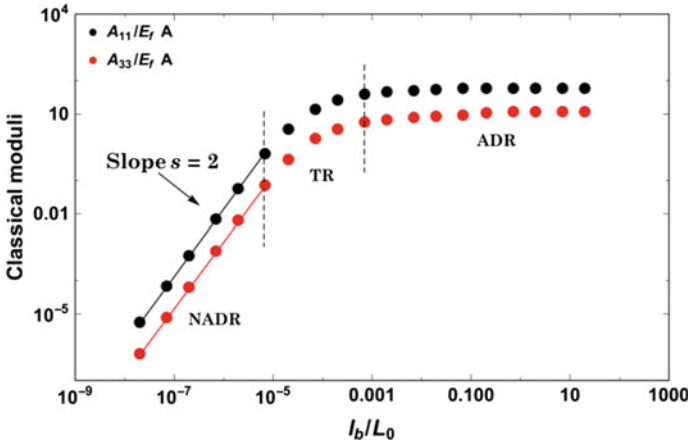

Fig. 2.38 Evolution of classical elastic constants versus normalized fiber bending length l_b/L_0 for a constant normalized network density (Berkache et al. 2018)

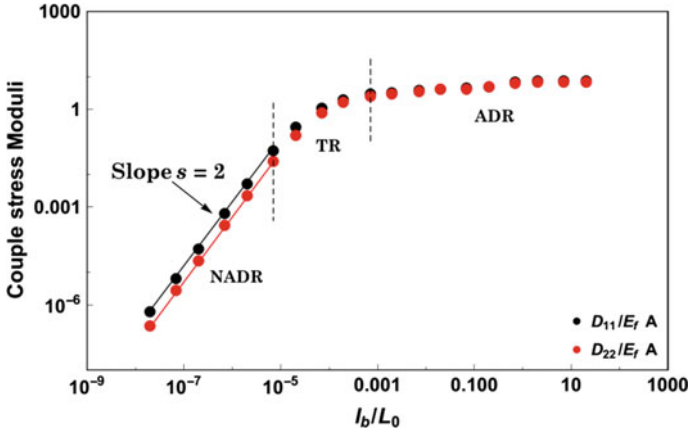

Fig. 2.39 Evolution of couple stress moduli versus normalized fiber bending length l_b/L_0 for a constant normalized network density $DL_0 = 75$ (Berkache et al. 2018)

two out of the four classical moduli with l_b (A_{11} and A_{33}) is shown in Fig. 2.38; the vertical axis is normalized with the tensile rigidity of the fibers, quantity $E_f A$, and the horizontal axis is normalized by the fiber length L_0. In these computations, the network density is kept constant at $DL_0 = 75$. It is noticed that the variable in the horizontal axis is proportional to the aspect ratio of fibers $\frac{l_b}{L_0} \propto \frac{d}{L_0}$, where d is the fiber diameter. The transition from affine to non-affine regimes is controlled by a number of parameters: l_b, the network density D which is inversely proportional to the distance between cross-links $\bar{l} = \frac{\pi}{2D}$, and the coordination number z (Shahsavari and Picu 2012; Onck et al. 2005).

For large l_b/L_0 values, the classical moduli are proportional to $E_f A$, and thus the strain energy is stored predominantly in the axial deformation mode of fibers and the deformation field is approximately affine. At small l_b/L_0 ratio, the classical moduli are proportional to the mechanical parameter $E_f A\left(\frac{l_b}{L_0}\right)^s \alpha\, E_f I$, and accordingly the strain energy is stored predominantly in the bending deformation mode of fibers and the deformation is non-affine. Figure 2.39 shows the variation of couple stress moduli D_{11} and D_{22}; interestingly, the nonclassical moduli exhibit the same behavior as the classical moduli. Additionally, the transition from ADR to NADR happens in the same range of values of the ratio l_b/L_0.

The influence of large strains developed by random fibrous networks and the consideration of time-dependent effects due to the viscoelastic properties of the fibers on wave propagation are important aspects encountered in real situations that shall be investigated in future contributions.

Summary and Future Work

The development of suitable micromechanical schemes for the computation of the effective mechanical response of fibrous materials is quite important, in order to have at hand predictive models to analyze the overall computed response in terms of the underlying microscopic mechanisms. When a RUC can be identified for a quasi-periodic fibrous network, it is possible to develop specific homogenization schemes relying on the assumption of inherent periodicity. Although a lot of attention has been devoted to replacing fibrous large-scale structures by effective continuum models, less attention has been paid to the consideration of both geometrical nonlinearities and microstructure effects leading to generalized continua at the continuum level.

We presently extended the linear discrete asymptotic homogenization framework to the nonlinear setting, based on an update of the lattice geometry and elastic computations done incrementally under a kinematic control. A novel procedure for predicting the effective nonlinear elastic responses of these repetitive lattices through a combined linear and nonlinear discrete homogenization scheme has been presented. The nonlinear stress–strain response has been analyzed incrementally for different 2D and 3D structures under different loading cases including uniaxial, biaxial, simple shear, and bending, taking into consideration changes of the structure geometry. The combination of the incremental scheme with the homogenization method delivers both the classical and nonclassical properties; especially, the micropolar framework allows deriving the bending response. These theoretical developments have been implemented into a dedicated code using the lattice geometry and microstructural properties as an input, and delivering as an output the effective response in the nonlinear range at the mesoscopic continuum level of the RUC. These nonlinear homogenization schemes have been applied to meso-level analyses of the mechanical behavior of textile monolayers, 2.5D layer-to-layer interlock to construct their effective anisotropic micropolar continuum response at the mesoscopic level.

The proposed micromechanical approach is particularly appealing, due to the difficulty to measure such effective properties for textiles considering their discreteness. The proposed homogenization technique proves efficient from a numerical point of view, and it has a great versatility as to the topology of the textile armor, which makes it a suitable tool to explore and compare in future developments various textile architectures for both single and multilayer 3D configurations in terms of their mechanical performances. More generally speaking, the potentiality and versatility of the method shall enable to compute the mechanical response of architectured materials having a repetitive microstructure and assess intrinsic microstructural effects in the framework of effective generalized continua.

References

Aublin, M., Boncompain, R., Boulatonm M., Caron, D., Jeay, E., & Lacage, B. (1998). *Systemes mecaniques. Theorie et dimensionnement*. Paris: Dunod.

Berkache, K., Deogekar, S., Goda, I., Ganghoffer, J. F., & Picu, K. (2018). Identification of equivalent couple-stress continuum models for planar random fibrous media. *Continuum Mechanics and Thermodynamics*. https://doi.org/10.1007/s00161-018-0710-2.

Chaouachi, F., Rahali, Y., & Ganghoffer, J. F. (2014). A micromechanical model of woven structures accounting for yarn-yarn contact based on Hertz theory and energy minimization. *Composite Part B: Engineering, 66,* 368–380.

Cox, D. R. (1952). The inter-fibre pressure in slivers confined in rectangular grooves. *Journal of the Textile Institute, 43,* 87.

Dixit, A., Mali, H. S., & Misra R. K. (2013). Unit cell model of woven fabric textile composite for multiscale analysis. In *The Malaysian International Tribology Conference (MITC2013). Procedia Engineering, 68,* 352–358.

Dos Reis, F., & Ganghoffer, J. F. (2012). Construction of micropolar continua from the asymptotic homogenization of beam lattices. *Computers & Structures, 112–113,* 354–363.

ElNady, K., Goda, I., & Ganghoffer, J. F. (2016). Computation of the effective nonlinear mechanical response of lattice materials considering geometrical nonlinearities. *Computational Mechanics, 58*(6), 957–979.

Feyel, F., & Chaboche, J.-L. (2000). FE2 multiscale approach for modelling the elastoviscoplastic behaviour of long fibre SiC/Ti composite materials. *Computer Methods in Applied Mechanics and Engineering, 183*(3), 309–330.

Fratzl, P. (2008). *Collagen: Structure and mechanics*. Springer.

Goda, I., Assidi, M., & Ganghoffer, J. F. (2013a). Equivalent mechanical properties of textile monolayers from discrete asymptotic homogenization. *Journal of the Mechanics and Physics of Solids, 61*(12), 2537–2565.

Goda, I., Assidi, M., & Ganghoffer, J. F. (2014). A 3D elastic micropolar model of vertebral trabecular bone from lattice homogenization of the bone microstructure. *Biomechanics and Modeling in Mechanobiology, 13*(1), 53–83.

Goda, I., & Ganghoffer, J.-F. (2015). Identification of couple-stress moduli of vertebral trabecular bone based on the 3D internal architectures. *Journal of the Mechanical Behavior of Biomedical Materials, 51,* 99–118.

Goda, I., Rahouadj, R., & Ganghoffer, J.-F. (2013b). Size dependent static and dynamic behavior of trabecular bone based on micromechanical models of the trabecular. *International Journal of Engineering Science, 72,* 53–77.

Goda, I., Rahouadj, R., Ganghoffer, J.-F., Kerdjoudj, H., & Siad, L. (2016). 3D couple-stress moduli of porous polymeric biomaterials using μCT image stack and FE characterization. *International Journal of Engineering Science, 100,* 25–44.

Hatami-Marbini, H., & Picu, R. C. (2008). Scaling of nonaffine deformation in random semiflexible fiber networks. *Physical Review E, 77,* (062103).

Hatami-Marbini, H., & Picu, R. C. (2009). An eigenstrain formulation for the prediction of elastic moduli of defective fiber networks. *European Journal of Mechanics A/Solids, 28,* 305–316.

Holzapfel, G. A., Gasser, T. C., & Ogden, R. W. (2000). A new constitutive framework for arterial wall mechanics and a comparative study of material models. *Journal of Elasticity, 61,* 1–48.

Holzapfel, G. A., Gasser, T. C., & Stadler, M. (2002). A structural model for the viscoelastic behavior of arterial walls: Continuum formulation and finite element analysis. *European Journal of Mechanics A/Solids, 21,* 441–463.

Kallmes, O., & Corte, H. (1960). The structure of paper. I. The statistical geometry of an ideal two dimensional fiber network. *Tappi Journal, 43,* 737–752.

Lee, Y., & Jasiuk, I. (1995). Apparent elastic properties of random fiber networks. *Computational Materials Science, 79,* 715–723.

Mourad, A., Caillerie, D., & Raoult, A. (2003). A nonlinearly elastic homogenized constitutive law for the myocardium. In *Computational fluid and solid mechanics* (pp. 1779–1781).

Onck, P. R., Koeman, T., Van Dillen, T., & Van der Giessen, E. (2005). Alternative explanation of stiffening in cross-linked semiflexible networks. *Physical Review Letters, 95,* 178102.

Petterson, D. (1959). Mechanics of nonwoven fabrics. *Journal of Industrial and Engineering Chemistry, 51*(8), 902–903.

Pietraszkiewicz, W., & Eremeyev, V. A. (2009). On natural strain measures of the non-linear micropolar continuum. *International Journal of Solids and Structures, 46*(3), 774–787.

Rahali, Y., Goda, I., & Ganghoffer, J. F. (2016). Numerical identification of classical and non-classical moduli of 3D woven textiles and analysis of scale effects. *Composite Structures, 135,* 122–139.

Sab, K., & Pradel, F. (2009). Homogenisation of periodic Cosserat media. *International Journal of Computer Applications in Technology, 34,* 60–71.

Sanchez-Palencia, E. (1980). Non-inhomogeneous media and vibration theory. In *Lecture notes in physics* (Vol. 127). Berlin, New York: Springer.

Shahsavari, A., & Picu, R. (2012). Model selection for athermal cross-linked fiber networks. *Physical Review E, 86*, (011923).

Shahsavari, A., & Picu, R. C. (2013). Size effect on mechanical behavior of random fiber networks. *International Journal of Solids and Structures, 50,* 3332–3338.

Trovalusci, P., & Masiani, R. (1999). Material symmetries of micropolar continua equivalent to lattices. *International Journal of Solids and Structures, 36,* 2091–2108.

Vigliotti, A., Deshpande, V. S., & Pasini, D. (2014). Non linear constitutive models for lattice materials. *Journal of the Mechanics and Physics of Solids, 64,* 44–60.

Warren, W. E., & Byskov, E. (2002). Three-fold symmetry restrictions on two-dimensional micropolar materials. *European Journal of Mechanics A/Solids, 21,* 779–792.

Wu, X. F., & Dzenis, Y. A. (2005). Elasticity of planar fiber networks. *Journal of Applied Physics, 98*(093501), 1–9.

Younes, R., & Zaki, W. (2011). Optimal weaving for 2.5D interlocks. *Composite Structures, 93*(4), 1255–1264.

Chapter 3
Heuristic Homogenization of Euler and Pantographic Beams

Luca Placidi, Francesco dell'Isola and Emilio Barchiesi

Abstract In the present contribution, we address the following problem: is it possible to find a microstructure producing, at the macro-level and under loads of the same order of magnitude, a beam which can be both extensible and flexible? Using an asymptotic expansion and rescaling suitably the involved stiffnesses, we prove that a pantographic microstructure does induce, at the macro-level, the aforementioned desired mechanical behavior. Thus, in an analogous fashion to that of variational asymptotic methods, and following a mathematical approach resembling that used by Piola, we have employed asymptotic expansions of kinematic descriptors directly into the postulated energy functional and a heuristic homogenization procedure is presented and applied to the cases of Euler and pantographic beams.

Introduction

While in the standard finite deformation Euler beam theory the energy functional depends only on the material curvature, i.e., the normalized projection of the second gradient of the placement on the normal vector to the current configuration, the energy functional for the nearly inextensible pantographic beam model depends also on the projection of the second gradient of the placement on the tangent vector to the current configuration. Thus, the full decomposition of the second gradient of the placement is present in the latter model. In order to analyze this fact, a heuristic homogenization

L. Placidi (✉)
Faculty of Engineering, International Telematic University Uninettuno, Rome, Italy
e-mail: luca.placidi@uninettunouniversity.net

F. dell'Isola
Dipartimento di Ingegneria Strutturale e Geotecnica, Universitá degli Studi di Roma "La Sapienza", Via Eudossiana 18, 00184 Rome, Italy

E. Barchiesi
MeMoCS, International Research Center for the Mathematics & Mechanics of Complex Systems, Universitá dell'Aquila, L'Aquila, Italy

C. Picu and J.-F. Ganghoffer (eds.), *Mechanics of Fibrous Materials and Applications*, CISM International Centre for Mechanical Sciences 596,
https://doi.org/10.1007/978-3-030-23846-9_3

procedure is presented and applied to the cases of Euler (in section "Euler Beams") and pantographic (in section "Pantographic Beams") beams.

Pantographic structures belong to the class of metamaterials that have to be treated as non-standard (or generalized) continua. Generalized continua (Alibert et al. 2003; Carcaterra et al. 2015; Abali et al. 2017; Pietraszkiewicz and Eremeyev 2009; Altenbach and Eremeyev 2009), and in particular higher gradient theories, see dell'Isola et al. (2016b) or dell Isola et al. (2015) for a comprehensive review, are able to describe behaviors which cannot be accounted for in classical Cauchy theories (dell'Isola et al. 2015b, 2016a, e; Reiher et al. 2016; Boutin et al. 2017; Seppecher et al. 2011; Cuomo et al. 2016; Placidi et al. 2016c). In the literature, several examples can be found motivating the importance of generalized continua: electromechanical (Enakoutsa et al. 2015) and biomechanical (Placidi et al. 2016a; Giorgio et al. 2015; Andreaus et al. 2013, 2014) applications, elasticity theory (Andreaus et al. 2010; Giorgio et al. 2017; Turco et al. 2017; Placidi et al. 2015; dell'Isola et al. 2015a; Abali et al. 2015), capillary fluids analysis (Auffray et al. 2015), granular micromechanics (Yang and Misra 2012; Misra and Poorsolhjouy 2015; Misra and Singh 2015), robotic systems analysis (Della Corte et al. 2016; Del Vescovo and Giorgio 2014), damage theory (Rinaldi and Placidi 2014; Placidi 2015; Madeo et al. 2014c; Misra 2002; Misra and Singh 2013; Yang and Misra 2010), and wave propagation analysis (Madeo et al. 2014a; Bersani et al. 2016; Placidi et al. 2008; Madeo et al. 2014b, 2016). Furthermore, second gradient continuum models always appear when the considered micro-system is a pantographic structure (Giorgio 2016; dell'Isola et al. 2016c, d; Scerrato et al. 2016; Giorgio et al. 2016; Rahali et al. 2015; Alibert and Della Corte 2015; Eremeyev et al. 2017). A comprehensive review of the modeling of pantographic structures can be found in Placidi et al. (2016b), Barchiesi and Placidi (2017). Several results of numerical investigations can be found in Turco et al. (2016a, b, c, d), Spagnuolo et al. (2017), Andreaus et al. (2010), Battista et al. (2015, 2016), Greco et al. (2016), and Turco and Rizzi (2016), while for an outline of recent experimental results we refer to dell'Isola et al. (2015c) and Ganzosch et al. (2016).

Euler Beams

Introduction

Customarily, the theory of nonlinear beams is either postulated by means of a suitable least action principle in the so-called "direct way" or is deduced, by means of a more or less rigorous procedure, starting from a three-dimensional elasticity theory. The first example of direct model can be found in the original paper by Euler (Euler and Carathéodory 1952). Many epigones of Euler used this approach: a comprehensive account for this procedure can be found in Antman Antman (1995). On the other hand, by following the procedure described by De Saint-Venant, one can try to identify

the constitutive equation of a Euler type (1D) model in terms of the geometrical and mechanical properties, at microlevel, of the considered mechanical systems. This is done, in more modern textbooks, using a more or less standard asymptotic micro–macro identification procedure, which generalizes the one used by De Saint-Venant for bodies with cylindrical shape (see, for instance, Placidi et al. 2017). It can be rigorously proven, under a series of well-precised assumptions, that only flexible and inextensible beams can be obtained (Murat and Sili 1999; Mora and Müller 2004; Jamal and Sanchez-Palencia 1996; Pideri and Seppecher 2006; Allaire 1992; Bensoussan et al. 1978).

Long fibers are often modeled as Euler beams. Here, we will define a Euler beam from a continuum point of view for the extensible and for the inextensible cases. A discrete model for the same beam will be also introduced and a heuristic homogenization procedure, see, e.g., dell'Isola et al. (2016d), applied. A rescaling law will be derived for the extensible and for the inextensible cases.

Continuous Euler Beams

Kinematics

At each point S of $\mathcal{C}_0$, see Fig. 3.1, is associated a copy of the rigid section $\mathcal{R}$ through O such that $\mathcal{C}_0$ and $\mathcal{R}$ are orthogonal. $\mathcal{B}_0$ is the reference configuration of a beam. $\mathcal{B}$ is the present configuration, which is defined as

(i) A vector function $\chi(S)$ that gives the present position of $q_0(S)$.
(ii) An orthogonal tensor field $R(S)$ that gives the rotation of $\mathcal{R}$ from the reference to the present configuration.

The kinematics is therefore defined by the following fields (Fig. 3.2):

$$\chi(S), R(S). \tag{3.1}$$

The admissible motion is, e.g., for a cantilever, those kinematic fields such that

$$\chi(0) = 0, \qquad R(0) = 0.$$

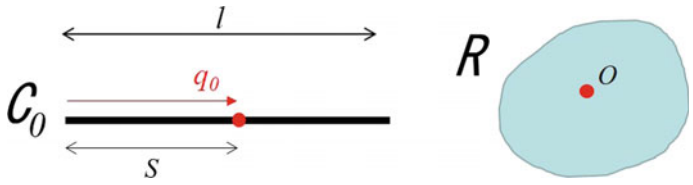

Fig. 3.1 Reference configuration $\mathcal{B}_0$. $q_0(S)$ is the position of the origin O of the section $\mathcal{R}$

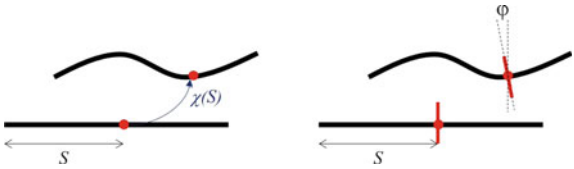

Fig. 3.2 Definition of the fundamental kinematical fields, where the rotation φ defines the rotation matrix R, in the two-dimensional case via Eq. (3.7)

Action

Physical intuition and definition of the action functional

$$\mathcal{A} = \left[\int_0^L W\left(\chi, R, \chi', R'\right) - W^{ext}\left(\chi, R\right)\right] - W_S^{ext}\big|_{S=0,S=L},$$

where W is the strain energy that is assumed to depend upon the fundamental kinematical fields and their derivative. W^{ext} is the energy of the distributed forces and W_S^{ext} that of the concentrated ones.

Objectivity and Representation of the Invariants

Let us assume that the fundamental kinematical fields in one frame of reference are represented in (3.1). In another frame of reference they are as

$$\widetilde{\chi} = U + Q\chi, \qquad \widetilde{R} = QR, \tag{3.2}$$

where U and Q are the translation and the rotation of the second frame of reference with respect to the first one. The derivative of (3.2) yields

$$\widetilde{\chi}' = Q\chi', \qquad \widetilde{R}' = QR'. \tag{3.3}$$

Let us define the following two fields in the first frame of reference

$$E = R^T R' \tag{3.4}$$

$$e = R^T \chi' - q_0'\left(S\right). \tag{3.5}$$

In the second frame of reference, they are from (3.2) to (3.5)

$$\tilde{E} = \widetilde{R}^T \tilde{R}' = R^T Q^T Q R' = R^T R' = E$$

$$\tilde{e} = \widetilde{R}^T \tilde{\chi}' - q_0'\left(S\right) = R^T Q^T Q \chi' - q_0'\left(S\right) = R^T \chi' - q_0'\left(S\right) = e,$$

which means that they are invariant. In order to represent E and e, we assume a Cartesian frame of reference. The origin of such a frame of reference is $q_0\left(0\right)$with basis

$$D_1 = q_0', \qquad D_2 \qquad D_3.$$

If S is a curvilinear abscissa of straight frame of reference

$$q_0 = S\, D_1$$

that yields

$$q_0' = D_1 = \begin{pmatrix} 1 \\ 0 \\ 0 \end{pmatrix}.$$

The 2D assumption is

$$\chi \in span\,\{D_1, D_2\}\,.$$

We define the displacement vector field

$$u = \chi - q_0,$$

and therefore its derivative

$$u' = \chi' - D_1 \quad \Rightarrow \quad u' = \begin{pmatrix} u_1' \\ u_2' \end{pmatrix} = \begin{pmatrix} \chi_1' - 1 \\ \chi_2' \end{pmatrix},$$

so that the derivative of the placement is

$$\chi' = \begin{pmatrix} \chi_1' \\ \chi_2' \end{pmatrix} = \begin{pmatrix} 1 + u_1' \\ u_2' \end{pmatrix}$$

and its squared modulus,

$$\left\|\chi'\right\|^2 = \left(1 + u_1'\right)^2 + u_2'^2.$$

A representation of R is given in terms of the rotation angle φ,

$$R = \cos\varphi D_1 \otimes D_1 - \sin\varphi D_1 \otimes D_2 + \sin\varphi D_2 \otimes D_1 + \cos\varphi D_2 \otimes D_2 \tag{3.6}$$

$$= \begin{pmatrix} \cos\varphi & -\sin\varphi \\ \sin\varphi & \cos\varphi \end{pmatrix}. \tag{3.7}$$

Thus, the two invariants are represented as follows:

$$E = R^T R' = \begin{pmatrix} \cos\varphi & \sin\varphi \\ -\sin\varphi & \cos\varphi \end{pmatrix} \begin{pmatrix} -\sin\varphi & -\cos\varphi \\ \cos\varphi & -\sin\varphi \end{pmatrix} \varphi' \tag{3.8}$$

$$= \begin{pmatrix} 0 & -\varphi' \\ \varphi' & 0 \end{pmatrix} = \begin{pmatrix} 0 & -\kappa \\ \kappa & 0 \end{pmatrix}$$

$$e = \begin{pmatrix} \varepsilon \\ \gamma \end{pmatrix} = R^T \chi' - q_0' (S) = \tag{3.9}$$
$$= \begin{pmatrix} \cos\varphi & \sin\varphi \\ -\sin\varphi & \cos\varphi \end{pmatrix} \begin{pmatrix} 1 + u_1' \\ u_2' \end{pmatrix} - \begin{pmatrix} 1 \\ 0 \end{pmatrix}$$
$$= \begin{pmatrix} \left(1 + u_1'\right) \cos\varphi + u_2' \sin\varphi - 1 \\ -\left(1 + u_1'\right) \sin\varphi + u_2' \cos\varphi \end{pmatrix},$$

which means in terms of κ, ε, and γ. A representation of the internal energy W that is compatible with the indifference frame principle is given by the function g

$$W\left(\chi, R, \chi', R'\right) = g\left(\kappa, \varepsilon, \gamma\right).$$

Let us give a representation for κ andε whether the beam is assumed to be shear un-deformable, i.e., with $\gamma = 0$. Thus, from the second equation of (3.9) we have

$$\left(1 + u_1'\right) \sin\varphi = u_2' \cos\varphi, \quad \Rightarrow \quad \tan\varphi = \frac{u_2'}{1 + u_1'}, \tag{3.10}$$

that means

$$\varphi = \arctan \frac{u_2'}{1 + u_1'} = \arctan \frac{\chi_2'}{\chi_1'}. \tag{3.11}$$

Besides from the first equation of (3.9), we have

$$\varepsilon = -1 + \left(1 + u_1'\right) \cos\varphi + u_2' \sin\varphi \tag{3.12}$$

Keeping in mind that

$$\tan^2\varphi = \frac{\sin^2\varphi}{\cos^2\varphi} = \frac{1 - \cos^2\varphi}{\cos^2\varphi} = \frac{1}{\cos^2\varphi} - 1$$

that yields

$$1 + \tan^2\varphi = \frac{1}{\cos^2\varphi},$$

we have from (3.10)

$$\cos^2\varphi = \frac{1}{1 + \tan^2\varphi} = \frac{1}{1 + \left(\frac{u_2'}{1+u_1'}\right)^2} = \frac{\left(1 + u_1'\right)^2}{\left(1 + u_1'\right)^2 + u_2'^2},$$

that yields

$$\cos\varphi = \frac{1 + u_1'}{\sqrt{\left(1 + u_1'\right)^2 + u_2'^2}} \tag{3.13}$$

and

$$\sin\varphi = \tan\varphi\cos\varphi = \frac{u_2'}{1+u_1'}\frac{1+u_1'}{\sqrt{\left(1+u_1'\right)^2+u_2'^2}} = \frac{u_2'}{\sqrt{\left(1+u_1'\right)^2+u_2'^2}}. \tag{3.14}$$

Therefore, from (3.12), (3.13), and (3.14)

$$1+\varepsilon = \left(1+u_1'\right)\frac{1+u_1'}{\sqrt{\left(1+u_1'\right)^2+u_2'^2}} + u_2'\frac{u_2'}{\sqrt{\left(1+u_1'\right)^2+u_2'^2}} = \tag{3.15}$$

$$= \frac{\left(1+u_1'\right)^2+u_2'^2}{\sqrt{\left(1+u_1'\right)^2+u_2'^2}} = \sqrt{\left(1+u_1'\right)^2+u_2'^2} = \left\|.\chi'\right\| \tag{3.16}$$

Besides, the derivative of (3.11) is

$$\kappa = \varphi' = \frac{1}{1+\left(\frac{\chi_2'}{\chi_1'}\right)^2}\frac{\chi_2''\chi_1' - \chi_2'\chi_1''}{\chi_1'^2} = \frac{\chi''\cdot\left(*\chi'\right)}{\|\chi'\|^2}, \tag{3.17}$$

where the 90° rotation matrix is defined as follows:

$$* = \begin{pmatrix} 0 & -1 \\ 1 & 0 \end{pmatrix},$$

so that

$$\chi''\cdot\left(*\chi'\right) = \begin{pmatrix}\chi_1'' & \chi_2''\end{pmatrix}\begin{pmatrix} 0 & -1 \\ 1 & 0 \end{pmatrix}\begin{pmatrix}\chi_1' \\ \chi_2'\end{pmatrix} \tag{3.18}$$

$$= \begin{pmatrix}\chi_1'' & \chi_2''\end{pmatrix}\begin{pmatrix}-\chi_2' \\ \chi_1'\end{pmatrix} = -\chi_2'\chi_1'' + \chi_2''\chi_1'. \tag{3.19}$$

Let us call

$$\hat{e} = \frac{\chi'}{\|\chi'\|}, \quad \tilde{c} = \frac{\chi''}{\|\chi'\|}. \tag{3.20}$$

Thus, the curvature (3.17) is

$$\kappa = \varphi' = \left(*\hat{e}\right)\cdot\tilde{c}. \tag{3.21}$$

Macroscopic Strain Energy for the General Case

A quadratic form of the strain energy in terms of the two invariants κ, from (3.21), and ε, from (3.16), is

$$U_{macro} = \int_0^l \left[\frac{1}{2} K_b \kappa^2 + \frac{1}{2} k_e \varepsilon^2 \right] dS \tag{3.22}$$

$$= \int_0^l \left[\frac{1}{2} K_b \left(\frac{\chi'' \cdot (*\chi')}{\|\chi'\|^2} \right)^2 + \frac{1}{2} K_e \left(\|\chi'\| - 1 \right)^2 \right] dS. \tag{3.23}$$

It is worth to be noted that the strain energy is of second gradient type only for the normal component $(*\hat{e}) \cdot \chi''$. The tangential component $\hat{e} \cdot \chi''$ do not have any contribution in the strain energy. In pantographic structures, we will see that also this tangential contribution is able to accumulate strain energy.

Macroscopic Strain Energy for the Inextensible Case

For inextensible beams, χ' is the unit vector $\hat{e}$,

$$\|\chi'\|^2 = 1 = \chi' \cdot \chi' \tag{3.24}$$

that means

$$\chi'' \cdot \chi' + \chi' \cdot \chi'' = 0 \quad \Longrightarrow \quad \chi' \cdot \chi'' = 0,$$

and

$$\|\chi''\|^2 = \chi'' \cdot \chi'' = \chi'' \cdot \left[\left((*\chi') \cdot \chi'' \right) * \chi' + \left((\chi') \cdot \chi'' \right) \chi' \right] =$$
$$= \chi'' \cdot \left[\left((*\chi') \cdot \chi'' \right) * \chi' \right] = \left[\chi'' \cdot (*\chi') \right]^2. \tag{3.25}$$

Thus, from (3.24) and (3.25), the strain energy (3.23) for the inextensible case is

$$U_{macro} = \int_0^l \left[\frac{1}{2} K_b \left(\frac{\chi'' \cdot (*\chi')}{\|\chi'\|^2} \right)^2 \right] dS = \int_0^l \frac{1}{2} K_b \|\chi''\|^2 dS. \tag{3.26}$$

Discrete Henky-Type Beam

Microscopic models for the inextensible Euler beams in the reference configuration are plotted in Fig. 3.3 (bottom). The bars are rigid and of length ε

Piola's Ansatz

$$p_i = \chi(P_i), \tag{3.27}$$

Thus, the position of the other points is

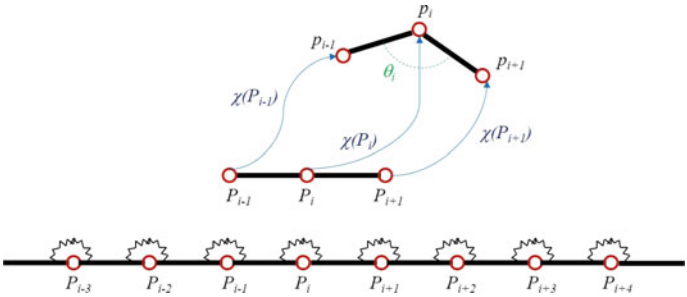

Fig. 3.3 Microscopic models for the inextensible Euler beams in (bottom) the reference configuration. Definition (top) of the angle θ_i

$$p_{i+1} = \chi(P_{i+1}) = \chi(P_i) + \varepsilon\chi'(P_i) + \frac{1}{2}\varepsilon^2\chi''(P_i). \tag{3.28}$$

$$p_{i-1} = \chi(P_i) - \varepsilon\chi'(P_i) + \frac{1}{2}\varepsilon^2\chi''(P_i), \tag{3.29}$$

so that the cosine of the angle θ_i is defined, in the inextensible case (3.24), by

$$\cos\theta_i = \frac{(p_{i+1}-p_i)\cdot(p_{i-1}-p_i)}{\|p_{i+1}-p_i\|\,\|p_{i-1}-p_i\|} \tag{3.30}$$

$$= \frac{\left[\varepsilon\chi'(P_i) + \frac{1}{2}\varepsilon^2\chi''(P_i)\right]\cdot\left[-\varepsilon\chi'(P_i) + \frac{1}{2}\varepsilon^2\chi''(P_i)\right]}{\varepsilon^2}, \tag{3.31}$$

$$= \frac{-\varepsilon^2\left\|\chi'\right\|^2 + \frac{1}{2}\varepsilon^3\chi'\cdot\chi'' - \frac{1}{2}\varepsilon^3\chi'\cdot\chi'' + \frac{1}{4}\varepsilon^4\chi''\cdot\chi''}{\varepsilon^2} \tag{3.32}$$

$$= -1 + \frac{1}{4}\varepsilon^2\chi''\cdot\chi''. \tag{3.33}$$

Discrete energy in the inextensible case is defined as

$$U_{micro} = \sum_{i=1}^{N} k_b\left(1+\cos\theta_i\right) = \sum_{i=1}^{N}\frac{1}{4}k_b\varepsilon^2\left\|\chi''\right\|^2.$$

With the homogenization formula,

$$\sum_{i=1}^{N}\varepsilon(\cdot) \longrightarrow \int_0^l (\cdot)\,dS, \tag{3.34}$$

we have

$$U_{micro} = \int_0^l \frac{1}{4}k_b\varepsilon\left\|\chi''\right\|^2 dS. \tag{3.35}$$

An identification of (3.26) and (3.35) implies

$$k_b \varepsilon = 2K_b. \tag{3.36}$$

Thus, in order to have a finite macro-energy, even in the limit $\varepsilon \to 0$, we need to impose the scaling law (3.36). This means that, if one wants a finite macro-energy, then the lower the size of the cell, the higher is the rigidity of the rotational spring. Besides, in the limit of $\varepsilon \to 0$, k_b should be infinite, i.e., $k_b \to \infty$.

For extensible beams, the distance between internal hinges is not fixed to be equal to ε. The extensible bar at the right-hand side of P_i has the following length:

$$\|p_{i+1} - p_i\| = \sqrt{\left[\varepsilon\chi'(P_i) + \frac{1}{2}\varepsilon^2\chi''(P_i)\right] \cdot \left[\varepsilon\chi'(P_i) + \frac{1}{2}\varepsilon^2\chi''(P_i)\right]} \tag{3.37}$$

$$= \sqrt{\varepsilon^2 \|\chi'\|^2 + \frac{1}{2}\varepsilon^3\chi' \cdot \chi'' + \frac{1}{2}\varepsilon^3\chi' \cdot \chi'' + \frac{1}{4}\varepsilon^4\chi'' \cdot \chi''} \tag{3.38}$$

$$= \varepsilon\sqrt{\|\chi'\|^2 + \varepsilon\chi' \cdot \chi'' + \frac{1}{4}\varepsilon^2\chi'' \cdot \chi''} = \varepsilon \left\|\chi'\right\| + \varepsilon^2 \frac{\chi' \cdot \chi''}{2\|\chi'\|}. \tag{3.39}$$

The extensible bar on the left-hand side of P_i has the following length:

$$\|p_{i-1} - p_i\| = \sqrt{\left[-\varepsilon\chi'(P_i) + \frac{1}{2}\varepsilon^2\chi''(P_i)\right] \cdot \left[-\varepsilon\chi'(P_i) + \frac{1}{2}\varepsilon^2\chi''(P_i)\right]}$$

$$= \sqrt{\varepsilon^2 \|\chi'\|^2 - \frac{1}{2}\varepsilon^3\chi' \cdot \chi'' - \frac{1}{2}\varepsilon^3\chi' \cdot \chi'' + \frac{1}{4}\varepsilon^4\chi'' \cdot \chi''}$$

$$= \varepsilon\sqrt{\|\chi'\|^2 - \varepsilon\chi' \cdot \chi'' + \frac{1}{4}\varepsilon^2\chi'' \cdot \chi''} = \varepsilon \left\|\chi'\right\| - \varepsilon^2 \frac{\chi' \cdot \chi''}{2\|\chi'\|}.$$

The representation of the cosine of the angle θ_i in the extensible case, from (3.31) to (3.33), is

$$\cos\theta_i = \frac{(p_{i+1} - p_i) \cdot (p_{i-1} - p_i)}{\|p_{i+1} - p_i\| \, \|p_{i-1} - p_i\|} \tag{3.40}$$

$$= \frac{\left[\varepsilon\chi'(P_i) + \frac{1}{2}\varepsilon^2\chi''(P_i)\right] \cdot \left[-\varepsilon\chi'(P_i) + \frac{1}{2}\varepsilon^2\chi''(P_i)\right]}{\left(\varepsilon\|\chi'\| + \varepsilon^2\frac{\chi' \cdot \chi''}{2\|\chi'\|}\right)\left(\varepsilon\|\chi'\| - \varepsilon^2\frac{\chi' \cdot \chi''}{2\|\chi'\|}\right)} \tag{3.41}$$

$$= \frac{-\varepsilon^2 \left\|\chi'\right\|^2 + \frac{1}{4}\varepsilon^4\chi'' \cdot \chi''}{\varepsilon^2\|\chi'\|^2 - \frac{1}{4}\varepsilon^4\left(\frac{\chi' \cdot \chi''}{\|\chi'\|}\right)^2} = \frac{-\left\|\chi'\right\|^2 + \frac{1}{4}\varepsilon^2\chi'' \cdot \chi''}{\|\chi'\|^2 - \frac{1}{4}\varepsilon^2\left(\frac{\chi' \cdot \chi''}{\|\chi'\|}\right)^2}. \tag{3.42}$$

The Taylor series expansion of the function $f(x)$ around $x = 0$

$$f(x) = \frac{-a + bx}{a - cx} = -1 + f'(0)\, x, \tag{3.43}$$

$$f'(x) = \frac{b(a - cx) - (-a + bx)(-c)}{(a - cx)^2}, \tag{3.44}$$

$$f'(0) = \frac{ba - ac}{a^2} = \frac{b - c}{a} \tag{3.45}$$

that imply

$$\cos\theta_i = -1 + \frac{\chi'' \cdot \chi'' - \left(\frac{\chi' \cdot \chi''}{\|\chi'\|}\right)^2}{4\|\chi'\|^2}\varepsilon^2. \tag{3.46}$$

Discrete energy for the extensible case is therefore

$$U_{micro} = \sum_{i=1}^{N} \frac{k_e}{2}\left(\|p_{i+1} - p_i\| - \varepsilon\right)^2 + k_b\left(1 + \cos\theta_i\right),$$

that, because of (3.39) and (3.46)

$$U_{micro} = \sum_{i=1}^{N} \frac{k_e}{2}\left(\|p_{i+1} - p_i\| - \varepsilon\right)^2 + k_b\left(1 + \cos\theta_i\right) \tag{3.47}$$

$$= \sum_{i=1}^{N} \frac{k_e}{2}\varepsilon^2\left(\|\chi'\| - 1\right)^2 + k_b\frac{\chi'' \cdot \chi'' - \left(\frac{\chi' \cdot \chi''}{\|\chi'\|}\right)^2}{4\|\chi'\|^2}\varepsilon^2. \tag{3.48}$$

The last addend, because of the definitions (3.20), is rearranged as

$$\frac{\chi'' \cdot \chi'' - \left(\frac{\chi' \cdot \chi''}{\|\chi'\|}\right)^2}{\|\chi'\|^2} = \tilde{c} \cdot \tilde{c} - \left(\tilde{c} \cdot \hat{e}\right)^2 \tag{3.49}$$

$$= \tilde{c} \cdot \left(\tilde{c} - \hat{e}\left(\tilde{c} \cdot \hat{e}\right)\right) = \tilde{c} \cdot \tilde{c}_\perp = \tilde{c}_\perp \cdot \tilde{c}_\perp = \left[\tilde{c} \cdot \left(*\hat{e}\right)\right]^2, \tag{3.50}$$

which imply another form of the discrete strain energy

$$U_{micro} = \sum_{i=1}^{N} \frac{k_e}{2}\varepsilon^2\left(\|\chi'\| - 1\right)^2 + \frac{1}{4}k_b\left[\frac{\chi'' \cdot \left(*\chi'\right)}{\|\chi'\|^2}\right]^2\varepsilon^2. \tag{3.51}$$

With the homogenization formula (3.34), the equation (3.51) yields

$$U_{micro} = \int_0^l \frac{1}{2}\varepsilon k_e\left(\|\chi'\| - 1\right)^2 + \frac{1}{4}k_b\varepsilon\left[\frac{\chi'' \cdot \left(*\chi'\right)}{\|\chi'\|^2}\right]^2 dS.$$

Thus, in order to have a finite macro-energy, we need to impose the following rescaling law:

$$k_b\varepsilon = 2K_b, \qquad \varepsilon k_e = K_e. \tag{3.52}$$

Thus, in order to have a finite macro-energy, even in the limit $\varepsilon \to 0$, we need to impose the scaling laws (3.52). This means that, if one wants a finite macro-energy, then the lower the size of the cell, the higher is the rigidity of the tensional and of the rotational springs. Besides, in the limit of $\varepsilon \to 0$, k_b should be infinite, i.e., $k_b \to \infty$.

Pantographic Beams

Introduction

In this section, we discuss the discrete micro-mechanical model which is employed throughout this paper. We begin giving a geometrical description and then we give a mechanical characterization, by choosing a deformation energy. It is a Hencky-type spring model with the geometrical arrangement of a pantographic strip. Once the energy of the micro-model is chosen in its general form, we assume a particular asymptotic behavior for some relevant kinematic quantities, i.e., the elongation of oblique springs, as will be clear in the sequel. We consider the quasi-inextensibility case, i.e., the relative elongation of the oblique springs is small. As a further specialization, the inextensibility case is considered. Finally, after having defined a micro–macro identification, we express the energy of the micro-system in terms of macroscopic kinematic descriptors to prepare the field to the homogenization procedure which will be discussed in details in the next section.

Discrete Micro-model

Geometry

In the spirit of dell'Isola et al. (2016d), Alibert and Della Corte (2015), and Alibert et al. (2017), in this section, we introduce a discrete-spring model (also referred to as the *micro-model*, since it resembles the features of a specific microstructure). The topology and features of the undeformed and deformed discrete-spring system are summarized in Figs. 3.4 and 3.5, respectively. In the undeformed configuration, $N + 1$ material particles are arranged upon a straight line at positions P_i's, $i \in [0; N]$, with a uniform spacing ε. The basic ith unit cell centered in P_i is formed by four springs joined together by a hinge placed at P_i. Between two oblique springs, belonging to the same cell and lying on the same diagonal, a rotational spring opposing to their relative rotation is placed. Rotational springs are colored in Fig. 3.4 in blue and red.

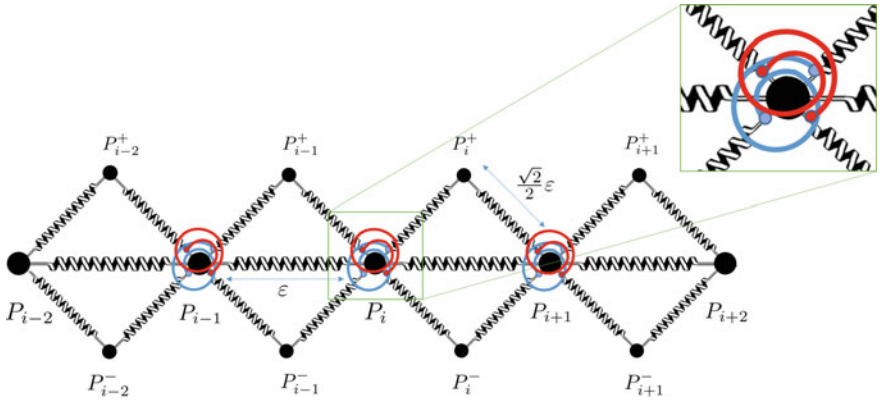

Fig. 3.4 Undeformed spring system resembling the microstructure

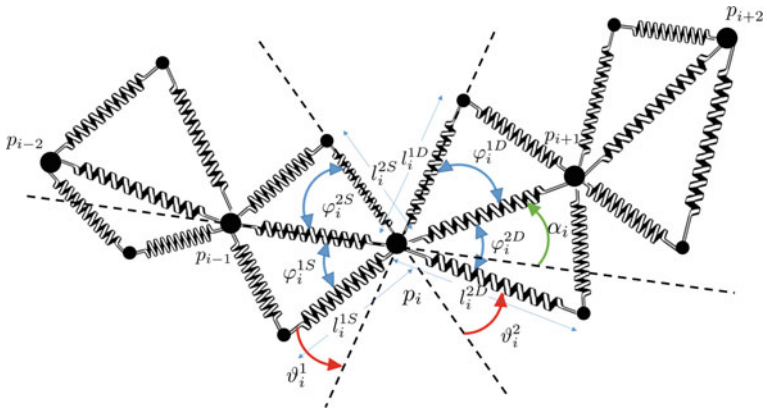

Fig. 3.5 Deformed spring system resembling the microstructure

We denote with p_i the position in the deformed configuration corresponding to position P_i in the reference one. In order to completely describe the kinematics of the micro-model, we have to introduce other descriptors. At this end, the length of the oblique deformed springs, indicated with $l_i^{\alpha\beta}$, is introduced, the indices α and β belonging, respectively, to the sets $\{1, 2\}$ and $\{D, S\}$ and referring to the first and second diagonal and left and right, respectively. Referring to Fig. 3.5, we consider the ith node, notwithstanding that the same quantities can be defined for each node. We define α_i as the angle between the vectors $p_i - p_{i-1}$ and $p_i - p_{i+1}$, respectively. We define as ϑ_i^α the angle measuring the deviation of two opposite oblique springs from being collinear. In order to illustrate the definition of $\varphi_i^{\alpha\beta}$, we consider the case $\alpha = 1$ and $\beta = D$. The quantity φ_i^{1D} is the angle between the vector $p_{i+1} - p_i$ and the upper oblique spring hinged at p_i. By means of elementary geometric considerations, we have that

$$\begin{aligned}\vartheta_i^1 &= \alpha_i + \varphi_i^{1D} - \varphi_i^{1S}\\ \vartheta_i^2 &= \alpha_i + \varphi_i^{2S} - \varphi_i^{2D},\ i \in [0; N]\,.\end{aligned} \tag{3.53}$$

In the undeformed configuration, see Fig. 3.4, we have

$$\begin{aligned}&l_i^{\alpha\beta} = \frac{\sqrt{2}}{2}\varepsilon,\ \alpha = 1, 2 \quad \beta = D,\ S \quad i \in [0; N]\\ &\vartheta_i^1 = \vartheta_i^2 = 0\\ &\|p_i - p_{i-1}\| = \varepsilon,\ i \in [0; N]\,.\end{aligned} \tag{3.54}$$

Considering that $\varphi_i^{\alpha D}$, $\varphi_i^{\alpha S} \in [0, \pi]$, by means of the law of cosines, we get

$$\begin{aligned}\varphi_i^{1D} &= \cos^{-1}\left(\frac{\|p_{i+1} - p_i\|^2 + \left(l_i^{1D}\right)^2 - \left(l_{i+1}^{2S}\right)^2}{2l_i^{1D}\|p_{i+1} - p_i\|}\right)\\ \varphi_i^{2D} &= \cos^{-1}\left(\frac{\|p_{i+1} - p_i\|^2 + \left(l_i^{2D}\right)^2 - \left(l_{i+1}^{1S}\right)^2}{2l_i^{2D}\|p_{i+1} - p_i\|}\right)\\ \varphi_i^{1S} &= \cos^{-1}\left(\frac{\|p_i - p_{i-1}\|^2 + \left(l_i^{1S}\right)^2 - \left(l_{i-1}^{2D}\right)^2}{2l_i^{1S}\|p_i - p_{i-1}\|}\right)\\ \varphi_i^{2S} &= \cos^{-1}\left(\frac{\|p_i - p_{i-1}\|^2 + \left(l_i^{2S}\right)^2 - \left(l_{i-1}^{1D}\right)^2}{2l_i^{2S}\|p_i - p_{i-1}\|}\right).\end{aligned} \tag{3.55}$$

Mechanical Model

The micro-model energy, written as a combination of the elastic energy contributions of the springs, is defined as

$$\begin{aligned}\mathcal{M} &= \sum_i \sum_{\alpha,\beta} \frac{k^e_{\alpha\beta,i}}{2}\left(l_i^{\alpha\beta} - \frac{\sqrt{2}}{2}\varepsilon\right)^2 + \sum_i \sum_\alpha \frac{k^f_{\alpha,i}}{2}\left(\vartheta_i^\alpha\right)^2 +\\ &+ \sum_i \frac{k_i^m}{2}\left(\|p_{i+1} - p_i\| - \varepsilon\right)^2.\end{aligned} \tag{3.56}$$

Reminding that $\vartheta_i^\alpha = \alpha_i + (-1)^\alpha\left(\varphi_i^{\alpha S} - \varphi_i^{\alpha D}\right)$, then (3.56) recasts as

$$\mathcal{M} = \sum_i \sum_{\alpha,\beta} \frac{k^e_{\alpha\beta,i}}{2}\left(l_i^{\alpha\beta} - \frac{\sqrt{2}}{2}\varepsilon\right)^2 \tag{3.57}$$

$$+\sum_i \sum_\alpha \frac{k^f_{\alpha,i}}{2}\left[\alpha_i + (-1)^\alpha \left(\varphi_i^{\alpha S} - \varphi_i^{\alpha D}\right)\right]^2 + \\ +\sum_i \frac{k_i^m}{2}\left(\|p_{i+1} - p_i\| - \varepsilon\right)^2 .$$

In the next subsections, we will specialize this form of the energy by means of assumptions on the properties of the micro-system. In particular, we will discuss in detail the representation of the micro-energy for the quasi-inextensibility assumption that will be made clear next and, subsequently, for the (complete) inextensibility cases.

Toward the Continuum Model

Asymptotic Expansion and Quasi-inextensibility Assumption

We postulate that the following asymptotic expansion holds for $l_i^{\alpha\beta}$:

$$l_i^{\alpha\beta} = \varepsilon \tilde{l}_{i1}^{\alpha\beta} + \varepsilon^2 \tilde{l}_{i2}^{\alpha\beta} + o\left(\varepsilon^2\right), \tag{3.58}$$

where the constant (with respect to ε) term is not present. We now turn to what we refer to as the quasi-inextensibility case. It consists in fixing the value of the first-order term in (3.58) as $\tilde{l}_{i1}^{\alpha\beta} = \frac{\sqrt{2}}{2}$. Moreover, to lighten the notation, we drop the subscript "2" of $\tilde{l}_{i2}^{\alpha\beta}$, i.e., $\tilde{l}_i^{\alpha\beta} = \tilde{l}_{i2}^{\alpha\beta}$. Hence, (3.58) reads as

$$l_i^{\alpha\beta} = \frac{\sqrt{2}}{2}\varepsilon + \varepsilon^2 \tilde{l}_i^{\alpha\beta} + o\left(\varepsilon^2\right). \tag{3.59}$$

Piola's Ansatz

The reference shape of the macro-model is a one-dimensional straight segment $\mathcal{S}$ and we introduce on it an abscissa $s \in [0, B]$ – where $B = N\varepsilon$ is the length of $\mathcal{S}$ which labels each position in $\mathcal{S}$. Proceeding as in the pioneering works of Gabrio Piola, an Italian mathematician and physicist who lived in the 1800s (see Dell'Isola et al. 2015 for a historical review), we introduce the so-called *kinematical maps*, i.e., some fields in the macro-model that uniquely determine p_i and $\tilde{l}_i^{\alpha\beta}$:

$$\begin{aligned} &\chi : [0, B] \to \mathcal{E} \\ &\tilde{l}^{\alpha\beta} : [0, B] \to \mathbb{R}^+, \end{aligned} \tag{3.60}$$

with $\mathcal{E}$ the Euclidean space on $\mathbb{V} \equiv \mathbb{R}^2$. We choose χ to be the placement function of the $1D$ continuum and, hence, it has to be injective. The current shape can be regarded as the image of the (sufficiently smooth) curve $\boldsymbol{\chi} : [0, B] \rightarrow \mathcal{E}$ and, unlike the reference shape, it is not parameterized by its arc length and it is not a straight line in general. In order for these fields to uniquely determine the kinematical descriptors of the micro-model (i.e., p_i and $\tilde{l}_i^{\alpha\beta}$), we use the *Piola's Ansatz* and impose

$$\begin{aligned} &\chi(s_i) = p_i \\ &\tilde{l}^{\alpha\beta}(s_i) = \tilde{l}_i^{\alpha\beta}, \ \forall i \in [0; N]. \end{aligned} \tag{3.61}$$

Micro-model Energy as a Function of Macro-model Descriptors

In this subsection, we obtain the micro-model energy for the quasi-inextensibility case in terms of the macroscopic kinematical maps. Assuming that χ is at least twice continuously differentiable with respect to the space variable in s_i's, we have

$$\begin{aligned} \chi(s_{i+1}) &= \chi(s_i) + \varepsilon\chi'(s_i) + \frac{\varepsilon^2}{2}\chi''(s_i) + o\left(\varepsilon^2\right) \\ \chi(s_{i-1}) &= \chi(s_i) - \varepsilon\chi'(s_i) + \frac{\varepsilon^2}{2}\chi''(s_i) + o\left(\varepsilon^2\right). \end{aligned} \tag{3.62}$$

Plugging (3.61) in (3.59) and (3.62), we get the following expressions:

$$\begin{aligned} l_i^{\alpha\beta} &= \frac{\sqrt{2}}{2}\varepsilon + \varepsilon^2\tilde{l}^{\alpha\beta}(s_i) + o\left(\varepsilon^2\right) \\ p_{i+1} - p_i &= \varepsilon\chi'(s_i) + \frac{\varepsilon^2}{2}\chi''(s_i) + o\left(\varepsilon^2\right) \\ p_{i-1} - p_i &= -\varepsilon\chi'(s_i) + \frac{\varepsilon^2}{2}\chi''(s_i) + o\left(\varepsilon^2\right). \end{aligned} \tag{3.63}$$

Substituting (3.63) into (3.55) and expanding $\varphi_i^{\alpha S} - \varphi_i^{\alpha D}$ up to first order with respect to ε, we get

$$\begin{aligned} &\varphi_i^{\alpha S} - \varphi_i^{\alpha D} = \\ &\frac{\frac{\sqrt{2}}{4}\left[\|\chi'(s_i)\|^2\right]' + \left[\tilde{l}^{(3-\alpha)D}(s_{i-1}) - \tilde{l}^{(3-\alpha)S}(s_{i+1})\right]}{\|\chi'(s_i)\|\sqrt{1 - \frac{\|\chi'(s_i)\|^2}{2}}}\varepsilon + \\ &+\frac{\left[\|\chi'(s_i)\|^2 - 1\right]\left[\tilde{l}^{\alpha S}(s_i) - \tilde{l}^{\alpha D}(s_i)\right]}{\|\chi'(s_i)\|\sqrt{1 - \frac{\|\chi'(s_i)\|^2}{2}}}\varepsilon + o(\varepsilon). \end{aligned} \tag{3.64}$$

Finally, substituting (3.64) in (3.57) yields the micro-model energy $\mathcal{M}$ as a function of the kinematical descriptors χ and $\tilde{l}^{\alpha\beta}$ of the macro-model

$$\begin{aligned}\mathcal{M} = &\sum_i \sum_{\alpha,\beta} \frac{k^e_{\alpha\beta,i}\varepsilon^4}{2}\left(\tilde{l}_i^{\alpha\beta}\right)^2 + \sum_i \frac{k_i^m \varepsilon^2}{2}\left(\|\chi_i'\| - 1\right)^2 \\ &+ \sum_i \sum_\alpha \frac{k^f_{\alpha,i}\varepsilon^2}{2}\Bigg\{\vartheta'(s_i) \\ &+ (-1)^\alpha \frac{\frac{\sqrt{2}}{4}\left[\|\chi'(s_i)\|^2\right]' + \left[\tilde{l}_i^{(3-\alpha)D}(s_{i-1}) - \tilde{l}_i^{(3-\alpha)S}(s_{i+1})\right]}{\|\chi'(s_i)\|\sqrt{1 - \frac{\|\chi'(s_i)\|^2}{2}}} + \\ &+ (-1)^\alpha \frac{\left[\|\chi'(s_i)\|^2 - 1\right]\left[\tilde{l}_i^{\alpha S}(s_i) - \tilde{l}_i^{\alpha D}(s_i)\right]}{\|\chi'(s_i)\|\sqrt{1 - \frac{\|\chi'(s_i)\|^2}{2}}}\Bigg\}^2,\end{aligned} \tag{3.65}$$

where $\alpha_i = \varepsilon\vartheta'(s_i)$ has been used and

$$\vartheta' = \frac{\chi_\perp' \cdot \chi''}{\|\chi'\|^2},$$

with $\chi_\perp'$ the 90° anticlockwise rotation of χ', is the material curvature, i.e., rate of change with respect to the reference abscissa of the orientation of the tangent $\chi'(s) = \rho(s)\left[\cos\vartheta(s)\,\mathbf{e}_1 + \sin\vartheta(s)\,\mathbf{e}_2\right]$ to the deformed centerline. We remark that the micro-model energy, when written in terms of macroscopic fields, contains already a contribution from the second gradient of $\chi(s)$. Finally, it is worth to be noticed that, for a fixed ε, Eq. (3.65) provides an upper bound for $||\chi'||$, i.e., $\|\chi'\| < \sqrt{2}$, even if no kinematic restrictions directly affect $||\chi'||$.

The Case of Inextensible Fibers

We consider now the case of inextensible oblique springs. This translates in considering $\tilde{l}_i^{\alpha\beta} = 0$ and it is referred as the *inextensibility case*. Moreover, for the sake of simplicity, we consider the elastic constants of the rotational springs to satisfy $k^1_{F,i} = k^2_{F,i} := k_{F,i}$, $\forall i \in [1; N]$. We remark that $\tilde{l}_i^{\alpha\beta} = 0$ implies, through a purely geometric argument, that $\varphi_{i+1}^{S1} = \varphi_{i+1}^{S2} = \varphi_i^{D1} = \varphi_i^{D2} := \varphi_i$. Once the kinematic restrictions implied by the inextensibility assumption have been presented, we are ready to define the micro-model energy (3.57) as

$$\mathcal{I} = \sum_i k_i^f \sum_\alpha \frac{\left[\alpha_i + (-1)^\alpha(\varphi_i - \varphi_{i-1})\right]^2}{2} \tag{3.66}$$

$$+\sum_i \frac{k_i^m}{2}\left(\|p_{i+1}-p_i\|-\varepsilon\right)^2.$$

Proceeding in analogy with the previous construction, we introduce the *kinematical map*

$$\varphi:\ [0,B]\to\left[0,\frac{\pi}{2}\right]$$

and, then, we perform the *Piola's Ansatz* by imposing

$$\varphi(s_i)=\varphi_i,\ \ \forall i\in[0;N]. \tag{3.67}$$

Assuming both χ and φ to be at least one time continuously differentiable with respect to the space variable in s_i and taking into account the *Piola's Ansatz* (3.67), we have

$$\begin{aligned} p_{i+1}-p_i &= \varepsilon\chi'(s_i)+o(\varepsilon)\\ \varphi_{i-1}-\varphi_i &= -\varepsilon\varphi'(s_i)+o(\varepsilon). \end{aligned} \tag{3.68}$$

Substituting (3.68) into (3.66) yields the micro-model energy for the inextensibility case in terms of the kinematical quantities of the macro-model

$$\mathcal{I}=\sum_i k_i^f\varepsilon^2\left[\vartheta'^2(s_i)+\varphi_i'^2(s_i)\right]+\sum_i\frac{k_i^m\varepsilon^2}{2}\left(\|\chi_i'\|-1\right)^2. \tag{3.69}$$

We now impose the so-called *internal connection* constraint:

$$\sqrt{2}\varepsilon\cos\varphi(s_i)=\|\chi(s_{i+1})-\chi(s_i)\|, \tag{3.70}$$

which, up to ε-terms of order higher than one, reads

$$\sqrt{2}\cos\varphi=\|\chi'\|. \tag{3.71}$$

This constraint ensures that, in the deformed configuration, the upper-left spring of the ith cell is hinge joint with the upper-right spring of the $(i-1)$th cell, and the lower-left spring of the ith cell is hinge joint with lower-right spring of the $(i-1)$th cell. Due to this constraint, the maps φ and χ are not independent and it is possible to rewrite the expression of the micro-model energy in terms of the placement field $\chi(s)$ only. Indeed, deriving (3.71) with respect to the space variable yields

$$-\sqrt{2}\varphi'(s_i)\sin\varphi(s_i)=\|\chi'(s_i)\|', \tag{3.72}$$

which, in turn, implies

$$\varphi'(s_i) = -\frac{\|\chi'(s_i)\|'}{\sqrt{2}\sin\varphi(s_i)}.$$

Reminding $\varphi \in [0, \pi]$ and taking into account (3.71), we get

$$\varphi_i' = -\frac{\|\chi_i'\|'}{\sqrt{2}\sqrt{1-\cos^2\varphi(s_i)}} = \\ = -\frac{\|\chi_i'\|'}{\sqrt{2-\|\chi_i'\|^2}}.$$

Hence, in the inextensibility case, the micro-model energy (3.69) can be recast, as a function of the macro-model descriptor χ only, as

$$\mathcal{I} = \\ \sum_i k_i^f \varepsilon^2 \left[\left[\vartheta'(s_i)\right]^2 + \left(\frac{\|\chi'(s_i)\|'}{\sqrt{2-\|\chi'(s_i)\|^2}} \right)^2 \right] + \sum_i \frac{k_i^m \varepsilon^2}{2} \left(\|\chi'(s_i)\| - 1 \right)^2. \tag{3.73}$$

Clearly, since the inextensibility case is just a special case of the quasi-inextensibility case, it is possible to show that this expression can be also obtained in a more direct way from (3.65) by setting $\tilde{l}^{\alpha S}(s_i) = 0$ and $k_{F,i}^1 = k_{F,i}^2 := k_{F,i}$.

Continuum-Limit Macro-model

In this section, by performing the final steps of the heuristic homogenization procedure presented throughout this paper, we derive a $1D$ continuum model, also referred to as the *macro-model,* associated to the aforementioned microstructure. Besides, we analyze the quasi-inextensibility and inextensibility cases and we obtain the corresponding macro-model energies in terms of the displacement field χ.

Rescaling of Stiffnesses and Heuristic Homogenization

The preliminary step to perform the homogenization procedure consists of the definition of the quantities $\mathbb{K}^e_{\alpha\beta,i}$, $\mathbb{K}^f_{\alpha,i}$, and $\mathbb{K}^m_i$. These quantities are scale-invariant, meaning that they do not depend on ε. Their role is to keep track of the asymptotic behavior of the stiffnesses $k^e_{\alpha,\beta,i}$, $k^f_{\alpha,i}$, and k^m_i of the micro-model springs. More explicitly, we assume

$$k^e_{\alpha\beta,i}(\varepsilon) = \frac{\mathbb{K}^e_{\alpha\beta,i}}{\varepsilon^3}; \qquad k^f_{\alpha,i}(\varepsilon) = \frac{\mathbb{K}^f_{\alpha,i}}{\varepsilon}; \qquad k^m_i(\varepsilon) = \frac{\mathbb{K}^m_i}{\varepsilon}. \tag{3.74}$$

We remark that in this rescaling, as ε approaches zero, the ratio between the stiffness $k^e_{\alpha\beta,i}$ of the oblique springs and the stiffness $k^f_{\alpha,i}$ will approach infinity with a rate of divergence in ε equal to two, i.e., $\frac{k^e_{\alpha\beta,i}}{k^e_{\alpha,i}} \sim \varepsilon^2$. Now, we are ready to perform the homogenization procedure. First, we consider the more general quasi-inextensibility case. For simplicity, let us set

$$\mathbb{K}^e_{1D,i} = \mathbb{K}^e_{1S,i} = \mathbb{K}^e_{2D,i} = \mathbb{K}^e_{2S,i} := \mathbb{K}^e_i; \qquad \mathbb{K}^f_{1,i} = \mathbb{K}^f_{2,i} := \mathbb{K}^f_i. \tag{3.75}$$

Let us introduce the kinematical maps

$$\mathbb{K}^e : [0, B] \to \mathbb{R}^+; \qquad \mathbb{K}^f : [0, B] \to \mathbb{R}^+; \qquad \mathbb{K}^m : [0, B] \to \mathbb{R}^+$$

such that they satisfy the following Piola's Ansatz:

$$\mathbb{K}^e(s_i) = \mathbb{K}^e_i; \qquad \mathbb{K}^f(s_i) = \mathbb{K}^f_i; \qquad \mathbb{K}^m(s_i) = \mathbb{K}^m_i. \tag{3.76}$$

Substituting (3.74) in (3.65), taking into account (3.75) and (3.76), and letting $\varepsilon \to 0$ yield

$$\begin{aligned}
&\mathcal{E} = \\
&\int_{\mathcal{S}} \frac{\mathbb{K}^e}{2} \left(\tilde{l}^{1S}\right)^2 \mathrm{ds} + \int_{\mathcal{S}} \frac{\mathbb{K}^e}{2} \left(\tilde{l}^{1D}\right)^2 \mathrm{ds} \\
&+ \int_{\mathcal{S}} \frac{\mathbb{K}^e}{2} \left(\tilde{l}^{2S}\right)^2 \mathrm{ds} + \int_{\mathcal{S}} \frac{\mathbb{K}^e}{2} \left(\tilde{l}^{2D}\right)^2 \mathrm{ds} + \\
&+ \int_{\mathcal{S}} \frac{\mathbb{K}^f}{2} \left\{ \vartheta' \right. \\
&\left. + \frac{-\sqrt{2}\left(\|\chi'\|^2\right)' - 4\left[\left(\tilde{l}^{2D} - \tilde{l}^{2S}\right) - \left(\|\chi'\|^2 - 1\right)\left(\tilde{l}^{1D} - \tilde{l}^{1S}\right)\right]}{\|\chi'\|\sqrt{2 - \|\chi'\|^2}} \right\}^2 \mathrm{ds} + \\
&+ \int_{\mathcal{S}} \frac{\mathbb{K}^f}{2} \left\{ \vartheta' \right. \\
&\left. + \frac{\sqrt{2}\left(\|\chi'\|^2\right)' + 4\left[\left(\tilde{l}^{1D} - \tilde{l}^{1S}\right) + \left(\|\chi'\|^2 - 1\right)\left(\tilde{l}^{2S} - \tilde{l}^{2D}\right)\right]}{\|\chi'\|\sqrt{2 - \|\chi'\|^2}} \right\}^2 \mathrm{ds} + \\
&+ \int_{\mathcal{S}} \frac{\mathbb{K}^m}{2} \left(\|\chi'\| - 1\right)^2 \mathrm{ds},
\end{aligned} \tag{3.77}$$

which is the continuum-limit macro-model energy for a $1D$ pantographic beam under the hypothesis of quasi-inextensible oblique micro-springs. It is worth to remark that, when $\mathbb{K}^m = 0$, $\tilde{l}^{\alpha\beta} = 0$ and $\chi(s) = Cs\mathbf{e}_1$, with $C \in \mathbb{R}$, the beam undergoes a floppy mode, i.e., (3.77) vanishes. Thus, under the above conditions, the configuration $\chi(s) = Cs\mathbf{e}_1$ is isoenergetic to the undeformed configuration for any C. For a fixed

ε, considering $k_i^m = 0$ and $\tilde{l}_i^{\alpha\beta} = 0$ in the micro-model energy (3.65), we have that $\chi(s_i) = Cs_i\mathbf{e}_1$ is a floppy mode for the micro-model as well. This means that the homogenization procedure that we have carried out has preserved a key feature of the micro-model. Up to now, the expression of the continuum-limit homogenized energy depends both on the kinematical maps χ and $\tilde{l}$. In the next section, we show that, at equilibrium, it is possible to write the macro-energy in terms of the placement field only.

Macro-model Energy as a Function of the Placement Field

We now equate to zero the first variations of (3.77) with respect to $\tilde{l}^{\alpha\beta}$'s, i.e., we look for stationary points, with respect to $\tilde{l}^{\alpha\beta}$, of (3.77). This is a necessary first-order condition for optimality. In the continuum limit homogenized energy, no spatial derivatives of $\tilde{l}^{\alpha\beta}$ appear. Such energy depends only by linear and quadratic contributions in $\tilde{l}^{\alpha\beta}$. Hence, this process yields four algebraic linear equations in $\tilde{l}^{\alpha\beta}$. Solving these equations gives $\tilde{l}^{\alpha\beta}$ at equilibrium

$$\begin{aligned}
\tilde{l}^{1D} &= \frac{\sqrt{2}}{2}\mathbb{K}^f\left(\chi''\cdot C + \vartheta' D\right)\\
\tilde{l}^{2D} &= \frac{\sqrt{2}}{2}\mathbb{K}^f\left(\chi''\cdot C - \vartheta' D\right)\\
\tilde{l}^{1S} &= \frac{\sqrt{2}}{2}\mathbb{K}^f\left(-\chi''\cdot C - \vartheta' D\right)\\
\tilde{l}^{2S} &= \frac{\sqrt{2}}{2}\mathbb{K}^f\left(-\chi''\cdot C + \vartheta' D\right)
\end{aligned} \tag{3.78}$$

with

$$\begin{aligned}
C &= \frac{\chi'}{2\mathbb{K}^f\|\chi'\|^2 - \frac{1}{2}\left(\mathbb{K}^e\|\chi'\|^2 + 8\mathbb{K}^f\right)}\\
D &= \frac{\|\chi'\|\sqrt{4\tilde{L}^2 - \|\chi'\|^2}}{\mathbb{K}^e\tilde{L}^2\left(\|\chi'\|^2 - 2\right) - 2\mathbb{K}^f\|\chi'\|^2}.
\end{aligned}$$

From (3.78), we can get, in some particular cases, interesting information about the properties of the pantographic beam. First, let us notice that $\tilde{l}^{1D} = -\tilde{l}^{1S}$ and $\tilde{l}^{2D} = -\tilde{l}^{2S}$. Moreover, we also notice that when $\chi' = \rho\mathbf{e}_1$, with ρ independent of the abscissa s, then, as χ'' vanishes, $\tilde{l}^{\alpha\beta} = 0$, i.e., the fibers undergo no elongation. Instead, when $\chi'(s) = \rho(s)\,\mathbf{e}_1$, with ρ depending on s, then $\tilde{l}^{1D} = \tilde{l}^{2D} = -\tilde{l}^{1S} = -\tilde{l}^{2S}$. This remarkable and counterintuitive feature can be used as a possible benchmark test to validate, as ε approaches zero, a numerical scheme based on the discrete micro-model. Let us consider the case of nonzero bending curvature, i.e., $\vartheta' \neq 0$, when $\chi''\cdot C << \vartheta' D$, which implies that $\tilde{l}^{1D} = -\tilde{l}^{2D} = -\tilde{l}^{1S} = \tilde{l}^{2S}$. If $\vartheta' > 0$ then

$\tilde{l}^{1D}, \tilde{l}^{2S} > 0$ and $\tilde{l}^{2D}, \tilde{l}^{1S} < 0$ while, if $\vartheta' < 0$ then $\tilde{l}^{1D}, \tilde{l}^{2S} < 0$ and $\tilde{l}^{2D}, \tilde{l}^{1S} > 0$. We are now ready to express the macro-model energy $\overline{\mathcal{E}}(\chi)$ as a function of the placement χ only, by substituting (3.78) in (3.77):

$$
\begin{aligned}
&\overline{\mathcal{E}}(\chi(\cdot)) = \min_{\tilde{l}^{\alpha\beta}(\cdot)} \mathcal{E} = \qquad (3.79)\\
&\int_{\mathcal{S}} \mathbb{K}^e \mathbb{K}^f \left\{ \frac{\left(\rho^2 - 2\right)}{\rho^2 \left(\mathbb{K}^e - 4\mathbb{K}^f\right) - 2\mathbb{K}^e} \vartheta'^2 \right.\\
&\left. + \frac{\rho^2}{\left(2 - \rho^2\right)\left[\rho^2 \left(\mathbb{K}^e - 4\mathbb{K}^f\right) + 8\mathbb{K}^f\right]} \rho'^2 \right\} \mathrm{ds} +\\
&+ \int_{\mathcal{S}} \frac{\mathbb{K}^m}{2} (\rho - 1)^2 \, \mathrm{ds} =\\
&= \int_{\mathcal{S}} \frac{\mathbb{K}^e \mathbb{K}^f \left(\|\chi'\|^2 - 2\right)}{\|\chi'\|^4 \left[\|\chi'\|^2 \left(\mathbb{K}^e - 4\mathbb{K}^f\right) - 2\mathbb{K}^e\right]} \left(\chi'_\perp \cdot \chi''\right)^2 \mathrm{ds} +\\
&+ \int_{\mathcal{S}} \frac{\mathbb{K}^e \mathbb{K}^f}{\left(2 - \|\chi'\|^2\right)\left[\|\chi'\|^2 \left(\mathbb{K}^e - 4\mathbb{K}^f\right) + 8\mathbb{K}^f\right]} \left(\chi' \cdot \chi''\right)^2 \mathrm{ds} +\\
&+ \int_{\mathcal{S}} \frac{\mathbb{K}^m}{2} \left(\|\chi'\| - 1\right)^2 \mathrm{ds}.
\end{aligned}
$$

We observe that, for $0 < \rho < \sqrt{2}$ and for any choice of the positive macro-stiffnesses $\mathbb{K}^e$, $\mathbb{K}^f$, and $\mathbb{K}^m$, (3.79) is positive definite. Moreover, not only we can classify this homogenized model as a second gradient theory, but we notice that the full second gradient χ'' of χ contributes to the strain energy. Indeed, beyond the usual term $\left(\chi'_\perp \cdot \chi''\right)$ related to the Lagrangian curvature, also the term $\left(\chi' \cdot \chi''\right)$, deriving from the presence of the oblique springs, appears. There is a remarkable feature in this model which deserves to be discussed. From (3.79), it is clear that in the limit $||\chi'|| \to \sqrt{2}$ the model exhibits a so-called phase transition: it locally degenerates into the model of an uniformly extensible cable, notwithstanding that $\sqrt{2}$ is an upper bound for ρ. Indeed,

$$
\begin{aligned}
&\frac{\left(\rho^2 - 2\right)}{\rho^2 \left(\mathbb{K}^e - 4\mathbb{K}^f\right) - 2\mathbb{K}^e} \to 0\\
&\frac{\rho^2}{\left(2 - \rho^2\right)\left[\rho^2 \left(\mathbb{K}^e - 4\mathbb{K}^f\right) + 8\mathbb{K}^f\right]} \to +\infty,
\end{aligned}
$$

so that no deformation energy is stored for finite bending curvature and, in order for the energy to be bounded for bounded deformations, ρ' must approach zero, meaning that the elongation must be locally uniform. Further developments of this model could consist in contemplating a phase transition to a model that, for finite bending curvature, entails a nonzero stored deformation energy.

Nondimensionalization

In order to handle more easily the model in the numerical implementation and in the interpretation of the corresponding results, we turn to the use of nondimensional quantities. Therefore, we introduce the following nondimensional fields:

$$s = B\bar{s}; \quad \chi = B\bar{\chi}; \quad \mathbb{K}^e = K\overline{\mathbb{K}}^e; \quad \mathbb{K}^f = K\overline{\mathbb{K}}^f; \quad \mathbb{K}^m = K^m\overline{\mathbb{K}}^m.$$

In terms of these new quantities, we can recast (3.79) as

$$\begin{aligned}
&\frac{K}{B}\int_0^1 \frac{\overline{\mathbb{K}}^e\overline{\mathbb{K}}^f\left(\|\bar{\chi}'\|^2-2\right)}{\|\bar{\chi}'\|^4\left[\|\bar{\chi}'\|^2\left(\overline{\mathbb{K}}^e-4\overline{\mathbb{K}}^f\right)-2\overline{\mathbb{K}}^e\right]}\left(\bar{\chi}'_\perp\cdot\bar{\chi}''\right)^2 \mathrm{d}\bar{s} + \\
&+\frac{K}{B}\int_0^1 \frac{\overline{\mathbb{K}}^e\overline{\mathbb{K}}^f\left(\bar{\chi}'\cdot\bar{\chi}''\right)^2}{\left(2-\|\bar{\chi}'\|^2\right)\left[\|\bar{\chi}'\|^2\left(\overline{\mathbb{K}}^e-4\overline{\mathbb{K}}^f\right)+8\overline{\mathbb{K}}^f\right]}\mathrm{d}\bar{s} + \\
&+K^mB\int_0^1 \frac{\overline{\mathbb{K}}^m}{2}\left(\|\bar{\chi}'\|-1\right)^2\mathrm{d}\bar{s},
\end{aligned} \tag{3.80}$$

where the symbol $\bar{}'$ denotes differentiation with respect to the dimensionless abscissa $\bar{s}$.

The Inextensibility Case

Let us focus now on the inextensibility case. The homogenization procedure follows the same lines of the previous case. Indeed, keeping in mind (3.75) and (3.76), letting $\varepsilon \to 0$ in (3.73) yields the continuum-limit macro-model energy for the inextensibility case

$$\begin{aligned}
&\int_{\mathcal{S}}\left\{\mathbb{K}^f\left[\vartheta'^2+\frac{\rho'^2}{2-\rho^2}\right]+\frac{\mathbb{K}^m}{2}(\rho-1)^2\right\}\mathrm{ds} = \\
&=\int_{\mathcal{S}}\left\{\mathbb{K}^f\left[\frac{\left(\chi_\perp\cdot\chi''\right)^2}{\|\chi'\|^4}+\frac{\left(\chi\cdot\chi''\right)^2}{\|\chi'\|^2\left(2-\|\chi'\|^2\right)}\right]+\frac{\mathbb{K}^m}{2}\left(\|\chi'\|-1\right)^2\right\}\mathrm{ds}.
\end{aligned} \tag{3.81}$$

This result is consistent with the quasi-inextensibility case. Indeed, we could have found (3.81) also by letting $\mathbb{K}^e \to +\infty$ in (3.79). Let us remark that, also in this case, the homogenized continuum model, due to the richness of the microstructure, gives rise to a full second gradient theory.

Linearization

An interesting connection can be traced with the existing literature on the formulation of 1D continuum homogenized model for microstructured media and, in particular, for pantographic ones. Indeed, this connection is traced by considering a linearization of the pantographic beam energy in the (complete) inextensibility case. We set $\chi(s) = \begin{pmatrix} s \\ 0 \end{pmatrix} + \eta\tilde{u}$, with $\tilde{u}$ independent of η, i.e., we linearize with respect to the displacement $u = \chi(s) - \begin{pmatrix} s \\ 0 \end{pmatrix}$, and $\mathbb{K}^m = 0$. By means of simple algebra manipulations, it is possible to derive the deformation energy in Eq. (5) (with $K^+ = K^-$) of Alibert et al. (2003) (see also Seppecher et al. 2011):

$$\int_{\mathcal{S}} \mathbb{K}^f \|u''\|^2 \, \mathrm{ds}. \tag{3.82}$$

We remark that in the linearized energy (3.82) the transverse displacement and the axial one decouple.

Numerical Simulations of the Continuous Model

Preliminaries

Using the so-obtained 1D continuum model, we show some equilibrium shapes exhibiting highly non-standard features, essentially related to the complete dependence of the homogenized continuum energy density functional on the second gradient of the placement field.

In the sequel, $\mathbb{K}^m = 0$ will be considered, which means that the standard quadratic additive elongation/shortening contribution to the deformation energy will be turned off. This is made in order to better highlight some non-standard features of the nearly inextensible pantographic beam model. In this section, we show numerical results for the quasi-inextensible and inextensible pantographic beam model and for the geometrically nonlinear Euler model. We remind that these cases stand for $\mathbb{K}^e < +\infty$ and $\mathbb{K}^e \to +\infty$, respectively. Two benchmark tests are exploited in order to illustrate peculiar and non-standard features of the pantographic beam model. Convergence of the quasi-inextensible pantographic beam model to the completely inextensible one is shown, by means of a numerical example, as the macro-stiffness $\mathbb{K}^e$ related to elongation of the oblique springs approaches $+\infty$. This is due to the fact that, as it is clear from Eq. (3.77), if $\mathbb{K}^e \to +\infty$, then $\tilde{l}^{\alpha\beta} \to 0$. Of course, the same discussion and simulations can be made for the micro-model and this could be the subject of a further investigation. For the sake of self-consistence, we recall that the deformation energy of the geometrically nonlinear Euler model employed in the following simulations is the following:

$$\int_{\mathcal{S}} \left\{ \frac{K^e}{2} \left(\|\chi'\| - 1 \right)^2 + \frac{K^b}{2} \left[\frac{\chi'' \cdot \chi''}{\|\chi'\|^2} - \left(\frac{\chi' \cdot \chi''}{\|\chi'\|^2} \right)^2 \right] \right\} \, \mathrm{ds} =$$
$$= \int_{\mathcal{S}} \left\{ \frac{K^e}{2} (\rho - 1)^2 + \frac{K^b}{2} \vartheta'^2 \right\} \, \mathrm{ds},$$

and we notice that, while in the nearly inextensible pantographic beam model both ρ and ϑ can be enforced at the boundary, for the nonlinear Euler model it can be done for ϑ only, as no spatial derivative of ρ appears in the energy.

Semi-circle Test

We consider for both the nearly inextensible pantographic beam model and the geometrically nonlinear Euler beam model the reference domain to be the interval $[0, 2\pi]$. We enforce the following boundary conditions for both models

$$1.\ \chi(0) = \mathbf{0}; \quad 2.\ \chi(2\pi) = 2\mathbf{e}_1; \quad 3.\ \vartheta(0) = -\frac{\pi}{2}; \quad 4.\ \vartheta(2\pi) = \frac{\pi}{2}$$

and, for the nearly inextensible pantographic beam model, we also have the following two additional constraints:

$$5.\ \rho(0) = \rho_0; \quad 6.\ \rho(2\pi) = \rho_0.$$

In Fig. 3.6 (up), the deformed shapes for the nearly inextensible pantographic beam model and for the geometrically nonlinear Euler beam model (GNEM) are shown for different values of ρ_0 reported in the legend. In Fig. 3.6 (down), the elongation $\rho - 1$ for the nearly inextensible pantographic beam model and for the geometrically nonlinear Euler beam model (GNEM) is shown for different values of ρ_0 reported in the legend. It is remarkable that passing from $\rho_0 > 1$ to $\rho < 1$, there is a change

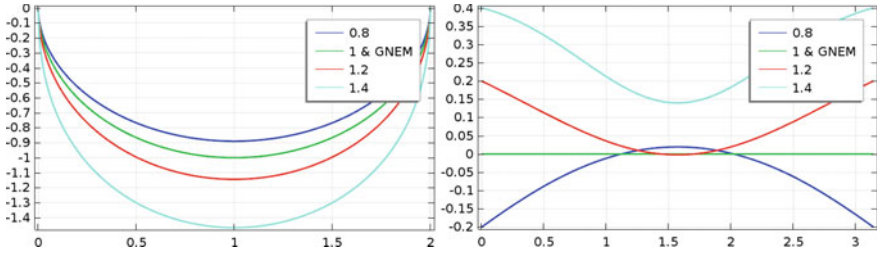

Fig. 3.6 Semi-circle test. Deformed shapes for the nearly inextensible pantographic beam model and for the geometrically nonlinear Euler beam model (GNEM). (left) Elongation $\rho - 1$ versus the reference abscissa for the nearly inextensible pantographic beam model and for the geometrically nonlinear Euler beam model (GNEM) (right). Numbers in the legends stand for different dimensionless values of ρ_0

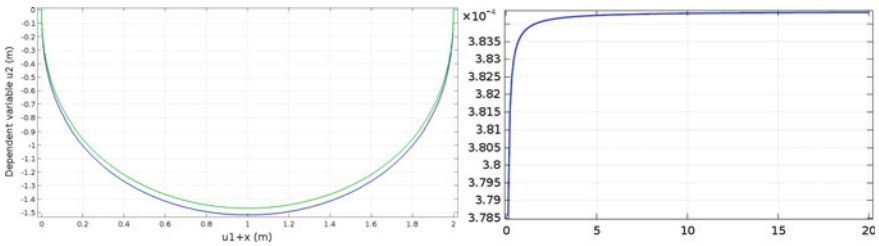

Fig. 3.7 Semi-circle test. Deformed shapes for the nearly inextensible pantographic beam model (blue) and for the inextensible pantographic beam model (green) with $\rho_0 = 1.4$ (left). Energy of the nearly inextensible pantographic beam model (ordinate) asymptotically tends to the energy of the inextensible pantographic beam model (asymptote) as $\mathbb{K}^e$ (abscissa) $\to +\infty$ (right)

of concavity in the elongation for the pantographic beam model. In Fig. 3.7 (up), the deformed shapes for the nearly inextensible pantographic beam model (blue) and for the inextensible pantographic beam model (green) with $\rho_0 = 1.4$ are compared. Of course, the area spanned by the quasi-inextensible pantographic beam includes that of the (completely) inextensible one. In Fig. 3.7 (down), it is numerically shown that the energy of the nearly inextensible pantographic beam model (ordinate) asymptotically tends to the energy of the inextensible pantographic beam model (asymptote) as $\mathbb{K}^e$ (abscissa) $\to +\infty$.

Three-Point Test

We consider for both the quasi-inextensible pantographic beam model and the geometrically nonlinear Euler beam model the reference domain to be the interval $[0, 2]$. We enforce the following boundary conditions for both models:

$$1.\ \chi(0) = \mathbf{0}; \quad 2.\ \chi(1) \cdot \mathbf{e}_2 = \overline{u}; \quad 3.\ \chi(2) = \mathbf{0};$$
$$4.\ \vartheta(0) = 0; \quad 5.\ \vartheta(2) = 0.$$

In Fig. 3.8, the deformed shapes for the nearly inextensible pantographic beam model (red, light blue) and for the geometrically nonlinear Euler beam model (blue, green) are shown for different values of $\overline{u}$ in the legend. Figure 3.9 shows, for different values of the parameter $\overline{u}$, the elongation $\rho - 1$ versus the reference abscissa for the nearly inextensible pantographic beam model. The parameter $\overline{u}$ is increasing from bottom to top. We observe that, as $\overline{u}$ increases, at some point, there is a concavity change in the elongation plot and, increasing further the parameter $\overline{u}$, curves start to intersect. This means that, for some points of the beam, an increase of the prescribed displacement $\overline{u}$ implies a decrease in the elongation. Figure 3.10 shows the pulling force, i.e., Lagrange multiplier associated to the weak constraint $\chi(1) \cdot \mathbf{e}_2 = \overline{u}$, changed of sign, applied at the midpoint in order to vertically displace it of an amount $\overline{u}$. In the nearly inextensible pantographic beam model (blue) negative stiffness property, also

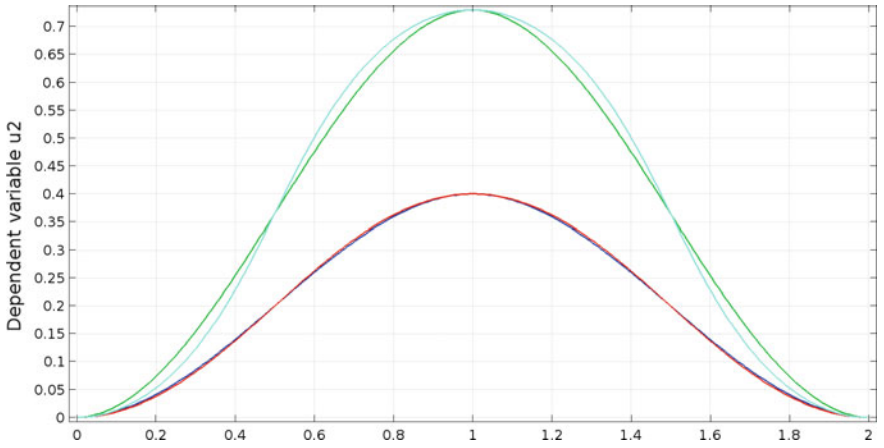

Fig. 3.8 Three-point test. Deformed shapes for the nearly inextensible pantographic beam model (red, light blue) and for the geometrically nonlinear Euler beam model (blue, green) for different values of $\overline{u}$ in the legend

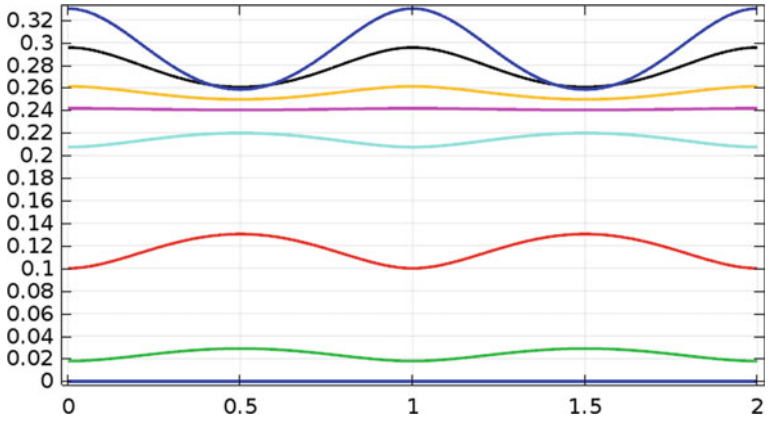

Fig. 3.9 Three-point test. Elongation $\rho - 1$ versus the reference abscissa for the nearly inextensible pantographic beam model. The parameter $\overline{u}$ is increasing from bottom to top. We observe that, while increasing $\overline{u}$, there is a concavity change at some point. Increasing further the parameter $\overline{u}$, curves start to intersect

known as elastic softening, is observed, while in the geometrically nonlinear Euler beam model (green) elastic softening is not observed. Figure 3.11 shows the plot of $\tilde{l}^{1D}$ versus reference abscissa for different values of $\overline{u}$ in the legend. Analogous plots hold for $\tilde{l}^{2D}$, $\tilde{l}^{1S}$, and $\tilde{l}^{2S}$.

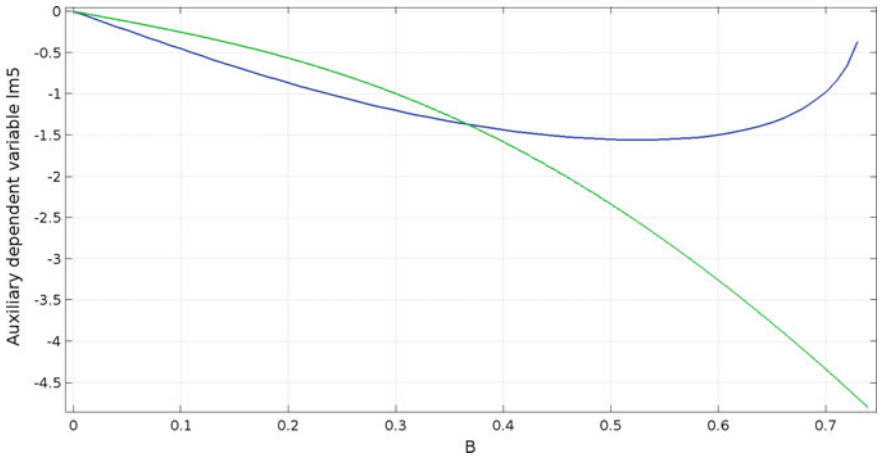

Fig. 3.10 Three-point test. Pulling force (i.e., Lagrange multiplier associated to the weak constraint $\chi(1) \cdot \mathbf{e}_2 = \overline{u}$), changed of sign, applied at the midpoint in order to vertically displace it of an amount $\overline{u}$ (abscissa). In the nearly inextensible pantographic beam model (blue) elastic softening is observed, while in the geometrically nonlinear beam model (green) elastic softening is not observed

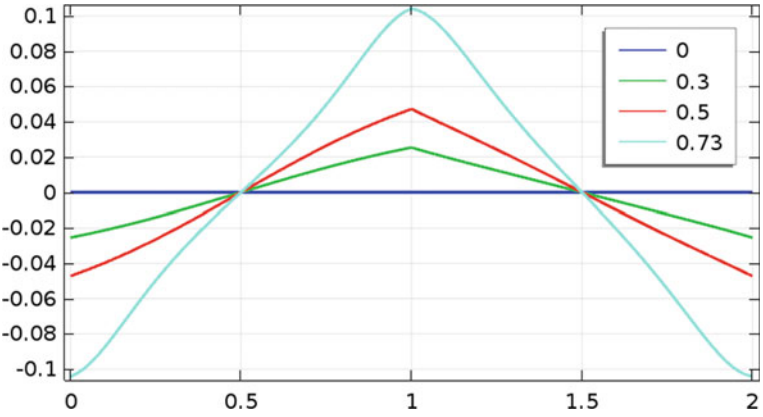

Fig. 3.11 Three-point test. Plot of $\tilde{l}^{1D}$ versus reference abscissa for different values of $\overline{u}$ in the legend. Analogous plots hold for $\tilde{l}^{2D}$, $\tilde{l}^{1S}$ and $\tilde{l}^{2S}$

Modified Three-Point Test

We consider for both the quasi-inextensible pantographic beam model and the geometrically nonlinear Euler beam model the reference domain to be the interval $[0, 2]$. We enforce the three-point test boundary conditions for both models

$$1.\ \chi(0) = \mathbf{0}; \quad 2.\ \chi(1) \cdot \mathbf{e}_2 = \overline{u}; \quad 3.\ \chi(2) = \mathbf{0};$$
$$4.\ \vartheta(0) = 0; \quad 5.\ \vartheta(2) = 0$$

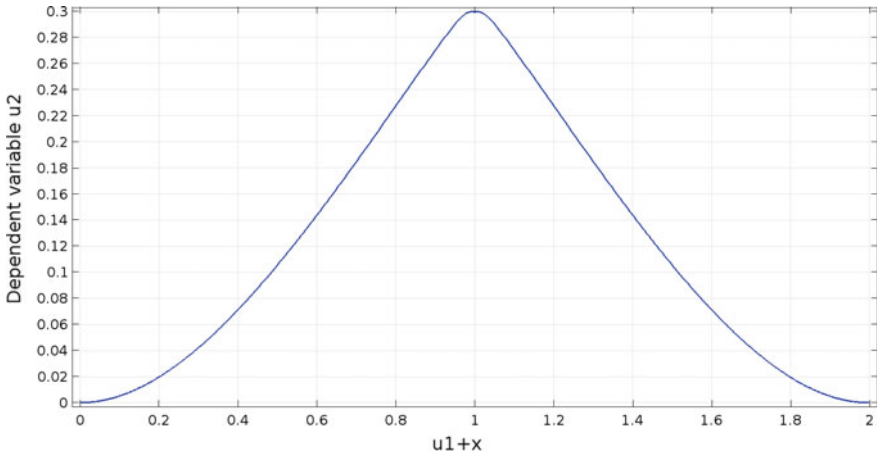

Fig. 3.12 Modified three-point test. Deformed configuration for the nearly inextensible pantographic beam model

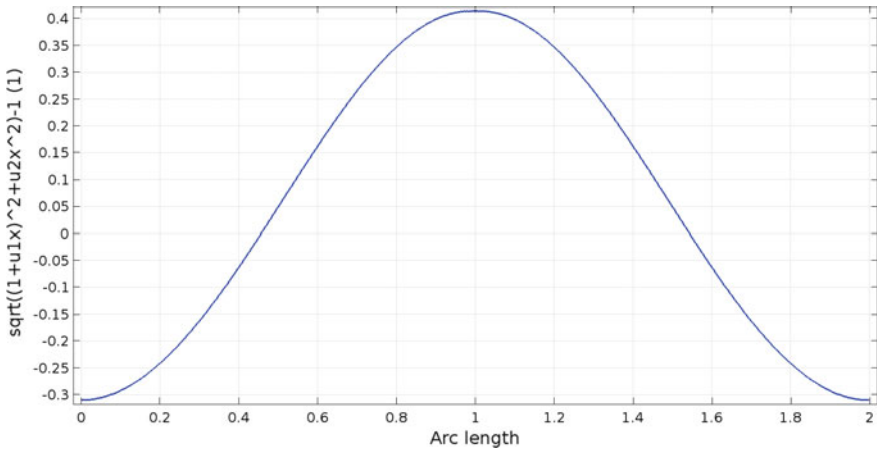

Fig. 3.13 Modified three-point test. Elongation $\rho - 1$ versus reference abscissa for the nearly inextensible pantographic beam model

with the additional condition, at the midpoint $s = 1$,

$$6.\ \rho(1) \simeq \sqrt{2}.$$

Figure 3.12 shows the deformed configuration for the nearly inextensible pantographic beam model, while in Fig. 3.13 the elongation $\rho - 1$ versus the reference abscissa for the nearly inextensible pantographic beam model is shown.

References

Abali, B. E., Müller, W. H., & dell'Isola, F. (2017). Theory and computation of higher gradient elasticity theories based on action principles. *Archive of Applied Mechanics*, 1–16.

Abali, B. E., Müller, W. H., & Eremeyev, V. A. (2015). Strain gradient elasticity with geometric nonlinearities and its computational evaluation. *Mechanics of Advanced Materials and Modern Processes*, *1*(1), 4.

Alibert, J., & Della Corte, A. (2015). Second-gradient continua as homogenized limit of pantographic microstructured plates: A rigorous proof. *Zeitschrift für angewandte Mathematik und Physik, 66*(5), 2855–2870.

Alibert, J.-J., Della Corte, A., Giorgio, I., & Battista, A. (2017). Extensional elastica in large deformation as Γ-limit of a discrete 1d mechanical system. *Zeitschrift für angewandte Mathematik und Physik, 68*(2), 42.

Alibert, J.-J., Seppecher, P., & dell'Isola, F. (2003). Truss modular beams with deformation energy depending on higher displacement gradients. *Mathematics and Mechanics of Solids*, *8*(1), 51–73.

Allaire, G. (1992). Homogenization and two-scale convergence. *SIAM Journal on Mathematical Analysis*, *23*(6), 1482–1518.

Altenbach, H., & Eremeyev, V. (2009). On the linear theory of micropolar plates. *ZAMM-Journal of Applied Mathematics and Mechanics/Zeitschrift für Angewandte Mathematik und Mechanik*, *89*(4), 242–256.

Andreaus, U., Giorgio, I., & Lekszycki, T. (2013). A 2D continuum model of a mixture of bone tissue and bio-resorbable material for simulating mass density redistribution under load slowly variable in time. *Zeitschrift für Angewandte Mathematik und Mechanik*, *13*, 7.

Andreaus, U., Giorgio, I., & Madeo, A. (2014). Modeling of the interaction between bone tissue and resorbable biomaterial as linear elastic materials with voids. *Zeitschrift für angewandte Mathematik und Physik*, *66*(1), 209–237.

Andreaus, U., Placidi, L., & Rega, G. (2010). Numerical simulation of the soft contact dynamics of an impacting bilinear oscillator. *Communications in Nonlinear Science and Numerical Simulation*, *15*(9), 2603–2616.

Antman, S. S. (1995). Nonlinear problems of elasticity. In *Applied mathemathical science* (Vol. 107). Berlin and New York: Springer.

Auffray, N., dell'Isola, F., Eremeyev, V., Madeo, A., & Rosi, G. (2015). Analytical continuum mechanics à la Hamilton-Piola least action principle for second gradient continua and capillary fluids. *Mathematics and Mechanics of Solids*, *20*(4), 375–417.

Barchiesi, E., & Placidi, L. (2017). A review on models for the 3d statics and 2d dynamics of pantographic fabrics. In *Wave dynamics and composite mechanics for microstructured materials and metamaterials* (pp. 239–258). Springer.

Battista, A., Cardillo, C., Del Vescovo, D., Rizzi, N. L., & Turco, E. (2015). Frequency shifts induced by large deformations in planar pantographic continua. *Nanomechanics Science and Technology: An International Journal,6*(2).

Battista, A., Rosa, L., dell'Erba, R., & Greco, L. (2016). Numerical investigation of a particle system compared with first and second gradient continua: Deformation and fracture phenomena. *Mathematics and Mechanics of Solids*, 1081286516657889.

Bensoussan, A., Lions, J.-L., & Papanicolaou, G. (1978). *Asymptotic analysis for periodic structures* (Vol. 5). Amsterdam: North-Holland Publishing Company.

Bersani, A. M., Della Corte, A., Piccardo, G., & Rizzi, N. L. (2016). An explicit solution for the dynamics of a taut string of finite length carrying a traveling mass: The subsonic case. *Zeitschrift für angewandte Mathematik und Physik, 67*(4), 108.

Boutin, C., Giorgio, I., Placidi, L., et al. (2017). Linear pantographic sheets: Asymptotic micro-macro models identification. *Mathematics and Mechanics of Complex Systems*, *5*(2), 127–162.

Carcaterra, A., dell'Isola, F., Esposito, R., & Pulvirenti, M. (2015). Macroscopic description of microscopically strongly inhomogeneous systems: A mathematical basis for the synthesis of

higher gradients metamaterials. *Archive for Rational Mechanics and Analysis*, *218*(3), 1239–1262.

Cuomo, M., dell'Isola, F., Greco, L., & Rizzi, N. L. (2016). First versus second gradient energies for planar sheets with two families of inextensible fibres: Investigation on deformation boundary layers, discontinuities and geometrical instabilities. *Composites Part B: Engineering*.

Del Vescovo, D., & Giorgio, I. (2014). Dynamic problems for metamaterials: Review of existing models and ideas for further research. *International Journal of Engineering Science*, *80*, 153–172.

dell Isola, F., Seppecher, P., & Della Corte, A. (2015). The postulations á la d alembert and á la cauchy for higher gradient continuum theories are equivalent: A review of existing results. *Proceedings of the Royal Society A, 471*, 20150415 (The Royal Society).

Della Corte, A., Battista, A., & dell'Isola, F. (2016). Referential description of the evolution of a 2d swarm of robots interacting with the closer neighbors: Perspectives of continuum modeling via higher gradient continua. *International Journal of Non-Linear Mechanics, 80*, 209–220.

dell'Isola, F., Cuomo, M., Greco, L., & Della Corte, A. (2016a). Bias extension test for pantographic sheets: Numerical simulations based on second gradient shear energies. *Journal of Engineering Mathematics*, 1–31.

dell'Isola, F., Della Corte, A., Giorgio, I., & Scerrato, D. (2016c). Pantographic 2d sheets: Discussion of some numerical investigations and potential applications. *International Journal of Non-Linear Mechanics, 80*, 200–208.

dell'Isola, F., Della Corte, A., & Giorgio, I. (2016b). Higher-gradient continua: The legacy of Piola, Mindlin, Sedov and Toupin and some future research perspectives. *Mathematics and Mechanics of Solids*, 1081286515616034.

dell'Isola, F., Della Corte, A., Greco, L., & Luongo, A. (2015a). Plane bias extension test for a continuum with two inextensible families of fibers: A variational treatment with lagrange multipliers and a perturbation solution. *International Journal of Solids and Structures*.

Dell'Isola, F., Andreaus, U., & Placidi, L. (2015). At the origins and in the vanguard of peridynamics, non-local and higher-gradient continuum mechanics: An underestimated and still topical contribution of gabrio piola. *Mathematics and Mechanics of Solids*, *20*(8), 887–928.

dell'Isola, F., Giorgio, I., & Andreaus, U. (2015b). Elastic pantographic 2d lattices: A numerical analysis on static response and wave propagation. *Proceedings of the Estonian Academy of Sciences*, *64*, 219–225.

dell'Isola, F., Giorgio, I., Pawlikowski, M., & Rizzi, N. (2016d). Large deformations of planar extensible beams and pantographic lattices: Heuristic homogenization, experimental and numerical examples of equilibrium. *Proceedings of the Royal Society A*, *472*(2185), 20150790.

dell'Isola, F., Lekszycki, T., Pawlikowski, M., Grygoruk, R., & Greco, L. (2015c). Designing a light fabric metamaterial being highly macroscopically tough under directional extension: First experimental evidence. *Zeitschrift für angewandte Mathematik und Physik*, *66*, 3473–3498.

dell'Isola, F., Madeo, A., & Seppecher, P. (2016e). Cauchy tetrahedron argument applied to higher contact interactions. *Archive for Rational Mechanics and Analysis*, *219*(3), 1305–1341.

Enakoutsa, K., Della Corte, A., & Giorgio, I. (2015). A model for elastic flexoelectric materials including strain gradient effects. *Mathematics and Mechanics of Solids*, 1081286515588638.

Eremeyev, V. A., dell'Isola, F., Boutin, C., & Steigmann, D. (2017). Linear pantographic sheets: Existence and uniqueness of weak solutions.

Euler, L., & Carathéodory, C. (1952). *Methodus inveniendi lineas curvas maximi minimive proprietate gaudentes sive solutio problematis isoperimetrici latissimo sensu accepti* (Vol. 1). Springer Science & Business Media.

Ganzosch, G., dell'Isola, F., Turco, E., Lekszycki, T., & Müller, W. H. (2016). Shearing tests applied to pantographic structures. *Acta Polytechnica CTU Proceedings, 7*, 1–6.

Giorgio, I. (2016). Numerical identification procedure between a micro-cauchy model and a macro-second gradient model for planar pantographic structures. *Zeitschrift für angewandte Mathematik und Physik, 67*(4)(95).

Giorgio, I., Andreaus, U., Lekszycki, T., & Della Corte, A. (2015). The influence of different geometries of matrix/scaffold on the remodeling process of a bone and bioresorbable material mixture with voids. *Mathematics and Mechanics of Solids*, 1081286515616052.

Giorgio, I., Della Corte, A., & dell'Isola, F. (2017). Dynamics of 1d nonlinear pantographic continua. *Nonlinear Dynamics, 88*(1), 21–31.

Giorgio, I., Della Corte, A., dell'Isola, F., & Steigmann, D. (2016). Buckling modes in pantographic lattices. *Comptes rendus Mecanique*.

Greco, L., Giorgio, I., & Battista, A. (2016). In plane shear and bending for first gradient inextensible pantographic sheets: Numerical study of deformed shapes and global constraint reactions. *Mathematics and Mechanics of Solids*, 1081286516651324.

Jamal, R., & Sanchez-Palencia, E. (1996). Théorie asymptotique des tiges courbes anisotropes. *Comptes rendus de l'Académie des sciences. Série 1, Mathématique, 322*(11), 1099–1106.

Madeo, A., Barbagallo, G., d'Agostino, M., Placidi, L., & Neff, P. (2016). First evidence of non-locality in real band-gap metamaterials: Determining parameters in the relaxed micromorphic model. *Proceedings of the Royal Society A, 472*, 20160169. The Royal Society.

Madeo, A., Della Corte, A., Greco, L., & Neff, P. (2014a). Wave propagation in pantographic 2d lattices with internal discontinuities. arXiv:1412.3926.

Madeo, A., Neff, P., Ghiba, I., Placidi, L., & Rosi, G. (2014b). Band gaps in the relaxed linear micromorphic continuum. arXiv:1405.3493.

Madeo, A., Placidi, L., & Rosi, G. (2014c). Towards the design of metamaterials with enhanced damage sensitivity: Second gradient porous materials. *Research in Nondestructive Evaluation*, *25*(2), 99–124.

Misra, A., & Poorsolhjouy, P. (2015). Granular micromechanics model for damage and plasticity of cementitious materials based upon thermomechanics. *Mathematics and Mechanics of Solids*, 1081286515576821.

Misra, A., & Singh, V. (2013). Micromechanical model for viscoelastic materials undergoing damage. *Continuum Mechanics and Thermodynamics*, 1–16.

Misra, A., & Singh, V. (2015). Thermomechanics-based nonlinear rate-dependent coupled damage-plasticity granular micromechanics model. *Continuum Mechanics and Thermodynamics, 27*(4–5), 787.

Misra, A. (2002). Effect of asperity damage on shear behavior of single fracture. *Engineering Fracture Mechanics*, *69*(17), 1997–2014.

Mora, M. G., & Müller, S. (2004). A nonlinear model for inextensible rods as a low energy γ-limit of three-dimensional nonlinear elasticity. *Annales de l'IHP Analyse non linéaire*, *21*, 271–293.

Murat, F., & Sili, A. (1999). Comportement asymptotique des solutions du système de l'élasticité linéarisée anisotrope hétérogène dans des cylindres minces. *Comptes Rendus de l'Académie des Sciences-Series I-Mathematics*, *328*(2), 179–184.

Pideri, C., & Seppecher, P. (2006). Asymptotics of a non-planar rod in non-linear elasticity. *Asymptotic Analysis, 48*(1, 2), 33–54.

Pietraszkiewicz, W., & Eremeyev, V. (2009). On natural strain measures of the non-linear micropolar continuum. *International Journal of Solids and Structures*, *46*(3), 774–787.

Placidi, L., Andreaus, U., & Giorgio, I. (2016a). Identification of two-dimensional pantographic structure via a linear d4 orthotropic second gradient elastic model. *Journal of Engineering Mathematics*, 1–21.

Placidi, L., Andreaus, U., Della Corte, A., & Lekszycki, T. (2015). Gedanken experiments for the determination of two-dimensional linear second gradient elasticity coefficients. *Zeitschrift für angewandte Mathematik und Physik, 66*(6), 3699–3725.

Placidi, L., Barchiesi, E., & Battista, A. (2017). An inverse method to get further analytical solutions for a class of metamaterials aimed to validate numerical integrations. In *Mathematical Modelling in Solid Mechanics* (pp. 193–210). Springer.

Placidi, L., Barchiesi, E., Turco, E., & Rizzi, N. L. (2016b). A review on 2d models for the description of pantographic fabrics. *Zeitschrift für angewandte Mathematik und Physik, 67*(5)(121).

Placidi, L., Greco, L., Bucci, S., Turco, E., & Rizzi, N. L. (2016c). A second gradient formulation for a 2d fabric sheet with inextensible fibres. *Zeitschrift für angewandte Mathematik und Physik, 67*(5)(114).

Placidi, L. (2015). A variational approach for a nonlinear 1-dimensional second gradient continuum damage model. *Continuum Mechanics and Thermodynamics*, *27*(4–5), 623.

Placidi, L., dell'Isola, F., Ianiro, N., & Sciarra, G. (2008). Variational formulation of pre-stressed solid-fluid mixture theory, with an application to wave phenomena. *European Journal of Mechanics-A/Solids*, *27*(4), 582–606.

Rahali, Y., Giorgio, I., Ganghoffer, J. F., & Dell'Isola, F. (2015). Homogenization à la piola produces second gradient continuum models for linear pantographic lattices. *International Journal of Engineering Science*, *97*, 148–172.

Reiher, J. C., Giorgio, I., & Bertram, A. (2016). Finite-element analysis of polyhedra under point and line forces in second-strain gradient elasticity. *Journal of Engineering Mechanics*, *143*(2), 04016112.

Rinaldi, A., & Placidi, L. (2014). A microscale second gradient approximation of the damage parameter of quasi-brittle heterogeneous lattices. *ZAMM-Journal of Applied Mathematics and Mechanics/Zeitschrift für Angewandte Mathematik und Mechanik*, *94*(10), 862–877.

Scerrato, D., Giorgio, I., & Rizzi, N. (2016). Three-dimensional instabilities of pantographic sheets with parabolic lattices: Numerical investigations. *Zeitschrift für angewandte Mathematik und Physik*, *67*(3), 1–19.

Seppecher, P., Alibert, J.-J., & dell'Isola, F. (2011). Linear elastic trusses leading to continua with exotic mechanical interactions. In *Journal of Physics: Conference Series* (Vol. 319, p. 012018). IOP Publishing.

Spagnuolo, M., Barcz, K., Pfaff, A., dell'Isola, F., & Franciosi, P. (2017). Qualitative pivot damage analysis in aluminum printed pantographic sheets: Numerics and experiments. *Mechanics Research Communications*.

Turco, E., Barcz, K., Pawlikowski, M., & Rizzi, N. L. (2016a). Non-standard coupled extensional and bending bias tests for planar pantographic lattices. Part I: Numerical simulations. *Zeitschrift für angewandte Mathematik und Physik, 67*(5), 122.

Turco, E., dell'Isola, F., Cazzani, A., & Rizzi, N. L. (2016b). Hencky-type discrete model for pantographic structures: Numerical comparison with second gradient continuum models. *Zeitschrift für angewandte Mathematik und Physik, 67*.

Turco, E., dell'Isola, F., Rizzi, N. L., Grygoruk, R., Müller, W. H., & Liebold, C. (2016c). Fiber rupture in sheared planar pantographic sheets: Numerical and experimental evidence. *Mechanics Research Communications*, *76*, 86–90.

Turco, E., Golaszewski, M., Cazzani, A., & Rizzi, N. L. (2016d). Large deformations induced in planar pantographic sheets by loads applied on fibers: Experimental validation of a discrete lagrangian model. *Mechanics Research Communications*, *76*, 51–56.

Turco, E., Golaszewski, M., Giorgio, I., & D'Annibale, F. (2017). Pantographic lattices with non-orthogonal fibres: Experiments and their numerical simulations. *Composites Part B: Engineering*, *118*, 1–14.

Turco, E., & Rizzi, N. L. (2016). Pantographic structures presenting statistically distributed defects: Numerical investigations of the effects on deformation fields. *Mechanics Research Communications*, *77*, 65–69.

Yang, Y., & Misra, A. (2010). Higher-order stress-strain theory for damage modeling implemented in an element-free Galerkin formulation. *CMES: Computer Modeling in Engineering & Sciences*, *64*(1), 1–36.

Yang, Y., & Misra, A. (2012). Micromechanics based second gradient continuum theory for shear band modeling in cohesive granular materials following damage elasticity. *International Journal of Solids and Structures*, *49*(18), 2500–2514.

Chapter 4
Simulation of Continuous Fibre Composite Forming

Philippe Boisse

Abstract The quality and properties of a composite material part depend not only on the fibres and matrix but also on how they have been manufactured. The numerical simulation of the forming of composites makes it possible not only to analyse the feasibility of a process and its defects but also to determine the directions of the reinforcements after the forming process. These directions strongly influence the mechanical behaviour of the composite part in service. Some approaches used to simulate the forming of woven reinforcements are described. In particular, a stress resultant triangular shell finite element specific to textile reinforcements is presented. The tests used for textile reinforcements in biaxial tension, in-plane shear and bending are presented. Finally, the simulation of thermoforming of thermoplastic prepreg is presented. During simulations, thermal and mechanical calculations are performed sequentially to update the mechanical properties with the evolution of the temperature field and the temperature field with the contact with the tools.

Introduction

The manufacture of composite textiles on doubly curved surfaces needs draping of prepreg or dry fabrics. In the case of dry reinforcements, the injection moulding process (LCM) consists in giving the form of the final part to a dry reinforcement and then to be injected the resin (Advani 1994; Rudd and Long 1997). The textile reinforcement can be subjected to large strains. Large in-plane shear angles may be necessary to obtain the desired shape. Depending on the geometry of the parts, the type of reinforcement and the manufacturing parameters (loading of the tools, blank holder loads, …), doubly curved shapes can be correctly manufactured or not. Simulations are necessary to avoid the long and costly development by trial and error of the manufacturing processes. Simulation software for composites forming have been developed to determine the parameters of feasibility of the process (De Luca

P. Boisse (✉)
Université de Lyon, LaMCoS, CNRS, INSA-Lyon, 69621 Villeurbanne, France
e-mail: philippe.boisse@insa-lyon.fr

C. Picu and J.-F. Ganghoffer (eds.), *Mechanics of Fibrous Materials and Applications*, CISM International Centre for Mechanical Sciences 596,
https://doi.org/10.1007/978-3-030-23846-9_4

and Pickett 1998; Hsiao and Kikuchi 1999; Pickett 2002; Hamila and Boisse 2007; Boisse 2007; Hamila et al. 2009; Gereke et al. 2013; Bussetta and Correia 2018). This chapter is based on a simplified form of internal virtual work in the case of textile reinforcements. The virtual work in tension, in-plane shear and bending of each elementary cell are decoupled. The form of these virtual works is simple and close to the physics of textile materials. The material parameters involved are directly identified by mechanical tests developed for textile reinforcements. Mechanical tests include biaxial tension tests for the tension rigidity (Buet and Boisse 2001; Carvelli et al. 2008), picture frame and bias-extension test for in-plane shear stiffness (Prodromou and Chen 1997; Potter 2002; Lebrun et al. 2003; Sharma et al. 2003; Zhu et al. 2009; Boisse et al. 2017) and bending tests (Lahey 2004; De Bilbao et al. 2010; Boisse et al. 2018). A three-node shell finite element specific to woven reinforcements, based on this form of virtual work, has been developed (Hamila et al. 2009). It is used to simulate the draping of textile composite reinforcements. The in-plane shear stiffness of a woven fabric increases significantly with shear angle and reaches a 'locking angle'. It is nevertheless difficult to establish a simple relationship between shear and appearance of wrinkles (Boisse et al. 2011). After the analysis of the simulation of the forming simulation of dry textile reinforcements used for LCM processes, the chapter presents the modelling of the thermoforming of thermoplastic prepregs.

Mechanical Behaviour of the Textile Composite Reinforcements: Stiffnesses of an Elementary Woven Cell

A composite textile reinforcement consists of representative unit cells (RUCs). These are geometric patterns, which through simple translation allow to represent the entire woven fabric. The mechanical behaviour of a fibrous fabric is specific due to possible relative slippage between the yarns and relative slippage between the fibres inside the yarns. The following stress resultants can be distinguished (Fig. 4.1a):

- The tensions T_1 and T_2 are the tensile loads on the warp and weft yarns, respectively, corresponding to the strains in the directions f_1 and f_2 of the yarns (Fig. 4.2a).
- The plane shear moment M_s, in the centre of the RUC in the direction of the normal to the surface of the fabric, results from the interactions between warp and weft yarns. It is associated with the shear angle between warp and weft yarns (Fig. 4.2b).
- The bending moments M_1 and M_2 are on warp and weft yarns, associated to the curvatures in both directions (Fig. 4.2c).

This is a simplified modelling, but the physical meaning of these quantities is quantifiable. In addition, they can directly be measured during standard tests on composite reinforcements for different cases of strains. Finally, these loads T_1, T_2, M_s, M_1 and M_2 are, respectively, associated to axial strains ε_{11} and ε_{22} in warp and weft direction, at γ the shear angle in the plane, and curvatures χ_{11} and χ_{22} in

Fig. 4.1 Loads on an RUC

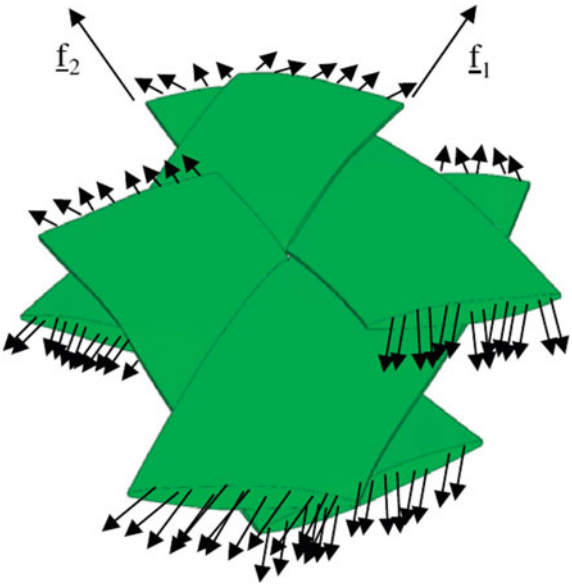

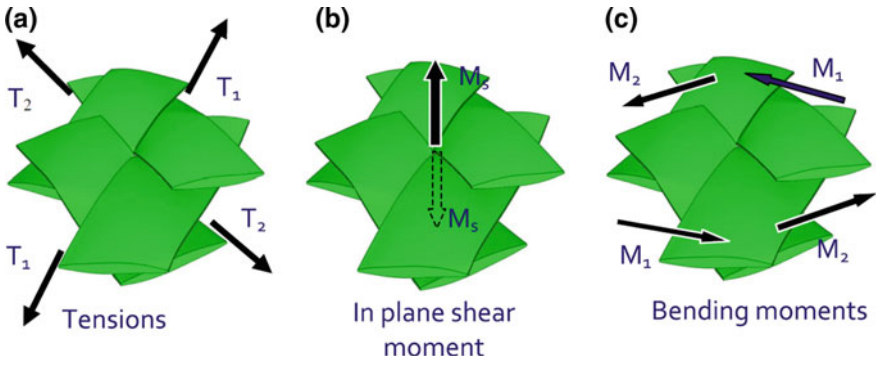

Fig. 4.2 Stress resultants on an RUC: **a** tensions, **b** in-plane shear moment, **c** bending moments

warp and weft directions. This leads to the simple form of the internal virtual work presented below.

Noting $W_{ext}(\underline{\eta})$, $W_{int}(\underline{\eta})$ and $W_{acc}(\underline{\eta})$ the virtual external, internal and inertial virtual works in a virtual displacement field $\underline{\eta}$ equal to zero on the boundary with prescribed displacements:

$$W_{ext}(\underline{\eta}) - W_{int}(\underline{\eta}) = W_{acc}(\underline{\eta}) \tag{4.1}$$

with

$$W_{int}(\underline{\eta}) = W^{t}_{int}(\underline{\eta}) + W^{b}_{int}(\underline{\eta}) + W^{s}_{int}(\underline{\eta}) \tag{4.2}$$

$W^{t}_{int}(\underline{\eta})$, $W^{b}_{int}(\underline{\eta})$, $W^{s}_{int}(\underline{\eta})$, are the virtual internal works of tension, and bending and in-plane shear.

$$W^{t}_{int}(\underline{\eta}) = \sum_{p=1}^{ncell} {}^{p}\varepsilon_{11}(\underline{\eta})\ {}^{p}T_1\ {}^{p}L_1 + {}^{p}\varepsilon_{22}(\underline{\eta})\ {}^{p}T_2\ {}^{p}L_2 \tag{4.3}$$

$$W^{b}_{int}(\underline{\eta}) = \sum_{p=1}^{ncell} {}^{p}\chi_{11}(\underline{\eta})\ {}^{p}M_1\ {}^{p}L_1 + {}^{p}\chi_{22}(\underline{\eta})\ {}^{p}M_2\ {}^{p}L_2 \tag{4.4}$$

$$W^{s}_{int}(\underline{\eta}) = \sum_{p=1}^{ncell} {}^{p}\gamma(\underline{\eta})\ {}^{p}M_s \tag{4.5}$$

The quantity A is noted ${}^{p}A$ when it is associated to the RUC p. The internal virtual work $W^{b}_{int}(\underline{\eta})$ is due to tensions. $\varepsilon_{11}(\eta)$ and $\varepsilon_{22}(\eta)$ are the virtual deformations due to elongation of the fibres in the warp and weft directions. L_1 and L_2 are the lengths of the warp and weft yarns. $W^{s}_{int}(\underline{\eta})$ is the internal virtual work due to in-plane shear in the plane. $\gamma(\eta)$ is the virtual angle variation between directions warp and weft in the virtual displacement field η. $W^{b}_{int}(\underline{\eta})$ is the internal virtual work due to bending. $\chi_{11}(\underline{\eta})$ and $\chi_{22}(\underline{\eta})$ are virtual curvatures in warp and weft directions. Virtual kinematic quantities $\varepsilon_{11}(\underline{\eta})$, $\varepsilon_{22}(\underline{\eta})$, $\gamma(\underline{\eta})$, $\chi_{11}(\underline{\eta})$ and $\chi_{22}(\underline{\eta})$ are only function of the virtual displacement field $\underline{\eta}$.

Stress Resultant Shell Finite Element for Textile Composite Reinforcements

The three-node shell finite element used in this chapter is based on the simplified form of the principle of virtual work given in Eqs. (4.1)–(4.5). Details of its formulation are given in Hamila and Boisse (2007), Hamila et al. (2009). It is summarized below. Tension, in-plane shear and bending stiffnesses are separated which makes it possible to analyse their influences in particular on wrinkle onset and development.

The three-node shell finite element $M_1M_2M_3$ (Fig. 4.3) is composed of ncelle woven RUC. The vectors $k_1 = AM_2$ and $k_2 = BM_3$, respectively, in the warp and weft directions are defined. The virtual internal work in the element due to tensions (Eq. 4.3) defines the elementary nodal loads $\mathbf{F}^{te}_{int}$:

$$\sum_{p=1}^{ncelle} {}^{p}\varepsilon_{11}(\underline{\eta})\ {}^{p}T_1\ {}^{p}L_1 + {}^{p}\varepsilon_{22}(\underline{\eta})\ {}^{p}T_2\ {}^{p}L_2 = \boldsymbol{\eta}^{eT}\mathbf{F}^{te}_{int} \tag{4.6}$$

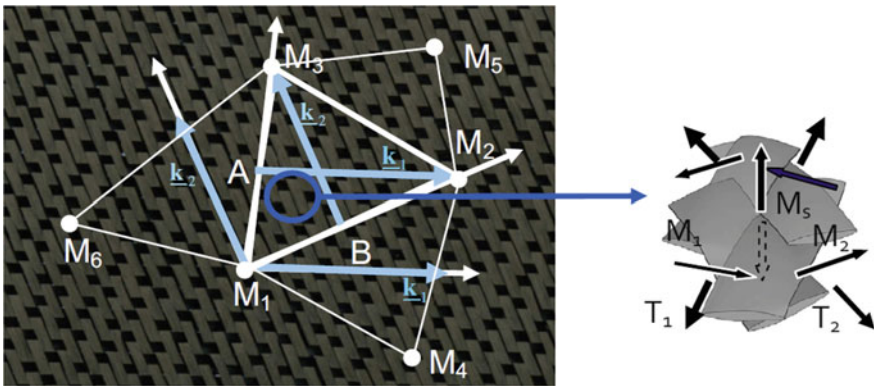

Fig. 4.3 Three-node shell finite element composed of elementary cells

The components of the nodal loads in tension are calculated from the tensions T_1 and T_2:

$$\left(F_{int}^{te}\right)_{ij} = ncelle\left(B_{1ij}T_1\frac{L_1}{\left\|\underline{k}_1\right\|^2} + B_{2ij}T_2\frac{L_2}{\left\|\underline{k}_2\right\|^2}\right) \tag{4.7}$$

i is the index of the dimension in space (i = 1–3), and j is the index of the node (j = 1–3). B_{1ij} and B_{2ij} are the interpolations of the tensile strains. They are constant on the element because the interpolation functions are linear.

In order to avoid increasing the number of degrees, the bending stiffness is processed using an approach with no degrees of freedom in rotation (Onate et al. 2000; Sabourin and Brunet 2006). To do this, the element curvatures are calculated from the positions of the nodes of adjacent elements (Fig. 4.3). The virtual internal bending work of the element (Eq. 4.4) makes it possible to express the bending elementary nodal loads:

$$\sum_{p=1}^{ncelle} {}^{p}\chi_{11}(\underline{\eta})\ {}^{p}M_1{}^{p}L_1 + {}^{p}\chi_{22}(\underline{\eta}){}^{p}M_2{}^{p}L_2 = \boldsymbol{\eta}^{eT}\mathbf{F}_{int}^{be} \tag{4.8}$$

$$\left(F_{int}^{be}\right)_{km} = n_{celle}\left(Bb_{1km}M^{11}\frac{L_1}{\left\|\underline{k}_1\right\|^2} + Bb_{2km}M^{22}\frac{L_2}{\left\|\underline{k}_2\right\|^2}\right) \tag{4.9}$$

The internal in-plane shear virtual work in the element (Eq. 4.5) defines the internal elementary loads:

$$\sum_{p=1}^{ncelle} {}^{p}\gamma(\underline{\eta}){}^{p}M_s = \boldsymbol{\eta}^{eT}\mathbf{F}_{int}^{se} \tag{4.10}$$

$$\left(F_{int}^{se}\right)_{ij} = \text{ncelle } B_{\gamma ij} M_s(\gamma) \tag{4.11}$$

Experimental Analyses of the Tensile, In-plane Shear and Bending Stiffnesses of Textile Composite Reinforcements

The objective is to determine experimentally for a given textile reinforcement, the relationship between the stress resultants T_1, T_2, M_1, M_2 and Ms and the associated deformations ε_{11}, ε_{22}, γ, χ_{11} and χ_{22}. These behaviours are necessary to perform a finite element simulation based on Eqs. 4.6–4.11.

Biaxial Tension

Tensile tests carried out on the fabric in the yarn directions (Figs. 4.4 and 4.5) typically show the presence of progressive stiffening followed by a linear behaviour (Fig. 4.7). The non-linearity at the beginning of loading is explained by phenomena occurring at lower scales. Due to the weaving of the yarns, the fabric has a natural waving of its tows. However, under the effect of tension, the yarns tend to become straight. In an extreme case where the other direction is left free to move, the yarns under load become straight and the others strongly undulated (Fig. 4.6). In intermediate cases, an equilibrium state is reached, where both directions undergo variations in

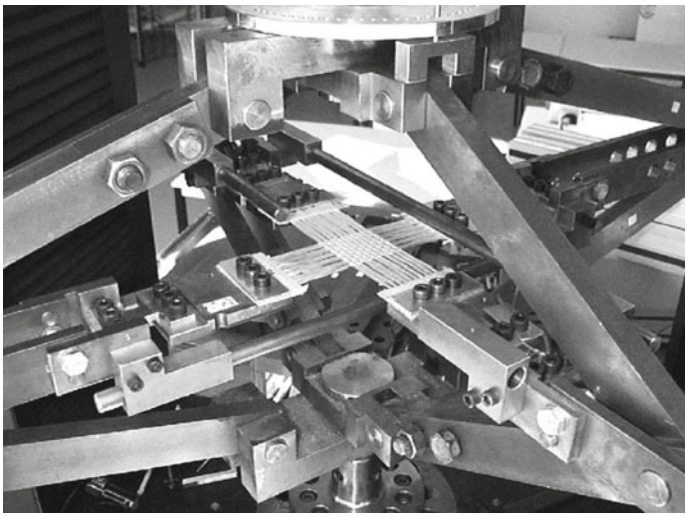

Fig. 4.4 Biaxial tensile test on a cross-shaped specimen

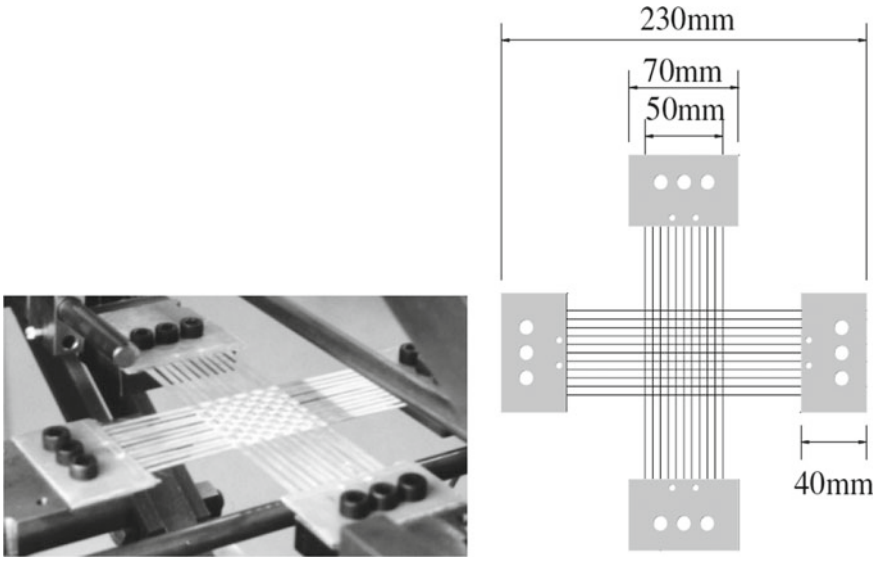

Fig. 4.5 Cross-shaped specimen for biaxial tensile test

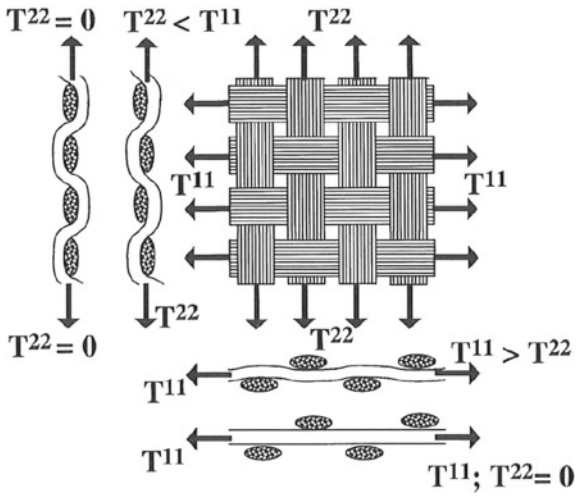

Fig. 4.6 Undulations and interactions during biaxial tension

undulation. It is clear that this phenomenon is biaxial and that the two yarn directions interact. These non-linear phenomena, of geometric origin, are mesoscopic (scale of the RUC). Their effect is complemented and amplified by phenomena at the fibre level (microscopic scale). Under the effect of the different tensile forces along the yarn directions, and transverse compression at the contact between the two networks, the filaments rearrange themselves, and the shape of the transverse section of the yarns varies. The non-linearities involved at this scale are related to friction between

the fibres and generate geometric non-linearities at the mesoscopic scale. All these phenomena are at the origin of the material non-linearities observed in tension at the macroscopic scale of the fabric, during its deformation.

In order to understand the specific behaviour of the textiles and to highlight the characteristics mentioned, it is necessary to carry out tests using a device capable of testing woven materials in two directions simultaneously. The device shown in Figs. 4.4 and 4.5 is based on the principle of two deformable lozenges (Buet and Boisse 2001). Strain measurements are made either by optical methods (Launay et al. 2002) or by mechanical systems. Figure 4.7 shows the results of the stress tests for different ratios k = warp strain/weft strain. The yarns used are identical in the warp and weft. These yarns are made of 6000 high-strength carbon fibres assembled without torsion. The fabric is almost balanced, which means that the results are

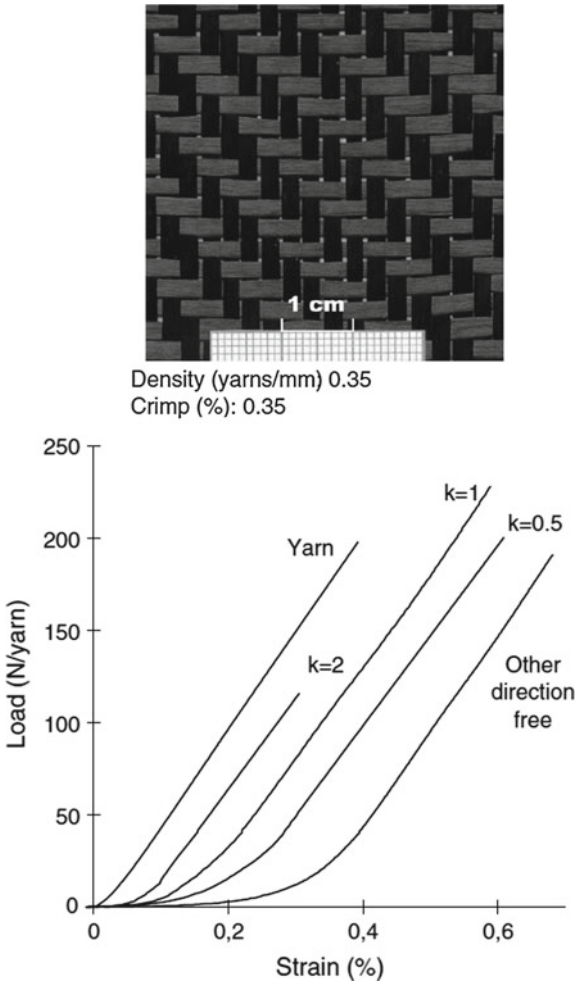

Fig. 4.7 Biaxial tensile test on a 2 × 2 carbon twill

only presented in one direction. Although the yarns alone have a linear behaviour, the tension–deformation behaviour curves of the fabric are very clearly non-linear at low forces and then linear at higher forces. This non-linearity of behaviour is a consequence of non-linear phenomena occurring at lower scales (variations in undulation) and crushing of the yarns. The extent of the non-linear zone is important with respect to fracture strain. In addition, it depends on the ratio k of imposed strains, which highlights the biaxial nature of tissue behaviour, with each direction influencing the behaviour of the other. The non-linearity zone is maximum for tests where a direction is free. The yarns tend towards a completely straight state under very low forces. When the straightness of the yarn is reached, the behaviour of the yarn alone is found. The value of the deformation corresponding to this transition is significant for the crimp of the fabric in this direction. Finally, the non-linear zone is followed by a linear part of the behaviour characterized by a rigidity close to that of the single yarn in tension.

In-plane Shear

The strongest stiffnesses of a woven reinforcement are those of tension. They are the ones who mainly drive the shape changes when manufacturing a composite by forming the reinforcement. The in-plane shear stiffness is low (at least initially) and results from large distortions which are the main membrane forming mode. This shear stiffness can be increased if the fabric is coated with a matrix (non-polymerized thermoset or thermoplastic above the melting temperature) or significantly increased if the shear locking angle is exceeded. Studies concerning in-plane shear behaviour are numerous, probably because it is the major mode of deformation of woven fabrics (Prodromou et al. 1997; Harrison et al. 2004; Launay et al. 2008; Cao et al. 2008; Boisse et al. 2017).

There are two main tests available to experimentally analyse the in-plane shear of textile composite reinforcements: the picture frame (Fig. 4.8) and the bias-extension test (Fig. 4.9). Their relative merit has been discussed in several studies (Harrison et al. 2004; Launay et al. 2008). The bias-extension test is more complex to analyse because there are three areas where the shear is different. In addition, there is a tendency for slippage between the warp and weft yarns when the shear angle exceeds 40°. On the other hand, the tension forces in the bias-extension test specimen are effectively zero, whereas they are not always zero in the picture frame (especially in the event of a misalignment of the specimen fibres). They then disrupt the test result in a major way (Launay et al. 2008). The picture frame device shown in Fig. 4.8 is based on the principle of a frame with four equal and articulated sides whose directions are those of the yarns of the fabric. It is installed on a conventional tensile machine. A pre-tension can be applied to the yarns before shearing.

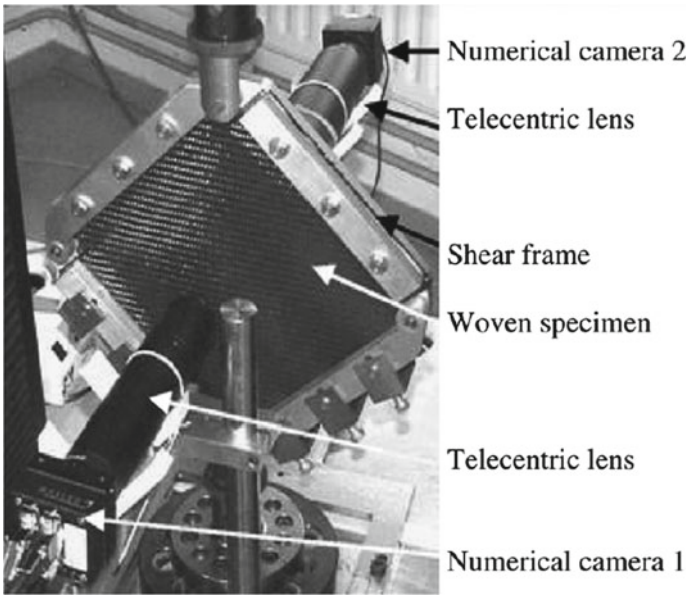

Fig. 4.8 In-plane shear analysis by picture frame and optical measurements

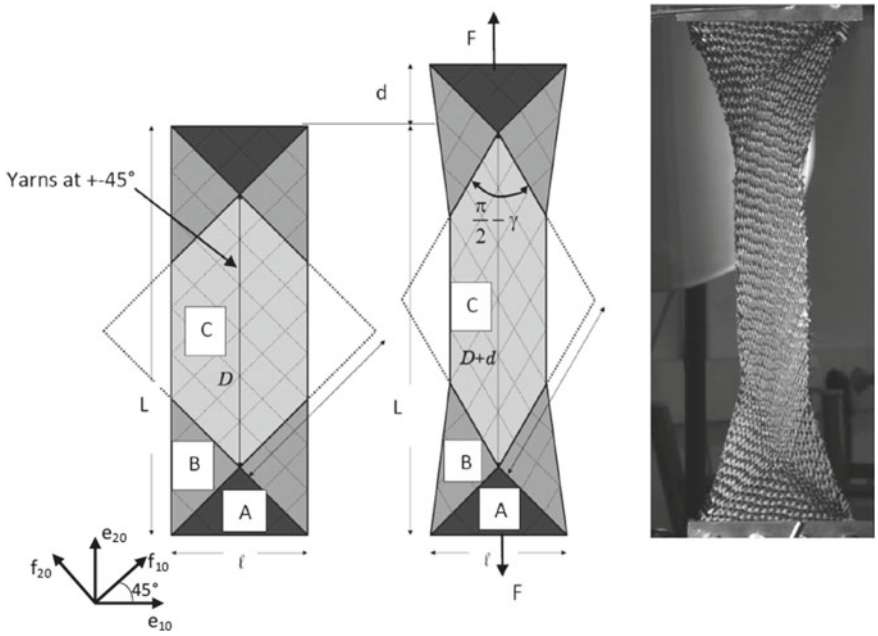

Fig. 4.9 Bias-extension test

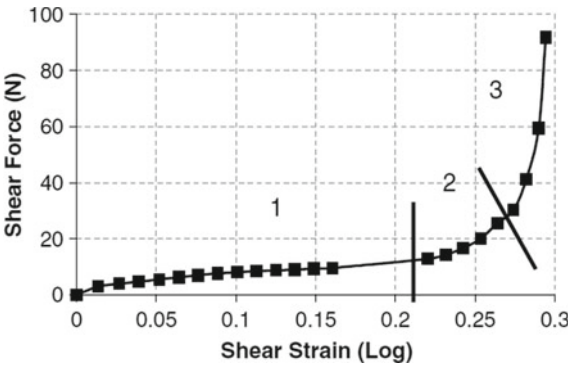

Fig. 4.10 Load versus in-plane shear in a picture frame on a glass plain weave

Shear analysis can also be performed by the bias-extension test on a specimen where the warp and weft yarns are oriented at 45° (Boisse et al. 2017; d'Agostino et al. 2015). Deformation measurements can be carried out by optical methods (Fig. 4.8). This makes it possible to effectively measure the deformations of the woven fabric in the useful area of the specimen and to make measurements from images of the entire frame (macro scale) or only a small number of meshes or a single yarn (meso- and micro-scale). In the case of a specimen made of glass plain weave, Fig. 4.10 shows the measurement of shear force as a function of shear strain (Boisse et al. 2005). The shear response curve can be divided into three areas. Figure 4.11a shows during phase 1 (see Fig. 4.10 for the different zones), the movements at the micro-scale, i.e. inside the fibrous yarns. The average displacement was subtracted from all measured displacements. It can be seen that the yarns are subjected to a rigid body rotation which, given the lack of contact with the adjacent wicks, results in fabric shearing (seen as a continuous medium). There is no shear inside the yarns. This explains why the fabric shear corresponds to low forces since only the rotational frictions between warp and weft yarns are opposed to shear. The passage to zone 2 corresponds to a limit angle sometimes called shear locking angle. From this angle, the yarns come into contact with their neighbours and are compressed laterally (Fig. 4.11b), first partially (zone 2) and then completely (zone 3) which explains the rapid increase in shear stress and therefore in shear stiffness. In practice, in zone 3, wrinkles appear, caused by the shear locking.

Bending

Textile material bending rigidity is low. In geometrical approaches (Fishnet) (Van Der Ween 1991; Long and Rudd 1994; Potluri et al. 2001) and in membrane-based methods (Lin et al. 2007; Lee et al. 2007; Ten Thije et al. 2007), bending stiffness is not taken into account. Bending rigidity is low because of the possible slip between the fibres during bending.

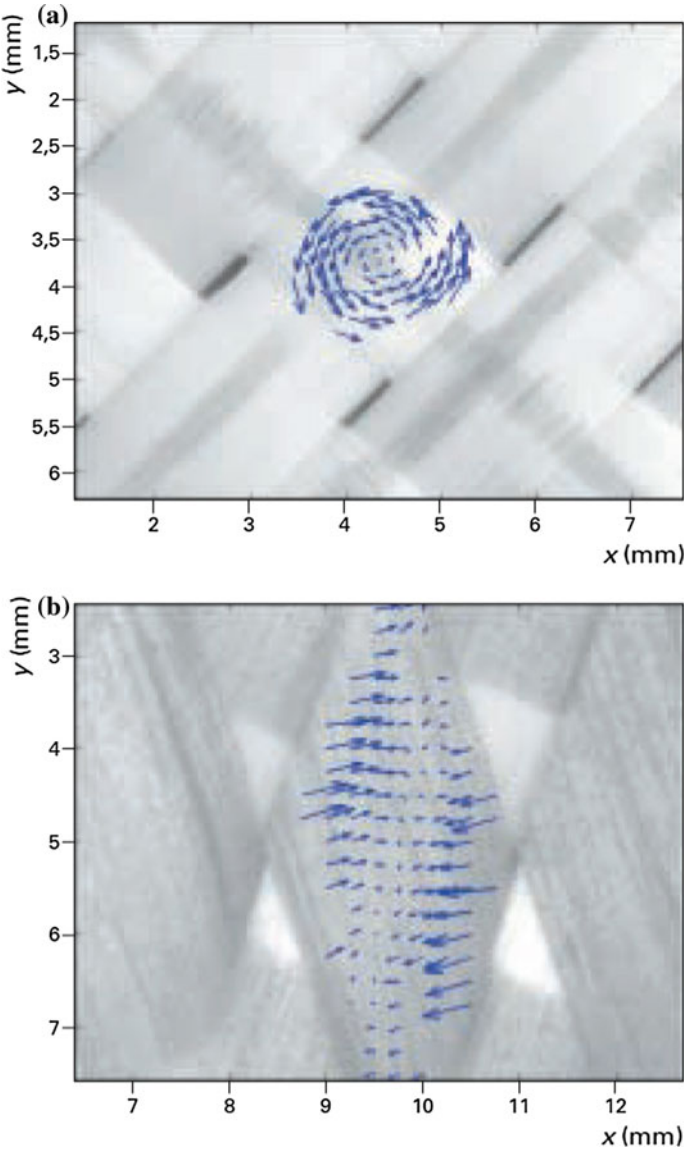

Fig. 4.11 Displacement fields of fibres within a yarn during a picture frame. **a** In zone 1, **b** beyond shear angle locking

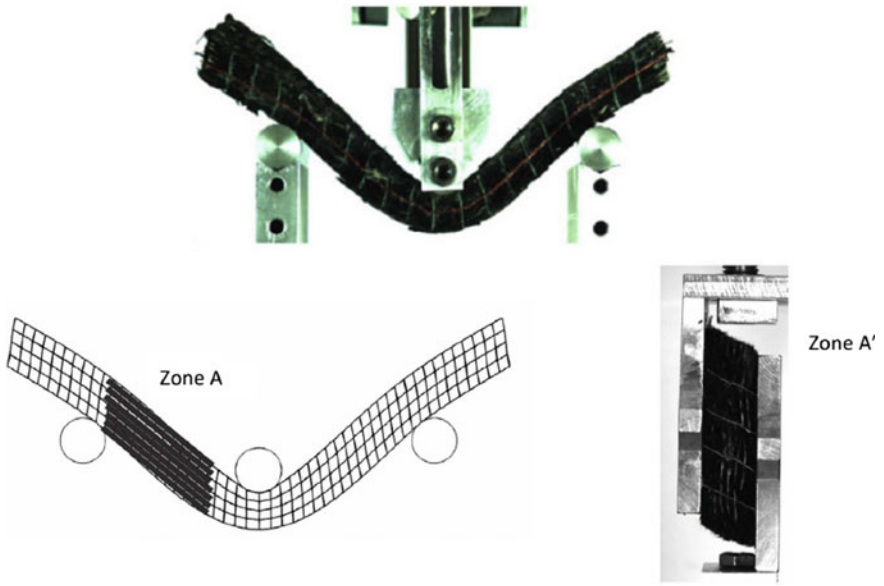

Fig. 4.12 Slippage between fibres during bending

The three-point bending Fig. 4.12 of a 3D textile reinforcement shows that the bending of the reinforcement is mainly due to the slip between the fibres. From the macroscopic point of view, this deformation is a shear stress. The strains in zone A (Fig. 4.12) are of the same type as that of the A′ zone during a shear test. The potential slippage results in low shear rigidity of fibrous reinforcements.

The fibre quasi-inextensibility is the second specific feature of the textile reinforcement behaviour. The normals after deformation are fixed by inextensibility in the bending test shown in Fig. 4.12. These normals are not perpendicular to the mean surface in the deformed state. Bending of textile materials does not correspond to standard plate theories (Kirchhoff, Mindlin) because it is driven by the inextensibility of the fibres and the slippage between the fibres. For metal sheet or other continuous materials, membrane and bending rigidities are linked in plate theories and given by the thickness of the plate and properties of the material. The bending stiffness of textile material would be overestimated by this approach that does not account for the slippage between fibres. Therefore, it is not possible to use classical shell finite elements that are used in commercial programmes, the bending stiffness of which is calculated from membrane modulus. To carry out a correct analysis of the forming of fibrous reinforcements, membrane and bending stiffnesses must be decoupled in the analysis (Hamila et al. 2009; Döbrich et al. 2014).

The relationship between the curvature and the bending moment M(χ) is necessary to take into account bending in the simulation by shell elements of the deformation of a textile reinforcement. Among the experimental analyses of textile bending, the cantilever bending test (Peirce 1930) has been proposed by Peirce (1930). Its extensions are still in use today (ASTM 2002, ISO 2011). In this test, a textile specimen is subjected to cantilever bending under its own weight. The sample is gradually pushed forward until the free end contacts the sloped plane of the instrument (Fig. 4.13). The position of a point on the centerline of the textile sample is in (x, y) (Fig. 4.13). w is the linear weight and ℓ is the cantilever length of the sample.

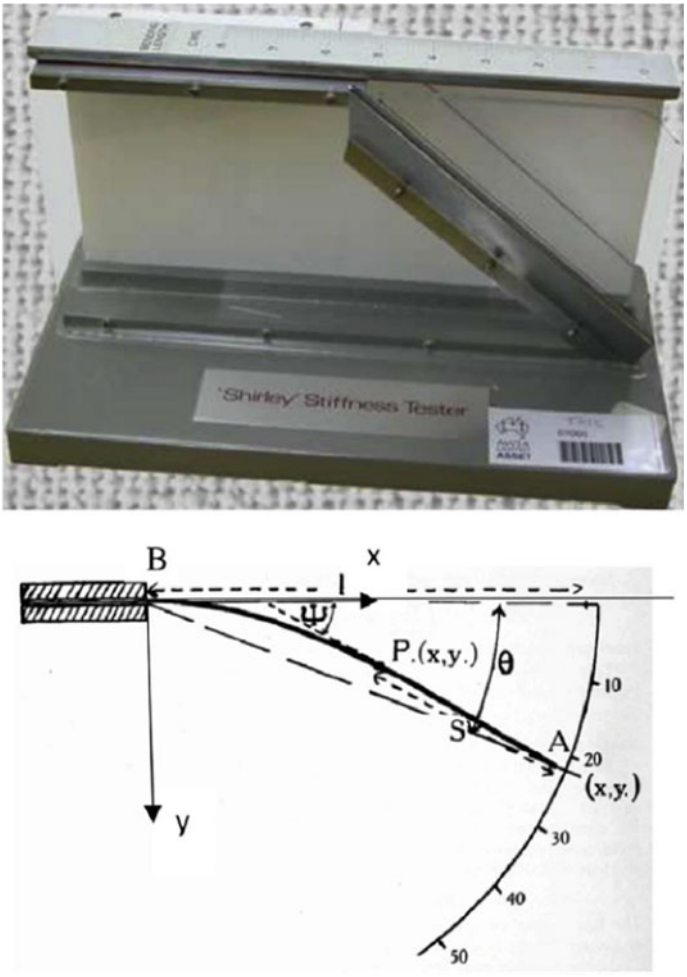

Fig. 4.13 Peirce's cantilever tester

The relationship $M(\chi)$ is assumed to be linear. (This is a simplifying hypothesis.) Noting G the bending stiffness:

$$M = G\chi \tag{4.12}$$

For small deflections, by integration of the curvature ($\chi = y''$), the deflection at the free edge of the specimen is

$$\delta = y(\ell) = \frac{w\ell^4}{8G} \tag{4.13}$$

The flexural rigidity S is

$$S = \frac{G}{w} = \frac{\ell^3}{8\,\mathrm{tg}\,\theta} \tag{4.14}$$

A corrective function $\cos\theta/2$ has been introduced for large displacements,

$$S = \frac{G}{w} = \frac{\ell^3 \cos\theta/2}{8\,\mathrm{tg}\,\theta} \tag{4.15}$$

For a given angle θ, the length of the overhang ℓ gives the stiffnesses S and G.

The inclined plane is fixed at 41.5° in the standard flexometers (Fig. 4.13). In this case,

$$S = \frac{G}{w} \approx \frac{\ell^3}{8} \tag{4.16}$$

Although empirical, the use of the term $\cos\theta/2$ in the case of geometrical non-linearities (Eq. 4.15) can be justified by a finite element analysis of the bending of a specimen (Boisse et al. 2018). The error made using the empirical Eq. 4.15 is less than 3%. The realization of the test with a 41.5° inclined plane associated with Eq. 4.16 is very simple to carry out. However, it gives a bending modulus G constant in function of the curvature, which is not always true.

Cantilever tests for vertical samples at the beginning were developed by Dangora et al. (2015a, b, 2018) and Alshahrani and Hojjati (2017) in order to reduce the effects of gravity.

Methods have been developed that make it possible to carry out an optical analysis of the deflected line over the entire bending specimen (De Bilbao et al. 2010; Liang et al. 2014, 2017). In Fig. 4.14, the centre line of the deformed sample is obtained from the image and approached by an analytical function. The curvature can be determined at any point. The bending moment at each point is given by the dead weight. By analysing a single test, the bending moment curve is obtained as a function of the curvature which varies from zero at the free end to a maximum value at the fixed

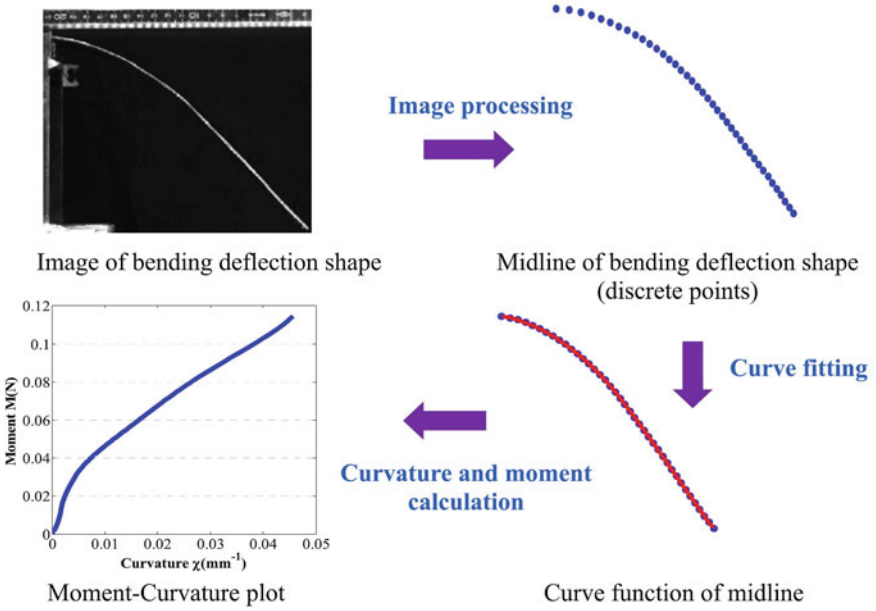

Fig. 4.14 Moment–curvature identification curve in a single cantilever bending test

end. Larger curvatures may be required, especially to model wrinkles. An additional mass can be added at the free end of the sample (Liang et al. 2014).

The second type of bending test is the Kawabata test (KES-FB2) (Fig. 4.15) (Kawabata 1980) and its extensions (Sachs 2017). The rotation of a clamp imposes a constant curvature on a textile sample. The required moment is measured and corresponds to the bending moment.

It is possible on this type of device to control the bending test rate. The identification of parameters of bending models depending on the loading rate is then possible (Sachs et al. 2017; Dörr et al. 2017; Margossian et al. 2015).

Influence of the Different Stiffnesses on Wrinkles

Draping on a Hemispherical Shape

A woven reinforcement is draped on a hemisphere (Fig. 4.16a). The initial geometry of the fabric is 150 mm × 150 mm square. The diameter of the hemisphere is 100 mm. The tensile stiffness of the fabric is 1000 N/yarn in warp and weft directions. The in-plane shear torque is in the form

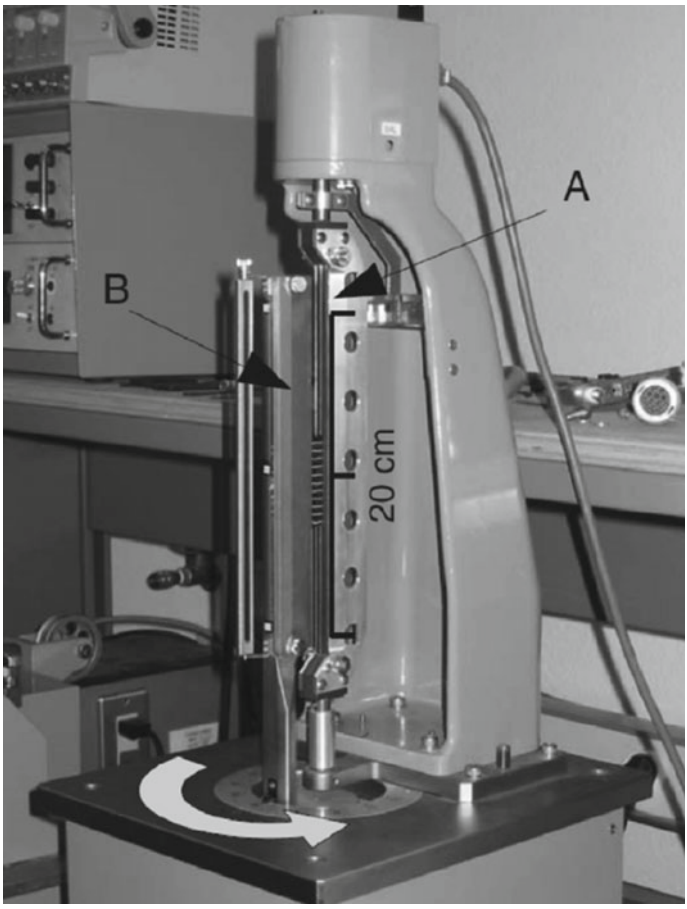

Fig. 4.15 Kawabatta test

$$M_s(\gamma) = 0.37044\gamma - 0.84105\gamma^3 + 1.03113\gamma^5 \tag{4.17}$$

The first deformed shape (Fig. 4.16b) only takes into account the tensile stiffness (Eq. 4.3). The draping is obtained with an absence of wrinkling, but the shear angles near the corners of the fabric are close to the 90°. The obtained solution is close to that given by a fishnet algorithm. Only the deformations in the direction of the yarns due to tension be the difference. But these strains are small because of the low tensions during draping.

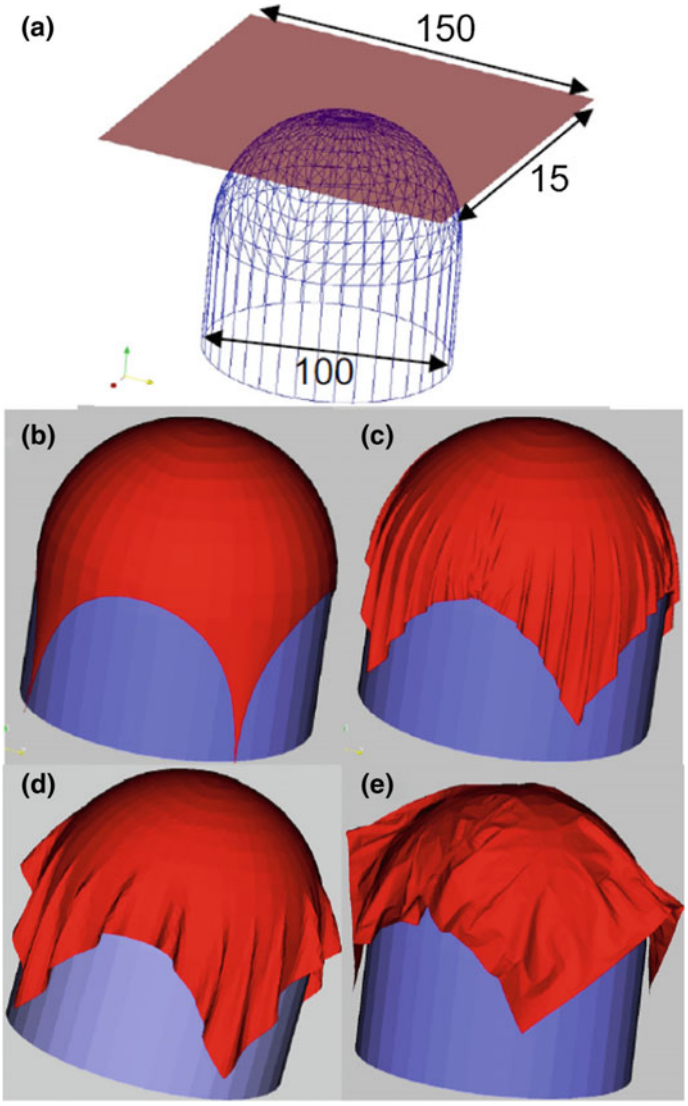

Fig. 4.16 Textile reinforcement forming on a hemisphere, **a** punch and fabric dimensions, **b** tensile stiffness only, **c** in-plane shear and tensile stiffnesses, **d** in-plane shear, tensile and bending stiffnesses, **e** isotropic sheet

The second deformed shape (Fig. 4.16c) is obtained when the tension (Eq. 4.3) and in-plane shear (Eq. 4.5) stiffnesses are taken into account. Many small wrinkles are present. The third deformed shape (Fig. 4.16d) is obtained by taking into account all the rigidities. In this case, the draping leads to wrinkles less numerous, larger and more realistic in shape.

Forming an Unbalanced Textile Reinforcement

The textile reinforcement shown in Fig. 4.17 is very unbalanced. The tension stiffness is equal to 50 N/yarn in the warp direction and 0.2 N/yarn in the weft direction (Daniel et al. 2003). A forming test with a hemispherical punch was carried out (Fig. 4.18). In order to avoid the appearance of wrinkles in the hemispheric area, a 6 kg circular blank holder was used. Figure 4.20e shows the experimental deformed shape. The

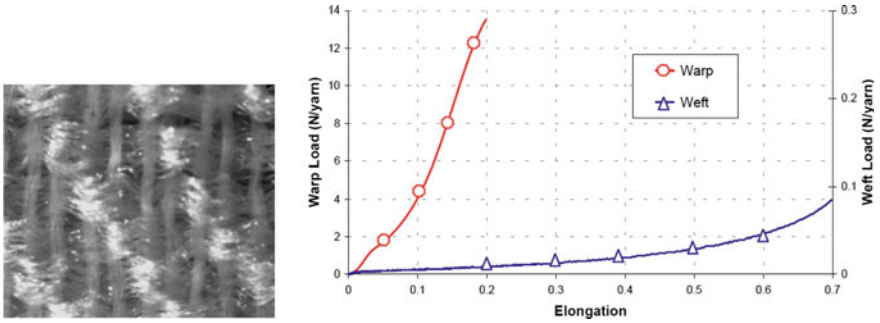

Fig. 4.17 Unbalanced fabric. Warp and weft tensile behaviours

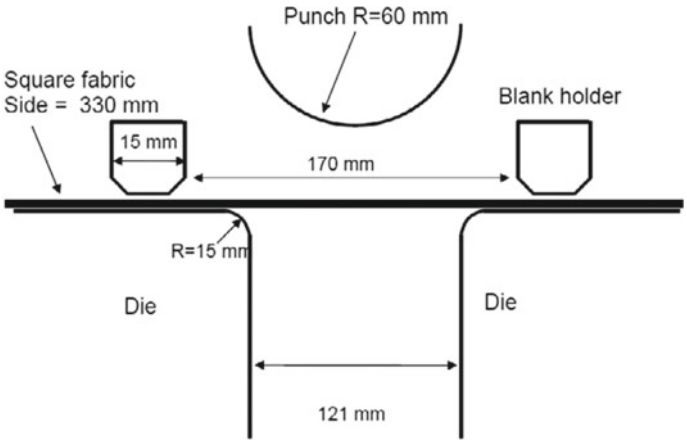

Fig. 4.18 Unbalanced fabric: tool geometry

deformation in warp and weft directions are very different with no movement in the weft direction. A square drawn on the fabric in the initial state becomes a rectangle after forming with a ratio of 1.8 between the two sides. The tension stiffness is only taken into account in Fig. 4.19b. The dissymmetry of the shape is properly achieved. But the simulation gives no wrinkles. In-plane shear and tensile stiffnesses are taken into account in Fig. 4.20d. Many small wrinkles are obtained. When bending stiffness is added (Fig. 4.19c), the wrinkles are much broader and their general forms are in fairly good agreement with the experience. In all three simulations, the tensile strain ratio in the hemisphere (1.8) is properly calculated. On the other hand, the form and the number of wrinkles are very different. If this case is analysed using a fishnet algorithm, the deformation in warp and weft directions are identical and there are no wrinkles.

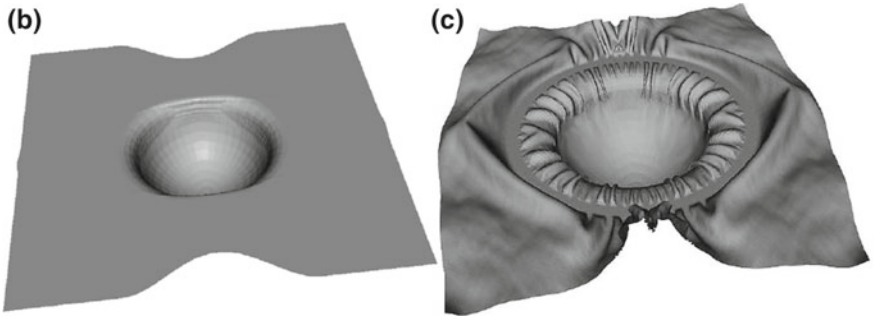

Fig. 4.19 Simulation, **b** with only the tension stiffness, **c** with all the rigidities

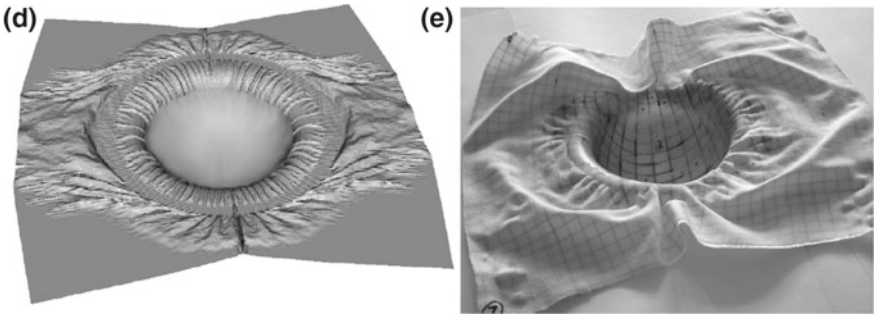

Fig. 4.20 Simulation **d** with the tension and in-plane shear stiffness **e** experiments

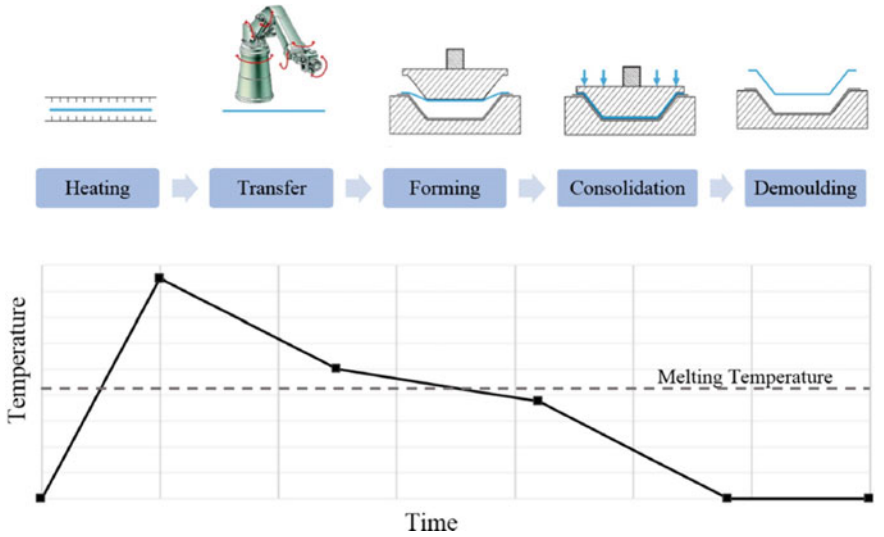

Fig. 4.21 Stages of the thermostamping process

Thermostamping of Prepreg Composites with Thermoplastic Matrix

The Thermostamping Process

Thermostamping is an interesting solution for the mass production of composite structures. This process is rather close to sheet metal forming.

After heating above the melting temperature, the material is transported to the press (Fig. 4.21). The forming is done between two complementary tools. The next step is the consolidation phase where the composite is maintained under pressure in order to remove porosity and ensure cohesion between the different layers. The structure is finally cooled with ambient air. All the steps are completed in a few minutes. Thermostamping can be used for the mass production of composite parts, particularly in the automotive sector.

Viscohyperelastic Model for Prepreg Forming

A prepreg reinforcement can be considered as an orthotropic material. The three orthotropic directions ($\underline{L}_1$, $\underline{L}_2$, $\underline{L}_3$) are defined by the warp, weft and weft and perpendicular directions, respectively, and a third direction to the two previous ones. Some hyperelastic models have been developed for dry fabrics (Criscione et al. 2001; Charmetant et al. 2012). This type of formulation is based on a decoupling of the

deformation modes. The deformation modes considered in the case of a composite reinforcement initially orthotropic as well as its respective invariants are as follows:

Elongation invariant in the warp direction:

$$I^1_{elong} = \frac{1}{2}\ln\left(\underline{\underline{C}} : \underline{L}_1 \otimes \underline{L}_1\right) \tag{4.18}$$

Elongation invariant in the weft direction:

$$I^2_{elong} = \frac{1}{2}\ln\left(\underline{\underline{C}} : \underline{L}_2 \otimes \underline{L}_2\right) \tag{4.19}$$

In-plane shear invariant:

$$I_{sh} = \frac{\left(\underline{\underline{C}} : \underline{L}_1 \otimes \underline{L}_2\right)}{\sqrt{\left(\underline{\underline{C}} : \underline{L}_1 \otimes \underline{L}_1\right)\left(\underline{\underline{C}} : \underline{L}_2 \otimes \underline{L}_2\right)}} = \sin(\gamma) \tag{4.20}$$

Bending invariants:

$$I^1_{bending} = \underline{l}_1 \cdot \underline{\underline{\chi}} \cdot \underline{l}_1 = \chi_{11} \quad I^2_{bending} = \underline{l}_2 \cdot \underline{\underline{\chi}} \cdot \underline{l}_2 = \chi_{22} \tag{4.21}$$

$\underline{\underline{C}}$ is the right Cauchy Green strain tensor. $\underline{\underline{\chi}}$ is the tensor of curvatures and $\underline{l}_1, \underline{l}_2$ are the unit vector in the warp and weft directions.

The deformation energy is expressed as a function of these physical invariants:

$$\underline{\underline{S}} = 2\frac{\partial w}{\partial \underline{\underline{C}}} = 2\frac{\partial w_k}{\partial I_k}\frac{\partial I_k}{\partial \underline{\underline{C}}} \tag{4.22}$$

The internal energy potential is defined as the sum of the energy potentials associated with membrane deformations and bending.

$$w = w_{mem} + w_{bend} \tag{4.23}$$

A viscoelastic behaviour is only associated with in-plane shear. For this purpose, a non-linear viscohyperelastic model is constructed (Simo 1987).

$$\psi(\underline{\underline{C}}, \underline{\underline{L}}_1, \underline{\underline{L}}_2) = w_{mem}\left(\underline{\underline{C}}, \underline{\underline{L}}_1, \underline{\underline{L}}_2\right) - \frac{1}{2}\sum_{i=1}^{N}\left(\underline{\underline{C}} : \underline{\underline{Q}}_i\right) + \Xi\left(\sum_{i=1}^{N}\underline{\underline{Q}}_i\right) \tag{4.24}$$

where Qi represents a set of internal variables that cannot be measured in the reference configuration. These variables are associated with the different mechanisms of relaxation due to interactions within the material. Ξ is a function of internal variables. The second Piola–Kirchhoff tensor can be decomposed according to the

different deformation modes:

$$\underline{\underline{S}} = \underline{\underline{S}}_{elong_1} + \underline{\underline{S}}_{elong_2} + \underline{\underline{S}}_{sh} \tag{4.25}$$

$\underline{\underline{S}}_{elong_1}$ and $\underline{\underline{S}}_{elong_2}$ represent the purely hyperelastic contributions linked to elongation in the warp and weft directions, respectively, and $\underline{\underline{S}}_{sh}$ is the viscohyperelastic contribution related to in-plane shear:

$$\underline{\underline{S}}_{sh} = 2\frac{\partial w_{sh}(\underline{\underline{C}})}{\partial \underline{\underline{C}}} - \sum_{i=1}^{N} \underline{\underline{Q}}_i \tag{4.26}$$

The internal variables $\underline{\underline{Q}}_i$ are determined from the following system of evolution equations:

$$\left| \begin{array}{l} \dot{\underline{\underline{Q}}}_i + \frac{1}{\tau_i}\underline{\underline{Q}}_i = \frac{\gamma_i}{\tau_i}\left[2\frac{\partial w_{sh}(I_{sh})}{\partial \underline{\underline{C}}}\right] \\ \lim\limits_{t\to-\infty} \underline{\underline{Q}}_i(t) = 0 \end{array} \right. \tag{4.27}$$

where γ_i and τ_i represent the different material viscoelastic parameters and associated relaxation times.

Finally, the second Piola–Kirchhoff tensor associated with the viscohyperelastic membrane contribution is given (in its convolution form) by

$$\underline{\underline{S}}(t) = \underline{\underline{S}}_{elong_1} + \underline{\underline{S}}_{elong_2} + \int_{-\infty}^{t} G(t-s)\frac{\mathrm{d}}{\mathrm{d}s}\left[2\frac{\partial w_{sh}}{\partial \underline{\underline{C}}}\right]\mathrm{d}s \tag{4.28}$$

with G(t) the associated relaxation function:

$$G(t) = \gamma_\infty + \sum_{i=1}^{N} \exp\left(\frac{-t}{\tau_i}\right)\gamma_i \tag{4.29}$$

Identification of Parameters

This section describes possible tests for determining the parameters of the hyperviscoelastic model presented above. The material taken as an example in this chapter is a pre-consolidated thermoplastic composite. The plate is composed of five layers of Satin-8 fibreglass and prepregs of a Polyamide 6.6 resin (Fig. 4.2a). The melting

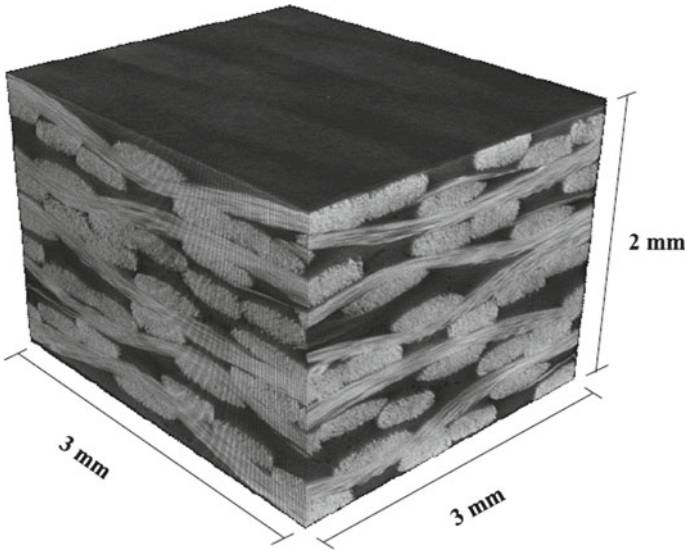

Fig. 4.22 Microtomography of the thermoplastic prepreg

temperature of the thermoplastic resin varies between 257 and 265 °C depending on the speed of heating. A micro-CT image shows the prepreg in Fig. 4.22.

The characterization of the in-plane shear behaviour can be performed using a bias-extension test at high temperatures (Fig. 4.23) (Lebrun et al. 2003; Wang et al. 2012; Guzman-Maldonado et al. 2015). Other tests can be used, such as the picture frame (Harrison et al. 2004; Dangora et al. 2015a, b). In the case of thermoplastic prepregs, the bias extension test is rather delicate to implement. In order to study the behaviour of prepregs during forming process, the specimen must be brought above the melting point. Boundary conditions must be insured, and the temperature must be controlled within the material.

To characterize the in-plane shear viscoelastic behaviour, the bias-extension test is carried out by steps (Fig. 4.24). From experimental results, an inverse approach (Schnur and Zabaras 1992) is used to identify the material parameters, the relaxation times, as well as the p_{sh} coefficients of the potential w_{sh}, defined by

$$w_{sh} = \sum_{i=1}^{3} p_{sh} (I_{sh})^{2i} \tag{4.30}$$

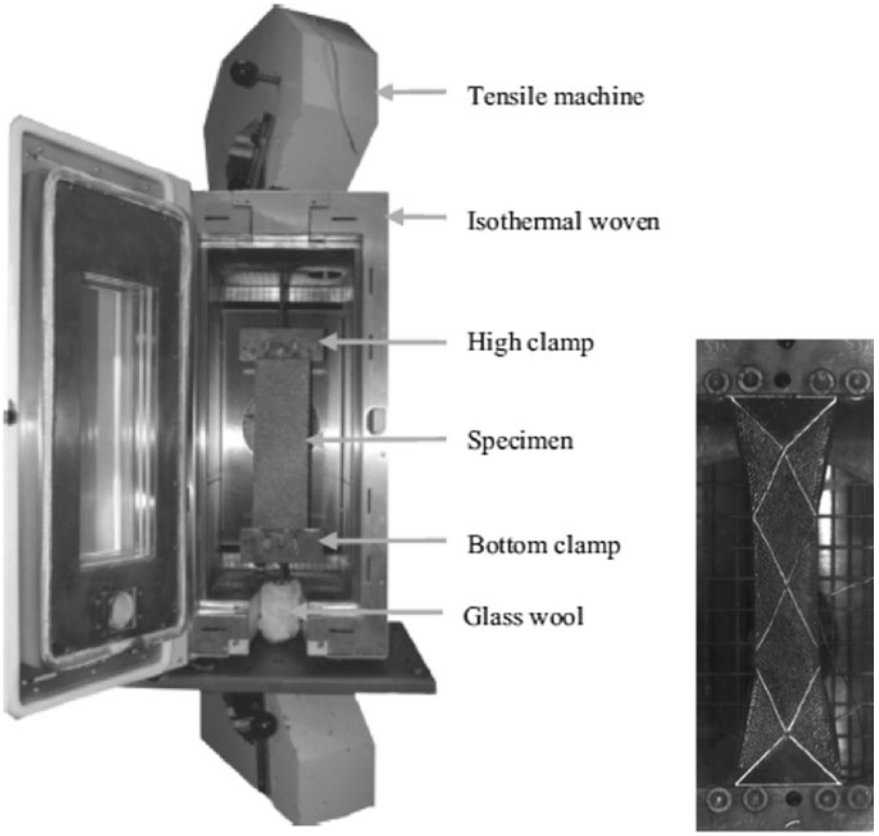

Fig. 4.23 Bias-extension test at high temperature

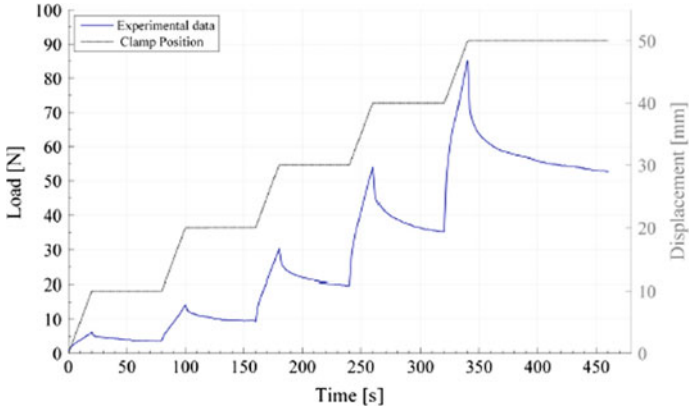

Fig. 4.24 Bias-extension test performed at 270 °C. Applied load versus time and imposed clamp displacement

The external load F_{ext} is deduced from the power developed by the in-plane shear loads:

$$\int_{\Omega_0} \frac{1}{2} \underline{\underline{S}} : \dot{\underline{\underline{C}}} dV = F_{ext} \dot{d} \tag{4.31}$$

Identification is performed from four temperatures between 260 and 300 °C. The intermediate parameters can be interpolated linearly according to the temperature.

A cantilever test at high temperatures was performed to characterize the bending properties (Liang et al. 2014; Liang 2016). The principle of the test is to bend a cantilevered sample subjected to its own weight and for a given temperature (Figs. 4.25 and 4.26). The resulting profile is recorded by optical capture for different temperatures. The bending moment is plotted as a function of the curvature, and then a stiffness as a function of temperature can be associated. In order to ensure a homogeneous temperature distribution, a set of thermocouples are placed in the vicinity of the specimen in the device.

A series of tests were carried out in the warp and weft direction on specimens over a temperature range [260–320 °C]. The deformed shapes as well as the bending moment versus curvature curve are shown in Fig. 4.27. The maximum deformation is obtained at a temperature of 300 °C. Above this temperature, the bending stiffness remains constant and is close to that of dry fabric. The bending stiffness in the case

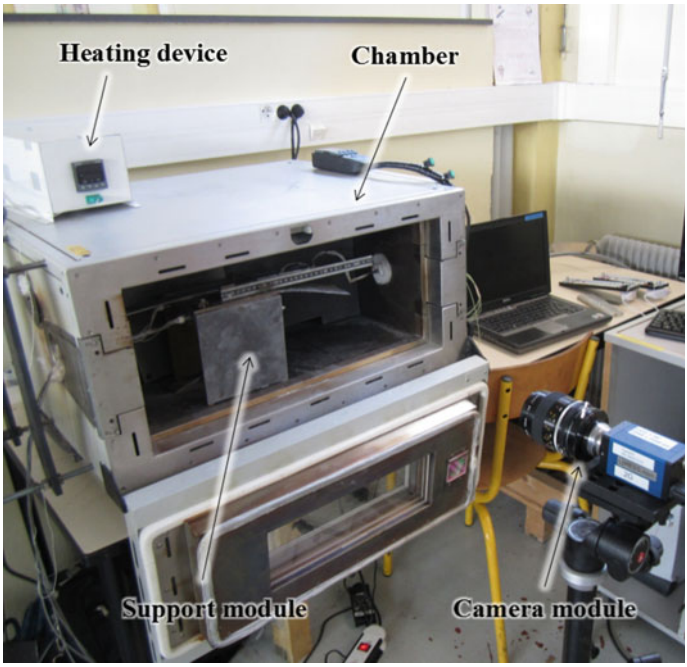

Fig. 4.25 Cantilever bending test at high temperature

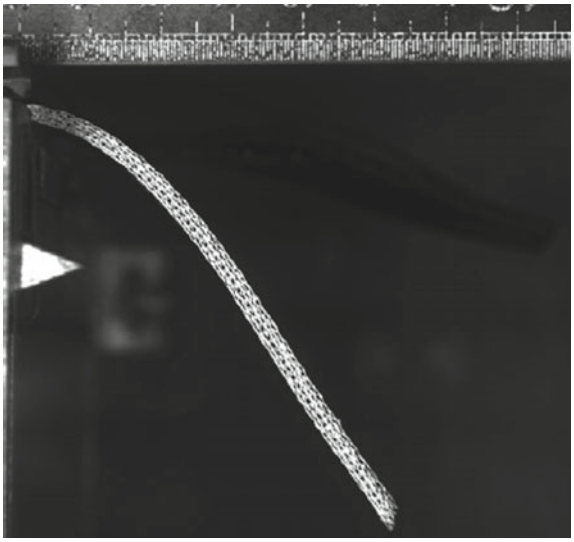

Fig. 4.26 Deformed shape of the bending specimen

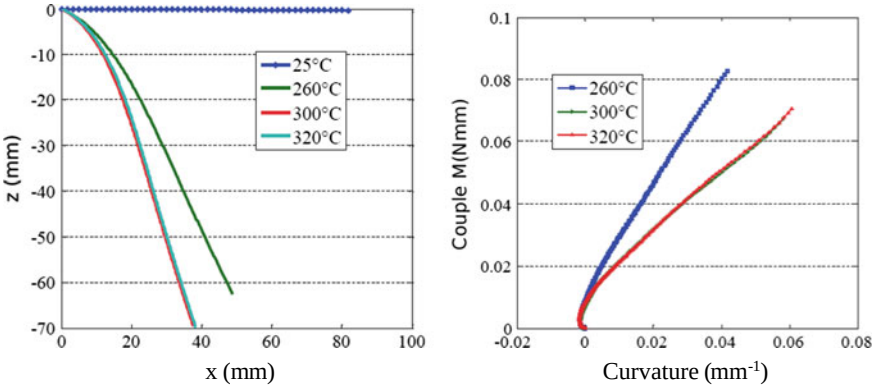

Fig. 4.27 Deflection and moment–curvature curves

of thermoplastics is highly dependent on the temperature. The potential associated with bending mode can be represented by a quadratic function:

$$w_{ben}\left(I_{\chi_i}\right) = p_{\chi_i}(T)\left(I_{\chi_i}\right)^2 \tag{4.32}$$

where p_{xi} depended on the temperature

$$p_{\chi_i}(T) = \alpha_i^{ben} \cdot T + \beta_i^{ben} \tag{4.33}$$

In a first step, it is assumed that the elongation stiffness of the material depends only on the stiffness of the fibres E_f. The tensile response of yarn is almost linear. The tensile potential of the prepreg is defined by

$$w_{elong_i} = p_{elong_i}(I_{elong_i})^2 \quad i = 1, 2 \tag{4.34}$$

where v_{f_i} is the volume fraction of fibres in the direction i.

$$p_{elong_i} \approx \frac{E_f \cdot v_{f_i}}{2} \tag{4.35}$$

v_{f_i} is, for instance, obtained from micro-CT image of the prepreg (Naouar et al. 2015).

Examples of Numerical Simulations of Thermoforming

The double-dome benchmark has been proposed in (Woven composites 2008; Willems et al. 2006, 2008; Fetfatsidis et al. 2009). The reasonably complex shape is double curved with flat surfaces. The geometry is shown in Fig. 4.28 (Khan 2009). The benchmark can be performed at room temperature (Khan et al. 2010; Peng and Rehman 2011) or at high temperature (Willems et al. 2008; Lee et al. 2010; Harrison et al. 2013) using corresponding constitutive models.

The viscohyperelastic model described in sections "Viscohyperelastic Model for Shaping Prepregs" and "Identification of Parameters" has been implemented in an explicit finite element code (Plasfib 2015). The prepreg is modelled by three-node shell elements (Hamila et al. 2009) where membrane and bending contributions are decoupled. The curvature is calculated from the position of the neighbouring

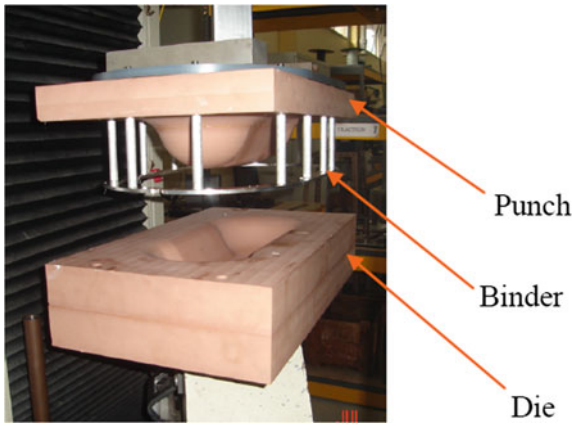

Fig. 4.28 Die, punch and blank holder of the double-dome benchmark

elements (Fig. 4.3) (Sabourin and Brunet 2006; Hamila et al. 2009). This reduces the overall number of degrees of freedom and therefore the calculation time.

The finite element model is composed of a punch, a die and the rectangular blank measuring 270 × 190 mm held in contact with the die by six blank holders (Fig. 4.29). The simulation was carried out for two material orientations: 0°/90° and +45°/−45° (Guzman-Maldonado 2016). The temperature before forming is assumed to be equal to 300°. The temperature of the tools is set at 250°. The speed of the punch is equal to 240 mm/min with a total displacement of 60 mm.

Simulations for both prepreg configurations (0°/90° and +45°/−45°) are first performed with a blank temperature kept constant during the shaping process. Then, the thermoforming simulations are carried out with an update of the temperature.

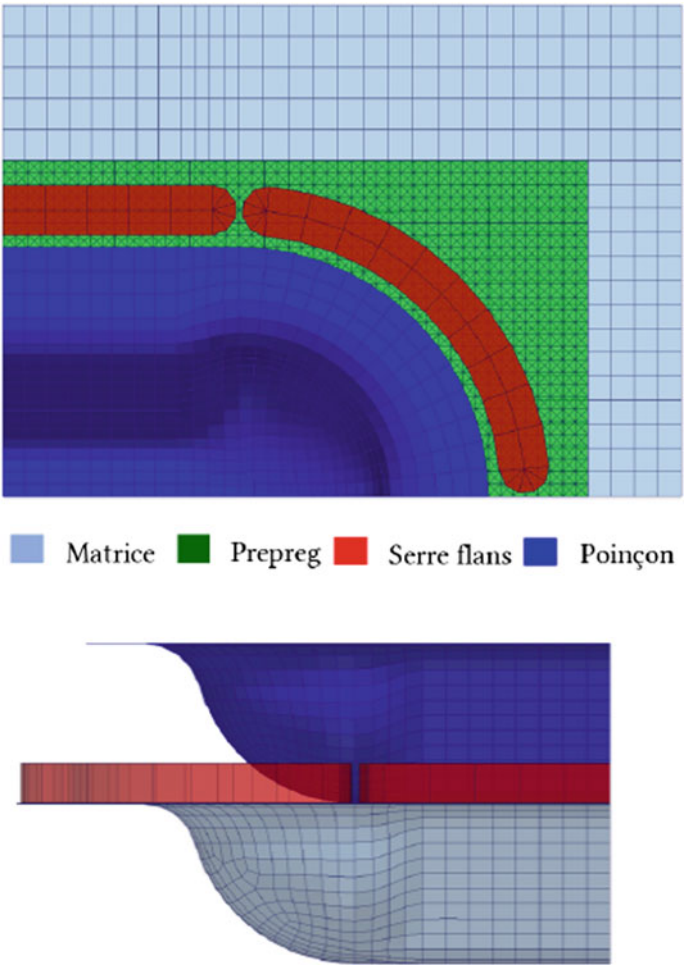

Fig. 4.29 Finite element model of the double-dome benchmark

The results obtained in both cases are compared. The mechanical and thermal problems are coupled. The temperature field at time t is obtained by solving the heat equation in the case of a transient conduction transfer, between t and $t + \Delta t_{th}$ where Δt_{th} represents the thermal update step. This calculation takes into account the orientation and the shear angle given by the mechanical calculation to at time t. The new temperature map is then considered for the determination of mechanical material parameters. The thermal update process goes on until the end of the forming process. Figure 4.30 shows the evolution of the temperature (averaged in the thickness) during the forming simulation. This temperature evolution in the prepreg is conditioned by the contact with the tools.

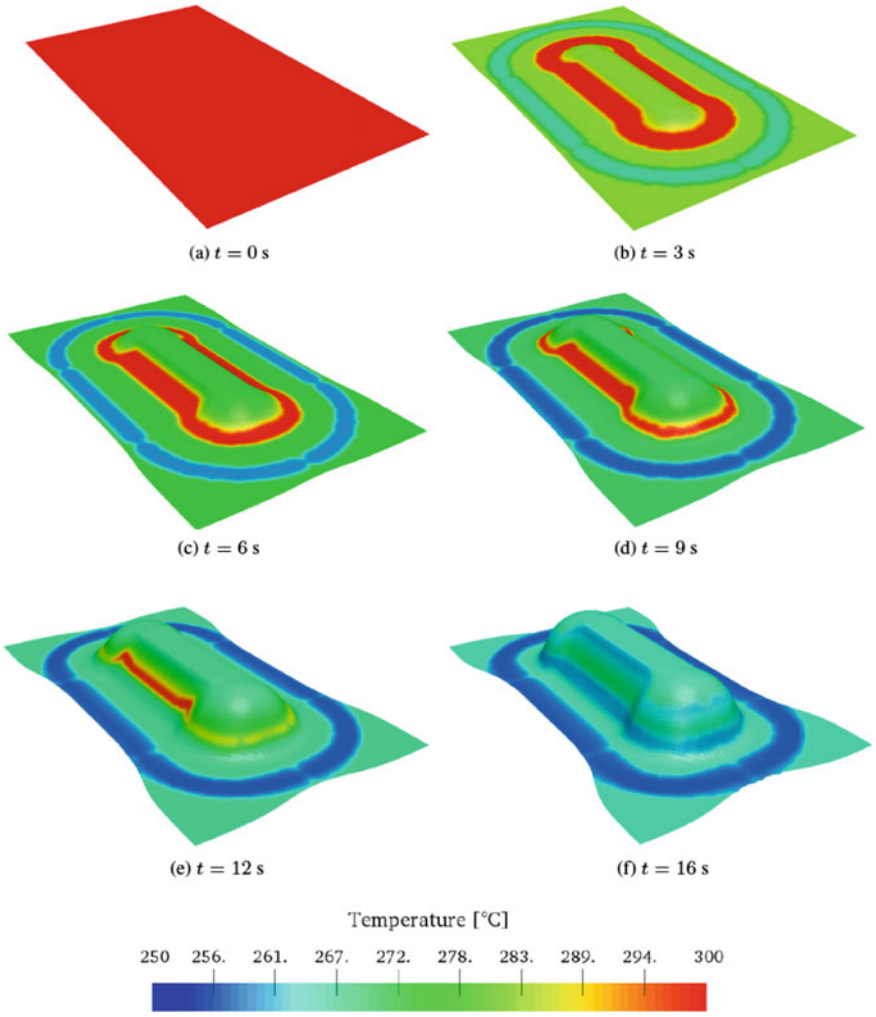

Fig. 4.30 Evolution of the temperature field during the forming process

The in-plane shear angles obtained by considering a homogeneous and constant temperature are presented in Fig. 4.31. Figure 4.32 shows in-plane shear angles obtained by taking into account the evolution of the temperature (and therefore the mechanical properties of the prepreg) during the process.

The comparison between the two results shows a difference between the shear angles in the range of 3°–5° and a slight change in the shape of the in-plane shear field.

Finally, Fig. 4.33 shows the temperature gradient in the thickness of the part at the end of the process. These temperatures in the thickness are known at any time of the process. The temperature is colder than the initial process temperature with lower values on the upper and lower surfaces of the prepreg that are in contact with the tools. These temperatures are 25–50 °C lower than the initial temperature, which is important with regard to mechanical properties.

Concerning thermoforming of thermoplastic prepregs and its simulation, details of the formulations, complementary simulations and other examples can be found in Guzman-Maldonado et al. (2015, 2016, 2018).

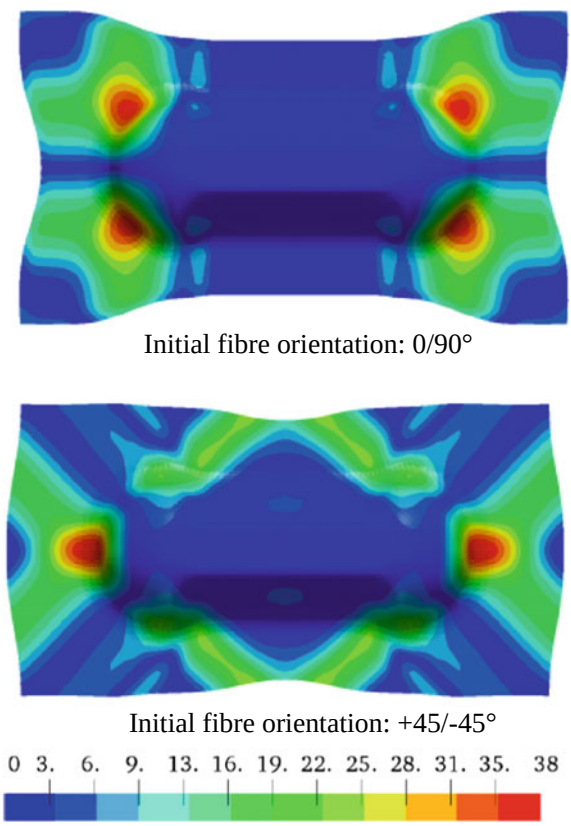

Fig. 4.31 Shear angle (in degree) in the case of a simulation at constant temperature T = 300 °C

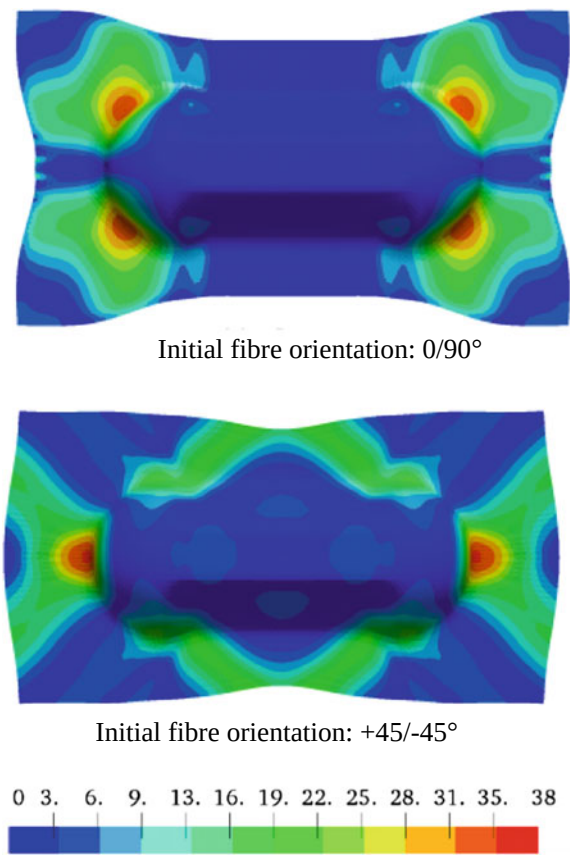

Fig. 4.32 Shear angle (in degree) in the case of a simulation taking into account the temperature evolution

Conclusions and Perspectives

Simulation of the forming processes of composite reinforcements is an important instrument for the development of these materials. It determines the conditions for processes to be carried out satisfactorily for a given geometry and material. The simulation also provides the position of the fibres after forming, which determines the mechanical properties of the composite part. Not all geometries can be achieved with a continuous fibre reinforcement. It is also a question that can be answered by simulation.

The simulation approaches described in this chapter are macroscopic, i.e. dry fibrous reinforcements or prepregs are modelled as continuous media, generally of the shell type. These macroscopic approaches are currently the most common for applications. Nevertheless, simulations at the microscopic (fibre scale) or mesoscopic scale are currently being developed (Durville 2010; Gatouillat et al. 2013; Rahali

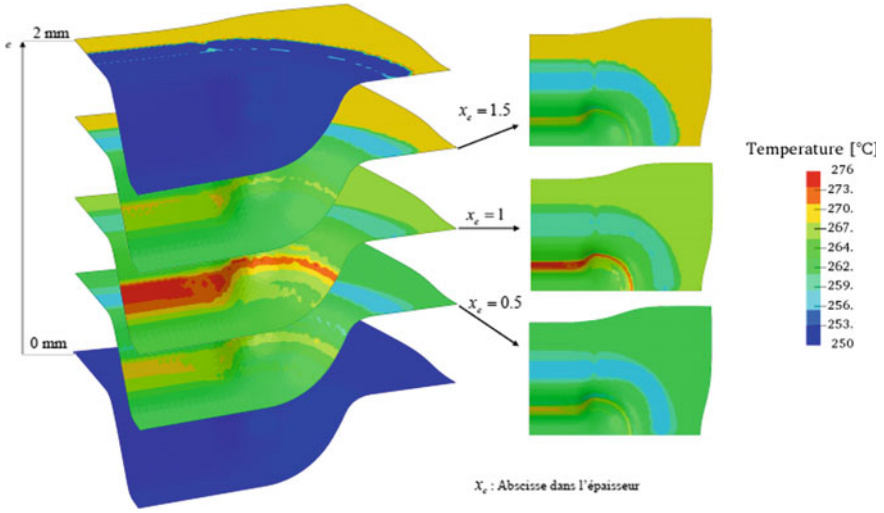

Fig. 4.33 Temperature gradient in the thickness at the end of process

et al. 2016). They have the advantage of naturally describing the physics of the deformation of the fibrous medium made up of fibres in contact. If they require a significant numerical effort, these approaches will probably develop in the future.

References

Advani, S. G. (Ed.). (1994). *Flow and rheology in polymer composites manufacturing* (No. 10). Elsevier Science.

Alshahrani, H., & Hojjati, M. (2017). A new test method for the characterization of the bending behavior of textile prepregs. *Composites Part A Applied Science and Manufacturing, 97,* 128–140.

ASTM. (2002). *Standard test method for stiffness of fabrics*, chap. D1388–D1396. Philadelphia: American Society for Testing and Materials.

Boisse, P. (2007) Finite element analysis of composite forming. In A. C. Long (Ed.), *Composite forming technologies*. Woodhead Publishing Limited.

Boisse, P., Colmars, J., Hamila, N., Naouar, N., & Steer, Q. (2018). Bending and wrinkling of composite fiber preforms and prepregs. A review and new developments in the draping simulations. *Composites Part B Engineering, 141,* 234–249.

Boisse, P., Hamila, N., Guzman-Maldonado, E., Madeo, A., Hivet, G., & Dell'Isola, F. (2017). The bias-extension test for the analysis of in-plane shear properties of textile composite reinforcements and prepregs: A review. *International Journal of Material Forming, 10*(4), 473–492.

Boisse, P., Hamila, N., Vidal-Sallé, E., & Dumont, F. (2011). Simulation of wrinkling during textile composite reinforcement forming. Influence of tensile, in-plane shear and bending stiffnesses. *Composites Science and Technology, 71*(5), 683–692.

Boisse, P., Zouari, B., & Gasser, A. (2005). A mesoscopic approach for the simulation of woven fibre composite forming. *Composites Science and Technology, 65*(3–4), 429–436.

Buet-Gautier, K., & Boisse, P. (2001). Experimental analysis and modeling of biaxial mechanical behavior of woven composite reinforcements. *Experimental Mechanics, 41*(3), 260–269.

Bussetta, P., & Correia, N. (2018). Numerical forming of continuous fibre reinforced composite material: A review. *Composites Part A Applied Science and Manufacturing, 113,* 12–31.

Cao, J., Akkerman, R., Boisse, P., Chen, J., et al. (2008). Characterization of mechanical behavior of woven fabrics: Experimental methods and benchmark results. *Composites Part A, 39,* 1037–1053.

Carvelli, V., Corazza, C., & Poggi, C. (2008). Mechanical modelling of monofilament technical textiles. *Computational Materials Science, 42*(4), 679–691.

Charmetant, A., Orliac, J. G., Vidal-Sallé, E., & Boisse, P. (2012). Hyperelastic model for large deformation analyses of 3D interlock composite preforms. *Composites Science and Technology, 72*(12), 1352–1360.

Criscione, J. C., Douglas, A. S., & Hunter, W. C. (2001). Physically based strain invariant set for materials exhibiting transversely isotropic behavior. *Journal of the Mechanics and Physics of Solids, 49*(4), 871–897.

D'Agostino, M. V., Giorgio, I., Greco, L., Madeo, A., & Boisse, P. (2015). Continuum and discrete models for structures including (quasi-) inextensible elasticae with a view to the design and modeling of composite reinforcements. *International Journal of Solids and Structures, 59,* 1–17.

Dangora, L. M., Hansen, C. J., Mitchell, C. J., Sherwood, J. A., & Parker, J. C. (2015a). Challenges associated with shear characterization of a cross-ply thermoplastic lamina using picture frame tests. *Composites Part A Applied Science and Manufacturing, 78,* 181–190.

Dangora, L. M., Mitchell, C. J., & Sherwood, J. A. (2015b). Predictive model for the detection of out-of-plane defects formed during textile-composite manufacture. *Composites Part A Applied Science and Manufacturing, 78,* 102–112.

Dangora, L. M., Mitchell, C., White, K. D., Sherwood, J. A., & Parker, J. C. (2018). Characterization of temperature-dependent tensile and flexural rigidities of a cross-ply thermoplastic lamina with implementation into a forming model. *International Journal of Material Forming, 11*(1), 43–52.

Daniel, J. L., Soulat, D., Dumont, F., Zouari, B., Boisse, P., & Long, A. C. (2003). Forming of a very unbalanced fabric experiment and simulation. *International Journal of Forming Processes, 6*(3–4), 465–480.

De Bilbao, E., Soulat, D., Hivet, G., & Gasser, A. (2010). Experimental study of bending behaviour of reinforcements. *Experimental Mechanics, 50*(3), 333–351.

De Luca, P. L. A. P. P., Lefébure, P., & Pickett, A. K. (1998). Numerical and experimental investigation of some press forming parameters of two fibre reinforced thermoplastics: APC2-AS4 and PEI-CETEX. *Composites Part A Applied Science and Manufacturing, 29*(1–2), 101–110.

Döbrich, O., Gereke, T., Diestel, O., Krzywinski, S., & Cherif, C. (2014). Decoupling the bending behavior and the membrane properties of finite shell elements for a correct description of the mechanical behavior of textiles with a laminate formulation. *Journal of Industrial Textiles, 44*(1), 70–84.

Dörr, D., Schirmaier, F. J., Henning, F., & Kärger, L. (2017). A viscoelastic approach for modeling bending behavior in finite element forming simulation of continuously fiber reinforced composites. *Composites Part A Applied Science and Manufacturing, 94,* 113–123.

Durville, D. (2010). Simulation of the mechanical behaviour of woven fabrics at the scale of fibers. *International Journal of Material Forming, 3*(2), 1241–1251.

Fetfatsidis, K. A., Sherwood, J. A., Chen, J., & Jauffres, D. (2009). Characterization of the fabric/tool and fabric/fabric friction during the thermostamping process. *International Journal of Material Forming, 2*(1), 165.

Gatouillat, S., Bareggi, A., Vidal-Sallé, E., & Boisse, P. (2013). Meso modelling for composite preform shaping—Simulation of the loss of cohesion of the woven fibre network. *Composites Part A Applied Science and Manufacturing, 54,* 135–144.

Gereke, T., Döbrich, O., Hübner, M., & Cherif, C. (2013). Experimental and computational composite textile reinforcement forming: A review. *Composites: Part A, 46,* 1–10.

Guzman-Maldonado, E. (2016). *Modelling and simulation of the forming of continuous bre thermoplastics composites.* Ph.D. thesis, INSA Lyon France.

Guzman-Maldonado, E., Hamila, N., Boisse, P., & Bikard, J. (2015). Thermomechanical analysis, modelling and simulation of the forming of pre-impregnated thermoplastics composites. *Composites Part A Applied Science and Manufacturing, 78,* 211–222.

Guzman-Maldonado, E., Hamila, N., Naouar, N., Moulin, G., & Boisse, P. (2016). Simulation of thermoplastic prepreg thermoforming based on a visco-hyperelastic model and a thermal homogenization. *Materials and Design, 93,* 431–442.

Guzman-Maldonado, E., Hu, X., Hamila, N., & Boisse, P. (2018). Modélisation du procédé de thermoestampage de composites préimprégnés à matrice thermoplastique. *Revue des Composites et des Matériaux Avances, 28*(1), 9–33.

Hamila, N., & Boisse, P. (2007). A meso–macro three node finite element for draping of textile composite preforms. *Applied Composite Materials, 14*(4), 235–250.

Hamila, N., Boisse, P., Sabourin, F., & Brunet, M. (2009). A semi-discrete shell finite element for textile composite reinforcement forming simulation. *International Journal for Numerical Methods in Engineering, 79*(12), 1443–1466.

Harrison, P., Clifford, M. J., & Long, A. C. (2004). Shear characterisation of viscous woven textile composites, a comparison between picture frame and bias-extension experiments. *Composites Science and Technology, 64,* 1453–1465.

Harrison, P., Gomes, R., & Curado-Correia, N. (2013). Press forming a 0/90 cross-ply advanced thermoplastic composite using the double-dome benchmark geometry. *Composites Part A Applied Science and Manufacturing, 54,* 56–69.

Hsiao, S. W., & Kikuchi, N. (1999). Numerical analysis and optimal design of composite thermoforming process. *Computer Methods in Applied Mechanics and Engineering, 177*(1–2), 1–34.

ISO. (2011). *Reinforcement fabrics—Determination of conventional flexural stiffness—Fixed-angle flexometer method ISO 4604.*

Kawabata, S. (1980). *The standardardization and analysis of hand evaluation*. Osaka: The Textile Machinary Society.

Khan, M. A. (2009). *Numerical and experimental forming analysis of textile composite reinforcements based on a hypoelastic approach*. Ph.D. thesis, INSA Lyon France.

Khan, M. A., Mabrouki, T., Vidal-Sallé, E., & Boisse, P. (2010). Numerical and experimental analyses of woven composite reinforcement forming using a hypoelastic behaviour. Application to the double dome benchmark. *Journal of Materials Processing Technology, 210*(2), 378–388.

Lahey, T. J., & Heppler, G. R. (2004). Mechanical modeling of fabrics in bending. *Journal of Applied Mechanics, 71*(1), 32–40.

Launay, J., Hivet, G., Duong, A. V., & Boisse, P. (2008). Experimental analysis of the influence of tensions on in plane shear behaviour of woven composite reinforcements. *Composites Science and Technology, 68,* 506–515.

Launay, J., Lahmar, F., Boisse, P., & Vacher, P. (2002). Strain measurement in tests on fibre fabric by image correlation method. *Advanced Composites Letters, 11*(1).

Lebrun, G., Bureau, M. N., & Denault, J. (2003). Evaluation of bias-extension and picture-frame test methods for the measurement of intraply shear properties of PP/glass commingled fabrics. *Composite Structures, 61*(4), 341–352.

Lee, J. S., Hong, S. J., Yu, W. R., & Kang, T. J. (2007). The effect of blank holder force on the stamp forming behavior of non-crimp fabric with a chain stitch. *Composites Science and Technology, 67*(3–4), 357–366.

Lee, W., Um, M. K., Byun, J. H., Boisse, P., & Cao, J. (2010). Numerical study on thermo-stamping of woven fabric composites based on double-dome stretch forming. *International Journal of Material Forming, 3*(2), 1217–1227.

Liang, B. (2016). *Experimental and numerical study of the bending behaviour of textile reinforcements and thermoplastic prepregs*. Ph.D. thesis, INSA Lyon France.

Liang, B., Chaudet, P., & Boisse, P. (2017). Curvature determination in the bending test of continuous fibre reinforcements. *Strain, 53*(1), e12213.

Liang, B., Hamila, N., Peillon, M., & Boisse, P. (2014). Analysis of thermoplastic prepreg bending stiffness during manufacturing and of its influence on wrinkling simulations. *Composites Part A Applied Science and Manufacturing, 67,* 111–122.

Lin, H., Wang, J., Long, A. C., Clifford, M. J., & Harrison, P. (2007). Predictive modelling for optimization of textile composite forming. *Composites Science and Technology, 67*(15–16), 3242–3252.

Long, A. C., & Rudd, C. D. (1994). A simulation of reinforcement deformation during the production of preforms for liquid moulding processes. *Proceedings of the Institution of Mechanical Engineers, Part B: Journal of Engineering Manufacture, 208*(4), 269–278.

Margossian, A., Bel, S., & Hinterhoelzl, R. (2015). Bending characterisation of a molten unidirectional carbon fibre reinforced thermoplastic composite using a dynamic mechanical analysis system. *Composites Part A Applied Science and Manufacturing, 77,* 154–163.

Naouar, N., Vidal-Salle, E., Schneider, J., Maire, E., & Boisse, P. (2015). 3D composite reinforcement meso FE analyses based on X-ray computed tomography. *Composite Structures, 132,* 1094–1104.

Onate, E., & Zárate, F. (2000). Rotation-free triangular plate and shell elements. *International Journal for Numerical Methods in Engineering, 47*(1–3), 557–603.

Peirce, F. T. (1930). The "handle" of cloth as a measurable quantity. *Journal of the Textile Institute Transactions, 21*(9), T377–T416.

Peng, X., & Rehman, Z. U. (2011). Textile composite double dome stamping simulation using a non-orthogonal constitutive model. *Composites Science and Technology, 71*(8), 1075–1081.

Pickett, A. K. (2002). Review of finite element simulation methods applied to manufacturing and failure prediction in composites structures. *Applied Composite Materials, 9*(1), 43–58.

Plasfib, Software. (2015). *Interdeposit certification*. Paris: Agency for the Protection of Programs.

Potluri, P., Sharma, S., & Ramgulam, R. (2001). Comprehensive drape modelling for moulding 3D textile preforms. *Composites Part A Applied Science and Manufacturing, 32*(10), 1415–1424.

Potter, K. (2002). Bias extension measurements on cross-plied unidirectional prepreg. *Composites Part A Applied Science and Manufacturing, 33*(1), 63–73.

Prodromou, A. G., & Chen, J. (1997). On the relationship between shear angle and wrinkling of textile composite preforms. *Composites Part A Applied Science and Manufacturing, 28*(5), 491–503.

Rahali, Y., Assidi, M., Goda, I., Zghal, A., & Ganghoffer, J. F. (2016). Computation of the effective mechanical properties including nonclassical moduli of 2.5 D and 3D interlocks by micromechanical approaches. *Composites Part B Engineering, 98,* 194–212.

Rudd, C. D., & Long, A. C. (1997). *Liquid molding technologies*. Cambridge: Woodhead Publishing.

Sabourin, F., & Brunet, M. (2006). Detailed formulation of the rotation-free triangular element "S3" for general purpose shell analysis. *Engineering Computations, 23*(5), 469–502.

Sachs, U., & Akkerman, R. (2017). Viscoelastic bending model for continuous fiber-reinforced thermoplastic composites in melt. *Composites Part A Applied Science and Manufacturing, 100,* 333–341.

Schnur, D. S., & Zabaras, N. (1992). An inverse method for determining elastic material properties and a material interface. *International Journal for Numerical Methods in Engineering, 33*(10), 2039–2057.

Sharma, S. B., Sutcliffe, M. P. F., & Chang, S. H. (2003). Characterisation of material properties for draping of dry woven composite material. *Composites Part A Applied Science and Manufacturing, 34*(12), 1167–1175.

Simo, J. C. (1987). On a fully three-dimensional finite-strain viscoelastic damage model: Formulation and computational aspects. *Computer Methods in Applied Mechanics and Engineering, 60*(2), 153–173.

Ten Thije, R. H. W., Akkerman, R., & Huétink, J. (2007). Large deformation simulation of anisotropic material using an updated Lagrangian finite element method. *Computer Methods in Applied Mechanics and Engineering, 196*(33–34), 3141–3150.

Van Der Weeën, F. (1991). Algorithms for draping fabrics on doubly-curved surfaces. *International Journal for Numerical Methods in Engineering, 31*(7), 1415–1426.

Wang, P., Hamila, N., Pineau, P., & Boisse, P. (2012). Thermomechanical analysis of thermoplastic composite prepregs using bias-extension test. *Journal of Thermoplastic Composite Materials, 27*(5), 679–698.

Willems, A., Lomov, S. V., Vandepitte, D., & Verpoest, I. (2006). Double dome forming simulation of woven textile composites. In *7th International Conference on ESAFORM* (pp. 26–28).

Willems, A., Lomov, S. V., Verpoest, I., Vandepitte, D., Harrison, P., & Yu, W. R. (2008). Forming simulation of a thermoplastic commingled woven textile on a double dome. *International Journal of Material Forming, 1*(1), 965–968.

Woven Composites Benchmark Forum. (2008). Retrieved from http://www.wovencomposites.org/index.php.

Zhu, B., Yu, T. X., Teng, J., & Tao, X. M. (2009). Theoretical modeling of large shear deformation and wrinkling of plain woven composite. *Journal of Composite Materials, 43*(2), 125–138.